Universität Potsdam
Institut für Physik und Astronomie

Mass Wasting and the Coriolis Effect on Asteroid Vesta

Dissertation
zur Erlangung des akademischen Grades
doctor rerum naturalium (Dr. rer. nat.)
in der Wissenschaftsdisziplin theoretische Physik

eingereicht an der
Mathematisch-Naturwissenschaftlichen Fakultät
der Universität Potsdam

von

Katharina Alexandra Otto

Potsdam, August 2015

1. Gutachter:	Prof. Dr. Ralf Jaumann
	Deutsches Zentrum für Luft- und Raumfahrt (DLR)
	Institut für Planetenforschung
	Freie Universität Berlin
	Institut für Geologische Wissenschaften
2. Gutachter:	Prof. Dr. Jürgen Blum
	Universität Braunschweig
	Institut für Geophysik und Extraterrestrische Physik
3. Gutachter:	Prof. Dr. Anders Levermann
	Universität Potsdam
	Potsdam-Institut für Klimafolgenforschung

Tag der Disputation: 15. Dezember 2015

Published online at the
Institutional Repository of the University of Potsdam:
URN urn:nbn:de:kobv:517-opus4-87390
http://nbn-resolving.de/urn:nbn:de:kobv:517-opus4-87390

Erklärung der Urheberschaft

Ich versichere, dass ich die vorliegende Arbeit selbstständig verfasst habe und dass ich keine anderen als die angegebenen Quellen und Hilfsmittel verwendet habe. Ich habe die Arbeit zuvor an keiner anderen Hochschule eingereicht.

Katharina A. Otto
Potsdam, 27. August 2015

In Erinnerung
an meine Oma Lilo

Acknowledgements

I would not have managed to complete this thesis without the support of my supervisors, colleagues, workplace, friends and family, and it is difficult to know where to begin when acknowledging so many people.

I will start with my supervisors, Prof. Ralf Jaumann and Prof. Frank Spahn. Prof. Jaumann, thank you for providing me with the opportunity to undertake my PhD research at DLR, for your detailed supervision whilst still giving me the chance to work independently and for all the inspiration and advice you provided. Prof. Spahn, thank you for the chance to submit this thesis at the University of Potsdam, for valuable discussion and for proofreading this thesis.

Thank you to my colleagues in the Dawn Team, especially Christopher Russell and Carol Raymond, for making me so welcome and providing such a friendly and helpful environment in which I have been able to discuss and improve my work.

Dr. Ekkehard Kührt, who together with Prof. Jaumann has shown great faith in my abilities and provided me with the opportunity to continue my research after my PhD, thank you for this, and thank you for your patience and understanding whilst I finished writing this thesis.

Thank you to my friends and colleagues at DLR, both former and current, for your support, encouragement, advice, proofreading and cooperation. You've made DLR a great place to work and I look forward to being there in the future.

I'd also like to thank DLR itself, for its technical and educational support. In particular I have greatly appreciated participating in the Graduate Programme.

Finally, last but certainly not least, I thank my family for their support over the years. I would not be here without you. Jon, thank you for your support and encouragement in busy and stressful times. Thank you for patiently digging through my English and for your versatile advice. I am particularly grateful for the motivation by my Opa Rolf who introduced me to the joy of physics and astronomy, and my Oma Lilo, who always believed in my success and diligence.

Kurzfassung

In dieser Arbeit wurden Massenbewegungen im Rheasilvia-Einschlagsbecken der Südhemisphäre des Asteroiden (4) Vesta untersucht. Die Besonderheiten des Beckens sind seine Größe von 500 km Durchmesser, die Lage des Zentrums, welche nahezu mit der Rotationsachse Vestas übereinstimmt und die Überlagerung mit dem ähnlich großen Einschlagsbecken Venenia.

Die meisten Massenbewegungen, wie Hangrutschungen oder Lawinen, sind aufgrund ihrer relativ kleinen Bewegungsdistanzen nicht sichtbar von der Corioliskraft beeinflusst worden. Jedoch weist die Krümmung von einigen radialen Bergrücken darauf hin, dass diese durch Massenbewegungen im Modifikationsprozess des Rheasilvia-Einschlags entstanden sein könnten. Danach wurden sie durch die Corioliskraft während der Bewegung in Richtung Kraterboden abgelenkt.

In dieser Arbeit wurden 32 gekrümmte Bergrücken untersucht, um herauszufinden, ob diese durch die Corioliskraft beeinflusst wurden. Dazu wurden mehrere Inertialkreise an die gekrümmten Bergrücken angepasst und mit Hilfe der Kenntnisse über Form und Rotation von Vesta Geschwindigkeitsprofile der Massenbewegungen erstellt. Zur Bestimmung der Geschwindigkeit an einem Punkt wurde eine interaktive und statistische Methode entwickelt, die automatisiert an jeden Punkt auf dem gekrümmten Bergrücken mehrere Interialkreise anpasste. Der am häufigsten vorkommende Intertialradius eines Punktes wurde folglich benutzt um die Geschwindigkeit an diesem Punkt zu bestimmen.

Das Ergebnis der Geschwindigkeitsanalyse bekräftigt die Corioliskraft als Ursache für die Krümmung der Bergrücken. Die Geschwindigkeiten (29.6 ± 24.6 m/s) stimmen nicht nur mit zuvor numerisch simulierten Geschwindigkeiten des Rheasilvia-Beckens überein, sondern topographische Eigenschaften, wie die Hangneigung und Massenablagerungen, sind ebenfalls mit den resultierenden Beschleunigungen und Verlangsamungen im Einklang.

Abschnitte mit konstanter Beschleunigung, Verlangsamung und Geschwindigkeit zeigen, dass die Massenbewegungen in heterogenem Regolith mit unterschiedlicher Topographie und Reibung stattgefunden haben müssen. Außerdem konnten Materialeigenschaften wie die effektive Viskosität (1.9–$9.0 \cdot 10^6$ Pa·s) und der effektive Reibungskoeffizient (0.02–0.81) des Materials abgeschätzt werden.

Die gemessenen Beschleunigungen an der Kraterwand weisen darauf hin, dass der Hangwinkel zur Zeit der Massenbewegungen steiler gewesen sein

muss als gegenwärtig beobachtet werden kann.

Diese Arbeit lieferte neue Einsichten in das Verhalten von Material während des Rheasilvia-Einschlags. Zum ersten Mal konnte so gezeigt werden, dass der Coriolis-Effekt einen Einfluss auf die Massenbewegungen während eines Einschlagsprozesses haben kann und dass die erzeugten Krümmungen bis heute beobachtbar sind.

Abstract

This work investigates the influence of the Coriolis force on mass motion related to the Rheasilvia impact basin on asteroid (4) Vesta's southern hemisphere. The giant basin is 500 km in diameter, with a centre which nearly coincides with the rotation axis of Vesta. The Rheasilvia basin partially overlaps an earlier, similarly large impact basin, Veneneia.

Mass motion within and in the vicinity of the Rheasilvia basin includes slumping and landslides, which, primarily due to their small linear extents, have not been noticeably affected by the Coriolis force. However, a series of ridges related to the basin exhibit significant curvature, which may record the effect of the Coriolis force on the mass motion which generated them.

In this thesis 32 of these curved ridges, in three geologically distinct regions, were examined. The mass motion velocities from which the ridge curvatures may have resulted during the crater modification stage were investigated. Velocity profiles were derived by fitting inertial circles along the curved ridges and considering both the current and past rotation states of Vesta. An iterative, statistical approach was used, whereby the radii of inertial circles were obtained through repeated fitting to triplets of points across the ridges. The most frequently found radius for each central point was then used for velocity derivation at that point.

The results of the velocity analysis are strongly supportive of a Coriolis force origin for the curved ridges. Derived velocities (29.6 ± 24.6 m/s) generally agree well with previously published predictions from numerical simulations of mass motion during the impact process. Topographical features such as local slope gradient and mass deposition regions on the curved ridges also independently agree with regions in which the calculated mass motion accelerates or decelerates.

Sections of constant acceleration, deceleration and constant velocity are found, showing that mass motion is being governed by varying conditions of

topography, regolith structure and friction. Estimates of material properties such as the effective viscosities (1.9–9.0·10^6 Pa·s) and coefficients of friction (0.02–0.81) are derived from the velocity profile information in these sections. From measured accelerations of mass motions on the crater wall, it is also shown that the crater walls must have been locally steeper at the time of the mass motion.

Together with these novel insights into the state and behaviour of material moving during the modification stage of Rheasilvia's formation, this work represents the first time that the Coriolis Effect on mass motions during crater formation has been shown to result in diagnostic features preserved until today.

Contents

1. Introduction

1.1. Motivation

Every solar system body experiences collisions with other objects throughout its lifetime. While smaller bodies may disrupt or simply disintegrate in the impact event, larger bodies, such as the Moon or asteroid Vesta, often show a landscape of impact craters on their surfaces [e.g. *Jaumann et al.*, 2012].

Understanding the morphology, distribution and formation of impact craters on planetary bodies is relevant to many scientific questions related to geophysics, planetary science and geology. For example, subsurface material is distributed over the surface during the impact excavation [e.g. *Melosh*, 1989]. Consequently, geologists can analyse the mineralogy and composition of material previously hidden in the underground. Furthermore, planetary scientists can determine relative and absolute surface ages from the size-frequency distribution of impact craters on geologic surfaces [e.g. *Neukum*, 1984].

Geophysicists may also be interested in the behaviour of material under the extreme pressure and temperature conditions experienced during an impact event. For example, the formation of complex craters exhibiting a central peak needs temporary low internal friction (e.g. acoustic fluidization [*Melosh*, 1979]) to explain the preservation of the central peak. Material mobility during the modification stage of the unstable crater cavity is thus larger than that expected for cohesive or granular materials. However this stage has never been observed in situ nor is it possible to set up an experiment with planetary dimensions to investigate the material properties and dynamics of the impact process. Therefore, the standard approach for investigating these characteristics is the use of numerical simulations [e.g. *Jutzi et al.*, 2013].

Promisingly for impact research, the asteroid Vesta - recently explored by NASA's Dawn mission [*Russell and Raymond*, 2011] - has a large complex central crater [*Thomas et al.*, 1997a; *Jaumann et al.*, 2012; *Schenk et al.*, 2012], named Rheasilvia. Rheasilvia exhibits a set of curved ridges that may have been formed by the Coriolis deflection of highly mobilized material during crater formation. The data collected by the Framing Camera on board the Dawn spacecraft [*Sierks et al.*, 2011] not only showed the curvature of these ridges in detail but was also used to determine the current shape, axes and rotation period [*Konopliv et al.*, 2014]. With this information it is

possible to determine the Coriolis-deflected mass-wasting velocities occurring during the impact event. The Rheasilvia impact therefore represents a unique opportunity to look into the impact dynamics of complex basin formation without a priori assumptions regarding material properties or impact energies, as necessary for impact simulations. The actual material properties can then be derived from the mass motion velocities.

The results of this investigation will not only verify numerical impact simulations, but it will also provide insight into one of the most violent events in Vesta's history. The geology of Vesta is highly modified by the Rheasilvia impact event and almost the entire southern hemisphere is shaped by the impact basin and ejecta [*Jaumann et al.*, 2012; *Schenk et al.*, 2012]. Understanding the Rheasilvia formation process is therefore key to interpreting the geology and evolution of Vesta.

1.2. Outline

This thesis is composed of eight further chapters. In Chapter 2 the general context including the Main Asteroid Belt, the Dawn Mission and asteroid Vesta is introduced. This chapter is followed by an introduction to the theoretical background, focussing on the dynamics of impact cratering and the Coriolis Effect (Chapter 3). Chapter 4 presents the data used in this thesis. The geologic setting of the curved ridges within the Rheasilvia basin with a focus on the Coriolis Effect on mass-wasting processes is introduced in Chapter 5. This chapter is an edited version of the publication "Otto, K.A., Jaumann, R., Krohn, K., Matz, K.-D., Preusker, F., Roatsch, T., Schenk, P., Scholten, F., Stephan, K., Raymond, C.A. and Russell, C.T. (2013) Mass-Wasting Features and Processes in Vesta's South Polar Basin Rheasilvia. *Journal of Geophysical Research: Planets*, 118(11):2279–2294, doi:10.1002/2013JE004333". The method for deriving mass-wasting velocities from the curved ridges is described in Chapter 6. The resulting mass-wasting velocities for three distinct geologic regions are presented in Chapter 7. Subsequently, Chapter 8 discusses the applicability of the Coriolis Effect on the Rheasilvia curved ridges and derives constraints on the cratering process. Furthermore, material properties such as the effective viscosity and coefficient of friction of the mass-wasting material are derived from the dynamic profile of the curved ridges. Finally, conclusions are reached and the results are summarised in Chapter 9.

2. The Main Asteroid Belt

2.1. The Main Asteroid Belt at a Glance

The Main Asteroid Belt is a population of asteroids orbiting the sun between the orbits of Mars and Jupiter. The largest member, (1) Ceres, was the first to be discovered in 1801 by Guiseppe Piazzi followed by (2) Pallas, discovered by Wilhelm Olbers in 1802, and (3) Juno, discovered by Karl Harding in 1804 [e.g. *Russell and Raymond*, 2011; *Foderà Serio et al.*, 2002]. In 1807 Olbers discovered the third largest and second most massive main-belt asteroid, (4) Vesta (Section 2.4), the focus of this thesis.

Since then hundreds of thousands more asteroids have been discovered. Today the population is estimated to number half a million objects larger than 1.6 km in diameter with fewer than 20 of them exceeding 250 km [*Garlick*, 2003]. Figure 2.1 shows some examples of asteroids visited by spacecraft. Their orbital semi-major axes range from ∼2.1 AU to ∼3.3 AU, with eccentricities up to ∼0.25[1] and inclinations up to ∼20°. Asteroids with similar orbital elements form dynamically linked families which, in most cases, arise via disruption of a larger asteroid [*Farinella et al.*, 1982].

The distribution of asteroid orbits is punctuated by gaps at various orbital distances (Figure 2.2), which are caused by orbital resonances with the giant planet Jupiter (Kirkwood resonances [*Garlick*, 1888]). For semi-major axes where the orbital periods are integer multiples of Jupiter's orbital period, the regularly repeated gravitational pull eventually causes an asteroid to leave the asteroid belt and potentially cross planetary orbits. Another important resonance is the υ_6 secular resonance with Saturn, which arises when the perihelion precession of an asteroid's orbit is synchronized with that of Saturn. This resonance sets the lower boundary to the semi-major axis and the maximum inclination of the Main Asteroid Belt [*Britt et al.*, 2007]. Today the total mass of the Main Asteroid Belt is $\sim 6 \cdot 10^{-4}$ Earth masses [*Krasinsky et al.*, 2002].

Based on their spectral reflectivities, which are related to their surface composition, the asteroids are divided into taxonomic classes. The commonly used Small Main-Belt Asteroid Spectroscopic Survey (SMASSII) classification

[1] For comparison, the eccentricities of Earth and Mars are 0.02 and 0.09, respectively.

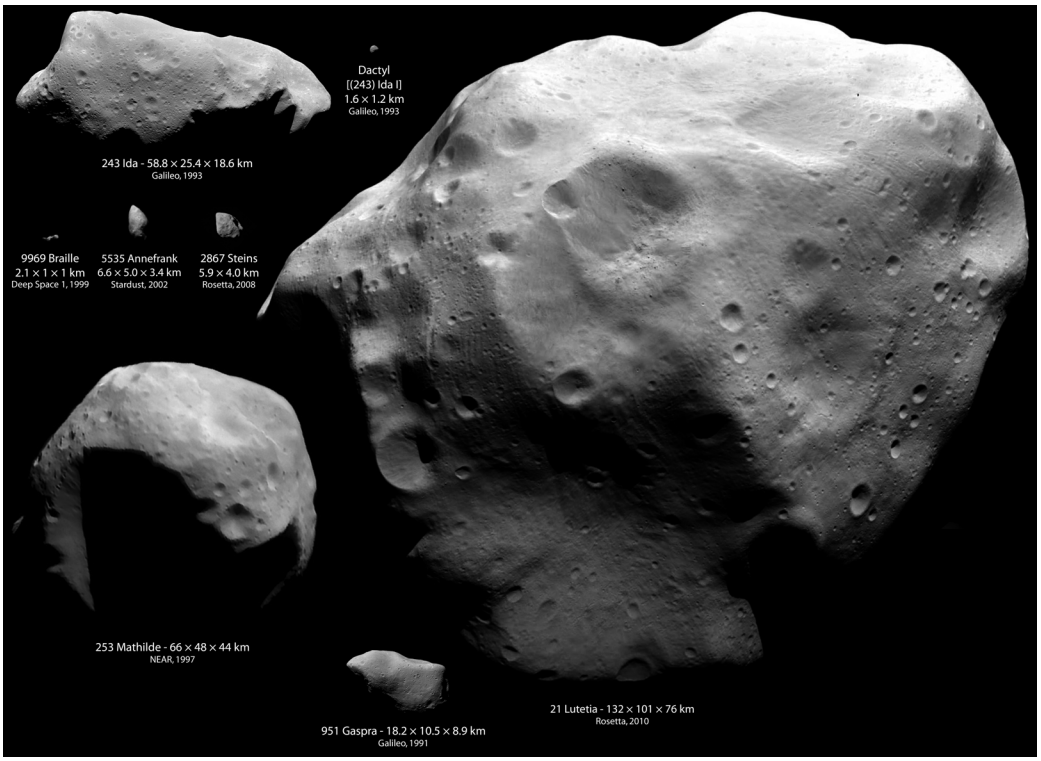

Figure 2.1.: Examples of some main-belt asteroids visited by spacecraft. The dimensions and visiting spacecraft are labelled. This image was modified from a version published at http://apod.nasa.gov/apod/ap100726.html. *Credit: ESA/NASA/JAXA/RAS/JHUAPL/UMD/OSIRIS.*

is based on predefined principal components, e.g. the slope in the visible wavelengths (0.435–0.925 µm) (Slope in Figure 2.3) and the presence and strength of the 1 µm absorption band (PC2' in Figure 2.3) [*Bus and Binzel*, 2002a,b; *Bus et al.*, 2002]. The three major groupings are the S-, C- and X-complexes. The S-types are dominant in the inner asteroid belt (near 2.1 AU) [*Gradie and Tedesco*, 1982] and of silicaceous or stony composition. The C-types are most abundant in the outer asteroid belt (near 3 AU) [*Gradie and Tedesco*, 1982] and of carbonaceous composition with low albedo. They form the largest group of asteroids. X-type asteroids are similar to C-type asteroids but generally exhibit higher albedos.

Figure 2.4 shows the spectrum of Vesta obtained by the Infrared Telescope Facility (IRTF) in 2011. Asteroid Vesta is the largest member of the V-type asteroids with a steep UV-slope and two strong absorptions centred at 0.9 µm

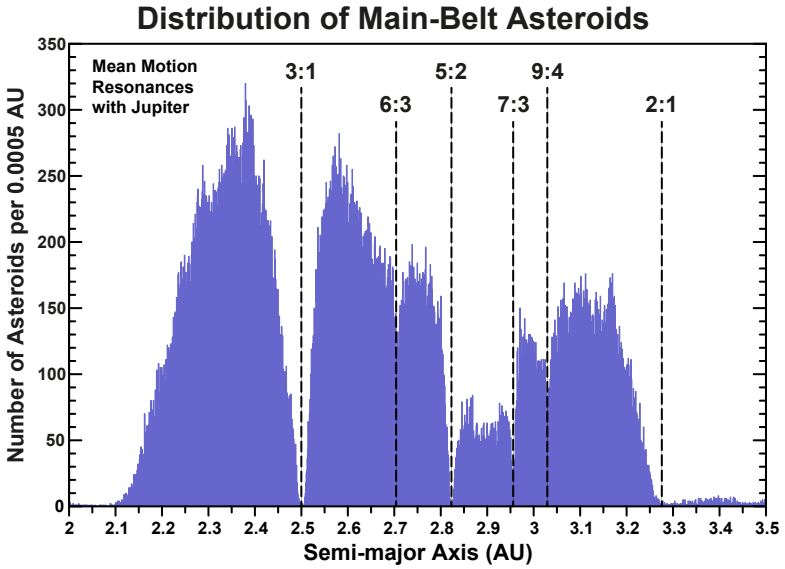

Figure 2.2.: The distribution of nearly 157,000 numbered asteroids of the Main Asteroid Belt binned in 0.0005 AU sections. The mean motion resonances with Jupiter are labelled. The υ_6 resonance sets the lower limit to the asteroid distribution at 2.1 AU but varies with inclination. This plot is reproduced from a graph provided by A. Chamberlin (JPL/Caltech, 2007) and is available at http://ssd.jpl.nasa.gov/?histo_a_ast.

and 2 µm caused by electronic absorption of Fe^{2+} in orthopyroxenes. The absorption features are easily distinguished from the S-, C- and X-complexes in Figure 2.3 due to their deeper absorption at ∼1 µm. The spectrally and dynamically connected V-type asteroids are most probably fragments of Vesta that were excavated through impacts. Samples of this family are the Howardite, Eucrite and Diogenite (HED) meteorites [e.g. *McSween et al.*, 2011; *Binzel and Xu*, 1993; *McCord et al.*, 1970] (Section 2.4.1).

The different taxonomic classes are indicative of different formation and evolutionary processes for the asteroids in the main belt. Dust and ice grains accreted in the early Solar System to form larger bodies, so-called planetesimals. Depending on the accretion location and time, larger planetesimals (a few tens to hundreds of kilometres) may have undergone subsequent differentiation[2] [e.g. *McCoy et al.*, 2006; *McSween et al.*, 2002]. Impacts have broken up most of these bodies into monolithic fragments with compositions repre-

[2]These asteroids are represented by the achondritic meteorites found on Earth, such as the HEDs.

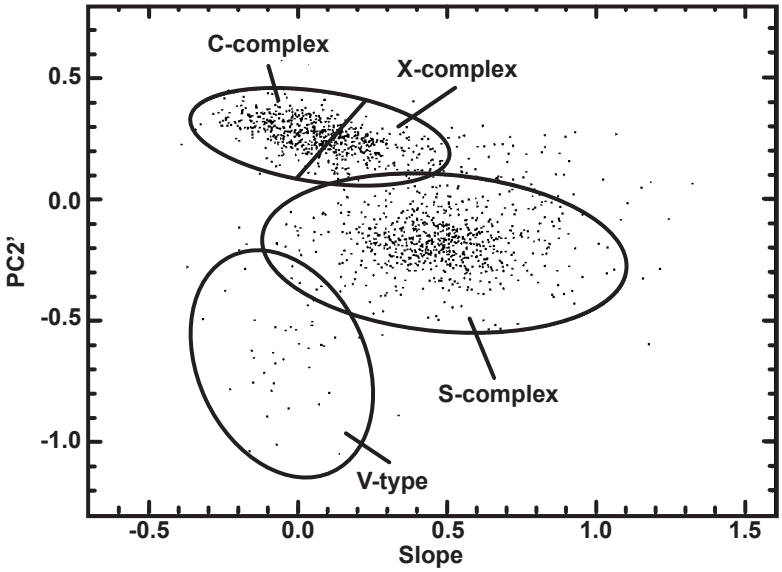

Figure 2.3.: Illustration of taxonomic classes based on the first two principal components (Slope and PC2', see text for details) for 1443 Small Main-Belt Asteroid Spectroscopic Survey (SMASSII) asteroids. The slope describes the change of reflectivity in the visible wavelengths and the principal component 2 (PC2') illustrates the strength of the 1 µm absorption band. The S-complex is easily distinguishable from the C- and X-complexes. The C- and X-complexes are mainly separated by their albedo. The location of V-type asteroids is sketched for reference. They form a separate class dynamically and spectrally associated with asteroid Vesta [*Binzel and Xu*, 1993]. The boundaries are approximate. Data extracted from *Bus and Binzel* [2002a], Copyright (2002), with permission from Elsevier Ltd.

senting those of their previous locations inside the parent body. Additionally, the debris may have coalesced to form rubble-pile asteroids [e.g. *Fujiwara et al.*, 2006; *Richardson et al.*, 2002; *Michel et al.*, 2001].

However, some planetesimals did not accumulate enough sources of heat, mainly the radioactive element ^{26}Al, and therefore did not differentiate. These asteroids consist of metamorphosed or aqueously altered material accreted from Solar System dust[3] [*Feierberg et al.*, 1982; *McSween et al.*, 2002]. Therefore the different types of asteroids reflect the planet-forming processes of the early Solar System, from accretion to differentiation. In other

[3]These asteroids are represented in meteorite collections by the ordinary and carbonaceous chondrites, respectively.

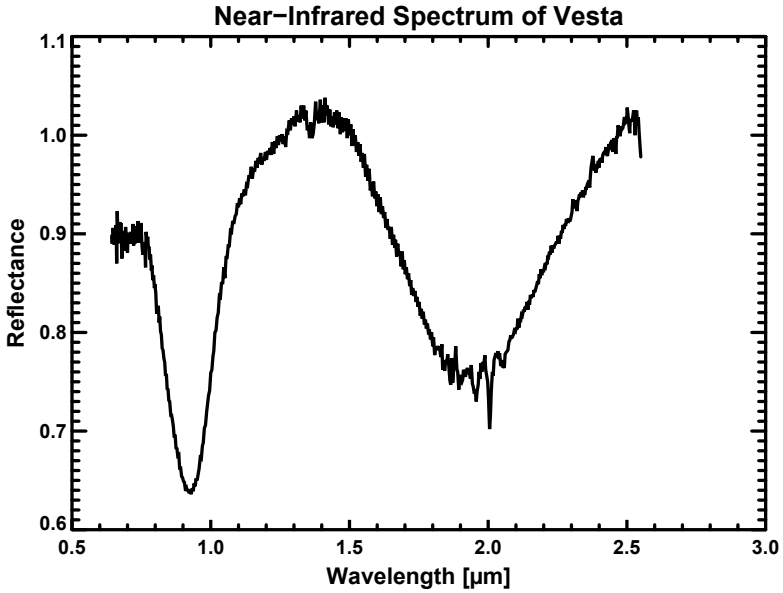

Figure 2.4.: Near-infrared spectrum of Vesta from the NASA Infrared Telescope Facility (IRTF), measured in 2011. The spectrum has been normalized to 1 at 1.5 µm. The strong absorption features at 0.9 µm and 1.9 µm are characteristic for V-type asteroids. The data were retrieved from the Planetary Data System (PDS) and are available at http://sbn.psi.edu/pds/resource/reddyvesta.html [*Reddy*, 2011].

words, the current asteroids are remnants from the planet-forming epoch of our Solar System, a fact that highlights their scientific significance and which has inspired many surveys, observation campaigns [e.g. *Bus and Binzel*, 2002a,b], and in particular the Dawn Mission [*Russell and Raymond*, 2011] (Section 2.3).

2.2. Asteroid Spin and Impact Rates

Asteroids not only vary in shape, size and composition, they also have different rotation rates, often influenced by collisions [*Paolicchi et al.*, 2002], gravitational interactions with planets [*Scheeres et al.*, 2000] or radiation pressure effects (e.g. YORP Effect [*Rubincam*, 2000]).

Generally their rotation periods range between 1 h and 30 h with larger asteroids typically possessing slower rotation rates. For very large asteroids (diameter >200 km) the average rotation period is ∼8 h. The upper limit to

the rotation rate of rubble pile asteroids is given by their cohesive strength which must exceed the centrifugal force for the asteroid to remain intact [*Pravec and Harris*, 2000].

Collisions on rotating targets may excavate spinning and tumbling fragments [*Fujiwara and Tsukamoto*, 1981]. Additionally, the angular momentum of the impactor may be transferred to the target affecting its spin [*Henych and Pravec*, 2013; *Paolicchi et al.*, 2002]. However, tumbling of asteroids is damped relatively quickly by dissipative forces [*Pravec et al.*, 2002]. When the rotation axis is not aligned with the principle axis of inertia of the asteroid, periodic stresses are exerted on the asteroid material inducing internal friction. The subsequent loss of rotational energy requires the convergence of the rotation axis and the principle axis of inertia in order to preserve the angular momentum [*Breiter et al.*, 2012; *Sharma et al.*, 2005; *Efroimsky*, 2001]. The time span of this process is dependent on the shape of the rotating asteroid and increases with decreasing size, angular velocity and density [*Efroimsky*, 2001; *Efroimsky and Lazarian*, 2000; *Burns et al.*, 1973].

Gravitational perturbation between asteroids and between asteroids and planets may transfer angular momentum between the interacting bodies. Considering an irregularly shaped rotating asteroid flying past a planet or massive asteroid, the rotation rate may be influenced depending on the orientation of the asteroid at the periapsis of fly-by. The asteroid's spin is increased if the periapsis lies along the leading edge and decreased if the periapsis lies along the trailing edge of the rotating asteroid [*Scheeres et al.*, 2000].

Small asteroids with irregular shape may spin-up or spin-down by the anisotropic reflection of sunlight when the net momentum of the reflected photons exerts a torque on the asteroid [*Komarov and Sazanov*, 1994; *Sazonov*, 1994]. Additionally, a torque may be produced by the radiation of thermal photons from an irregularly heated or shaped asteroid surface (Yarkovsky Effect) [*Rubincam*, 2000]. These effects are most significant for small asteroids. Although the momentum transferred by the reflected and emitted photons is relatively small, the asteroid spin may be altered on an appropriate time-scale ($\sim$100 Ma for a 10 km sized asteroid) [*Rubincam*, 2000].

The Yarkovsky Effect on smaller asteroids (diameter $\lesssim$10 km) with effective thermal inertia may also introduce a radial drift of their semi-major axis by the diurnal and seasonal delayed radiation of thermal photons [*Bottke et al.*, 2002, 2000]. Asteroids perturbed in this way may cross other asteroids' orbits and potentially collide with them. Strong and weak orbital and secular resonances with the planets (Section 2.1) are also able to deflect asteroids into chaotic, collisional paths [*Minton and Malhotra*, 2010].

The asteroids in the Solar System have experienced a series of epochs with increased impact rates. The Jovian Early Bombardment (triggered by the formation of Jupiter and occurring within the first 10 Ma after the formation of the Solar System [e.g. *Turrini et al.*, 2011; *Papaloizou et al.*, 2006]) and the Late Heavy Bombardment (caused by the migration and crossing of the 2:1 resonance of Jupiter and Saturn [*Gomes et al.*, 2005; *Tsiganis et al.*, 2005; *Morbidelli et al.*, 2005], occurring approximately between 3.8 Ga and 4.0 Ga ago [*Morbidelli et al.*, 2012]) are the most violent events in Solar System history. During these bombardments the impact rates were more frequent and energetic, resulting in the disruption of asteroids and a significant depletion of the asteroid belt [*Coradini et al.*, 2011; *Weidenschilling*, 1977].

Compared to these bombardments, the current dynamic state is relatively steady. The mean impact velocity on asteroids in the main belt is 5.1 km/s with an impact probability of $2.8{\cdot}10^{-18}$ $1/(\mathrm{km}^2{\cdot}\mathrm{a})$ [*O'Brien and Sykes*, 2011; *Bottke et al.*, 1994]. The mean impact velocity on Vesta is 4.7 km/s when excluding impacts of Vesta family members. The impact probability on Vesta is $2.7{\cdot}10^{-18}$ $1/(\mathrm{km}^2{\cdot}\mathrm{a})$ suggesting an impact of an asteroid with diameter >1 km onto Vesta every ∼4.2 Ma [*O'Brien and Sykes*, 2011].

2.3. The Dawn Mission

2.3.1. Mission Objectives

In September 2007 the NASA discovery mission Dawn was launched to explore the two most massive main-belt asteroids, Vesta and Ceres. Vesta and Ceres have survived the violent history of the Main Asteroid Belt as two intact terrestrial proto-planets. Consequently they preserve physical and chemical evidence of the planet-forming epoch, which makes them unique targets when investigating evolutionary processes in the Solar System, including those of the Main Asteroid Belt and the terrestrial planets [*Russell and Raymond*, 2011; *Rayman et al.*, 2006].

The role of size and water in the evolution of the terrestrial planets will be explored in particular by the Dawn Mission. Although today Vesta and Ceres are at similar distances from the Sun (2.36 AU and 2.76 AU, respectively), Vesta is dry, whereas Ceres shows evidence of water [*Perna et al.*, 2015; *Küppers et al.*, 2014; *Britt et al.*, 2002]. Thus the two contrasting asteroids enable the Dawn Mission to explore two evolutionary paths in one mission [e.g. *Russell and Raymond*, 2011; *Russell et al.*, 2004].

Additionally, Dawn is able to clarify and refine the suggested spectral and orbital connection of Vesta and the HED meteorites (Section 2.4.1). By

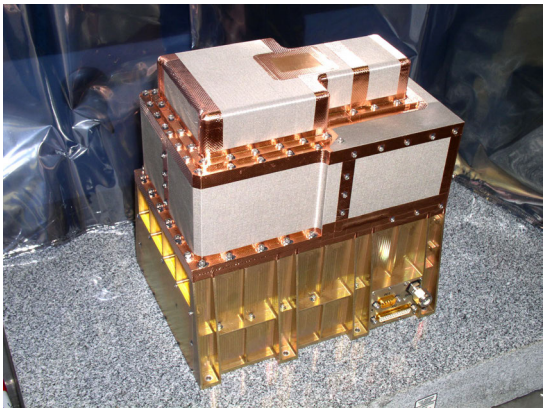

(a) GRaND.
Credit: UCLA.

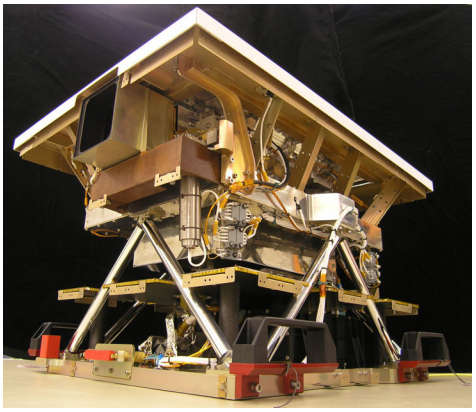

(b) VIR.
Credit: SELEX GALILEO/ASI/INAF.

Figure 2.5.: Dawn's Gamma Ray and Neutron Detector (a) and Visual and Infra-Red Spectrometer (b).

providing the geologic context, Dawn enables the interpretation of laboratory studies of HEDs in relation to the structure and evolution of Vesta [*McSween et al.*, 2011].

2.3.2. Scientific Instruments

To achieve these scientific objectives, three instruments are carried on board the Dawn spacecraft. They include a gamma ray and neutron detector (GRaND), a visual and infra-red spectrometer (VIR) and a framing camera (FC), constructed to compositionally and geologically map the surfaces of Vesta and Ceres. Additionally, Dawn performs a gravity investigation via the navigation system and a topography experiment using FC images [*Russell et al.*, 2004].

GRaND (Figure 2.5(a)) detects the abundance of thermal, epithermal and fast neutrons and performs gamma ray spectroscopy with a set of different scintillators. The neutrons and gamma rays are produced by cosmogenic nuclear reactions and radioactive decay in the upper layer of the surface material [*Prettyman et al.*, 2011]. The spectroscopy and abundance of gamma rays and neutrons detected by GRaND enable the mapping of surface elemental compositions at regional scales (∼270 km at Vesta). In particular at Vesta, GRaND mapped the mixing ratios of the HEDs and detected exogenic hydrogen [*Prettyman et al.*, 2012].

The VIR spectrometer (Figure 2.5(b)) images the surface at wavelengths

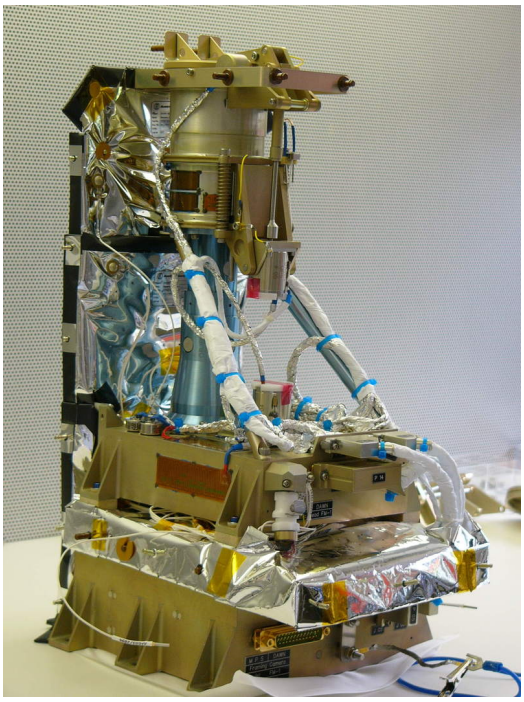

Figure 2.6.: The Dawn Framing Camera. *Credit: MPS.*

ranging from ultra-violet (0.25 µm) to near-infrared (5.0 µm). VIR is able to detect solid compounds such as oxides, silicates, organics and ices by analysing absorption features in the visible and infrared spectra [*De Sanctis et al.*, 2010]. Band depth at 0.9 µm and 1.9 µm are indicators for pyroxene absorption and these were found to be the most prominent spectral features on Vesta [*De Sanctis et al.*, 2012]. With a resolution of up to 70 m/pixel, the mineralogy of Vesta could be correlated with the geology of the surface and the HEDs [*McSween et al.*, 2013a].

The Framing Camera (FC, Figure 2.6) is built to image the surface of Vesta and Ceres and provides the spatial and geologic context of VIR and GRaND data, as well assisting orbit navigation of the spacecraft. FC's field of view of 5.5° × 5.5° is focussed by a refractive lens system (150 mm focal length) onto a 1024 × 1024 pixels frame-transfer CCD[4] [*Sierks et al.*, 2011]. With an overall spectral range of 400–1050 nm, the FC is equipped with a clear filter and a set of seven band-pass filters. Ranging between ∼430 nm and ∼980 nm, they enable a colour-based compositional interpretation of

[4]Charge Coupled Device

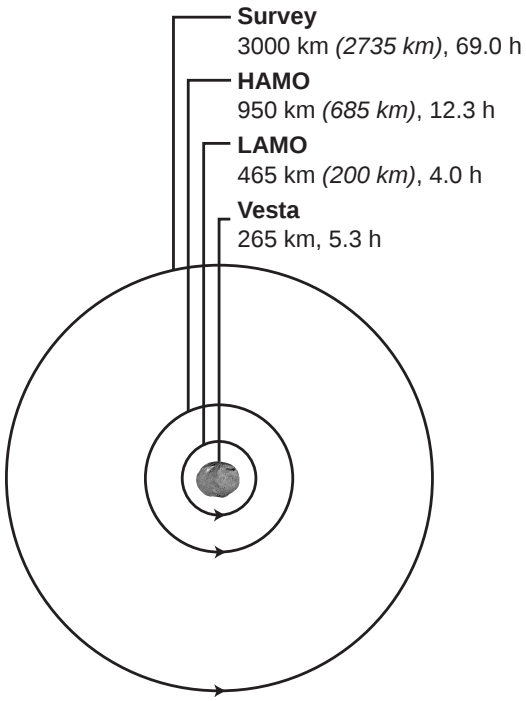

Figure 2.7.: Illustration of the science orbits at Vesta. The distance from Vesta's centre, the altitude (in brackets) and the orbital period are shown. Vesta with a rotation period of 5.3 hrs is shown in the centre. *Credit: UCLA/McREL, Elke Kersten (DLR).*

the surface. FC's stereo coverage of the surface also allows the production of a Digital Terrain Model (DTM) and a global shape reconstruction for geophysical analysis [*Sierks et al.*, 2011]. The resolution of the camera was as high as 20 m/pixel at Vesta and provided an extensive insight to Vesta's geology [e.g. *Jaumann et al.*, 2012; *Schenk et al.*, 2012; *Yingst et al.*, 2014] (Section 2.4.4).

2.3.3. Mission Operations

After some delay, on September 27, 2007 Dawn was launched from Cape Canaveral. Following a gravity assist manoeuvre at Mars in February 2009, Dawn arrived at Vesta on July 16, 2011. Dawn spent over 400 days in orbit around Vesta and left on September 5, 2012, to proceed to Ceres where it arrived in March, 2015 [*Russell et al.*, 2015, 2013].

While at Vesta, Dawn collected data in four scientific orbits: The Survey Orbit at 2735 km, the High Altitude Mapping Orbit (HAMO) at 685 km and

Table 2.1.: Vesta's physical properties derived from Dawn data (from *Russell et al.* [2012]).

Parameter	Value	Error
Major Axes[1] [km]	286.3 / 278.6 / 223.2	± 0.1
Mean Radius [km]	262.7	± 0.1
Volume[2] [km^3]	$74.54 \cdot 10^6$	$\pm 0.05 \cdot 10^6$
Mass [kg]	$2.59076 \cdot 10^{20}$	$\pm 0.00001 \cdot 10^{20}$
Bulk Density [kg/m^3]	3456	± 35
Gravitational Flattening [J_2]	0.0317799	± 0.0000002
Spin Pole Right Ascension [°]	309.03	± 0.01
Spin Pole Declination [°]	42.23	± 0.01
Rotation Rate[3] [°/day]	1617.333119	± 0.000003
Escape Velocity[4] [m/s]	362.4	± 0.1

[1] 284.50 km / 277.25 km / 226.43 km after *Konopliv et al.* [2014].
[2] Derived from the best fit ellipsoid.
[3] 1617.333128°/day after *Konopliv et al.* [2014].
[4] Applying Equation 2.1.

the Low Altitude Mapping Orbit (LAMO) at 210 km altitude (Figure 2.7). Before leaving Vesta, Dawn entered a second HAMO phase (HAMO2) allowing the investigation of the northern hemisphere which previously had been in seasonal shadow. While the HAMOs were flown with stereo pointing to allow the construction of a stereo-DTM, Dawn pointed towards the surface (nadir pointing) in LAMOs.

The Survey Orbit was mainly dedicated to the VIR spectrometer. In HAMO the FC was the prime instrument and GRaND was given priority at LAMO. Nevertheless, all instruments were able to collect data in every science orbit. As a result, the FC imaged 99% of Vesta's surface with HAMO resolution (∼70 m/pixel), 66% with LAMO resolution (∼20 m/pixel) and produced a DTM with 80% surface coverage from HAMO images [*Russell et al.*, 2013; *Preusker et al.*, 2012b].

2.4. Asteroid (4) Vesta

Our knowledge about Vesta increased tremendously with Dawn's recent visit (Figure 2.8). The Dawn instruments not only mapped the surface composition, mineralogy and geology but were also able to refine physical parameters, such

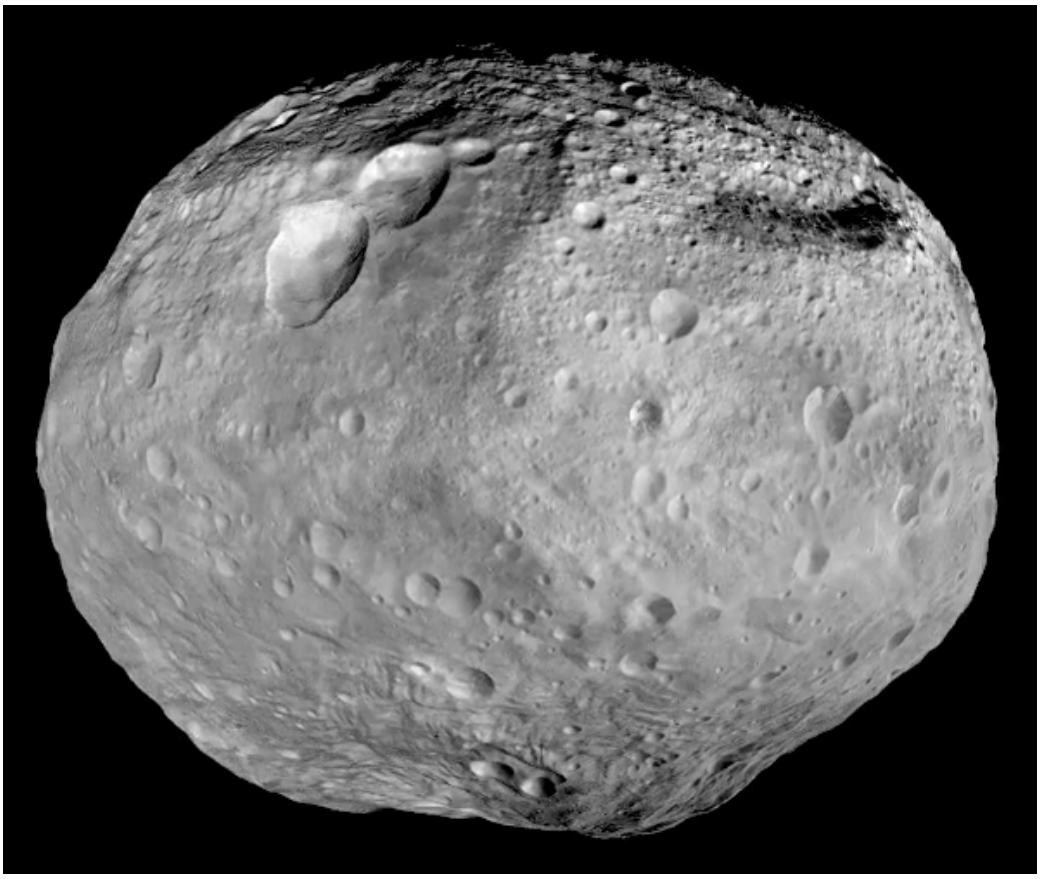

Figure 2.8.: Global mosaic of (4) Vesta derived from Dawn data. *Credit: NASA/JPL-Caltech/UCAL/MPS/DLR/IDA.*

as the spin pole, shape, density and rotation period (Table 2.1) [*Konopliv et al.*, 2014; *Russell et al.*, 2012]. Additionally, the osculating orbital elements were improved (Table 2.2).

Vesta is the second most massive object in the Main Asteroid Belt. It is a dry differentiated proto-planet which resembles a tri-axial ellipsoid with axes of 286.3 km × 278.6 km × 223.2 km. The rotation period of 5.3 h (angular frequency of $3.27{\cdot}10^{-4}$ s^{-1}) is relatively fast far this shape [*Konopliv et al.*, 2014]. Vesta possesses a crust of relatively light eucritic material, a mantle of denser diogenitic material and an iron core [*Russell et al.*, 2013]. With a mass of $2.6{\cdot}10^{20}$ kg, the bulk density of 3.5 kg/m^3 is comparable to silicate densities derived from HED analyses [*Russell et al.*, 2013, 2012].

Vesta exhibits a large number of geologic features (Section 2.4.4) including

Table 2.2.: Vesta's heliocentric ecliptic J2000 osculating orbital elements at epoch 2012-January-01.0 derived from Dawn data (from *Konopliv et al.* [2014]).

Element	**Value**	**1-σ Uncertainty**
Eccentricity	0.088267108519	$\pm$ 1.46·10^{-10}
Semi-Major Axis [AU]	2.361546970577	$\pm$ 8.85·10^{-10}
Inclination [°]	7.13436762265	$\pm$ 2.24·10^{-9}
Longitude of Ascending Node [°]	103.90115152105	$\pm$ 3.61·10^{-9}
Argument of Perihelion [°]	149.98494722851	$\pm$ 1.77·10^{-9}
Mean Anomaly [°]	90.806006254	$\pm$ 2.96·10^{-7}
Period [days]	1325.541438115	$\pm$ 7.46·10^{-7}

an extensive topographical variation, albedo variations, and impact craters of various sizes and ages (Section 2.4.3) [e.g. *Jaumann et al.*, 2012]. The regolith (Section 2.4.2) reveals lithologies of the different HED mineralogies supporting the relation between Vesta and the HEDs (Section 2.4.1).

2.4.1. The HED-Meteorites

As a subset of the achondrite meteorites, the Howardites, Eucrites and Diogenites (HEDs) are breccias with petrologic evidence for a common differentiated parent body. Eucrites are basalts indicating igneous processes (Figure 2.9). Diogenites are ultramafic pyroxene-rich meteorites indicating intrusive processes. Howardites are breccias composed of a mixture of eucrites and diogenites. These compositions lead to the conclusion that the HED parent body underwent magmatic differentiation where eucrites formed the basaltic crust and diogenites were intrusive material [*McSween et al.*, 2013b, 2011; *Duke and Silver*, 1967]. Although whether the HEDs originate from Vesta is still a matter of debate [*Wasson*, 2013], they certainly originated from a parent body that was compositionally and evolutionarily similar to Vesta.

Evidence that the HED meteorite collection originated from Vesta is their spectroscopic similarity to the asteroid [e.g. *McSween et al.*, 2013b; *Burbine et al.*, 2001; *McCord et al.*, 1970]. A catastrophic impact event on Vesta, possibly the impact forming the Rheasilvia basin near Vesta's south pole, may have produced the Vesta family (Section 2.4.3) [*Schenk et al.*, 2012; *Thomas et al.*, 1997a]. Members of the family were deflected by the 3:1 Jovian orbital resonance or the υ_6 secular (precession) resonance with Saturn into the inner

(a) Piece of the Millbillillie Eucrite fallen in Australia in 1960 from the meteorite collection of the University of Hawai'i (∼10 cm).

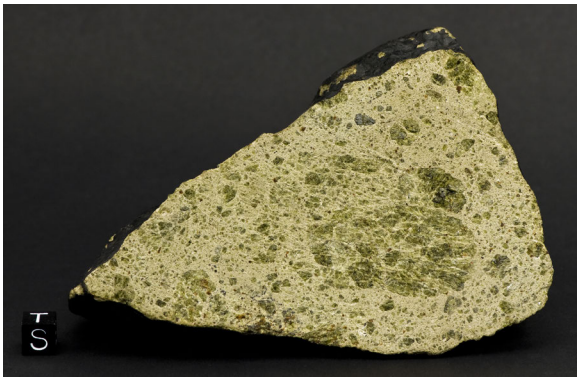

(b) Johnstown Diogenite fallen in Johnstown, Colorado in 1924 (∼15 cm). *Courtesy of Laurence Garvie, CMS, ASU.*

Figure 2.9.: Two examples of HED meteorites. Note the brecciated texture of the eucrite (a) and the large crystals in the diogenite (b). Howardites are a mixture of eucrites and diogenites.

Solar System, potentially crossing the Earth's orbit [*Cruikshank et al.*, 1991; *Migliorini et al.*, 1997].

2.4.2. Regolith

The uppermost layer of Vesta is composed of regolith which has formed through continuous impact gardening, breaking and redistributing the original crust.

The FC images (up to ∼20 m/pixel) are able to resolve the regolith properties on a macroscopic scale (e.g. boulders). In order to investigate the regolith on the microscopic scale, photometric and thermal properties of the surface are used. Evaluating the change of reflectance with varying phase angle, *Schröder et al.* [2013] measured the physical roughness of the regolith and found increased values on young ejecta blankets where fresh regolith is expected. *Gundlach and Blum* [2013] estimated the regolith grain size by analysing remote measurements of Vesta's thermal inertia. Making assumptions regarding the material properties and packing density of the regolith particles, they found a value of ∼54 µm. *Hiroi et al.* [1994] suggest an even finer regolith size of less than 25 µm by matching the spectra of dry sieved HED powders with telescopic spectra of Vesta.

Although observed on other airless bodies, such as the Moon [*Keller and*

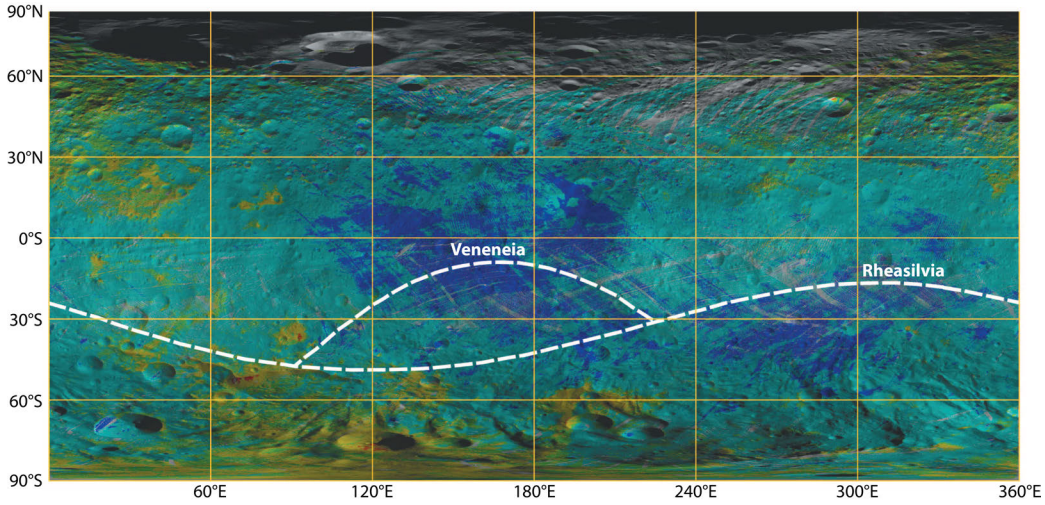

Figure 2.10.: Distribution of HED mineralogy on Vesta derived from VIR spectra (from *Ammannito et al.* [2013b], Copyright (2013), with permission from Macmillan Publishers Ltd). The colours correspond to diogenite (red), howardite (green) and eucrite (blue). Overlapping fields are diogenitic howardite (yellow) and eucritic howardite (cyan). The impact basins Rheasilvia and Venenia are labelled. Note the increased abundance of diogenitic material inside the basins and the more eucritic areas towards the north. The map is in equidistant projection.

McKay, 1997] and asteroid Itokawa [*Noguchi et al.*, 2011], there is no evidence for nano-phase iron produced by space weathering of micrometeorite impacts and solar wind interactions. Vesta's regolith is locally homogeneous due to fine-scale mixing [*Pieters et al.*, 2012].

The mineralogy of the HEDs is represented in Vesta's regolith where different areas show increased abundances of diogenites and eucrites. For example, the Rheasilvia impact basin (Section 2.4.3) exposes diogenitic material, whereas the older northern hemisphere is predominantly eucritic with a few diogenitic outcrops (Figure 2.10) [*Ruesch et al.*, 2014b; *Ammannito et al.*, 2013a; *De Sanctis et al.*, 2013].

2.4.3. Rheasilvia and Veneneia

One of Vesta's most prominent features is the Rheasilvia basin. Rheasilvia covers almost the entire southern hemisphere and was first detected on Hubble Space Telescope images [*Thomas et al.*, 1997a]. In Figure 2.8, Rheasilvia

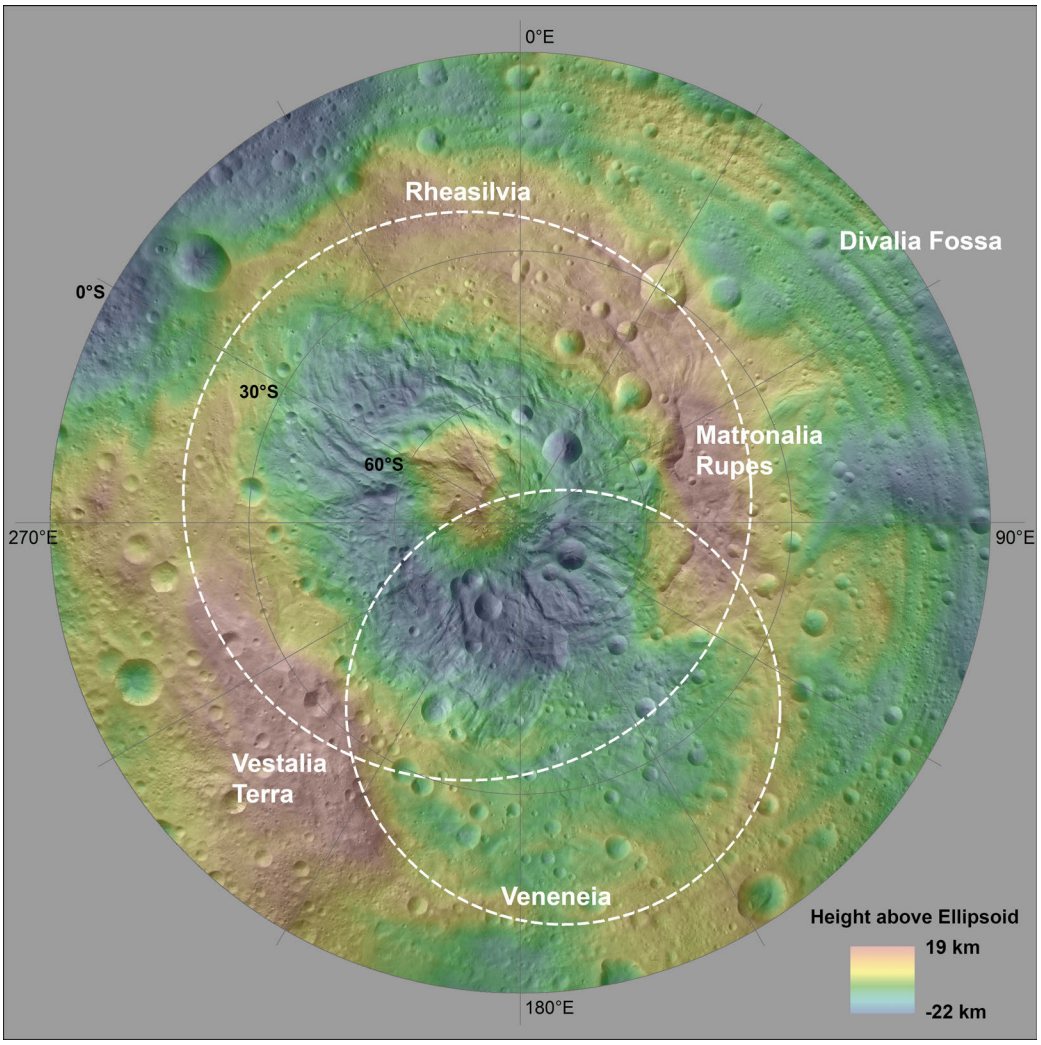

Figure 2.11.: Stereographic projection of the southern hemisphere of Vesta derived from a HAMO mosaic (resolution: ∼70 m/pixel, [*Roatsch et al.*, 2012]). The underlying Digital Terrain Model (DTM) is referenced to a 285 km × 229 km biaxial ellipsoid [*Preusker et al.*, 2012b]. The approximate locations of Rheasilvia and Veneneia are outlined. Matronalia Rupes and Vestalia Terra are labelled. The troughs and Divalia Fossa are most apparent near the equator between 0°E and 90°E.

appears as a cut off of the southern hemisphere with the central mount protruding near the pole.

Rheasilvia is centred approximately at 301°E and 75°S and with its diameter

of 500 ± 20 km it is comparable to Vesta's diameter of ∼525 km [*Jaumann et al.*, 2012; *Schenk et al.*, 2012]. Rheasilvia possesses a central peak of ∼180 km diameter and 20–25 km height (Figure 2.11). It nearly coincides with the rotation axis, which makes it quite a unique setting in terms of the Coriolis Effect.

Rheasilvia is 19 ± 6 km deep and exhibits a prominent ridge and groove terrain with a spiral deformation pattern [*Schenk et al.*, 2012]. Beyond the rim, the ejecta deposition extends ∼100 km. Scarps of landslides and slumping blocks appear developed along the inner basin rim [*Otto et al.*, 2013]. The most prominent scarp - Matronalia Rupes - is centred at 50°S and 83°E and extends ∼208 km [*Krohn et al.*, 2014b]. It exposes relatively fresh slumping areas and landslides emanating from the rim.

As the Rheasilvia basin is the setting of this thesis, details about the geology are described in Chapter 5.

A second, older impact basin of 400 ± 20 km diameter underlies Rheasilvia. It is named Veneneia and located at 170°E and 52°S (Figure 2.11). As it pre-dates Rheasilvia, Veneneia's topography is less extensive, with a depth of 12 ± 2 km [*Jaumann et al.*, 2012; *Schenk et al.*, 2012]. Only a few scarps and potential eroded landslides are observed inside the basin [*Otto et al.*, 2013].

Two sets of large-scale fault-bounded graben, so called troughs, partly encircle Vesta near the equator and ∼30° north of the equator [*Jaumann et al.*, 2012; *Buczkowski et al.*, 2012]. There are 86 equatorial troughs which extend between ∼349°E and ∼84°E with length varying from 19 km to 380 km. They encircle approximately two thirds of Vesta and are up to ∼5 km deep and ∼15 km wide. The roughly parallel troughs possess steep scarps and flat floors [*Buczkowski et al.*, 2012]. The largest equatorial trough is named Divalia Fossa (Figure 2.12).

The most prominent northern trough is called Saturnalia Fossa. There are a total of seven troughs aligned with Saturnalia Fossa with lengths of up to ∼366 km, widths of up to ∼38 km and depths of ∼8 km [*Buczkowski et al.*, 2012]. They appear between ∼180°E and ∼270°E [*Ruesch et al.*, 2014a]. These troughs are generally smoother compared to the equatorial troughs, with rounded edges and infilling on the floor. This indicates that the northern troughs formed earlier and are thus more eroded than the equatorial troughs [*Jaumann et al.*, 2012; *Buczkowski et al.*, 2012].

Both sets of troughs are believed to be related to the Rheasilvia and Veneneia impact basins because the centre positions of the circular troughs coincide with the centres of the basins. Hence, the northern troughs would correspond to Veneneia and the equatorial troughs to Rheasilvia [*Jaumann et al.*, 2012]. However, laboratory experiments with impacted plastic spheres

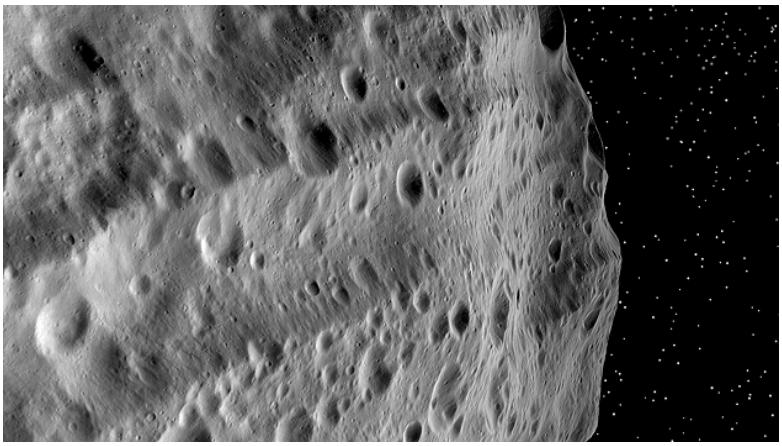

Figure 2.12.: Side view of the equatorial troughs of Divalia Fossa. *Credit: NASA/JPL-Caltech/UCLA/MPS/DLR/IDA.*

show that stress planes develop around the impact point antipode, so that the northern troughs could relate to Rheasilvia if the impactor hit Vesta at 5 km/s with an impact angle of 40° [*Stickle et al.*, 2015].

Rheasilvia's and Veneneia's ages were determined by two crater counting models: The lunar chronology, which is calibrated with the size-frequency distribution of craters on the Moon [*Schmedemann et al.*, 2014; *Neukum et al.*, 2001] and the asteroid flux chronology, which is estimated by using the model of the dynamical evolution of the asteroid belt [*O'Brien et al.*, 2014]. The lunar flux model reveals ages of 3.5 ± 0.1 Ga for Rheasilvia and 3.7 ± 0.1 Ga for Veneneia [*Schmedemann et al.*, 2014]. The asteroid flux model reveals ages of 1.0 ± 0.2 Ga for Rheasilvia and 2.1 ± 0.2 Ga for Veneneia [*O'Brien et al.*, 2014; *Schenk et al.*, 2012]. The errors given here are based on statistical analyses and do not represent errors of the model itself. The large discrepancy between the two models is still a matter of debate.

2.4.4. Geology

As mentioned above, Vesta is a remnant proto-planet with a differentiated interior which survived the epochs of earlier bombardment (Section 2.2). Consequently, the geology of Vesta exhibits evidence of these processes. Figure 2.13 provides a context map of the geologic features discussed in this section.

Upon arrival at Vesta, the FC revealed an extraordinary geologic scene including a complex topography, mass-wasting features, tectonics, albedo

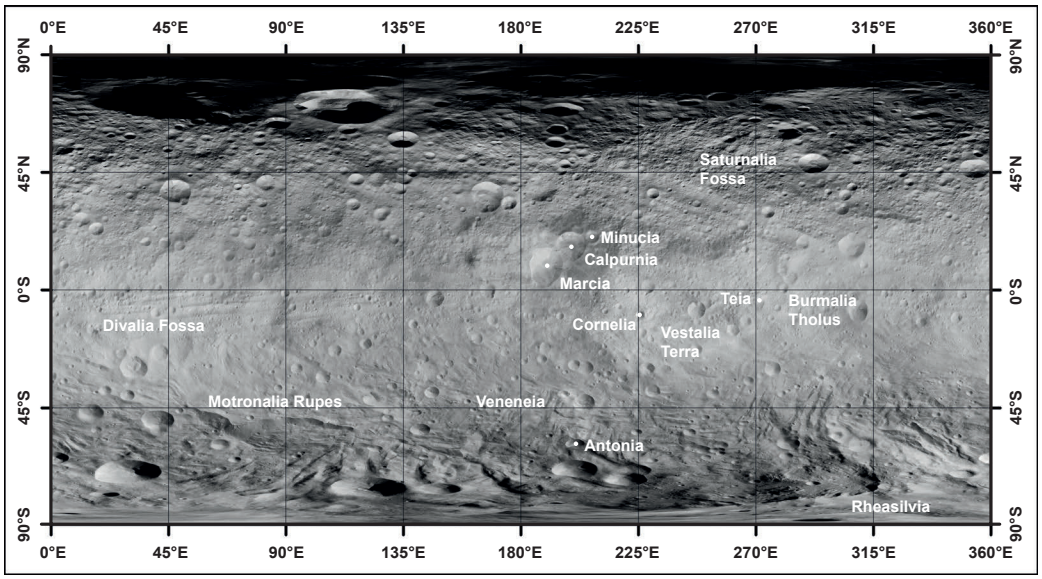

Figure 2.13.: Global equidistant map of Vesta derived from a HAMO mosaic (resolution: ∼70 m/pixel, [*Roatsch et al.*, 2012]). The geologic features discussed in the text are labelled.

variations and a variety of impact crater morphologies [*Jaumann et al.*, 2012] (Figure 2.14). Due to Vesta's relatively low gravity (2.5 m/s^2), the topography varies widely, ranging from -22.3 km to 19.1 km with respect to a reference ellipsoid of 285 km by 229 km [*Jaumann et al.*, 2012].

The distinct topography supports steep slopes, locally exceeding 40° referenced to the ellipsoid. However, gravitational slopes are slightly flatter, but also reach values of ∼40° [*Jaumann et al.*, 2012]. Due to the reduced gravity (compared to the Moon or Mars) deposits on Vesta are flatter while scarps tend to be steeper [*Kleinhans et al.*, 2011].

Impacts in this environment often form craters with asymmetric shapes in which the uphill side forms a sharp rim and the downhill side exhibits a smooth transition [*Krohn et al.*, 2014a; *Jaumann et al.*, 2012] (Figure 2.14(a)). This can be explained by the hindering of ejecta deposition on the uphill side due to topography, and slumping material superimposing the downhill ejecta.

Additionally, mass wasting is encouraged by the steep slopes and the gravitational environment [*Krohn et al.*, 2014b; *Otto et al.*, 2013; *Jaumann et al.*, 2012] (Figure 2.14(c)). *Otto et al.* [2013] identified various features such as landslides, slumping blocks, flow-like and rippled features. These features are particularly related to the Rheasilvia basin, which spans a large

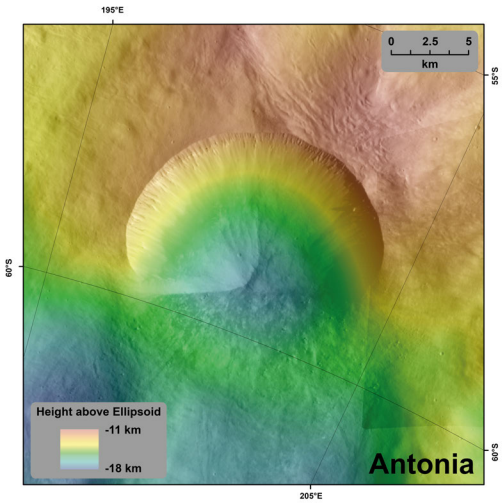

(a) The asymmetric crater Antonia.

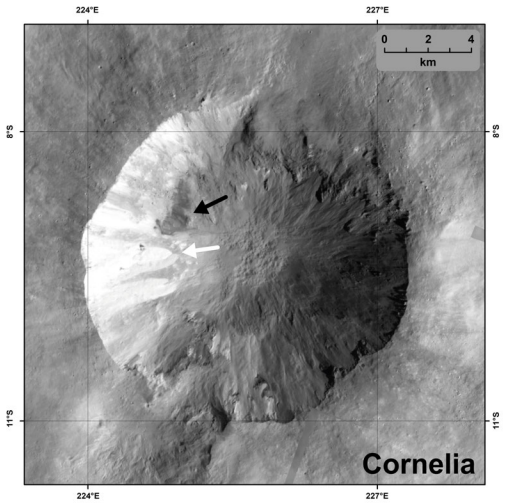

(b) Dark (black arrow) and bright (white arrow) material in crater Cornelia.

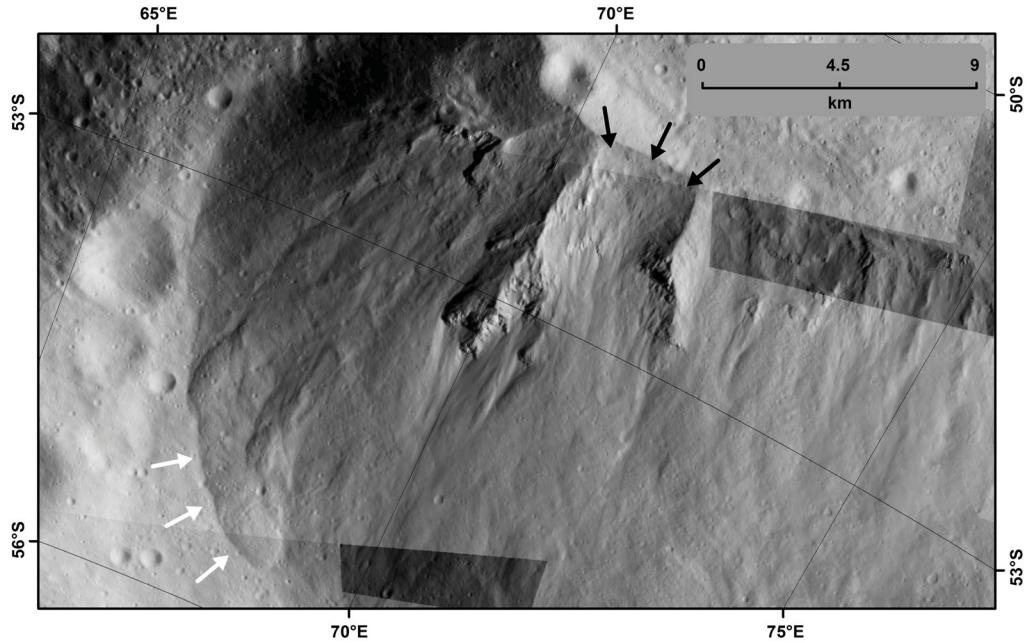

(c) Landslides emanating from Matronalia Rupes. White arrows indicate a lobate deposit, black arrows point out a slide chute.

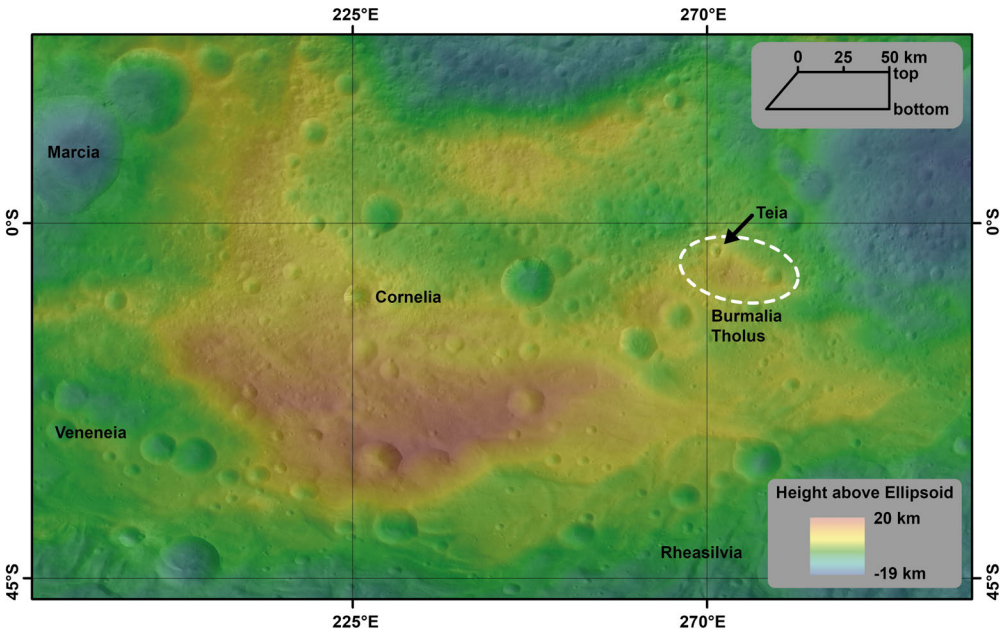

(d) The plateau Vestalia Terra (red-yellow) with laccolith uplift Burmalia Tholus (dashed circle) and crater Teia (arrow).

Figure 2.14.: Examples of features described in the text. (a), (b) and (c) are in stereographic projection. (d) is in equidistant projection. The images are extracted from a LAMO mosaic (resolution: ∼20 m/pixel, [*Roatsch et al.*, 2013]). The DTM is referenced to a 285 km × 229 km biaxial ellipsoid [*Preusker et al.*, 2012b].

elevation range (20–30 km). Mass movements are probably triggered by impact-related seismic shaking whose shock wave briefly destabilizes the material and thus induces a down-hill motion [*Richardson et al.*, 2005; *Titley*, 1966]. Mass-wasting features will be discussed in more detail in Chapter 5.

One of Vesta's largest individual features is Vestalia Terra, located at the outer intersection of the Rhesilvia and Veneneia basins (Figure 2.14(d)). It consists of a ∼20 km raised plateau covering ∼80,000 km^2 between approximately 25°N to 35°S and 200°E to 300°E [*Buczkowski et al.*, 2014; *Jaumann et al.*, 2012]. Besides various other features, Vestalia Terra also exhibits a ∼36 km wide and ∼68 km long dome, called Burmalia Tholus, situated at the eastern edge [*Buczkowski et al.*, 2014].

Although investigations of HED meteorites indicate that Vesta was volcanically active due to radioactive heating [*Keil*, 2002; *Wilson and Keil*, 1996],

the surface geology today does not show directly related features such as ancient lava flows or volcanoes. However, *Buczkowski et al.* [2014] describe the topographically raised Burmalia Tholus in the Vestalia Terra region as an ancient magmatic intrusion forming over a dyke. The pressure of this intrusion may have raised the surface material without breaking through, forming an underground laccolith. This hypothesis is supported by the spectral properties of the small crater Teia, on Burmalia Tholus, which is thought to have excavated upper mantle material of more orthopyroxene-rich composition relative to surrounding terrain [*De Sanctis et al.*, 2014].

At the western edge of Vestalia Terra, three prominent craters, Marcia, Calpurnia and Minucia, are aligned, resembling a snowman (Figure 2.8). Marcia, the largest and youngest of the three craters, shows a particular variety of geological features [*Williams et al.*, 2014]. These include impact melt deposits, pitted terrain and pristine bright and dark material [*Jaumann et al.*, 2014, 2012]. Marcia is located at ∼10°N and ∼190°E. Its shape is slightly asymmetric with a length of ∼63 km and a width of ∼58 km [*Williams et al.*, 2014]. This asymmetry is sustained by the undulating western rim which exhibits layers of emanating bright and dark material [*Jaumann et al.*, 2014]. Marcia's pitted terrain, which partly covers the crater floor and ejecta field, is believed to originate from the impact derived release of volatiles [*Williams et al.*, 2014; *Denevi et al.*, 2012]. The ejecta field of the three craters, highlighted by its low albedo, is prominent enough to be visible in Hubble Space Telescope images [*Thomas et al.*, 1997b].

In addition to the ejecta field of the snowman craters and along the Marcia rim, dark material is located at diverse places on Vesta [*Jaumann et al.*, 2012; *Reddy et al.*, 2012b] (Figure 2.14(b)). *Jaumann et al.* [2014] classified the dark material into three classes: outcropping dark material at crater walls, scarps and escarpments; dark material on crater rims, in ejecta and mass-wasting deposits, and dark regolith and linear dark features. These deposits suggest a possible delivery and distribution mechanism of dark material via impacts [*Jaumann et al.*, 2014; *Turrini et al.*, 2014; *McCord et al.*, 2012].

However, the distribution of dark material is not globally homogeneous and instead correlates with the rim and ejecta of the Veneneia basin [*Jaumann et al.*, 2014], a region which is also enriched in hydrogen [*Prettyman et al.*, 2012]. The spectrum of dark material is very similar to the average regolith on Vesta and can be reproduced by mixing average regolith with a small amount of a darkening agent, for instance carbonaceous material [*De Sanctis et al.*, 2013; *Reddy et al.*, 2012a; *McCord et al.*, 2012]. This suggests that Veneneia was probably produced by a carbon-rich low-velocity impactor (<2 km/s) whose remains are exposed as dark material and redistributed via subsequent

impact gardening [*Jaumann et al.*, 2014; *Reddy et al.*, 2012a; *McCord et al.*, 2012].

Despite the occurrence of dark material, Vesta is a relatively bright asteroid with a geometric albedo of 0.38 ± 0.04 at 554 nm [*Li et al.*, 2013]. Not surprisingly, Vesta also exhibits bright material (Figure 2.14(b)). Bright material can be classified in four groups: Crater wall and slope material, radial ejecta material, spot material localised in small craters, and diffuse material unrelated to impacts [*Zambon et al.*, 2014; *Mittlefehldt et al.*, 2012]. The distribution of bright material peaks in the mid southern latitudes (0–60°S) with the Rheasilvia basin being depleted in bright material. This suggests that impact craters may expose a bright lithologic unit [*Li et al.*, 2012].

The spectrum of bright materials resembles that of average Vesta regolith but hints at non-pyroxene components such as olivine or plagioclase [*Zambon et al.*, 2014]. Additionally, some spectral features, such as deeper band depth, are indicative of young and unweathered material [*Stephan et al.*, 2014; *Zambon et al.*, 2014; *Li et al.*, 2012]. Supporting this, the bright material is often associated with relatively fresh impact craters [*Stephan et al.*, 2014].

2.4.5. Shape and Gravity

Ermakov et al. [2014] used Dawn's gravity measurements and fitted a three-layered ellipsoidal body to the result in order to constrain the core-mantle-crust structure of Vesta. Best fit parameters reveal an iron core of ∼108 km, an olivine-rich mantle of ∼226 km and a HED-like crust of ∼254 km mean radius. The work also shows that Vesta today is not in hydrostatic equilibrium, possibly disturbed by the Rheasilvia and pre-dating Veneneia impact events.

Fu et al. [2014] determined Vesta's previous shape and rotation period by fitting the a tri-axial ellipsoid to the relic hydrostatic terrain of the northern hemisphere. They found that the best fit ellipsoid was described by axes of 280.6 km × 274.6 km × 236.8 km with the centre of mass being 5.7 km further to the south. They inferred a former rotation period of 5.02 h (6.3% faster than today's 5.34 h [*Konopliv et al.*, 2014]) and a 3.0° shifted rotation axis passing through longitude 182.7°E.

Ground-based Doppler tracking of Dawn combined with FC data allowed the determination of Vesta's gravity field [*Konopliv et al.*, 2011]. The gravitational acceleration on Vesta varies between 0.23 m/s^2 and 0.27 m/s^2 with a maximum centrifugal contribution of -0.03 m/s^2 at the equator [*Ermakov et al.*, 2014].

Using an average acceleration g_V of 0.25 ± 0.03 m/s and Vesta's mean

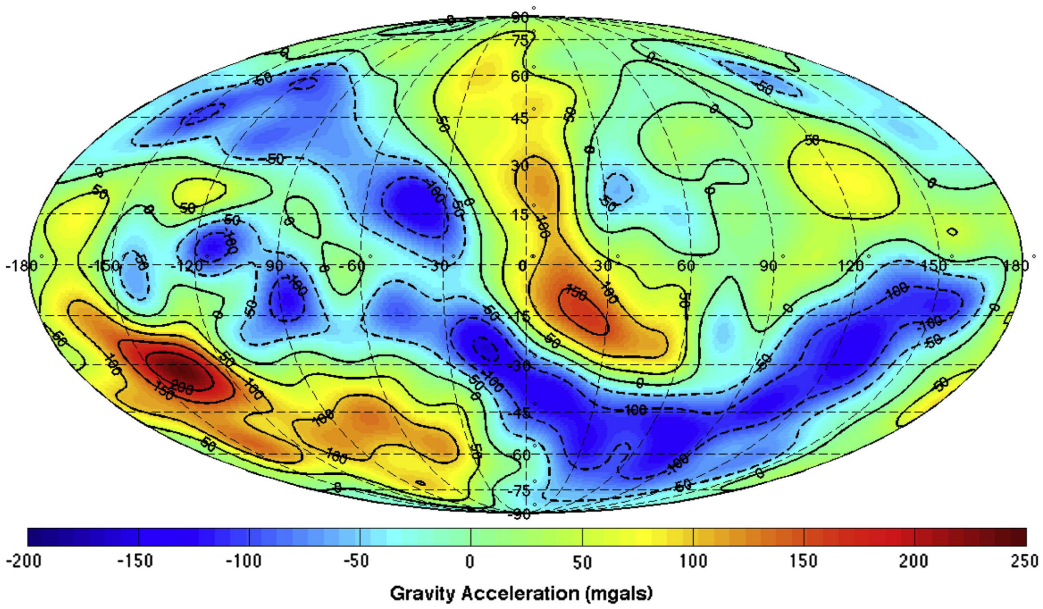

Figure 2.15.: Vesta's Bouguer anomaly mapped to a 290 km × 265 km ellipsoid through harmonic degree 15 (from *Konopliv et al.* [2014], Copyright (2014), with permission from Elsevier Ltd). 1 gal converts to 0.01 m/s^2. The Bouguer anomaly is defined as the residual gravity after subtracting the effects of shape and topography, indicating density variations. Note the high anomaly of Vestalia Terra around 30°S and -140°E (lower left of the map) and the low anomaly to the south related to the southern impacts Rheasilvia and Veneneia. The map is in Mollweide projection (equal area projection).

radius r from Table 2.1 the following equation provides an estimate of the escape velocity v_{esc} on Vesta's surface:

$$v_{\mathrm{esc}} = \sqrt{2 g_{\mathrm{V}} r} = 362.4 \pm 0.1 \text{ m/s}. \tag{2.1}$$

Fitting the measured gravity to a three-layered Vesta model reveals the gravity anomalies (Bouguer anomaly) due to density variations (Figure 2.15). The highest positive gravity anomaly is found in the region of Vestalia Terra possibly caused by dense ultramafic mantle material [*Buczkowski et al.*, 2014; *Raymond et al.*, 2013]. The area with the lowest gravity anomaly is connected with the giant impact basins Rheasilvia and Veneneia and indicates a thin crust [*Ermakov et al.*, 2014].

3. Theoretical Background

3.1. Impact Cratering Dynamics

Impact cratering has been common on planetary bodies throughout the history of the Solar System. During the current epoch, airless bodies with little erosion, such as Vesta, preserve a variety of crater morphologies such as simple bowl-shaped, complex or the previously mentioned asymmetric craters (Section 2.4.4). This section introduces the physics of impact cratering. Impact cratering can be divided into three stages [e.g. *Osinski and Pierazzo*, 2013; *French*, 1998; *Melosh*, 1989]: The contact and compression stage during which the impactor penetrates the target, producing a shock wave, the excavation stage when the crater cavity is formed as a result of particle motion induced by the shock wave and the modification stage during which initial collapse of the transient crater occurs [e.g. *Gault et al.*, 1974] (Figure 3.1). However, the stages represent a continuous physical process and therefore must have some overlap. Because this thesis focuses on the Rheasilvia impact basin, this chapter concentrates on the formation of large complex central peak craters. Nevertheless, the differences between simple and complex crater formation only occur after the end of the excavation stage. To simplify matters, the stages described below only consider vertical impacts[1].

3.1.1. Contact and Compression Stage

This first stage of crater formation describes the physics when the impactor penetrates the target and is therefore very brief. The duration τ is approximately described by:

$$\tau \approx \frac{L}{v \sin(\theta)}, \tag{3.1}$$

where L is the impactor's size, v its velocity and θ the impact angle [*Melosh*, 2013]. Using the Rheasilvia impact as an example, with an impactor size of 37 km, a velocity of 5.5 km/s and an impact angle of 90° [*Ivanov and Melosh*, 2013], the contact and compression stage would have lasted ∼7 s.

[1] Further information on oblique impacts can be found for example in *Elbeshausen et al.* [2009] or *Pierazzo and Melosh* [2000] and references therein.

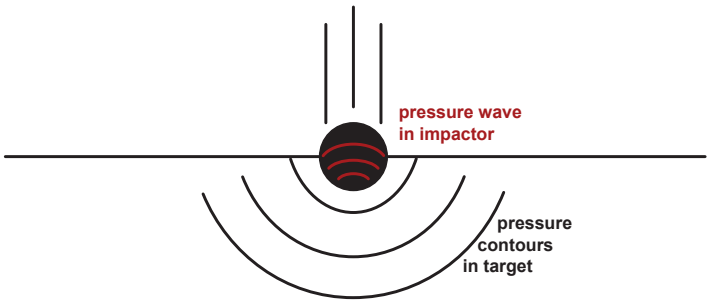

(a) Contact and compression stage.

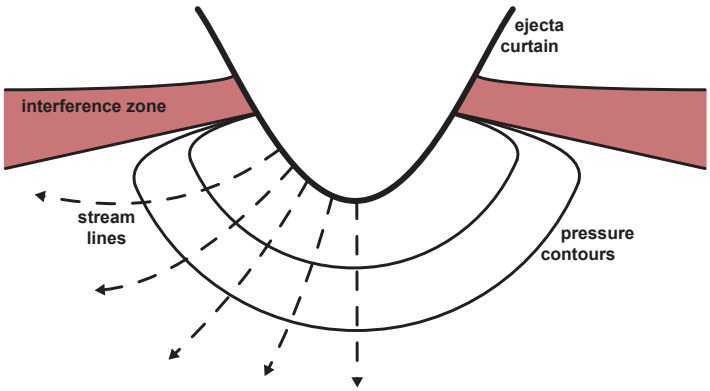

(b) Excavation stage.

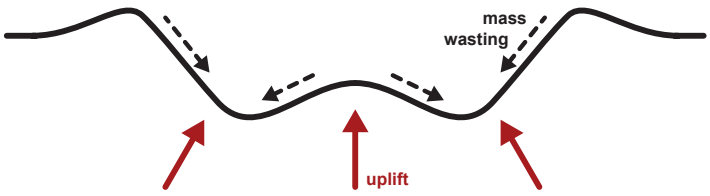

(c) Modification stage.

Figure 3.1.: Sketch illustrating the three stages of an impact event forming a complex crater: (a) contact and compression stage, (b) excavation stage and (c) modification stage. See text for explanations. Adapted from *Osinski et al.* [2011] and *French* [1998].

With the impactor touching the target, the involved materials irreversibly compress, increasing the density, pressure and temperature of the involved materials. Supersonic shock waves are generated and propagate into both the target and the impactor (Figure 3.1(a)). While the shock wave expands into the target, the shock wave in the impactor eventually reaches the back of the impactor contacting the free surface. A pressure relief (rarefaction) wave is then produced, propagating back into the impactor. The unloaded impactor moves into the target at reduced speed or vaporises if the shock was energetic enough. Upon arrival of the rarefaction wave at the boundary between impactor and target, the contact and compression stage finishes.

The processes of the contact and compression stage are identical for simple and complex craters. Differences occur at the end of the following stage when the central uplift begins as well as during the modification stage.

3.1.2. Excavation Stage

The excavation stage describes the propagation of the shock wave into the target and the opening of the crater cavity generated by the excavation flow (Figure 3.1(b)).

With the shock wave reaching the free surface of the target a rarefaction wave is produced analogously to the rarefaction wave in the impactor. The interference of the rarefaction and pressure waves in the near surface reduces the local pressure resulting in less shocked, but still fragmented target material (red in Figure 3.1(b)). The stress wave interference causes an up- and outward displacement of the fragmented material at high velocities (up to half the impact velocity [*Melosh*, 1989]) early in the excavation process, so-called *spallation*. The generated fragments may form asteroid families or meteorites if they reach the escape velocity of the target body [*Melosh*, 1984].

The expanding shock wave is nearly hemispherical beneath the impact point and flattened in the interference zone (Figure 3.1(b)). Therefore, the stream lines in the target material, which follow the negative pressure gradient, bend out- and upwards towards the surface (dashed lines in Figure 3.1(b)). Once the displaced material reaches the pre-impact surface, it follows ballistic trajectories to form an ejecta curtain at an emission angle of approximately 45° that propagates away from the impact location (Figure 3.1(b)).

The excavation flow first stops in the direction of most resistance which is beneath the crater. However, there is less resistance in the near surface, where the crater continues to grow. The end of the excavation stage is marked when the maximum diameter due to excavation is reached. At this point, the *transient crater* has formed [e.g. *Melosh*, 1989].

Given the gravity g and the final crater depth h_f, the time scale t_{exc} of the excavation flow can be estimated for gravity-driven deceleration [*Melosh and Ivanov*, 1999]:

$$t_{exc} \approx \sqrt{\frac{h_f}{g}}. \tag{3.2}$$

Using the 19 km deep Rheasilvia basin and Vesta's gravity of 0.25 m/s^2 as an example, the excavation stage would have lasted ∼275 s.

In complex craters, the transient crater might not necessarily be parabolic in shape as the central part of the crater cavity has already started to rise due to gravitational rebound of the target (Section 3.1.3). However, analogous to simple craters, the complex transient crater is often described as the parabolic transient crater that fits the maximum depth and diameter. In this case, the diameter is approximately three to four times larger than the crater depth [*Melosh*, 1989]. The concept of the transient crater is introduced to describe the initial shape of the crater that will be subject to further collapse and uplift in the following modification stage.

3.1.3. Modification Stage

The final modification stage of crater formation is marked by collapse due to gravity inducing an uplift of the crater floor and failure of the crater rim (Figure 3.1(c)). At the end of this stage the preliminary final crater has formed, which is then modified by subsequent geologic processes, such as erosion and infill, on longer time scales.

The modification stage starts when the major driving force to material motion is dominated by gravity. The transient crater cavity is supported by the material strength. When the negative buoyancy of the crater cavity exceeds this strength, the crater floor is uplifted and the rim collapses in terraces, forming prominent scarps along concentric normal faults (Section 5.1) [e.g. *Kenkmann et al.*, 2013]. In addition, shocked and fractured near-surface material on the crater wall and central peak wastes towards the crater floor (dashed arrows in Figure 3.1(c)).

The highly shocked and fractured material involved in the mass wasting of the modification stage is particularly mobile and reaches velocities in the order of 50 m/s [*Jutzi et al.*, 2013]. The extraordinary mobility is caused by the temporary reduction of internal friction induced by the embedded impact energy (Section 3.1.5).

The duration of the modification stage is similar to that of the excavation stage as stated in Equation 3.2 (∼275 s) [e.g. *Kenkmann et al.*, 2013]. The

stage ends when the initial gravity-driven material motion stops due to internal friction and material strength. After some initial mass wasting along the newly formed crater walls, the temporary final crater has formed. However, cooling of the impact-heated material may take the order of 10^5 years depending on the crater size and embedded energy [*Melosh*, 1989].

3.1.4. Crater Degradation

After the modification stage, the crater cavity is not in isostatic equilibrium as the target material tends to close the cavity by viscous relaxation [*Scott*, 1967]. In linear approximation, the depth h decreases exponentially with time:

$$h(t) = h_0 e^{(-t/t_{\mathrm{vr}})}, \tag{3.3}$$

where h_0 is the original crater depth and t_{vr} is the characteristic relaxation time needed to reduce the depth by a factor of e:

$$t_{\mathrm{vr}} = \frac{4\pi\eta_{\mathrm{t}}}{\rho g D}. \tag{3.4}$$

Here η_{t} is the viscosity of the target material, ρ is the density and g is the gravity of the target. D is the crater diameter [*Melosh and Ivanov*, 1999; *Scott*, 1967]. The Rheasilvia impact crater as it appears today, with $\eta = 10^{25}$ Pa·s [*Melosh and Ivanov*, 1999], $\rho = 3.5$ g/cm^3, $g = 0.25$ m/s^2 and $D = 500$ km, would have a relaxation time of $t_{\mathrm{vr}} \approx 10^{11}$ years. Assuming an age of $t = 3.5$ Ga [*Schmedemann et al.*, 2014] and a crater depth of $h = 19$ km, it is possible that the original basin has relaxed by ∼700 m in depth so far.

Finally, the crater is further degraded by other processes. On dry airless bodies, such as Vesta, these processes include mass wasting, space weathering and impact gardening [e.g. *Krohn et al.*, 2014a; *Otto et al.*, 2013; *Pieters et al.*, 2012]. The major result is infilling of the cavity so that the crater topography is smoothed.

3.1.5. Acoustic Fluidisation

The apparent preservation of the central peak of complex craters implies that the material properties of the modification flow are described by transient low internal friction and low strength (e.g. the internal coefficient of friction of large lunar craters during the modification stage is less than 0.03 [*McKinnon*, 1978]) followed by a loss of these properties which freezes the central peak in position. Otherwise the central peak would collapse back to a surface level, as it is the case for an impact into water.

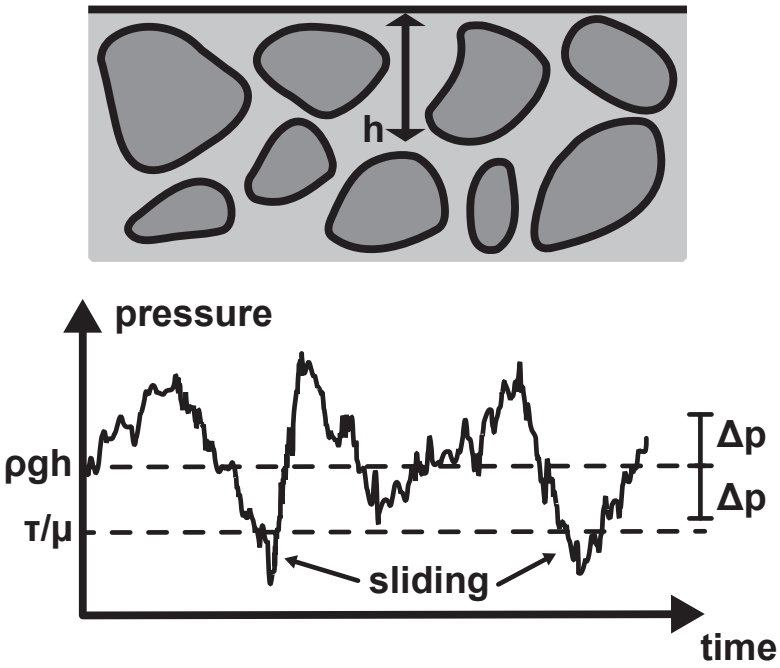

Figure 3.2.: Sketch illustrating acoustic fluidisation. At a depth h, the overburden pressure of ρgh is larger than the threshold for sliding given by τ/μ. The acoustic fluctuations oscillate with a variance of Δp around the overburden pressure. Sliding occurs whenever the total pressure drops below the threshold for sliding. Adapted from *Melosh* [1979].

The commonly accepted mechanism for temporary fluidising the target material during the modification stage of crater formation is presented by *Melosh* [1979] who introduced the theory of *acoustic fluidisation*. The theory states that the rheology of the debris surrounding the crater cavity is influenced by strong shaking and vibrations generated by the stress wave. These vibrations induce an acoustic field in the assumed homogeneous material and temporarily reduce the overburden pressure below the threshold for the material to flow[2] (Figure 3.2).

Given a target material with density ρ and a target body with gravity g, the overburden pressure p_o at depth h is given by $p_o = \rho gh$. Under non-fluidised conditions the overburden pressure may exceed the threshold for sliding $p_t = \tau/\mu$, defined by the applied shear stress τ and the coefficient

[2]The temporary low strength behaviour can also be described as a *Bingham fluid*, which behaves elastically below, and flows viscously above, an applied critical stress.

of friction μ. Assuming that the acoustic pressure field fluctuations can be described by Gaussian statistics, a variance Δp can be defined with which the pressure oscillates around the overburden pressure. If the combination of overburden pressure and fluctuation drops below the threshold for sliding, the material begins to flow. With increasing variance of the acoustic field, this condition is reached more frequently resulting in a more effectively fluidised material [*Melosh and Ivanov*, 1999; *Melosh*, 1989].

The oscillation intensity of the fluidised material drops exponentially with time and eventually falls below the threshold necessary for sliding. The fluidised material returns to dry Coulomb friction, bringing the central uplift and rim collapse to a halt.

Other mechanisms on dry airless bodies capable of reducing the strength of the material mobilized in the modification stage include: localised brittle deformation, impact heat and melt, and dust lubrication [e.g. *Singer et al.*, 2012]. Brittle faulting during the impact event generates a network of fractures which may reduce the strength on a macroscopic scale and can produce ductile behaviour of rocks [*Kenkmann*, 2002]. Impact heat may reduce the strength of rocks if temperatures approach their melting points [e.g. *Stesky et al.*, 1974] and impact melt mixed within the mobilized material may lubricate the rock contacts resulting in lower contact friction [*Dence et al.*, 1977]. A dust suspension may reduce the internal friction of larger blocks by reducing the effective normal pressure by buoyancy [*Hsü*, 1975]. Additionally, if present, volatiles such as water may reduce the internal friction by lubrication [*Singer et al.*, 2012; *Legros*, 2002]. Although these mechanisms are relevant during the modification stage, they are not sufficient to uplift the crater floor.

Acoustic fluidisation is also believed to be the reason for the reduced internal friction of very large landslides [*Collins and Melosh*, 2003; *Melosh*, 1986]. Here, the motion of the wasting debris generates acoustic vibrations which fluidise the material and increase the run-out length.

3.1.6. Acoustically Fluidised Material Properties

Acoustically fluidised masses moving during the modification stage can be described with an effective viscosity η_{eff} and coefficient of friction μ_{eff} different from those of the undisturbed target material.

For high enough acoustic energy densities the acoustically fluidised material

can be explained by a Newtonian fluid[3] with effective viscosity η_{eff}:

$$\eta_{\text{eff}} \approx \frac{\rho \lambda c_{\text{s}}^2}{2 c_{\text{p}}}, \tag{3.5}$$

where ρ is the bulk density of the granular debris, λ is the wavelength of the acoustic vibrations, c_{s} is the effective shear wave speed and c_{p} compressional wave velocity [*Collins and Melosh*, 2003]. Because the acoustic wavelength increases with the crater size, larger craters have larger viscosities [*Melosh*, 1986].

Alternatively, the viscosity of a Newtonian fluid moving down an inclined plane - a scenario described by the crater modification stage - can be estimated by Jeffreys' equation:

$$\eta_{\text{eff}} \approx \frac{g \rho \sin(\alpha) d^2}{3 v}, \tag{3.6}$$

where α is the inclination of the plane, d is the thickness and v is the migration velocity of the viscous material [e.g. *Takagi*, 2010; *De Blasio*, 2011]. The viscosity of an acoustically fluidised material roughly ranges between 10^5 Pa·s and 10^7 Pa·s [*Melosh*, 1986, 1979] - comparable to basaltic lava flows on Earth such as the Mauna Loa lava flows in Hawai'i [*Moore*, 1987].

The material involved in the modification stage can also be modelled as a body moving along an inclined plane with slope α in a gravity environment g (Figure 3.3). The friction coefficient μ is defined as the ratio between friction force F_{FR} and normal force F_{N}. Without friction the body would slide down the plane with acceleration $a_{\text{FF}} = g \sin(\alpha)$. However, the acceleration due to friction a_{FR} reduces the apparent acceleration $a = a_{\text{FF}} - a_{\text{FR}}$. Consequently the coefficient of friction is given by:

$$\mu = \frac{F_{\text{FR}}}{F_{\text{N}}} = \frac{a_{\text{FR}}}{g \cos(\alpha)} = \frac{a_{\text{FF}} - a}{g \cos(\alpha)}. \tag{3.7}$$

Alternatively the coefficient of friction can be calculated from the fall height h and the run-out length l of the sliding object (Figure 3.3):

$$\mu = \frac{h}{l}. \tag{3.8}$$

Note that Equation 3.7 and Equation 3.8 are equivalent definitions of the coefficient of friction.

Within the Rheasilvia basin, the masses on the crater wall and central peak travelled a distance of ∼160 km and ∼90 km, respectively, to reach

[3] A Newtonian fluid has a linear relationship between shear stress and shear rate.

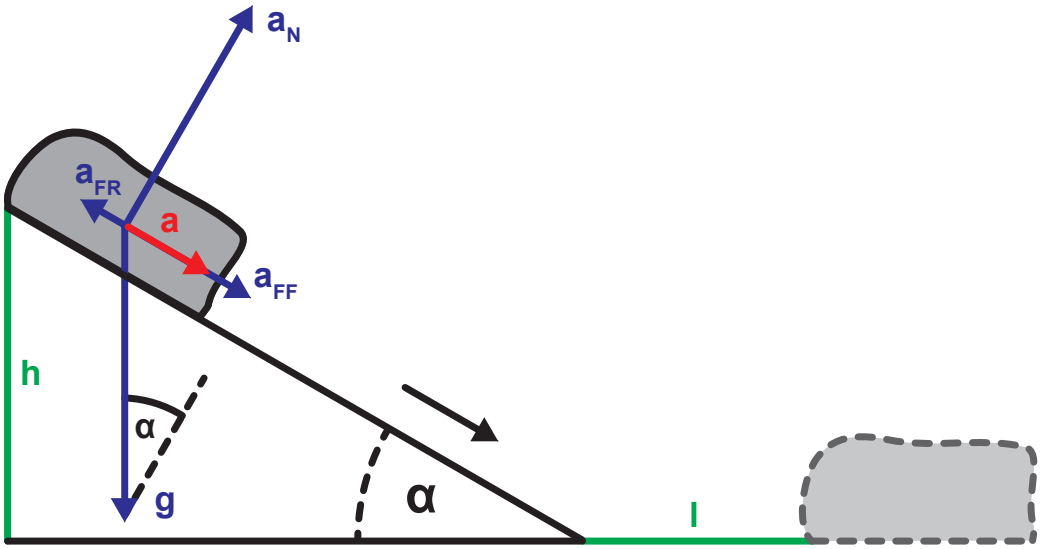

Figure 3.3.: Sketch illustrating the accelerations acting on a slab moving down an inclined plane at an angle α and with a coefficient of friction $\mu = 0.2$. The gravitational acceleration (g) points downwards. The normal (a_{N}) and friction-free sliding accelerations (a_{FF}) are derived from the magnitude of gravity and the inclination of the plane. The resulting acceleration down the plane (a, red arrow) is the sum of the friction-free sliding acceleration and the acceleration due to friction. The slab's fall height (h) and run-out length (l) are sketched (green).

the crater floor from a height of ∼19 km. This yields effective coefficients of friction of ∼0.12 and ∼0.21 for the crater wall and central peak, respectively, which is comparable to values of large landslides [*Legros*, 2002]. However, the run-out length is restricted by the crater size and shape and therefore this estimate can only be a rough approximation.

3.1.7. The Rheasilvia Impact Event

Numerical impact simulations are the common approach when reconstructing planet-scale impact events. Motivated by the Dawn mission, the Rheasilvia impact event has been analysed using various numerical models.

Ivanov and Melosh [2013] used the B version of the Simplified Arbitrary Lagrangian Eulerian code (SALEB). They set up a two-dimensional simulation with a maximum cell and time resolution of 930 m and 0.015 s, respectively. By trial and error they adjusted their model to simulate the observed topog-

raphy of Rheasilvia. Assuming a spherical Vesta of 540 km diameter with a crust of 40 km thickness and an iron core of 100 km in radius, they found that Rheasilvia could have been produced by a 37 km diameter basaltic impactor with a vertical impact velocity of 5.5 km/s. A maximum crater depth of 82 km was reached ∼400 s after the impact began and the transient crater diameter was found to be 264 km. Although the impact energy was not sufficient for extensive impact melting, it allowed 2–8×10^5 km^3 of material to escape from Vesta by spallation and excavation. A maximum excavation depth of ∼40 km was reached. Spallation displaced upper crust material ∼10 km away from the impact point and took place on almost the entire surface of Vesta.

Additionally, *Williams et al.* [2013] estimated the melt volume of a 5 km/s Rheasilvia impact. It ranges between 47 km^3 and 4400 km^3 depending on the target porosity, where the larger amount of melt volume corresponds to a higher porosity [*Wünnemann et al.*, 2008]. This is a relatively small amount compared to bodies with larger impact velocities, such as the Moon. However, the calculation is supported by the sparse geomorphologic evidence of impact melt.

Using the similar iSALE shock hydrodynamics code, *Bowling et al.* [2013] found that the shock wave might have generated an antipodal uplift. However, due to younger impacts near Rheasilvia's antipode, the feature is not confirmed by Dawn observations.

Jutzi et al. [2013] used a three-dimensional smooth particle hydrodynamics (SPH) impact code to simulate the Veneneia and Rheasilvia impacts. The basis of their simulation is a spherically layered, 550 km diameter Vesta and a 64 km diameter Veneneia impactor with an impact velocity of 5.4 km/s. They assumed a vertical impact to model the Veneneia impact and used the resulting shape as a base model to simulate the subsequent Rheasilvia impact event. The rotation axis (period of 5.3 h) was placed in the centre of the Veneneia basin. A 66 km diameter Rheasilvia impactor striking at 5.4 km/s (vertically), 40° from the centre of Veneneia, successfully reconstructed Vesta's current topography and ejecta distribution. As a result, they found that the ejecta which reaccumulated in the north came from a depth of 20 km and the area where Veneneia and Rheasilvia intersect probably exposes material from 60–100 km depth.

Additionally, the simulation shows that Vesta's rotation induces a deflection of mass motions during crater collapse (Figure 3.4). At typical velocities of 50 m/s, the trajectories resemble the curved structures observed in the Rheasilvia basin (Section 5.2).

The transition from the excavation to the modification stage of Rheasilvia's

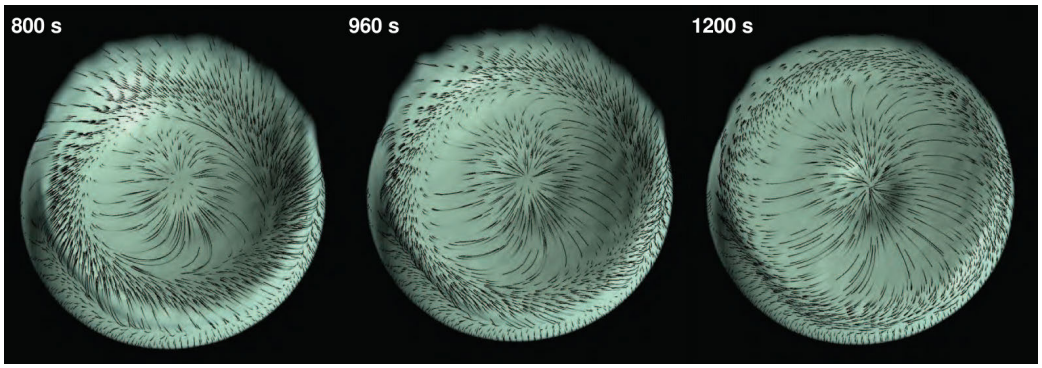

Figure 3.4.: Snapshots of the SPH simulation conducted by *Jutzi et al.* [2013]. Three stages of the Rheasilvia modification stage on a rotating Vesta are shown. The black lines illustrate the material flow. The Coriolis force causes the flow lines to be curved similarly to the observed curved structures in the Rheasilvia basin. Extracted from *Jutzi et al.* [2013], Copyright (2013), with permission from Macmillan Publishers Ltd.

formation roughly coincides with reaching the maximum crater depth. *Ivanov and Melosh* [2013] found a maximum depth of 82 km after ∼400 s which is of the same order as the ∼275 s estimated by Equation 3.2. Generally, the modification stage would roughly last for a similar time scale, however the simulations by *Jutzi et al.* [2013] and *Ivanov and Melosh* [2013] both indicate that the basin formation was still in progress after 1200 s.

Assuming a mass motion velocity of 50 m/s and a duration of the wasting process of 1200 s, the length of the trajectory of a moving mass during the modification stage is given by 60 km, which is approximately 1/4 of the Rheasilvia radius. However, it is likely that the mass wasting occurred over longer time scales, possibly extending over the entire basin walls [*Jutzi et al.*, 2013].

3.2. The Coriolis Effect

3.2.1. Forces in a Rotating Reference Frame

Asteroid Vesta rotates and this introduces two forces: The centrifugal and the Coriolis force. They can be easily explained by observing the rotating system from a non-rotating reference frame [e.g. *Etling*, 2008; *Knauss*, 1997; *Durran*, 1993].

Let Vesta's rotating reference frame be denoted by the index V and the non-rotating inertial system by the index I. Both systems have their origin in the centre of Vesta (geocentric coordinate system, Figure 3.5). Vesta rotates with the angular velocity $\vec{\Omega}$ and thus the time derivative of a vector transforms between the two systems as follows:

$$\left(\frac{d}{dt}\right)_{\mathrm{I}} = \left(\frac{d}{dt}\right)_{\mathrm{V}} + \vec{\Omega}\times \tag{3.9}$$

This implies that an object at point $\vec{r}$, moving with a velocity $\vec{v}_{\mathrm{V}}$ on Vesta's surface, moves with the velocity $\vec{v}_{\mathrm{I}}$ in the inertial system:

$$\vec{v}_{\mathrm{I}} = \left(\frac{d\vec{r}}{dt}\right)_{\mathrm{I}} = \left(\frac{d\vec{r}}{dt}\right)_{\mathrm{V}} + \vec{\Omega}\times\vec{r} = \vec{v}_{\mathrm{V}} + \vec{\Omega}\times\vec{r}. \tag{3.10}$$

The relation between accelerations in the inertial and Vesta system is given by applying Equation 3.9 on Equation 3.10:

$$\begin{aligned}
\left(\frac{d\vec{v}_{\mathrm{I}}}{dt}\right)_{\mathrm{I}} &= \left(\frac{d\vec{v}_{\mathrm{V}}}{dt}\right)_{\mathrm{I}} && + \underbrace{\left(\frac{d}{dt}(\vec{\Omega}\times\vec{r})\right)_{\mathrm{I}}}_{\Omega = \text{const.}} \\
&= \underbrace{\left(\frac{d\vec{v}_{\mathrm{V}}}{dt}\right)_{\mathrm{I}}}_{\text{Eq. 3.9}} && + \vec{\Omega}\times\underbrace{\left(\frac{d\vec{r}}{dt}\right)_{\mathrm{I}}}_{\text{Eq. 3.10}} \\
&= \left(\frac{d\vec{v}_{\mathrm{V}}}{dt}\right)_{\mathrm{V}} + \vec{\Omega}\times\vec{v}_{\mathrm{V}} && + \vec{\Omega}\times\vec{v}_{\mathrm{V}} + \vec{\Omega}\times\vec{\Omega}\times\vec{r} \\
&= \left(\frac{d\vec{v}_{\mathrm{V}}}{dt}\right)_{\mathrm{V}} + 2\vec{\Omega}\times\vec{v}_{\mathrm{V}} + \vec{\Omega}\times\vec{\Omega}\times\vec{r}
\end{aligned} \tag{3.11}$$

Consequently, a non-accelerated motion in the inertial system with no external forces ($\{d\vec{v}_{\mathrm{I}}/dt\}_{\mathrm{I}} = 0$) experiences an acceleration in the rotating frame. Rewriting without the index V the relation is:

$$\frac{d\vec{v}}{dt} = -2\vec{\Omega}\times\vec{v} - \vec{\Omega}\times\vec{\Omega}\times\vec{r}, \tag{3.12}$$

or in terms of the force $\vec{F}$:

$$\vec{F} = \underbrace{-2m\vec{\Omega}\times\vec{v}}_{\text{Coriolis Force}}\underbrace{-m\vec{\Omega}\times\vec{\Omega}\times\vec{r}}_{\text{Centrifugal Force}}. \tag{3.13}$$

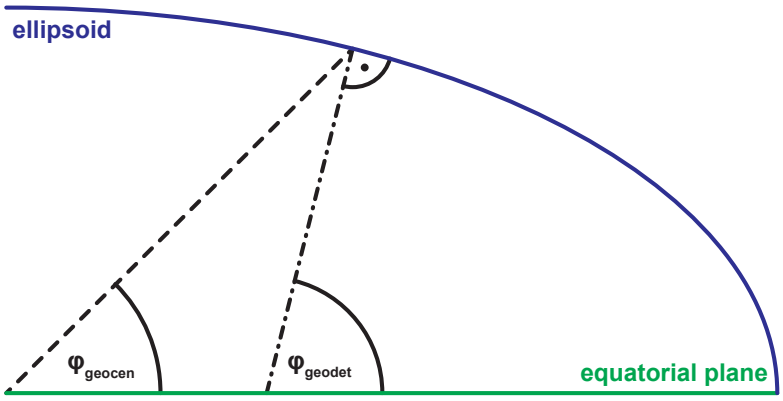

Figure 3.5.: Sketch illustrating geodetic and geocentric latitude of an ellipsoid (blue). The geodetic latitude of a point is defined as the angle between the ellipsoid's normal vector at that point and the equatorial plane (green). The geocentric latitude is defined as the angle between the vector spanning from the ellipsoid's centre to the point and the equatorial plane.

Whereas the centrifugal force exists on every point of the rotating object, the Coriolis force is only effective if an object is moving in the rotating frame.

On the southern hemisphere, the Coriolis Effect deflects mass motions to the left in the direction of motion and accordingly to the right on the northern hemisphere. This implies that masses moving towards and away from the rotation axis on the same hemisphere are deflected in opposite directions.

As seen in Section 2.4.5 the centrifugal acceleration on Vesta reaches up to 0.03 m/s^2 at the equator, which is ∼13% of the gravitational acceleration. Considering an object on Vesta moving perpendicular to the rotation axis with a velocity of 50 m/s, as suggested for typical mass wasting velocities during the Rheasilvia modification stage [*Jutzi et al.*, 2013], the Coriolis acceleration is also ∼0.03 m/s^2.

3.2.2. Geodetic Reference Frame[4]

Vesta's shape can be well described by a biaxial ellipsoid (also known as a spheroid). In Cartesian coordinates it is determined by:

$$\frac{x^2 + y^2}{a^2} + \frac{z^2}{b^2} = 1, \tag{3.14}$$

[4]Although usually used in purely terrestrial situations, for the sake of clarity the prefix 'geo' is used throughout this thesis when discussing standard geodetic terms, albeit relating to Vesta.

where a and b are the semi-major and semi-minor axes of the spheroid, respectively.

In the following, it will prove useful to apply a geodetic coordinate system to biaxial Vesta [*Ripa*, 1997]. A point on the surface of a spheroid centred at the origin of the coordinate system can be described by latitude and longitude when the two body axis are known. While a geocentric coordinate system used above defines latitude as the angle between the vector of the surface point and the equatorial plane, the geodetic system defines the latitude by the angle between the normal vector of the surface point and the equatorial plane (Figure 3.5). Thus, the major advantage of the geodetic coordinate system is that the normal vector of a surface point is determined by the longitude and the geodetic latitude. The longitude of the geocentric and geodetic systems are equivalent because of the biaxial symmetry. The geodetic latitude φ_{geodet} and geocentric latitude φ_{geocen} can be converted by the formula [e.g. *Snyder*, 1987]:

$$\tan(\varphi_{\text{geodet}}) = \frac{a^2}{b^2} \tan(\varphi_{\text{geocen}}). \tag{3.15}$$

3.2.3. Inertial Circles

The previously calculated Coriolis acceleration remains perpendicular to the velocity of the moving object. Therefore, it does not change the magnitude of the velocity, but only the direction. The deflection of a moving object at a point at latitude φ_{geodet} on Vesta can be obtained by defining a Cartesian coordinate system which is fixed to this point [e.g. *Etling*, 2008; *Knauss*, 1997; *Durran*, 1993]. The three axes of the body-fixed coordinate system are defined by the direction of constant latitude (x), the perpendicular vector to x lying in the tangent plane (y) and the surface normal vector (z) (Figure 3.6). In this system, the angular velocity $\vec{\Omega}$ can be represented by:

$$\vec{\Omega} = \Omega \cos(\varphi_{\text{geodet}})\hat{\text{e}}_{\text{y}} + \Omega \sin(\varphi_{\text{geodet}})\hat{\text{e}}_{\text{z}}, \tag{3.16}$$

where $\hat{\text{e}}_{\text{x,y,z}}$ are the unit vectors of the body fixed coordinate system and Ω is the magnitude of $\vec{\Omega}$. Consequently, the Coriolis acceleration $\vec{a}_{\text{C}}$ of an object moving with velocity $\vec{v} = (v_{\text{x}}, v_{\text{y}}, v_{\text{z}})$ in the body fixed system is described by:

$$\begin{aligned} \vec{a}_{\text{C}} &= -2\vec{\Omega} \times \vec{v} \\ &= -(\tilde{f}\hat{\text{e}}_{\text{y}} + f\hat{\text{e}}_{\text{z}}) \times (v_{\text{x}}\hat{\text{e}}_{\text{x}} + v_{\text{y}}\hat{\text{e}}_{\text{y}} + v_{\text{z}}\hat{\text{e}}_{\text{z}}) \\ &= (fv_{\text{y}} - \tilde{f}v_{\text{z}})\hat{\text{e}}_{\text{x}} \; - fv_{\text{x}}\hat{\text{e}}_{\text{y}} \; + \tilde{f}v_{\text{x}}\hat{\text{e}}_{\text{z}} \end{aligned} \tag{3.17}$$

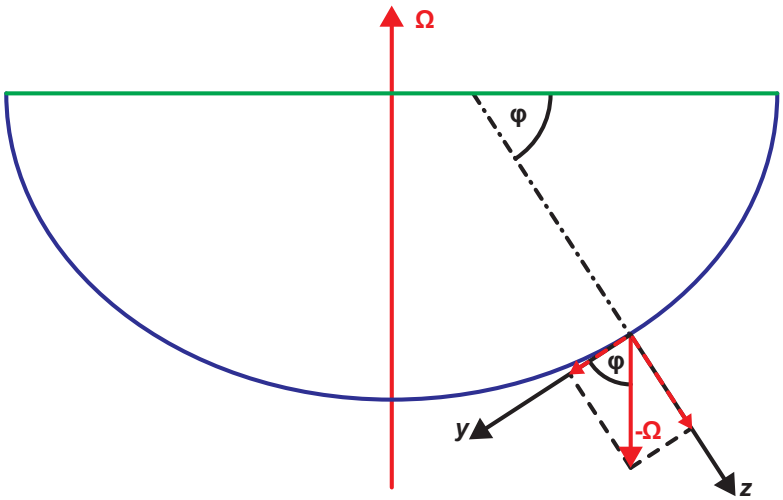

Figure 3.6.: Illustration of the body fixed coordinate system used to investigate the Coriolis deflection on Vesta's southern hemisphere (blue). Ω and φ are the angular velocity (red) and geodetic latitude, respectively. The y- and z-direction of the body fixed system and the components of Ω in this system (red dashed) are sketched. Note that in the southern hemisphere the geodetic latitude is negative.

Here, f and $\tilde{f}$ are the Coriolis parameters:

$$f = 2\Omega \sin(\varphi_{\text{geodet}}) \quad \text{and} \quad \tilde{f} = 2\Omega \cos(\varphi_{\text{geodet}}). \tag{3.18}$$

Considering a horizontal motion along the surface ($v_z = 0$), which is reasonable for mass-wasting processes, the Coriolis acceleration can be simplified:

$$\vec{a}_C = f v_y \hat{e}_x - f v_x \hat{e}_y, \tag{3.19}$$

or considering the separate components:

$$\frac{dv_x}{dt} - f v_y = 0, \quad \frac{dv_y}{dt} + f v_x = 0. \tag{3.20}$$

Further rearrangement yields:

$$\frac{d^2 v_x}{dt^2} + f^2 v_x = 0, \quad \frac{d^2 v_y}{dt^2} + f^2 v_y = 0. \tag{3.21}$$

These are a set of differential equations characteristic for oscillations and can thus be solved by the standard solution:

$$v_{x,y}(t) = A_{x,y} \sin(\omega t) + B_{x,y} \cos(\omega t), \tag{3.22}$$

where $A_{x,y}$ and $B_{x,y}$ are the amplitudes and ω the frequency of the oscillation. Solving the differential equations 3.20 and 3.21 with the standard solution 3.22 and appropriate initial conditions (e.g. $v_x|_{t=0} = |\vec{v}| = v$ and $v_y|_{t=0} = 0$), the velocity components are given by:

$$v_x(t) = v\cos(ft), \quad v_y(t) = -v\sin(ft). \tag{3.23}$$

Therefore, the horizontal motion of an object on a rotating body is described by an oscillation with frequency f and period $T = 2\pi/f$. Hence, the Coriolis parameter f is also often called *Coriolis frequency*. The trajectory of a moving object initially positioned at the origin of the tangent plane ($x|_{t=0} = 0$ and $y|_{t=0} = 0$) is found by integrating the equations for the velocities:

$$x(t) = \frac{v}{f}\sin(ft), \quad y(t) = \frac{v}{f}\cos(ft) - \frac{v}{f}. \tag{3.24}$$

Consequently, the motion is represented by a circle in the tangent plane [e.g. *Etling*, 2008]. The circle is called an *inertial circle* and its radius R is given by

$$R = \frac{v}{f} = \frac{v}{2\Omega\sin(\varphi_{\text{geodet}})}. \tag{3.25}$$

Equally, the mass motion velocity can be determined when the inertial radius and the Coriolis parameter are known:

$$v = Rf = 2R\Omega\sin(\varphi_{\text{geodet}}). \tag{3.26}$$

At 45° latitude on Vesta, the Coriolis period is 3:46 h which indicates that the Coriolis deflected mass motions related to the Rheasilvia impact, with ∼10–30 minutes duration, can only show a part of the inertial circle.

Strictly speaking, this solution is an approximation neglecting the fact that the Coriolis force is not constant at each position of an inertial circle due to the changing latitude (β-Effect) [*Ripa*, 1997]. However, this effect is negligible (in the order of ∼5% variation) for changes in latitude as described in Section 6.2. Additionally, the non-hydrostatic ellipsoidal shape of Vesta introduces a component of gravity which is parallel to the tangent plane [*Paldor and Sigalov*, 2001; *Ripa*, 1997; *Durran*, 1993] resulting in an acceleration of the order of ∼5% of the centrifugal acceleration. Therefore, a drift is added to the motion of the inertial circles. Nevertheless, this effect is superimposed by the acceleration introduced by Vesta's topography (Section 6.6) which predominates the drift motion.

3.2.4. Rossby Number

The above considerations are valid if the Coriolis force is the only force acting on a moving object. However, in many cases there are additional forces such as pressure gradients, friction or gravity [*Knauss*, 1997]. On airless Vesta, pressure gradients are not present, however effects such as friction and gravitational acceleration due to topography may additionally affect the trajectory of moving masses.

Therefore, it is useful to define a measure of the significance of the Coriolis Effect in a given scenario. The observed curvature of a mass moving horizontally on a rotating object corresponds to the centrifugal acceleration which keeps the mass on the curved trajectory. This centrifugal force is given by v^2/l, where v is the moving mass's velocity and l is the radius of curvature. It is counteracting the sum of all acceleration $|\vec{a}_{\text{tot}}|$ acting on the mass including the Coriolis acceleration and any other accelerations, e.g. gravity. The Coriolis acceleration $|\vec{a}_{\text{C}}|$ can be approximated to vf using Equation 3.17, where f is the Coriolis frequency.

The ratio of centrifugal and Coriolis acceleration is commonly used to estimate the importance of the Coriolis Effect under the influence of additional forces and is defined as the *Rossby number Ro*:

$$Ro = \frac{|\vec{a}_{\text{tot}}|}{|\vec{a}_{\text{C}}|} = \frac{v^2/l}{vf} = \frac{v}{fl}. \tag{3.27}$$

From Equations 3.27 it is clear that if there are no additional forces - a scenario that was assumed in Section 3.2.3 - the Rossby number equals 1. In this case, the Coriolis acceleration counteracts the centrifugal acceleration and the mass motion will describe an inertial circle. For $Ro \gg 1$ the Coriolis acceleration becomes negligible because the additional accelerations dominate the Coriolis acceleration. On the other hand, the Coriolis Effect becomes significant for $Ro \ll 1$. Thus, the Rossby number allows the influence of the Coriolis Effect to be estimated without specifying the additional forces that may superimpose the inertial motion [*Knauss*, 1997].

Considering the Rheasilvia impact basin to have a radius of 250 km and a mass wasting velocity of 50 m/s during the modification stage [*Jutzi et al.*, 2013], the Rossby number at 45° latitude is $Ro \approx 0.4$. Thus, the Coriolis Effect is important for mass motions during the modification stage (Section 5.3).

4. Data

The data analysed for this thesis are based on clear filter images provided by the Framing Camera of the Dawn spacecraft [*Sierks et al.*, 2011]. Two pre-processed data sets including a mosaic in LAMO resolution (∼20 m/pixel) [*Roatsch et al.*, 2013] and a stereo-DTM produced from HAMO (∼70 m/pixel) images [*Preusker et al.*, 2012b] were used.

4.1. Digital Terrain Model

For these analyses a HAMO DTM provided by *Preusker et al.* [2012b] was used. The DTM generation is based on stereophotogrammetric (SPG) mapping utilising image data, spacecraft position and camera pointing. The latter are available in the form of SPICE kernels - a package of mission-related geometric information on spacecraft, instruments and target (http://naif.jpl.nasa.gov/). As a first step, the surface was mapped with five different viewing angles. After a pre-rectification of these clear filter images based on a presumption of the geometry of the target, a set of control points were defined. Subsequently, the equivalent image points were determined in multiple stereo images. The intersection of the lines of sight from the FC to these image points yielded the three-dimensional position. Finally, this information was interpolated to global scale [*Preusker et al.*, 2012a; *Raymond et al.*, 2011; *Gwinner et al.*, 2009].

HAMO1 and HAMO2 provided sufficient stereo data (99% surface coverage [*Russell et al.*, 2013]) to calculate a Vesta DTM with a lateral spacing of 93 m/pixel and a mean ray intersection error of 7.5 m which translates to a vertical accuracy of ∼5 m. The reference body used to state elevation is an ellipsoid with major axis of 285 km and minor axis of 229 km [*Preusker et al.*, 2012b; *Roatsch et al.*, 2012; *Jaumann et al.*, 2012].

4.2. Mosaic

The DTM enabled the construction of a mosaic in HAMO and LAMO resolution [*Roatsch et al.*, 2013, 2012]. After ortho-rectifying each image with reference to the DTM, a mosaic was produced by combining these images

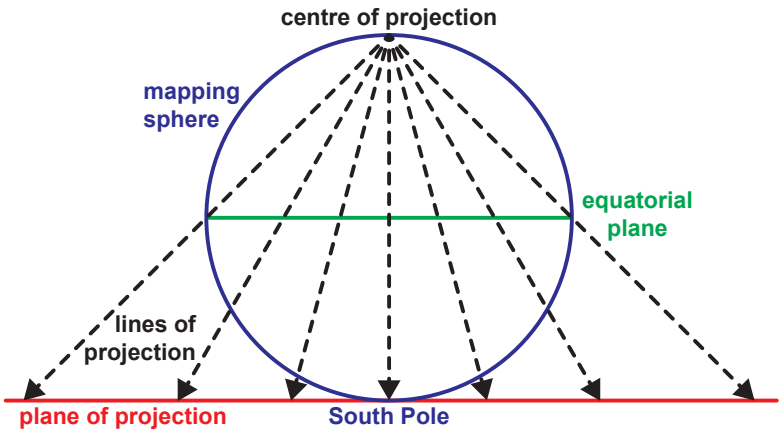

Figure 4.1.: Schematic to illustrate a stereographic projection of the souther hemisphere. The lines of projection (dashed lines) originate at the North Pole. The projection plane (red) is located at the South Pole and oriented parallel to the equatorial plane (green). The point where a line of projection intersects the mapping sphere (blue) is projected to the point where the same line intersects the projection plane. Adapted from *Snyder* [1987].

and averaging overlaps. Finally, the mosaic was projected by geocentric vectors onto a sphere of 255 km radius to simplify the interpretation and comparability of the data.

Vesta has a LAMO coverage of 66% [*Russell et al.*, 2013]. Missing image data in LAMO resolution was substituted with HAMO data. The missing data cluster around the North Pole which was in seasonal shade during the data acquisition. Fortunately, most of the southern hemisphere is covered at LAMO resolution and the reduced resolution in a few places does not hinder the scientific analysis.

The mosaic's coordinate system applies positive East longitudes. However, the zero longitude is different from the one used by the International Astronomical Union (IAU) [*Archinal et al.*, 2013] to publish data in the Planetary Data System (PDS) [*Li*, 2012]. The mosaic uses the "Claudia" system which is defined by the tiny crater Claudia. The conversion between IAU and Claudia longitude is given by φ(Claudia) = φ(IAU) - 150° [*Li*, 2012].

4.3. Map Projection

In this thesis I used a stereographic projection of Vesta's southern hemisphere. The projection preserves angles which means that circular objects on the sphere appear circular in the projection. Therefore, it is especially useful for identifying and measuring the curvatures of surface features.

The applied stereographic projection utilizes the North Pole as projection centre and the tangent plane at the South Pole as projection plane. Consequently, a point on the southern hemisphere is projected on the plane by the vector which originates at the North Pole and intersects the hemisphere at this point (Figure 4.1). Applying polar coordinates to describe the map, the longitude of the sphere and the polar angle of the map are identical. The latitude φ of the sphere converts to the polar radius r of the map [e.g. *Snyder*, 1987]:

$$r = 2R\frac{\sin(\varphi)}{1-\cos(\varphi)} = 2R\tan\left(\frac{90^\circ-\varphi}{2}\right), \tag{4.1}$$

where R is the radius of the sphere (255 km).

5. Mass-Wasting Features within Rheasilvia[1]

The geologic setting of this thesis is the Rheaslivia basin (Section 2.4.3). Of particular interest are the mass-wasting features in this region as only moving material can be affected by the Coriolis force.

Six different types of mass-wasting feature in the region inside and around the Rheasilvia impact basin were identified. These include: intra-crater mass-wasting features associated with young craters, flow-like and creep-like patterns of shocked and fractured material, landslides indicative of massive crater collapse, slumps of compact material and curved ridges from the early formation stage of Rheasilvia [*Otto et al.*, 2013]. This chapter concentrates on slumping (Section 5.1) and curved ridges (Section 5.2) within the Rheasilvia basin because they are relevant to the later analysis. A more detailed description on the other types of mass-wasting feature can be found in *Otto et al.* [2013] (Appendix C).

5.1. Slumping

Rotational slumping occurs on steep slopes, when the pressure of the slumping body exceeds the shear resistance of a sliding surface [e.g. *De Blasio*, 2011]. In cohesive materials, the grains do not detach from each other to slide downward, but a surface of rupture is formed by the shear stress of the overlying body. The body as a whole then slumps downward along the hemispherical or spoon-like shaped surface of rupture.

Features of rotational slumping include almost vertical scarps and heads that are tilted backward toward the scarp. Transverse cracks, ridges and a toe feature at the front of the slide can often be observed (Figure 5.1). Within the Rheasilvia basin, these features are less prominent than the scarps and thus difficult to identify. They are eroded by subsequent impact cratering or local seismic shaking. In some places, the toes are still represented as slightly elevated terrains.

[1] An edited version of this chapter and Figures 5.1, 5.2, 5.3, 5.7 and 5.8 are published in the journal article "Otto, K.A., Jaumann, R., Krohn, K., Matz, K.-D., Preusker, F., Roatsch, T., Schenk, P., Scholten, F., Stephan, K., Raymond, C.A. and Russell, C.T. (2013) Mass-Wasting Features and Processes in Vesta's South Polar Basin Rheasilvia. *Journal of Geophysical Research: Planets*, 118(11):2279–2294, doi:10.1002/2013JE004333".

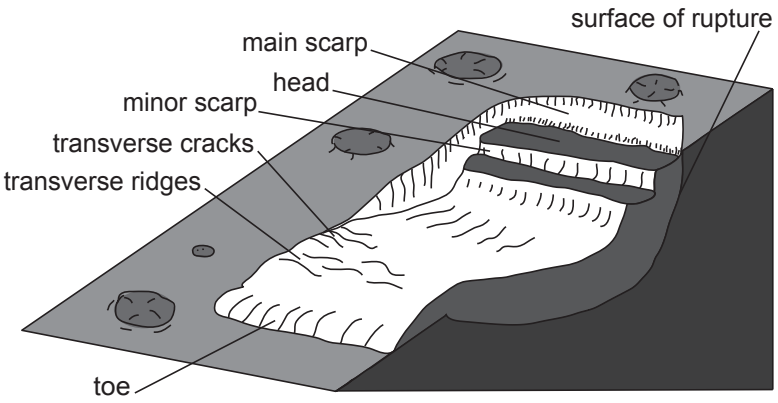

Figure 5.1.: Schematics of a rotational slump (from *Otto et al.* [2013]). The rotational slump slides on a curved surface of rupture generating a main scarp and head feature. Further slumping results in minor scarps. The slumping body exhibits transverse cracks and ridges due to the stretching and compression within the slumping body. The toe feature represents the front of the slump.

The crater of the Rheasilvia impact has degraded due to slumping in various regions. Some slumping areas are heavily eroded, while others are relatively well preserved. Therefore, slumping did not only occur as part of the modification stage of the impact event (Section 3.1.3), but also after the initial collapse (Section 3.1.4).

A prominent and relatively young area of rotational slumping blocks appears along the Matronalia Rupes scarp (Figure 5.2(a)) towards the centre of the Rheasilvia basin (within the area of 45°S to 65°S and 75°E to 115°E) [*Krohn et al.*, 2014b]. Matronalia Rupes represents the main scarp of the slumping body and numerous minor scarps of subsequent slumping, ridges and the toe of the slumping body are evident (Figure 5.2(a)). This slumping area proves the continuing erosional degradation of Rheasilvia.

Furthermore, three ancient relics of slumping blocks within the region of 35°S to 55°S and 165°E to 185°E, the area where Rheasilvia intersects Veneneia, within 20°S to 30°S and 290°E to 310°E, and within 25°S to 55°S and 320°E to 40°E (Figure 5.2(b)) could be identified (cf. Figure 5.3, purple lines). Younger geological activities, such as impact cratering or sliding of debris, eroded the original rotational slump scarps and heads, so that often only the upper parts of the slumping heads are visible as rounded elongated rims. The first two slumping areas have main scarps angled with respect to

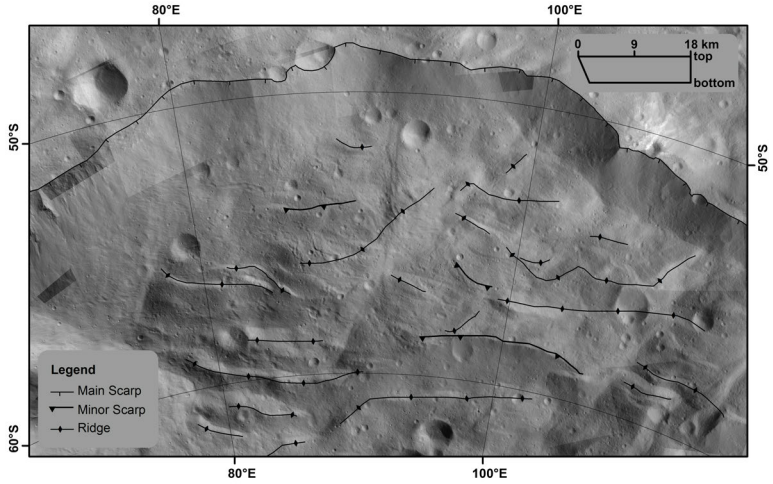

(a) Rheasilvia's youngest slumping area along the scarp of Matronalia Rupes (main scarp), within the region of 45°S to 65°S and 75°E to 115°E.

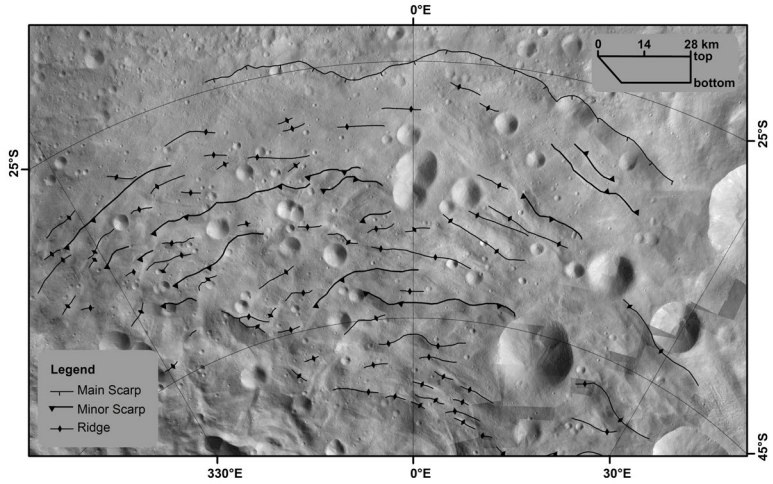

(b) An ancient slumping body, within the area of 25°S to 55°S and 320°E to 40°E. The major scarp represents Rheasilvia's rim. The advanced erosion may indicate that the slumping body originates from the modification stage of the impact event.

Figure 5.2.: Slumping bodies within the Rheasilvia basin (from *Otto et al.* [2013]). The minor scarps indicate slumping from previously wasted material and ridges represent degraded scarps and material accumulations. The scarps and ridges were identified using the DTM and LAMO mosaic. The images are in a stereographic projection with the scale bar applicable at the centre.

the rim of Rheasilvia, indicating that the basin did not collapse concentrically in these regions. This might be due to varying material strengths and substructures within the Rheasilvia wall. The third slumping region's scarps are parallel to the crater rim indicative of a concentric degradation of the Rheasilvia basin. Its size and relatively high crater density may indicate that this slumping feature is a relic from the modification stage of the impact event (Figure 5.2(b)).

Further slumping of previously wasted material on asteroids can be triggered by seismic activity due to impact processes [*Richardson et al.*, 2005, 2004]. The relaxation of the Rheasilvia basin may also have triggered slumping by deforming the base on which the masses rested. Younger geologic activities, such as impact cratering or sliding of debris, eroded the original rotational slump scarps and heads, so that often only the upper parts of the slumping heads are visible as rounded elongated rims.

5.2. Curved Ridges

The Rheasilvia floor is characterized by numerous ridges and grooves that extend radially and concentrically over the impact basin (Figure 5.3).

The concentric ridges are parallel to the crater rim with heights of up to 1 km and lengths of up to 10 km (Figure 5.4). They often occur perpendicular to the slope, making it likely that they originated from the concentric crater collapse and relaxation after Rheasilvia had formed. The area between 0°E and 90°E is dominated by this type of ridge and also exhibits multiple larger craters likely to have trigged the concentric collapse by means of rotational slumping (Section 5.1, Figure 5.2(b)). The Rheasilvia rim is interrupted at the intersection with Veneneia, between 90°E and 220°E. Here the curved and concentric ridges cross with angles greater than 130°.

The Rheasilvia basin also exhibits curved radial ridges. They are generally larger than the concentric ridges, at up to 200 km in length. The overall trend is one of curvature against the rotational movement of Vesta close to the rim and towards the direction of rotation at the central peak (Figure 5.3, grey lines). They often run in parallel, with smooth troughs separating them (Figure 5.5). In some cases, the troughs exhibit flow-like structures on the ridges' flanks indicating material migration.

The radial ridges, which are ∼2.5 km high with lateral slopes varying from 10° to 20°, are present throughout the entire Rheasilvia basin, but are most prominent between 270°E and 360°E, between 90°E and 220°E (Rheasilvia and Veneneia intersection) and on the central peak (Figure 5.3).

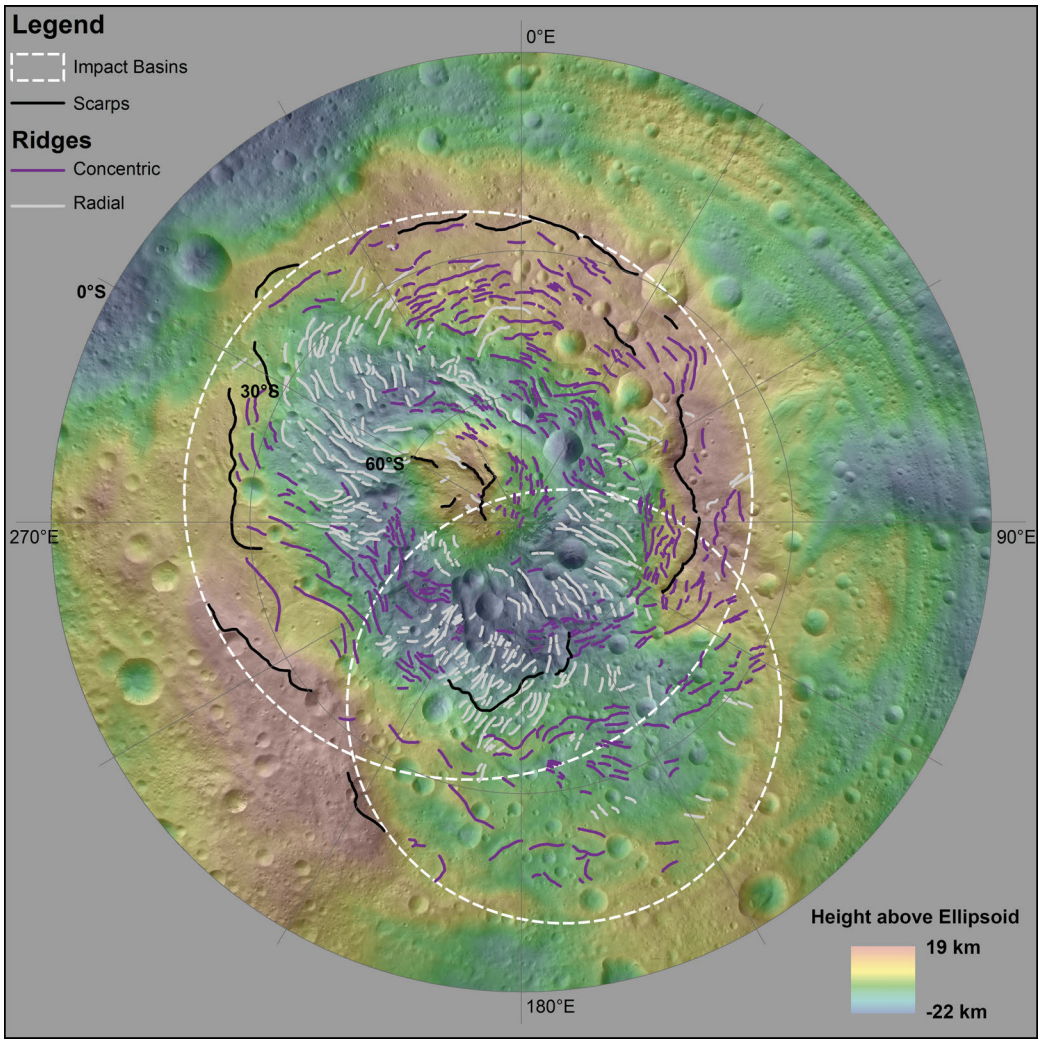

Figure 5.3.: Curved ridges within the south polar basins (from *Otto et al.* [2013]). The outer scarps of the Rheasilvia basin and central uplift are outlined (black lines). The Rheasilvia and Veneneia basins are outlined (white dashed circles). The curved ridges are divided into radial ridges (grey lines) and concentric ridges (purple lines). A feature is labelled as a ridge when it is elongated and elevated from its surroundings. Scarps are a drop-off from a plateau, resembling a step. The features were identified using the DTM. The map is a stereographic projection on a sphere of 255 km radius overlaid by a DTM referenced to a 285 km × 229 km biaxial ellipsoid.

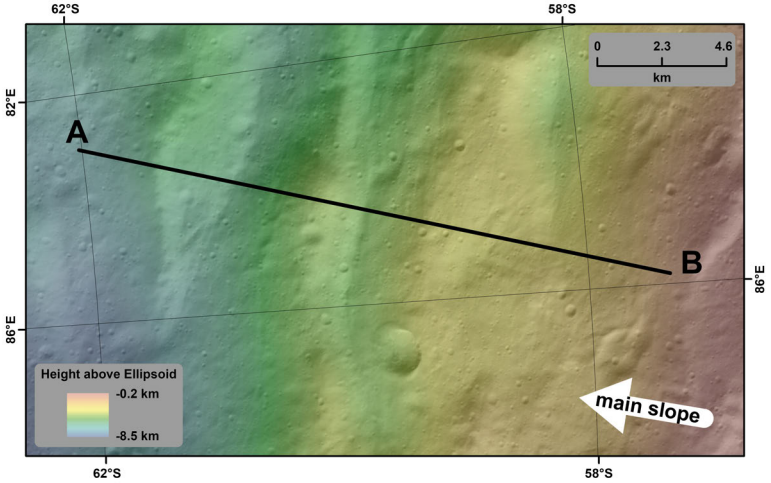

(a) Curved concentric ridges at the Matronalia Rupes scarp within the area of 56°S to 62°S and 80°E to 88°E.

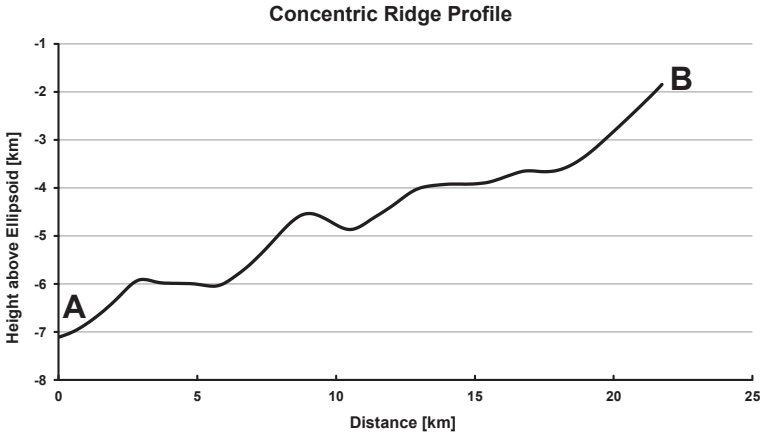

(b) Topographic profile.

Figure 5.4.: Morphology of curved concentric ridges. The ridges are perpendicular to the main slope (white arrow) and describe a step-like undulation. The topographic information is based on a DTM referenced to a 285 km × 229 km biaxial ellipsoid. It is in a stereographic projection with the scale bar applicable at the centre of the image.

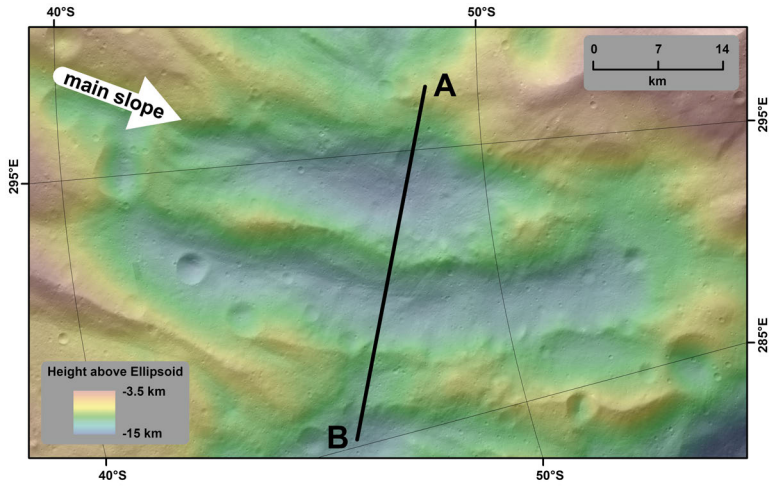

(a) Curved radial ridges pointing towards the central peak within the area of 40°S to 55°S and 280°E to 300°E.

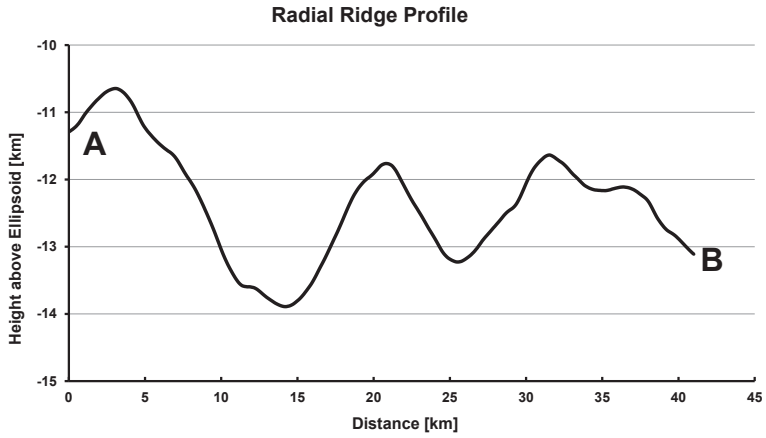

(b) Topographic profile.

Figure 5.5.: Morphology of curved radial ridges. The ridges are parallel to the main slope (white arrow) and describe an undulating surface. The material in the valleys between the ridges shows flow-like structures indicating mass movements. Also note the uniform slopes. The topographic information is based on a DTM referenced to a 285 km × 229 km biaxial ellipsoid. It is in a stereographic projection with the scale bar applicable at the centre of the image.

The structure of the radial ridges can be explained by them being artefacts of the crater's early formation stage, shortly after the Rheasilvia impact event. During the modification stage, material wasted towards the crater floor from the rim and rising central peak (Figure 3.1) [*Jutzi et al.*, 2013]. Once solidified, this highly shocked and fractured material formed the substructure which was subsequently covered by regolith mobilized by slumping, sliding and impact events. The relaxation of the Rheasilvia basin, impact events and cooling of material may have exerted stress on the subsurface material. This stress may have been released by following the path of least resistance producing fissures and faults aligned with the subsurface structure. As a consequence, the regolith covering the fissures and faults may have formed the troughs and ridges by adapting to the subsurface topography. Thus, the original substructure provides the general orientation of the ridges and grooves (Figure 5.3, grey lines).

The slopes of the ridges are similar, possibly representing the static angle of repose of subsided material (Figure 5.5(b)). Additionally, the evidence of material migrating downhill on the flanks of the radial ridges supports this scenario geomorphologically (Figure 5.5(a)). Possible explanations for the curved nature of the ridges are given in Section 5.3.

The radial ridges are unlikely to be levees, often lining debris flows channels. Such levees are produced by the reduced shear stress towards the sides of a debris flow [e.g. *De Blasio*, 2011], however there is no morphological evidence, in particular a region of deposition, associated with the ridges to support this origin.

Complex craters on Earth also show evidence of radial ridges and grooves. *Kenkmann and Dalwigk* [2000] describe radial transpression ridges as features caused by the volumetric uplift of material when moving into a narrowing crater cavity from the crater wall. Although, the expected widening of the ridges in the Rheasilvia basin is not apparent, it is possible that material migrating into the crater cavity bulged up the radial ridges along the subsurface structure.

5.3. Coriolis Effect on Mass Movements

The Coriolis Effect instantaneously affects any particles from dust grains to landslides moving with a perpendicular component to the rotation axis of Vesta. However, the LAMO resolution of 20 m/pixel sets a limit on the observable deflection. To estimate the travel distance and travel time of a mass, it is assumed that a deflection is identifiable if it crosses over at least

five pixels (∼100 m) and that the Rossby number (Equation 3.27) equals one, meaning that the Coriolis and centrifugal forces are equivalent (Section 3.2.4). Hence, a mass motion at a latitude of 45°S requires a minimum velocity of $v = lfRo \approx 5$ cm/s and a minimum travel time of ∼30 minutes at that speed to result in a deflection observable in LAMO resolution. In most cases masses move with larger velocities than the minimum velocity, however the travel times are generally shorter.

In the following paragraphs, the different types of mass wasting, including intra-crater mass-wasting features associated with young craters, flow-like and creep-like patterns of shocked and fractured material, landslides, slumps of compact material and curved radial ridges from the early formation stage of Rheasilvia as described in *Otto et al.* [2013] (Appendix C) will be analysed and the Rossby number (Equation 3.27) will be derived to examine the influence of the Coriolis force.

Most features associated with intra-crater mass-wasting regions, such as spurs, boulders, dark patches and talus material do not show any evidence of the Coriolis Effect because they do not preserve the trajectory of a mass motion. Instead, spurs, dark patches and talus material are immobile features. Only the rolling trace of a falling boulder could indicate the trajectory of a movement. However, because the observed boulders were carried within landslides, the rolling traces were immediately covered by landslide material.

Intra-crater landslides, however, preserve their trajectories along the travelled path. They have been detected in craters of up to 50 km diameter and thus the run-out length has a maximum of ∼25 km, but is shorter for smaller craters or if the landslide stopped before reaching the crater centre. As an example of how the Coriolis force affects intra-crater landslides, we consider the dark landslide in crater Canuleia (Figure 2(b) in Appendix C, latitude $\varphi \approx 34°$S, slope $\alpha \approx 24°$, length $l \approx 3$ km). The Coriolis frequency (Equation 3.18) is $f = 2\Omega \sin(\varphi) \approx 2.7{\cdot}10^{-4}\mathrm{s}^{-1}$. Using the modelling approach of *Lucas et al.* [2014], the wasting velocity can be estimated: $v \approx \sqrt{g_V D \cos(\alpha)}$, where g_V is Vesta's gravitational acceleration and D the mean thickness of the landslide. The mean thickness cannot be resolved in the DTM, but the lower limit can be estimated from the size of the largest blocks in the landslide (∼100 m). Thus, applying a thickness of 100 m results in a minimum wasting velocity of ∼4.8 m/s. Consequently, the lower limit for the Rossby number (Equation 3.27) is $Ro = v/(lf) \approx 5.9$, indicating that the Coriolis force had only a minor effect on the mass motion. Furthermore, the effect is reduced for landslides in regions of lower latitude and for those moving in the direction of rotation (for details see Section 3.2).

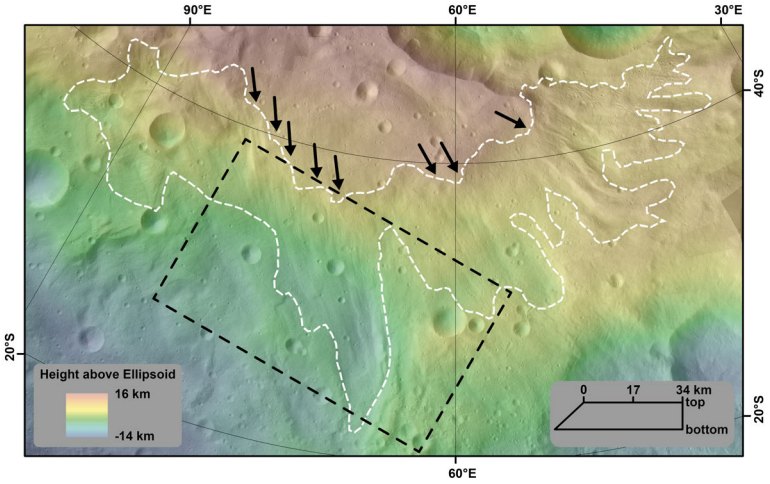

(a) The flow-like feature within the area of 20°S to 45°S and 35°E to 95°E.

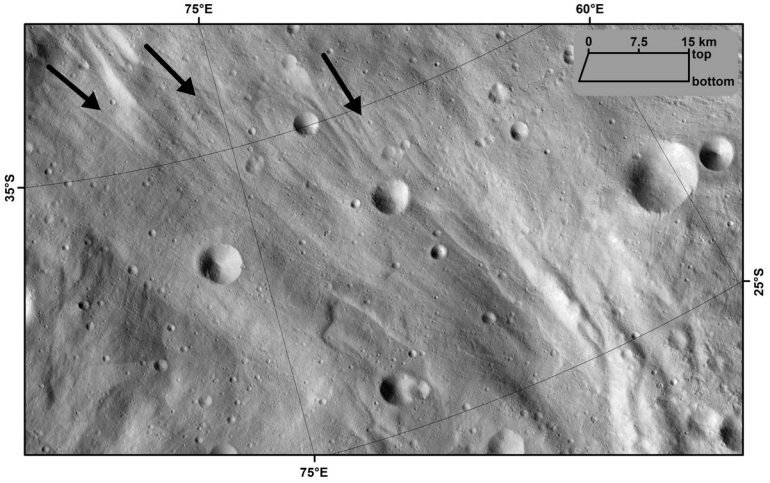

(b) Close-up image of striations developed on the flow-like feature.

Figure 5.6.: The flow-like feature north of the Matronalia Rupes scarp (a) and a close-up image of its striations (b). The arrows indicate the the flow direction along which striations developed. The dashed white line in (a) shows the extent of the feature and the rectangle illustrates the position of the close-up image (b). The images are in a stereographic projection with the scale bar applicable at the centre of the image. Image (a) is overlaid by a DTM referenced to a 285 km × 229 km biaxial ellipsoid.

When considering flow-like features, it is unreasonable to determine the Rossby number to find whether they may be affected by the Coriolis force. This is because the flow velocity is unknown as acoustic fluidisation (Section 3.1.5) may reduce the internal friction and increase the velocity [*Collins and Melosh*, 2003; *Melosh*, 1986]. However, analysing the flow-like feature opposite the Matronalia Rupes scarp (Figure 5.6(a)), it is noticeable that the main lobe shows a slight deflection to the east in accordance with the Coriolis Effect. On the other hand, the striations developed on the surface do not show a common deflection but rather follow the topography (Figure 5.6(b)). Hence, it remains disputable whether the Coriolis force is responsible for the deflected lobe.

Creep-like mass movement produces a pattern of small mounds which migrate slowly downhill (Figure 6 in Appendix C). However, the terrain is unlikely to maintain any Coriolis-affected deflection because the creep trajectory is not preserved in the morphology of the mounds. Additionally, the relatively slow creep velocity (in the order of millimetres to centimetres per day) is below the minimum velocity associated with the data resolution and therefore a deflection is not detectable.

Large landslides on Vesta usually spread during their migration (Figure 11(b) in Appendix C). The extent of the spreading overruns the morphologic evidences of the Coriolis force. However, following the calculations above for intra-crater landslides, the narrow landslide along the Matronalia Rupes scarp (Figure 2.14(c), latitude $\varphi \approx 55°$S, slope $\alpha \approx 40°$, length $l \approx 25$ km) yields a Rossby number of $\sim$0.3 and has thus probably been influenced by the Coriolis Effect. Indeed, the slide shows a curvature in agreement with the effect. It is, however, important to note that the topography also constrained the motion of the slide. In other regions, the landslides seem to be following the curved pattern of the ridge and groove terrain which is more likely to be related to the substructure rather than the Coriolis Effect on the specific landslides.

Slumping blocks and the related curved concentric ridges are much larger than intra-crater landslides or creep-like features. However, the distance of their motion is only approximately as long as the height of the main drop. For the Matronalia Rupes slumping block (Figure 5.2(a)) at a latitude of $\sim$55°S this drop is $\sim$5 km. Because the velocity of the slumping process is unknown it is not possible to derive a Rossby number. However, the slumping maximum velocity, when considering that the Rossby number needed to observe a Coriolis deflection has to be below 1, is $\sim$3 m/s. Nevertheless, even if these conditions were met, the block as a whole is embedded in the surface material which restricted the motion in any other than the main mass-wasting

direction.

As described in Section 5.2, the curved structures of the radial ridges appear to be remnants of the early gravitational crater collapse. The strength properties of material during the early formation stage were plastic, with negligible internal friction [*Melosh*, 1989], which made the mass motion relatively fast. Using a latitude of ∼40°S, a length of ∼200 km and a velocity of ∼50 m/s, *Jutzi et al.* [2013] estimated a relatively low Rossby number of ∼0.5 for the curved radial ridges within the Rheasilvia basin, which indicates that the material wasting downhill was influenced by the Coriolis force.

In accordance with the Coriolis Effect, the curvature points against the direction of rotation for motion towards the rotation axis, and in the direction of rotation for motion away from the axis (Figure 5.3). The curvature on the crater wall of Rheasilvia would therefore have been generated by a mass motion towards the rotation axis, which nearly agrees with the centre of Rheasilvia. The patterns on the central peak suggest motion away from the axis. This is consistent with the idea of masses moving downhill into the basin, off both the crater rim and central peak, as the crater collapses.

The Coriolis Effect was capable of generating curved structures across the entire Rheasilvia crater. However, in some regions, for example the central peak and the intersection of craters Rheasilvia and Veneneia, additional mechanisms may have produced curved features.

On Rheasilvia's central peak, an oblique impact might have been able to create curved scarps and ridges. A method for determining impact directions was devised by *Scherler et al.* [2006], who investigated the structure of ridges and faults of the central peak of Upheaval Dome (Utah, USA) to infer an impact direction. The Rheasilvia central peak exhibits bent fractures and faults visible as scarps from which material moved downhill (Figure 5.7). The analysis of the central imbrication structure of Rheasilvia after *Scherler et al.* [2006] is restricted by the small number of features and does not yield a definite impact direction or obliquity. However, the curved main scarps of the central peak, instead of straight radial expanded structures, may indicate a non-vertical stress component, e.g. an oblique impact (Figure 5.3).

At the intersection of Rheasilvia and Veneneia, the crater collapse of a two-layered target might have been able to produce the observed spiral pattern. The development of curved strike-slip faults has been demonstrated in experiments by *Allemand and Thomas* [1999]. They performed experiments in a two-layered target with a lower ductile layer and an upper brittle layer consisting of silicon and sand, respectively. A circular hole was cut through the layers and the relaxation process with variable layer thickness was observed. The collapse process produced spiral strike-slip faults for low brittle-ductile

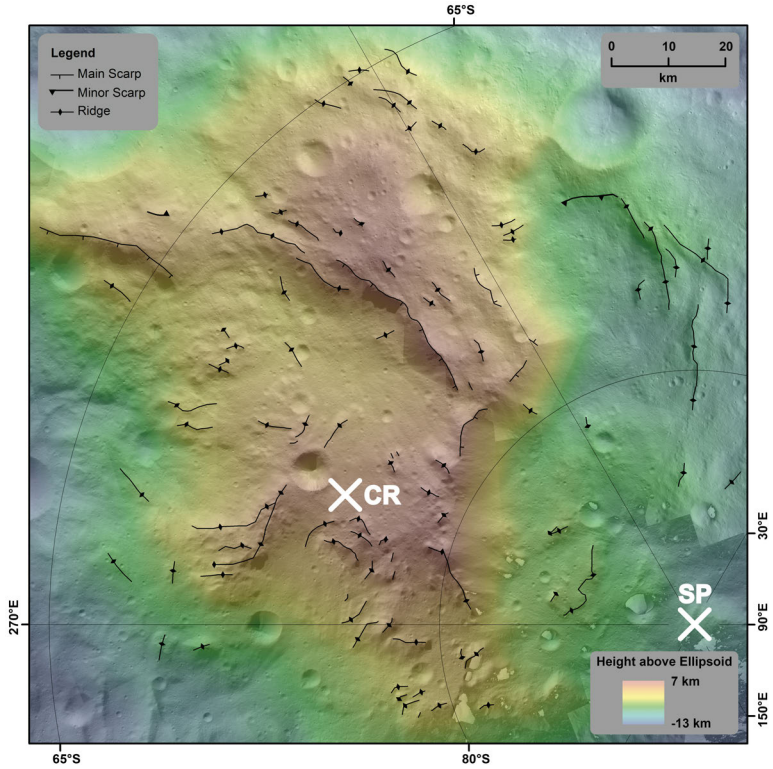

Figure 5.7.: Scarps and ridges of Rheasilvia's central peak (from *Otto et al.* [2013]). The minor scarps indicate slumping from previously wasted material and ridges represent degraded scarps and material accumulations. The main scarps are slightly curved suggesting a non-vertical stress component of the impact. The centre of Rheasilvia (301°E and 75°S [*Jaumann et al.*, 2012]) and the South Pole are labeled CR and SP, respectively. The image is in a stereographic projection with the scale bar applicable at the centre of the image. It is overlaid by a DTM referenced to a 285 km × 229 km biaxial ellipsoid.

thickness ratios. These faults crossed in a characteristic V-shaped pattern, meaning that the faults intersected at angles above 130° (Figure 5.8). The spirals developed on the crater wall, but more prominently beyond the crater rim.

The brittle-ductile thickness ratio of the intersection of Rheasilvia and Veneneia has likely been reduced, because the Veneneia impact may have removed parts of the brittle surface prior to the Rheasilvia impact. The

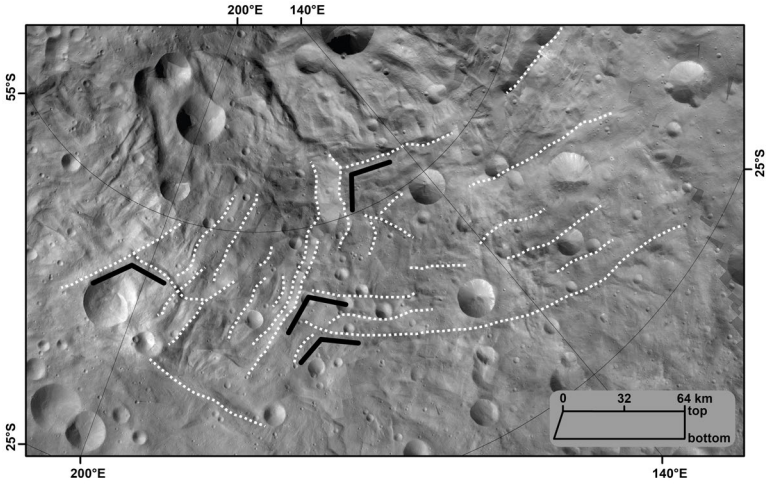

Figure 5.8.: Curved ridges at the intersection of Rheasilvia and Veneneia in the area within 25°S to 65°S and 110°E to 210°E (from *Otto et al.* [2013]). The dashed lines mark the most prominent structures. The V-shaped crossings are indicated with black chevrons. They might be caused by the relaxation of a bi-layered target with ductile and brittle components. The image is in a stereographic projection with the scale bar applicable at the centre of the image.

ratio might have been sufficiently low to allow spirals, represented by curved ridges, to have formed during the relaxation process. Furthermore, the spiral pattern in this region expands beyond the Rheasilvia rim as expected by the *Allemand and Thomas* [1999] theory.

The Coriolis Effect is thus the only process that can explain the curved pattern at all locations, however the oblique impact and crater relaxation theories cannot be completely ruled out for the central peak and Rheasilvia-Veneneia intersection, respectively.

6. The Coriolis Model

6.1. Aim

As described in Section 5.2 the Rheasilvia basin exhibits curved radial ridges which are probably related to the modification stage of the impact event. Section 3.2.3 shows how the magnitude of the velocity v of a mass moving in a rotating reference frame can be derived from the radius of curvature R of the trajectory of the moving mass when the Coriolis parameter f is known:

$$v = Rf. \tag{3.26}$$

Assuming that the curved radial ridges represent Coriolis-deflected mass motion trajectories, a computer-based method to calculate the mass motion velocity from the curvature of the Rheasilvia radial ridges using Equation 3.26 was developed for this work (Section 6.3). Velocities were derived for various mapping points (Section 6.2) along the curved ridges using the radius of curvature and the geodetic latitude at each location. Figure 6.1 shows a flow diagram of the analysis.

The following sections explain how the radii of curvature and geodetic latitudes were derived from the Dawn data and how they were used to determine the mass motion velocity by additionally considering Vesta's shape and evolution (Sections 6.6 and 6.4).

The results of this analysis (Chapter 7) will show whether or not the velocities agree with the postulated mass motion velocities of ∼50 m/s derived from numerical impact simulations (Section 3.1.7, [*Jutzi et al.*, 2013]). Velocity profiles along the extent of the Rheasilvia curved ridges will also be provided by this method (Section 6.8). Any acceleration or deceleration, caused by gravity and friction respectively, will result in varying velocity profiles. This will not only constrain the dynamics and material properties (Section 7.4) associated with the impact event, but will also allow these properties to be spatially resolved (Section 8.5).

6.2. Mapping

As a first step, the curved radial ridges from Figure 5.3 were mapped in detail. Each curved ridge was approximated by a set of mapping points (105 to 757

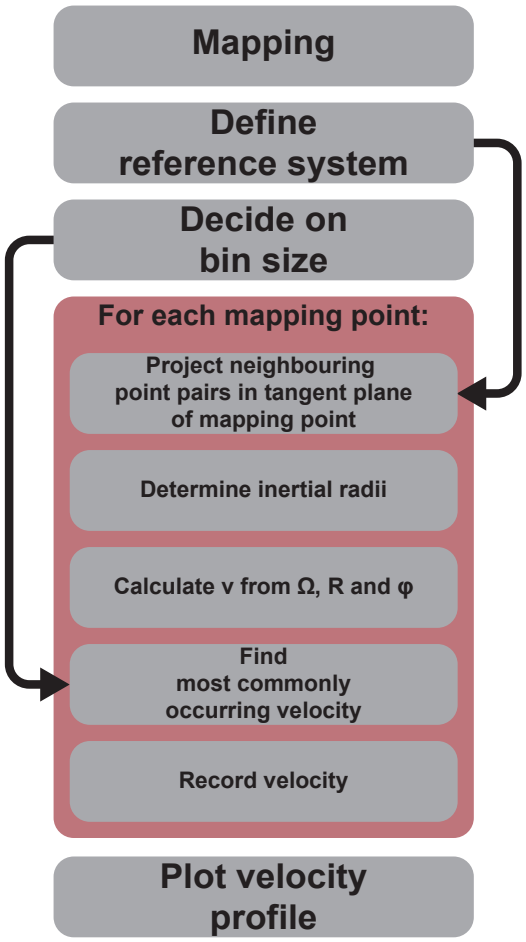

Figure 6.1.: Steps of the analysis to derive velocities from the curved ridges. The procedures of each box are explained in the text.

mapping points per curved ridge, Table 6.1) which outline the extent of each curved ridge. The alignment of these mapping points represents the curvature which is later used to derive the mass-wasting velocity using Equation 3.26.

In total, 32 continuous curved ridges were identified covering the three major areas of radial ridges as described in Section 5.2. There are 16 ridges between 270°E and 360°E (Region 1, red in Figure 6.2), eleven ridges between 90°E and 220°E, the area where Rheasilvia and Veneneia intersect (Region 2, blue in Figure 6.2), and five ridges on the central peak (Region 3, green in Figure 6.2). The three regions describe three different geologic settings within the Rheasilvia basin. In the following the curved ridges are labelled

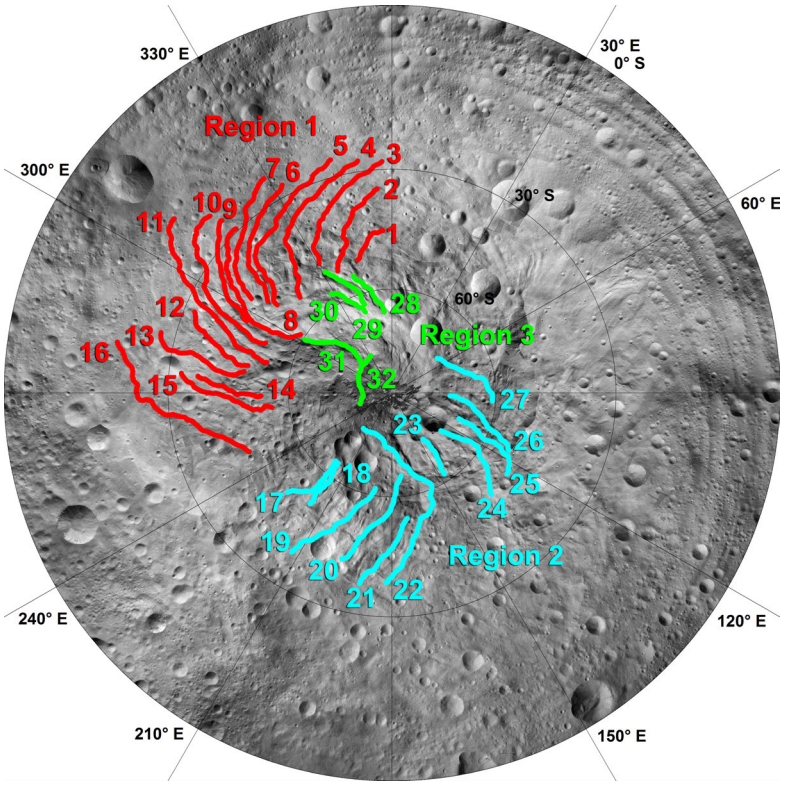

Figure 6.2.: The 32 curved radial ridges mapped using a stereographic LAMO mosaic and DTM of Vesta's southern hemisphere. The three regions include the area between 270°E and 360°E (Region 1, red lines), the area where Rheasilvia and Veneneia intersect (Region 2, blue lines) and the central peak region (Region 3, green lines). In the text, the curved ridges are named Curve 1–32 according to the labels.

Curve 1–32 as shown in Figure 6.2.

The mapping was performed on a stereographic projection of the LAMO mosaic (∼20 m/pixel resolution, Section 4.2) and DTM (93 m/pixel lateral resolution, Section 4.1) using the ArcGIS software package developed by *ESRI* [2010]. It is common in planetary mapping to project mapping data onto a sphere, because it simplifies the interpretation and comparison of features [e.g. *Roatsch et al.*, 2013; *Gwinner et al.*, 2010]. In the case of Vesta, a mapping sphere of 255 km radius was used as the reference body for the map projection [*Roatsch et al.*, 2013, 2012]. Therefore each mapping point along a curved ridge was described by the two-dimensional position on this

Table 6.1.: Number of mapping points of the 32 curved ridges.

Curve Number	1	2	3	4	5	6	7	8
Mapping Points	120	160	157	279	284	217	277	321
Curve Number	9	10	11	12	13	14	15	16
Mapping Points	336	279	407	305	249	280	369	757
Curve Number	17	18	19	20	21	22	23	24
Mapping Points	208	191	380	394	223	364	105	373
Curve Number	25	26	27	28	29	30	31	32
Mapping Points	149	195	283	179	160	173	356	160

mapping sphere. The coordinates of each mapping point were exported for further analysis with custom software written in *IDL* [2012].

A curved ridge is morphologically characterised by an elongated terrain of increased elevation with a significant topographic decrease in all directions other than the ridge direction. Thus, the first step in identifying mapping points outlining the current curved ridge was the analysis of the topographic information. The line of locally highest elevation related to the curved ridge was used as a starting location when identifying mapping points. However, the highest elevation was not necessarily coincident with the location of the ridge, for example when the topography was interrupted by impact craters or altered by erosion. Therefore, each mapping point location was additionally based on geologic interpretations of surface alterations apparent within the image data. As per standard geologic mapping techniques [e.g. *Smith et al.*, 2011; *R. Greeley and R.M. Batson*, 1990], a mapping point was finally assigned to a location when the combination of both surface and topographic interpretations supported the presence of a curved ridge at this location.

The distance between two neighbouring mapping points is therefore variable. Depending on the ease with which the mapping points could be identified, the distance between two mapping points varied between 150 m (∼8 pixels) and 1200 m (∼60 pixels). Table 6.1 lists the number of mapping points for each curved ridge.

6.3. Computer-Based Analysis

The previously described mapping information is the basis for determining the radii of curvature of the curved ridges, and subsequently the mass-wasting

velocities, related by Equation 3.26. The following sections explain how the velocities were derived and how basic assumptions on Vesta's shape and rotation influence the analysis.

6.3.1. Defining the Reference Frame

In order to find the radius of curvature of the curved ridges, the mapping on the reference sphere needed to be transferred to a reference frame describing Vesta's real shape more adequately. Based on the results of the DTM construction, Vesta is best described by an ellipsoid with axes of 285.4 km × 277.7 km × 223.8 km [*Preusker*, 2013, personal communication]. However, to simplify matters a biaxial reference ellipsoid with the average of the semi-major axes of 281.55 km and a semi-minor axis of 223.8 km was used instead. This approximation is suitable, as the difference to the ellipsoidal semi-major axes is only about 1%. It also extensively simplifies the analysis because it becomes independent of the longitude.

In order to project each mapping point from the 255 km reference sphere onto the 281.55 km × 223.8 km reference biaxial ellipsoid the geocentric coordinates were simply adopted. In other words, the centres of both bodies coincided with the centre of projection. Because this procedure was previously done in reverse when constructing the mosaic (Section 4.2), the technique resulted in a projection from Vesta's real shape to Vesta's ellipsoidal shape.

However, the following analysis requires geodetic coordinates for determining the mass-wasting velocities from the radii of curvature of the mapped curved ridges (Equation 3.26), because of the relation between geodetic coordinates and the surface normal and tangent plane of the spheroid. Thus, Equation 3.15 was applied to the geocentric coordinates of each mapping point to transform them to geodetic coordinates.

6.3.2. Calculating the Velocity

A few terms need to be defined prior the following explanations: As described above, each curved ridge was mapped and approximated by 105 to 757 *mapping points* depending on their length and mapping accuracy. Considering an arbitrary mapping point MP, a set of two mapping points with the same point distance from a MP is called the *neighbouring point pair* of MP (Figure 6.3). For example, the two direct adjacent mapping points of MP are the first order neighbouring point pair. The second order neighbouring point pair includes the points adjacent to the first order neighbouring point pair and so on. Thus, each mapping point can have as many neighbouring point

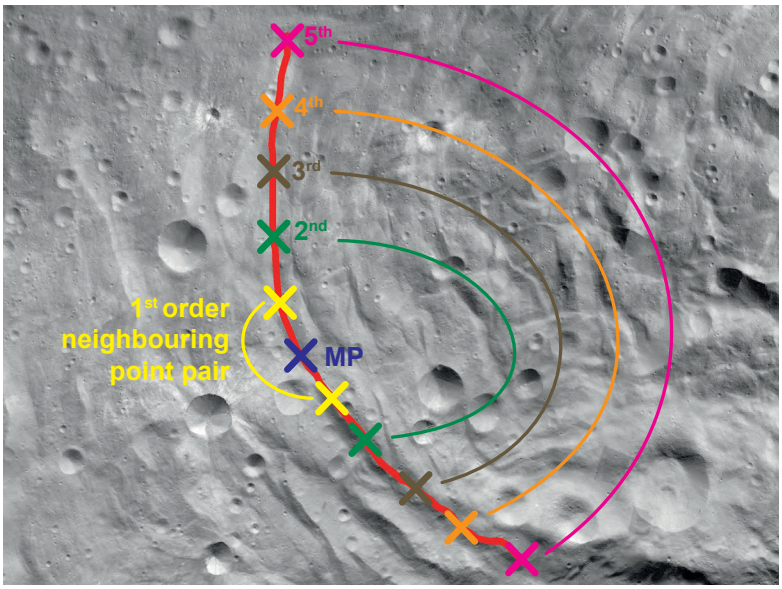

Figure 6.3.: Sketch illustrating the neighbouring point pairs of mapping point MP (blue cross) on a curved ridge (red). The colours and loops join the two members of a neighbouring point pair. For illustrative reasons, only a subset of mapping points (coloured crosses on red line) forming the mapped curved ridge are sketched.

pairs as it is away from the end or beginning of the curved ridge. In other words, the n^{th} point along a curved ridge has either $(n-1)$ or the $(total\ amount\ of\ points - n)$ neighbouring point pairs, whichever is smaller. Note that because the mapping was based on the geological analysis, the actual distance between a mapping point and the members of a neighbouring point pair can vary and is different for each mapping point.

The latitude and local curvature of each mapping point enables the derivation of a mass motion velocity according to Equation 3.26. To analyse the curvature at a mapping point, the tangent plane of the bi-axial ellipsoid at each mapping point's location was determined. The normal vector of the tangent plane is described by the vector spanned by the longitude and geodetic latitude of the mapping point. All neighbouring point pairs were then projected into this plane. Projecting the neighbouring point pairs into the tangent plane was necessary because the derivation of the inertial circles is in the body-fixed coordinate system of the mapping point with the x- and y-axes spanning the tangent plane (Section 3.2.3). Furthermore, if using the position on the spheroid instead of the tangent plane, the curvature of the

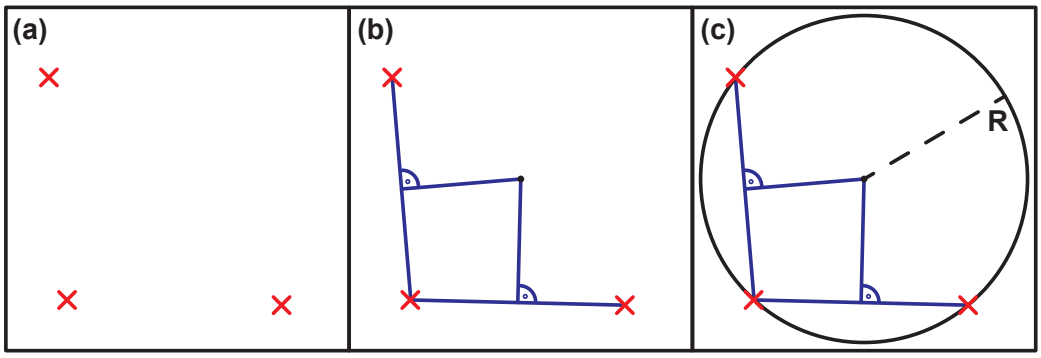

Figure 6.4.: Three steps to determine the unique circle that fits through three points in a plane. (a) Three points in a plane. (b) After connecting two points with one another, two perpendicular bisector are drawn. (c) The two perpendicular bisectors intersect at the centre of the circle that cuts through all three points. The radius is given by the distance from the circle's centre to any of the three points.

spheroid would limit the circles' radii.

For each neighbouring point pair and the mapping point, the unique circle with all three points lying on the circumference was determined. Figure 6.4 illustrates the technique. This circle was considered to be the inertial circle related to the Coriolis Effect at the length-scale given by the neighbouring point pair.

The normal vector to the vectors from the mapping point to the previous and the following neighbouring point pair member was determined. If this normal vector pointed outside the ellipsoid the radius at the mapping point was defined as positive. A negative radius was assigned if the normal vector pointed inwards. In this way, curvatures due to masses moving towards the rotation axis were defined as positive and curvatures due to masses moving away from the axis were defined as negative.

The radius of the inertial circle - typically of the order of ∼50 km - and the geodetic latitude of the mapping point were finally used to determine the velocity, by applying Equation 3.26. Consequently, each mapping point was assigned a set of velocities - one velocity derived from each neighbouring point pair.

Note that the distance between the two members of the neighbouring point pairs sets the lower limit for the velocity: the smallest circle which can be described by the neighbouring point pair is the circle with a diameter equal to the distance between the members. For instance, the minimum distance

between the two members of a point pair is ∼300 m. At 45°S this results in a threshold velocity of ∼0.1 m/s. Velocities below this threshold cannot be resolved by this method. With higher order neighbouring point pairs this threshold grows linearly with the distance between the members of the pair.

The distance between the two members of the neighbouring point pairs also determines the distance over which the velocity is assumed to be constant. A change in velocity is represented by a change in the inertial radius. However, it is uncertain over which distances the velocities producing the curved ridges in the Rheasilvia basin are constant. The masses are accelerated by gravity but also decelerated by friction or topography. Therefore, the most commonly occurring velocity was determined for each mapping point, filtering out infrequent results.

A histogram of all calculated velocities was produced for each mapping point, to determine the most commonly occurring velocity at that mapping point. The bin size was set to 5 m/s, 10% of the simulated velocity of 50 m/s, and the effect of changing the bin size is discussed in Section 6.5. All values in the most populated bin were considered to be within the most commonly occurring velocity range. If there was more than one most populated bin - a scenario especially relevant for mapping points with only few neighbouring point pairs (the points near the beginning or end of a curved ridge) - all relevant bins were considered. The average of all values in the most populated bin(s) were stored as the velocity of each mapping point.

Summarizing this procedure. the radii of curvature of each mapping point were determined at various length-scales, using Equation 3.26 these radii were then converted into mass-wasting velocities and subsequently the most commonly occurring velocity over all length-scales was determined by using a histogram and recorded as the "most likely" velocity of the mapping point.

The pseudo IDL-code used to perform this analysis is shown in Appendix A.2.

6.4. Ancient and Recent Vesta's Reference System

As described in Section 2.4.5, Vesta's current shape is not the shape it possessed when the Rheasilvia impact occurred. The impact basin itself forms the shape as we observe it today. Therefore it is necessary to investigate the effect of the ancient and recent shape of Vesta on the velocities derived with the method described in Section 6.3.

Because Vesta's real shape during the Rheasilvia impact was probably between the shape of today and the ancient one, it is reasonable to investigate

Table 6.2.: Comparison of recent and ancient Vesta's rotation and shape parameters according to *Fu et al.* [2014]. The values are given in Vesta's recent reference system.

Parameter	**Recent Vesta**	**Ancient Vesta**
Semi-Minor Axis [km]	223.8	236.8
Semi-Major Axis [km]	281.6	277.6
Rotation Period [h]	5.34	5.02
Angular Velocity [10^{-4} s^{-1}]	3.27	3.48
Position Rotation Axis [°S]	0.0	87.0
Centre Longitude [°E]	0.0	182.7
Centre Offset [km]	0.0	-5.7

the mass wasting based on both shapes as end-members of the real shape. Additionally, whenever the ancient shape of Vesta is used, the ancient rotation period of 5.02 h ($\Omega = 3.48{\cdot}10^{-4}$ s^{-1}) needs to be considered instead of Vesta's recent period of 5.34 h ($\Omega = 3.27{\cdot}10^{-4}$ s^{-1}). The centre of Rheasilvia in ancient Vesta's reference frame is located at 293°E and 74°S.

By fitting a bi-axial ellipsoid to the relic hydrostatic northern hemisphere of Vesta, *Fu et al.* [2014] found that the ancient rotation axis of Vesta before the Venenia and Rheasilvia impacts was offset by 3.0°, cutting through longitude 182.7°E, in comparison with the recent axis. The centre of mass was 5.7 km south of the current position (Section 2.4.5). They also found different best-fit bi-axial ellipsoid axes of 277.6 km × 236.8 km. Although the major axis is similar to the current one, the minor axes differ by ∼6%. Table 6.2 lists the parameters of the shape before and after the giant impacts.

Projecting the mapping points on ancient ellipsoidal Vesta was more complicated than the process described in Section 6.3, because the centre of the body is shifted south. The sphere to which the mapping was applied, was centred at the origin of the coordinate system. Before transferring the mapping points to the ellipsoidal shape, the axes were changed to the ancient system: the rotation axis was shifted to 87.0°S and 182.7°E, the zero longitude cut the equatorial plane at 2.9°S and 17.3°E [*Fu et al.*, 2014]. The geocentric coordinates of each mapping point were then calculated referenced to these new axes. The new mapping point coordinates were projected on the ancient ellipsoidal Vesta centred 5.7 km below the origin by finding the intersection point of the line of projection and the surface of ancient Vesta. The projection centre was the origin of the coordinate system. Figure 6.5 illustrates this procedure. Finally, the longitude and geodetic latitude were

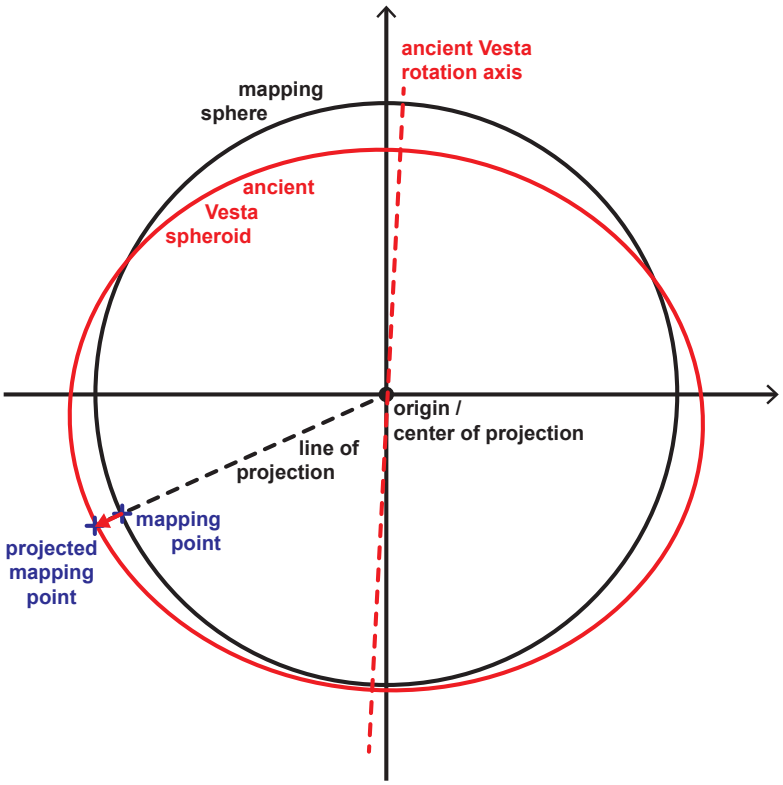

Figure 6.5.: Sketch illustrating the procedure of projecting mapping points into the ancient Vesta reference frame. The proportions are to scale. A mapping point (blue cross) on the mapping sphere of 255 km radius (black circle) is projected on ancient shape (red ellipsoid) by the line of projection (dashed black line) originating in the centre of the mapping sphere. Ancient Vesta is shifted 5.7 km south in relation to the mapping sphere and the axis (red dashed line) is shifted by 3°.

calculated with respect to ancient Vesta's centre. The pseudo IDL-code calculating the ancient Vestan coordinates is described in Appendix A.1.

Three independent factors influence the derived velocities for the mapped curved ridges: The rotation rate, the ellipsoid axes and the shift of the rotation axis. On ancient Vesta, the increased rotation rate yields higher velocities based on Equation 3.26. The change of the ellipsoid and rotation axes have variable effects on each mapping point depending on its location. At some points the velocity increase induced by the larger ancient rotation rate is compensated by these effects, at other points the effect adds to the

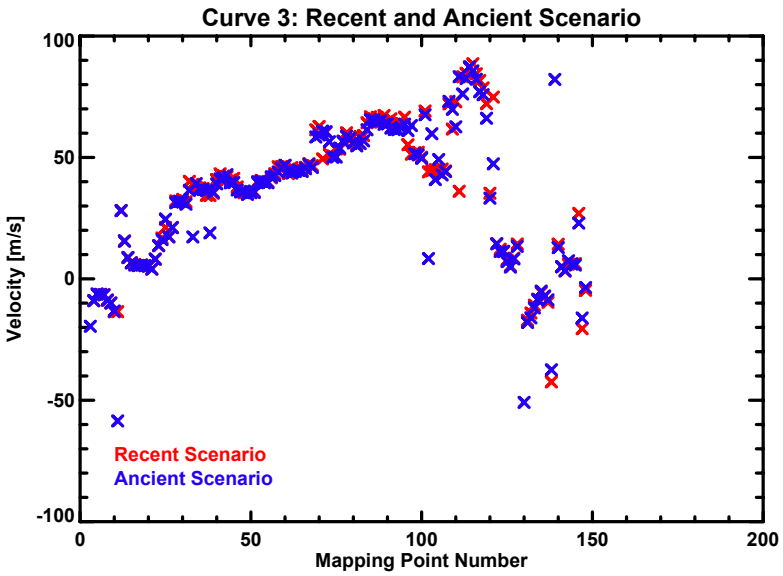

Figure 6.6.: The most commonly occurring velocities of each mapping point of Curve 3 with respect to Vesta's recent and ancient shape and rotation. The bin size is 5 m/s.

velocity. Due to the small difference in ellipsoid axes (6% and 1% for the semi-minor and semi-major axes, respectively) and orientation of the rotation axis (3°), the velocities derived in the two reference systems are similar. On average, the magnitudes of the velocities derived with respect to Vesta's ancient reference frame are ∼2% larger compared to Vesta's recent system. This is mostly caused by the increased angular velocity. A detailed error analysis is given in Section 6.7.

Figure 6.6 shows an example (Curve 3) of the velocities of mapping points with respect to Vesta's ancient and recent shape and rotation. On average, the velocities of Curve 3 on ancient Vesta are ∼3% lower than the velocities calculated with Vesta's recent shape. However, the velocities at some mapping points are significantly different. These are differences which arise from finding the most commonly occurring velocity from the velocity statistics of a mapping point rather than a real, physical effect, for which a smooth trend would be expected.

Because of the relatively small differences between the two scenarios and intrinsic uncertainties in the properties of ancient Vesta, the following analysis (Chapters 7 and 8) uses the recent shape and rotation of Vesta.

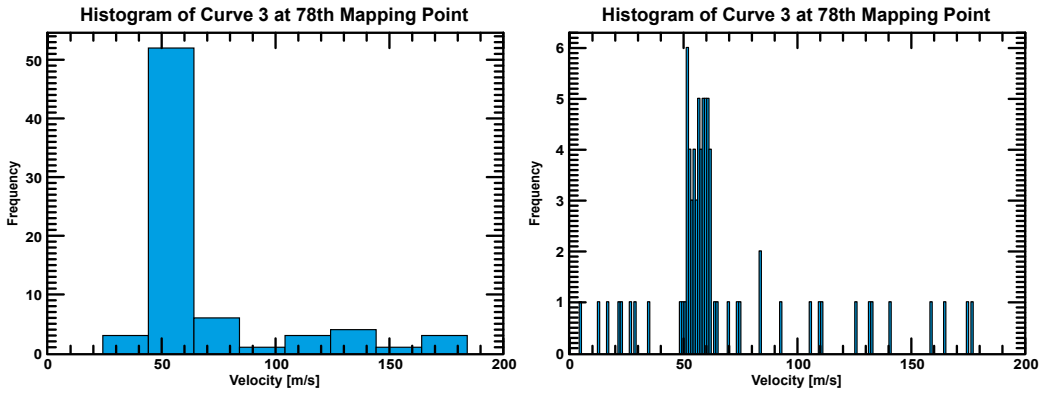

(a) Histogram with bin size of 20 m/s. **(b)** Histogram with bin size of 1 m/s.

Figure 6.7.: Histograms of Mapping Point 78 of Curve 3. (a) The bin size is so large that only nine bins fall within the data range. The velocity derived from this histogram is 56.4 m/s. (b) The bin size is so small that only a subset of the values that should contribute to determining the most commonly occurring velocity are considered. The velocity derived from this histogram is 51.8 m/s.

6.5. Changing the Histogram's Bin Size

As a result of the method described in Section 6.3, each mapping point is assigned a set of velocities. However, because only one mass-wasting velocity can be present at a mapping point, it is necessary to find the characteristic velocity out of the set of velocities for each mapping point. This characteristic velocity is the most commonly occurring velocity in the set.

To find the most commonly occurring velocity of a mapping point, the velocities derived from all neighbouring point pairs were binned (Section 6.3.2). The bin size (bin width) of this histogram sets the velocity range in which the most commonly occurring velocity is found. Consequently, the error of the most commonly occurring velocity is equivalent to half the bin size.

Figure 6.7 illustrates the effect of bin size on the velocity analysis of a mapping point. If the bin size chosen is too large, the values within induce large uncertainties in the velocity (Figure 6.7(a)). The velocity profile along a curved ridge would then be noisy. On the other hand, if the bin size is too small the most commonly occurring values may be split over multiple bins, neglecting values that should contribute to the determination of the most commonly occurring velocity (Figure 6.7(b)). Therefore, an appropriate bin size is necessary.

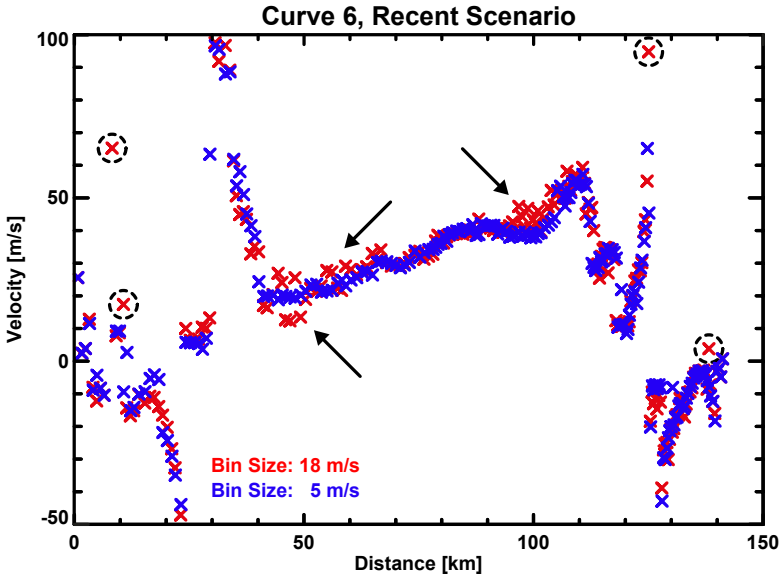

Figure 6.8.: The velocity distribution of Curve 6 with bin sizes of 5 m/s (blue) and 18 m/s (red). At some locations the larger bin size distribution is noisy while the smaller bin size is smooth (arrows). Also the larger bin size increases the number of outliers (encircled).

There is a different best bin size for each mapping point depending on the neighbouring point pairs and the location of the mapping point along the curved ridge. However, choosing a different bin size for every mapping point would result in variable errors and make the resulting velocities difficult to compare. Therefore, a constant bin size was defined for the entire evaluation.

Three characteristic velocities of Vesta were used in order to investigate the effect of the bin size: 18 m/s, 13 m/s and 5 m/s are 5% of the escape velocity, 7.5% of the velocity a friction-free object would reach after sliding down the Rheasilvia basin and 10% of the simulated expected velocity of 50 m/s (Section 3.1.7), respectively.

The velocities derived with these three bin sizes are similar. Considering all mapping points, the average magnitude of the velocity is 26.6 m/s, 27.9 m/s and 28.8 m/s for a bin size of 5 m/s, 13 m/s and 18 m/s, respectively. However, when looking at the velocity profiles of a curved ridge evaluated with different bin sizes (Figure 6.8), the velocity profiles are smoother when using a bin size of 5 m/s (blue in Figure 6.8). There are also fewer outliers at the 5 m/s bin size when compared to the larger bin sizes (encircled in Figure 6.8). This indicates that the 5 m/s bin size is small enough to smooth

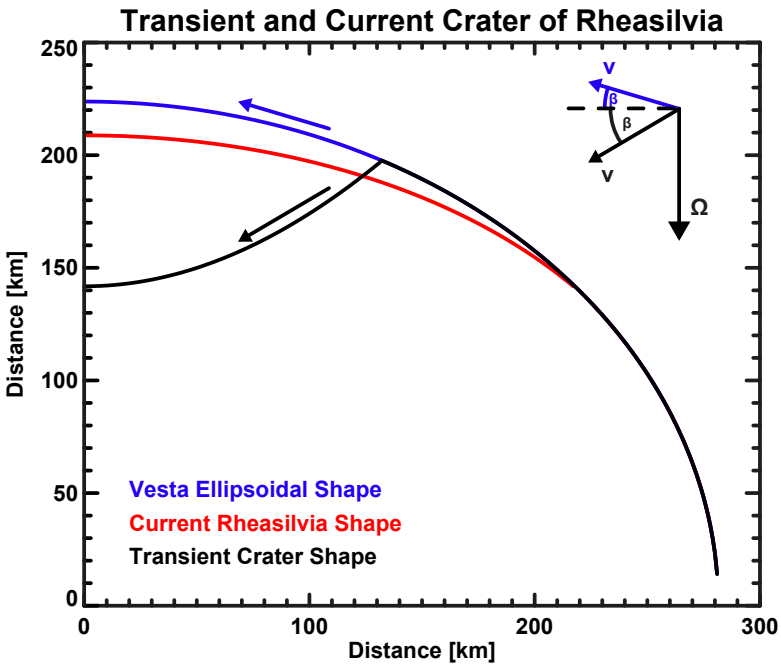

Figure 6.9.: The outlines of a symmetric transient crater (black, based on models by *Ivanov and Melosh* [2013]), a simplified (without central peak) representation of Rheasilvia (red) and the biaxial shape of Vesta (blue). The angular velocity $\vec{\Omega}$ and the mass motion velocity $\vec{v}$ with (black) and without (blue) transient crater topography are sketched. β is the angle between the equatorial plane and the direction of mass motion. The discrepancy between the current shape and current Rheasilvia is small because Vesta's spheroidal shape was fitted to Vesta superimposed by the current Rheasilvia basin. The component of the velocity relevant to the Coriolis force is parallel to the equatorial plane. For illustrative reasons the southern hemisphere was mirrored to the north.

the trend but is also large enough to minimise values escaping the trend. A bin size of 5 m/s represents the most appropriate bin size and is therefore used in the following analysis.

6.6. The Effect of Vesta's Topography

Vesta's ellipsoidal shape is highly modified by the Rheasilvia basin and therefore it is necessary to investigate the effect of the basin's topography on

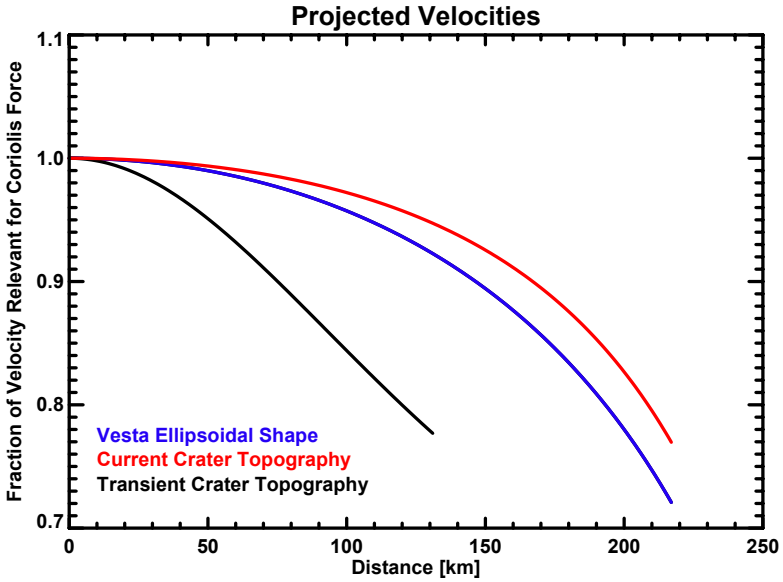

Figure 6.10.: The fraction of velocity which is projected into the equatorial plane as a function of the direct distance from the pole. The fractions of biaxial Vesta (blue) and Vesta superimposed by the transient (black) and current crater of Rheasilvia (red) are shown. This fraction is relevant for the Coriolis force and is given by $\cos(\beta)$, where β is the angle between the equatorial plane and the direction of mass motion (Figure 6.9). The Coriolis relevant fractions of the transient and current crater topography differ from the ellipsoidal shape by at most 15.8% and 4.9%, respectively.

the Coriolis force. As seen in Equation 3.13, the magnitude of the Coriolis force F_C is proportional to $\Omega v \cos(\beta)$, where Ω and v are the magnitude of the angular velocity and the mass motion velocity, respectively. β is the angle between v and the equatorial plane and is dependent on the topographic slope on which the mass motion occurred.

The transient crater of Rheasilvia describes the topography when the modification stage began. It is therefore a reasonable approximation for the topography on which the mass motion occurred. Subtracting the transient crater calculated by *Ivanov and Melosh* [2013] (depth of 82 km, width of 264 km) from the biaxial shape of Vesta results in the shape illustrated in black in Figure 6.9. In order to retain symmetry, the impact was considered at the pole. Nevertheless, this has a negligible effect on the slope compared to the uncertainty in the crater shape.

Only the velocity component parallel to the equatorial plane affects the

Coriolis force. Thus the fraction $\cos(\beta)$ of the magnitude of the velocity is relevant for the Coriolis force. This fraction was calculated for the transient and current crater topographies and for ellipsoidal Vesta (Figure 6.10). Near the pole the components relevant for the Coriolis force derived from the three shapes are similar, however, towards the rim of the craters, the differences increase and reach maximums of 15.8% (transient crater topography) and 4.9% (current crater topography) from the ellipsoidal shape of Vesta. Consequently the velocities near the rim of Rheasilvia are not as reliable as velocities derived near the centre.

6.7. Error Analysis

Sections 6.4 and 6.6 describe the current uncertainties in Vesta's shape, rotation and topography at the time when the Rheasilvia impact occurred. This section will investigate the combined effect of these uncertainties on the velocity.

The following error analysis is based on the prerequisite that the mapping approach used does not introduce any spatial errors. This is reasonable because the mapping was based on the geomorphologic interpretation of surface features which may include techniques such as interpolation when clearly justified (Section 6.2).

The velocity v of a mapping point is derived from the angular velocity Ω, the geodetic latitude φ_{geodet} and the inertial radius R of the mapping point by applying Equation 3.26:

$$v = 2R\Omega \sin(\varphi_{\text{geodet}}). \tag{3.26}$$

The relative error of the angular velocity can be estimated by the difference between the two values derived for the ancient and recent Vesta scenarios (Section 6.4). They differ by 6.3%. The error in the latitude is roughly given by the shift of the rotation axis of 3° (Section 6.4) and the relative error of the inertial radius can be estimated by the projection uncertainty due to the topography, of ∼15.8% (Section 6.6). Consequently the relative error of the velocity is given by:

$$\begin{aligned}\frac{\Delta v}{v} &= \sqrt{\left(\frac{\Delta R}{R}\right)^2 + \left(\frac{\Delta\Omega}{\Omega}\right)^2 + \left(\frac{\Delta \sin(\varphi_{\text{geodet}})}{\sin(\varphi_{\text{geodet}})}\right)^2} \\ &= \sqrt{\left(\frac{\Delta R}{R}\right)^2 + \left(\frac{\Delta\Omega}{\Omega}\right)^2 + \left(\frac{\Delta\varphi_{\text{geodet}}}{\tan(\varphi_{\text{geodet}})}\right)^2}.\end{aligned} \tag{6.1}$$

The latitude of the mapping points varies between 18.5° and 81.5°, resulting in relative errors of the velocity ranging between 17.0% and 23.1%.

Consequently, the major uncertainty of the velocities is introduced by the unknown topography during the modification stage and the subsequent distortion. Promisingly, the analysis of the velocities with respect to the slopes of Rheasilvia will provide insight to the crater shape during the modification stage (Chapter 8).

Nevertheless, the following comparative investigation of the velocity profiles of the curved ridges (Chapter 7) is based on Vesta's current biaxial ellipsoid and rotation period without any additional topography. Therefore, the derived velocities will not show any errors associated with uncertainties in the shape model.

6.8. Data Illustration

As described in Section 6.2, there are a total of 32 curved ridges[1] covering the three regions within the Rheasilvia basin (Figure 6.2). These 32 curved ridges were analysed using the method explained in Section 6.3 in order to derive mass-wasting velocity profiles from the local radii of curvature (Equation 3.26).

Two plots illustrating the calculated velocities were produced for each curved ridge. In all plots, the x-axis represents the distance along the mapping points starting at the point closest to the centre of Rheasilvia at 301°E and 75°S on recent Vesta. The y-axes of the two types of plots show either the velocity (*velocity plots*, e.g. Figure 6.11) and the topography (*topography plots*, e.g. Figure 6.13). In the topography plots the velocities are colour-coded with red labelling the highest, and black the lowest, speeds. To reduce the effect of outliers on the colour-scales, all values exceeding the three sigma interval around the mean velocity were clipped and neglected.

In the velocity plots (Figure 6.11), the beginning and end points of each curved ridge exhibit scattering. This is because the mapping points near the edges have only a few neighbouring point pairs and the histograms to find the most commonly occurring velocities are sparsely filled. Because the elements of all bins with the greatest number of members are averaged, the average varies widely until a preferred bin becomes clearly apparent with a high enough number of neighbouring point pairs. The number of values needed before the average stabilises depends on the mapping and thus varies for all curved ridges. For example, in Curves 10 (Figure 6.11(a)) and 13

[1]The curved ridges are named Curves 1–32 according to Figure 6.2.

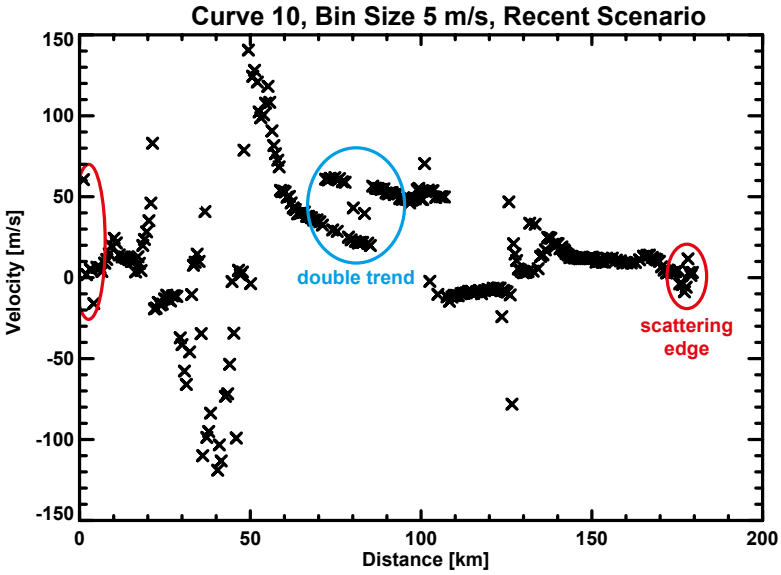

(a) Velocity plot Curve 10. Note the double trend around 80 km from (blue loop).

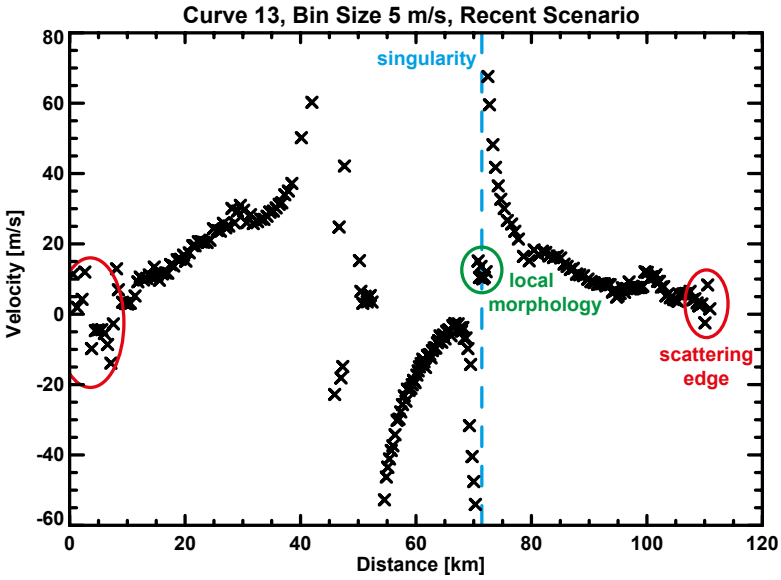

(b) Velocity plot Curve 13. Note the singularity at a change of sign (dashed blue line) and the clustering of data points representing the local curvature (green loop).

Figure 6.11.: Curves 10 (a) and 13 (b), illustrating features in the velocity plots. The scattering near the edges of the plot is caused by small number of neighbouring point pairs (red loops)

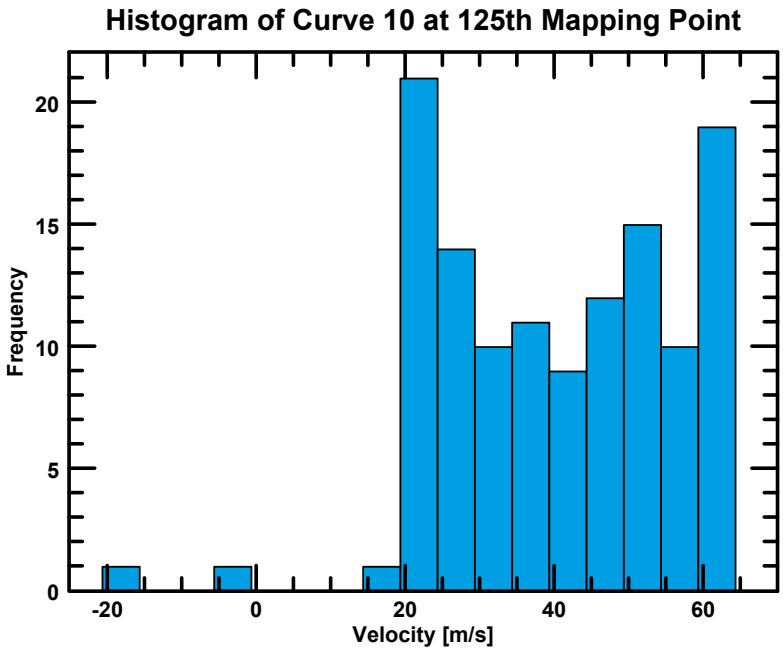

Figure 6.12.: The histogram of the velocities of Mapping Point 125 of Curve 10. Note the two peaks with similar heights at 20 m/s and 60 m/s. The changing dominance of these peaks produces the double line around 80 km in Figure 6.11(a).

(Figure 6.11(b)) approximately the ten mapping points closest to Rheasilvia's centre fall into the scattering region (red ellipses in Figure 6.11). At the other end of the curved ridge the scattering region is more clustered but also contains roughly ten mapping points.

Another feature is visible in the middle of Curve 10 at around the 125$^{\text{th}}$ mapping point, between 70 km and 90 km (Figure 6.11(a)). There are higher and lower regions of values that follow separate trends (blue ellipse in Figure 6.11(a)). This is caused by two commonly occurring velocities creating two bins with a similar number of members (Figure 6.12). Depending on the mapping point, one of the two bins has slightly more members and is thus used to determine the velocity while the other bin is neglected. Therefore, two trends develop - one for each bin. This feature illustrates that two curvatures on two different length scales are present. It is not possible to assign a definite velocity at this point, nevertheless this feature only occurs in four plots (Curves 8, 10, 12 and 22) and is thus relatively rare.

Curve 13 (Figure 6.11(b)) exhibits another common feature in the velocity

plot: the large rise in velocities followed by a change in sign (blue dashed line in Figure 6.11(b)). This singularity can be explained by a change in curvature. At the point where the curvature transfers to the opposite direction, a saddle point of locally infinite inertial radius is created which produces large velocities and a subsequent flip of the sign.

When approaching a saddle point, the larger velocities scatter across the histogram's bins so that most bins have only one member. However, the closest neighbouring point pairs (∼10 pairs) generate similar inertial radii of the local morphology at the saddle point. Thus, the velocity corresponding to the local morphology at the saddle point represents the most commonly occurring velocity in the histogram which is represented as a cluster of points in the velocity plot (green ellipse in Figure 6.11).

The major feature of the topography plots (Figure 6.13) is the presence of impact craters (black arrows in Figure 6.13(a)). Impact craters formed after the modification stage of Rheasilvia and therefore altered the surface structures which resulted from the Rheasilvia event. This subsequent deposition of impact ejecta, intra-crater mass wasting and the formation of the crater cavity itself may have influenced the morphology of the curved ridges. Consequently the velocity calculations are not reliable near impact craters. For example, a change in sign of the velocity, as described previously, can often be explained by subsequent impact craters that altered the surface after the formation of the curved ridges.

Some curved ridges show mounds near the basin floor as evident in Figure 6.13(b). As the lowest point of Rheasilvia, the basin floor is characterized by mass wasting and deposition due to gravity. The observed mounds in the topography plots are commonly caused by depositions of material from a direction non-parallel to the curved ridges near the basin floor. Here, the derived velocities are not reliable, because the surface has been covered by large volumes of mass wasting after the formation of the curved ridges.

6.9. Deriving Acceleration and Slope

The kinetic energy gained by a constantly accelerating object with mass m from the initial velocity v_i to the final velocity v_f equals the work done under the influence of the force ma along the travelled path Δd:

$$ma\Delta d = \frac{1}{2}m{v_\mathrm{f}}^2 - \frac{1}{2}m{v_\mathrm{i}}^2. \tag{6.2}$$

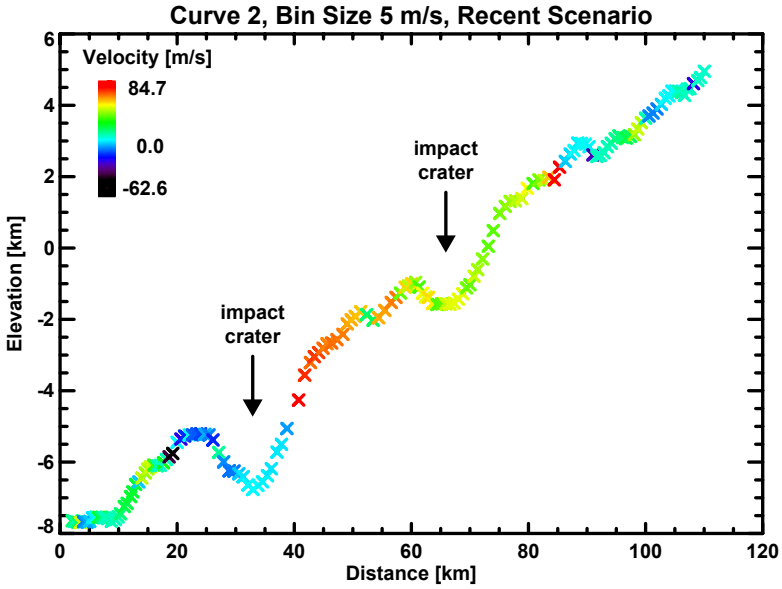

(a) Topography plot Curve 2. Two impact craters are located near 30 km and 65 km (black arrows).

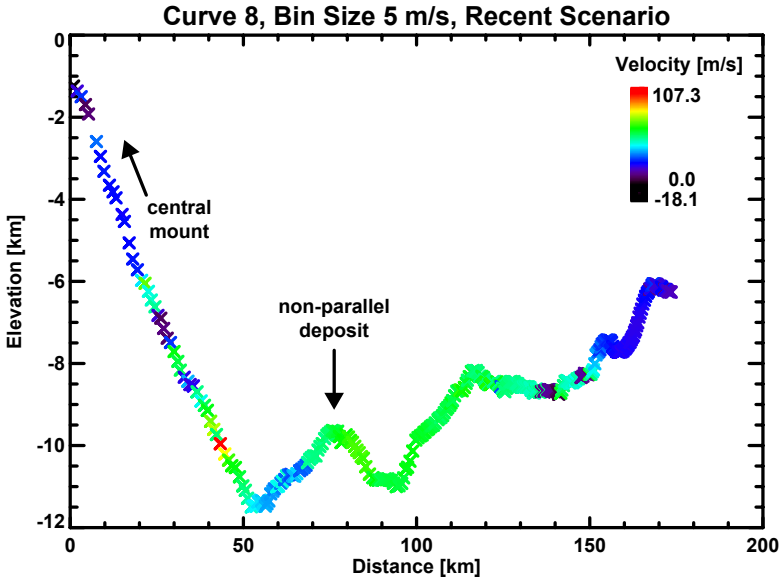

(b) Topography plot Curve 8. Around 75 km, at the foot of the central peak, a mound of non-parallel deposited material is evident.

Figure 6.13.: Curves 2 (a) and 8 (b), illustrating features in the topographic plots.

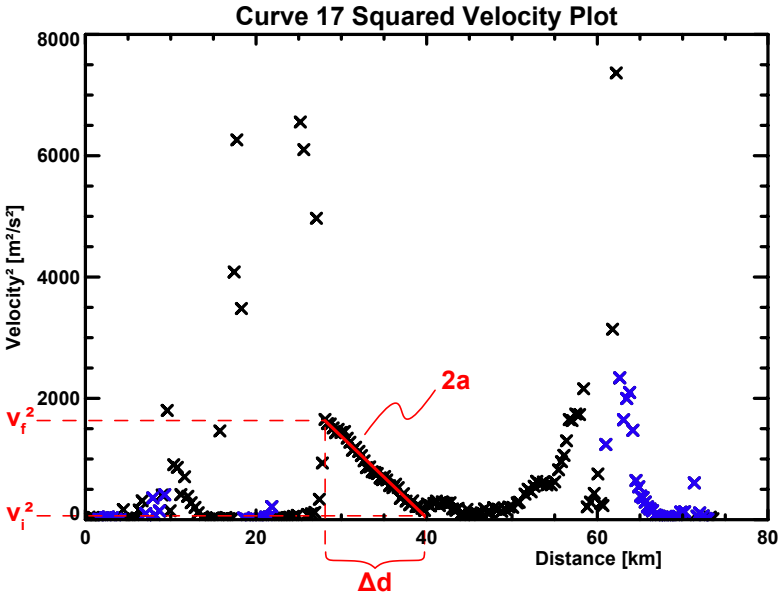

Figure 6.14.: Squared velocity plot of Curve 17. The blue mapping points are values derived from negative velocities. The red line fitted to the data is the least squares fit of the constantly accelerating section. The gradient of this line equals $2a$. Additionally the distance travelled Δd, the initial velocity v_i and final velocity v_f are labelled. The motion is from right to left towards smaller distances.

Rearranging yields the acceleration a:

$$a = \frac{{v_\mathrm{f}}^2 - {v_\mathrm{i}}^2}{2\Delta d} \tag{6.3}$$

or

$${v_\mathrm{f}}^2 = 2a\Delta d + {v_\mathrm{i}}^2. \tag{6.4}$$

Thus, the acceleration (deceleration is negative acceleration) can be determined from a linear trend when plotting the squared velocity over the travelled distance (*squared velocity plot*, Figure 6.14). The gradient of the linear trend in such a plot equals $2a$.

The acceleration was extracted from the data by applying a linear least squares fit[2] to the accelerating sections within the squared velocity plots

[2]The IDL function LINFIT used here is based on the methods described in *Press et al.* [1992].

(Appendix B.3). The fit produces the intercept and gradient, as well as their errors. The error of the intercept is the error in v_i^2, the error of the gradient $((v_f^2 - v_i^2)/\Delta d)$ divided by 2 is the error in the acceleration.

Additionally sections of constant velocity ($a = 0$) were identified in the velocity plots. The constant velocity of a section was determined by averaging the values contributing to the section. The standard deviation of these values was used as the error of the constant velocity.

Furthermore the slope is of interest when analysing the dynamic properties of mass wasting (Section 7.4). Thus, the geologically predominant slope was determined from the topographic data (e.g. Figure 7.3(b)). If topographic alterations due to, for example, impact cratering or mass wasting occurred, the predominant slope was interpolated across these features (e.g. Figure 7.4(b)). This slope was used for subsequent calculations (Section 7.4). For example in Curve 2 (Figure 6.13(a)), the predominant slope neglects the impact craters, resulting in a slope of 7.5°.

The statistical error related to the slope is not representative of the uncertainty introduced by geologic processes. Instead, the statistics illustrate the variation of the current slope as measured with the DTM. Therefore, the error of the slope is open to geologic interpretation and cannot be expressed as a physical error.

Chapter 7 presents the measurements of sections of constant acceleration and velocity and the slopes on which they are. A velocity trend was considered reliable if at least ten mapping points followed it and if it was at least 5 km long.

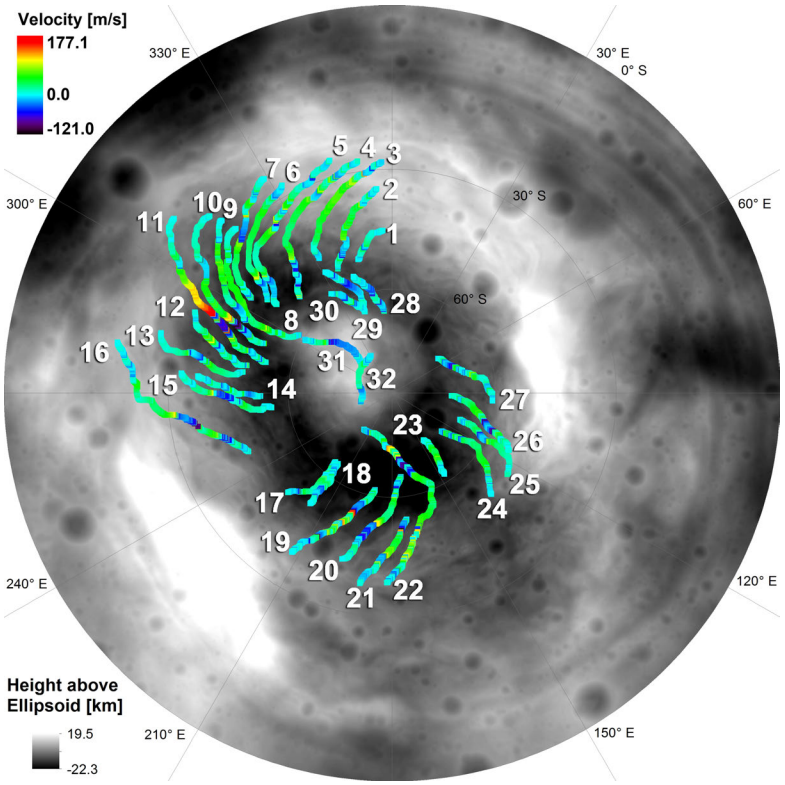

Figure 7.1.: The velocity distribution of the 32 curved ridges on a stereographic topographic map of Vesta's southern hemisphere. The individual mapping points of the curved ridges are colour-coded according to their velocity with red indicating high, and dark purple low, values. The colour bar is linear and the overall blue and green tone of the curved ridges illustrates that most mapping points fall in velocity range between approximately 0 and 100 m/s. However, some sections show higher (yellow to red colour) or negative velocities (blue to purple colour).

7. Results

The following sections present the velocities (Equation 3.26), dynamics and derived material properties of the curved ridges within the Rheasilvia basin. The evaluation was based on Vesta's recent shape and the bin size was set

to 5 m/s. Differences found when applying ancient Vesta's shape and when changing the bin size are discussed in Sections 6.4 and 6.5, respectively. The plots and statistics of all curved ridges are included in Appendix B.

As a graphical summary, Figure 7.1 shows the distribution of the velocities along all 32 curved ridges within the Rheasilvia basin. The colour shows the velocity with red representing high, and dark purple low, values. The average magnitude of the velocity is 26.9 ± 24.1 m/s. When neglecting velocities derived from curvatures which cannot be created by the Coriolis force, the average curved ridge velocity is given by 29.6 ± 24.6 m/s. The large scatter in the values indicates significant spatial variation of the mass-wasting velocities, induced by external and internal forces.

The uneven distribution of velocities along some curved ridges (e.g. Curve 2) may be produced by alterations of the surface after the formation of the curved ridges by, for instance, mass wasting or impact cratering (cf. Figure 6.13). Variable curvatures on different length scales also result in a range of velocities (Equation 3.26) which, when distributed in the histogram used to find the most commonly occurring velocity (cf. Figure 6.12), may produce an apparent abrupt change in velocity along a curved ridge (Section 6.8).

In certain sections, the mass motion causing the curved ridges is undergoing phases of acceleration and deceleration towards the Rheasilvia floor. These are evident as the gradual change in colour in Figure 7.1. On the crater wall, a change from blue to green indicates an acceleration, whilst a change from green to blue means a deceleration, towards the basin floor.

An acceleration may be caused by the resultant gravitational force on a moving mass, whereas internal and basal friction may decelerate moving masses. Deceleration can also occur as a consequence of the topography changing to flatter slopes which reduces the gravity component along the mass motion direction. A constant velocity is reached when gravitational and frictional accelerations cancel resulting in force-free movement. Sections 8.1, 8.2 and 8.3 will discuss how these processes relate to the crater formation process.

Dynamic trends are evident in all three geologically distinct regions described in Section 6.2 and will therefore be presented separately in further detail in the following sections. Section 8.5 will discuss how the properties of the three regions relate to each other.

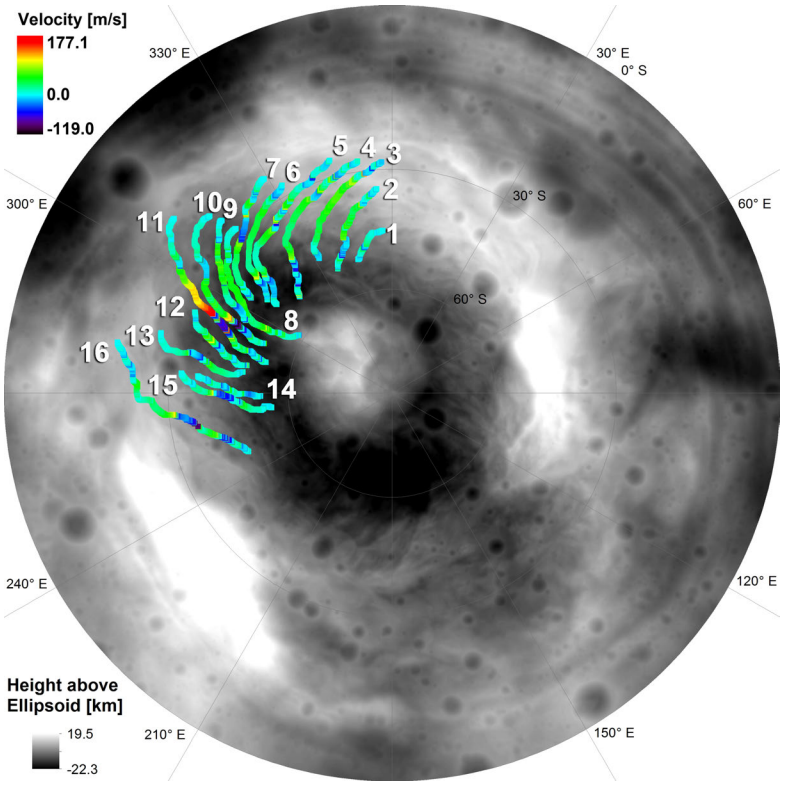

Figure 7.2.: The velocity distribution of the curved ridges in Region 1 on a stereographic topographic map of Vesta's southern hemisphere. The individual mapping points of the curved ridges are colour-coded according to their velocity with red indicating high, and dark purple low, values while the colour bar is linear. The average positive velocity of the illustrated mapping points is 31.2 ± 26.8 m/s.

7.1. Region 1: 270°E to 360°E

Figure 7.2 shows the curved ridges (Curves 1–16)[1] of Region 1 on a topographic map of Vesta's southern hemisphere. The gradual change in colour along the curved ridges represents accelerating (blue to green) and decelerating (green to blue) motion towards the Rheasilvia floor. For example, the blue to green to red colour change, towards the Rheasilvia floor, of Curve 11 indicates a velocity increase.

The average velocity of the curved ridges in Region 1 is 16.6 ± 33.9 m/s

[1]The curved ridges are named Curves 1–32 according to Figure 6.2.

(Table B.4). Neglecting negative velocities, which cannot be created by the Coriolis force but are likely to be an effect of later alteration such as impact cratering or mass wasting, the average velocity is 31.2 ± 26.8 m/s (Table B.4). These values are discussed in Section 8.1. The large scatter in the velocities, represented by the large error, is caused by the velocity changes along the curved ridges.

Three different smooth velocity trends, indicating sections of constant acceleration (Curves 1, 5, 6, 8–13, 15 and 16, e.g. Figure 7.3), of constant deceleration (Curves 3–9 and 13–15, e.g. Figure 7.4) and of constant velocity (Curves 4, 6, 7, and 10, e.g. Figure 7.5) are observed in Region 1. Some curved ridges show multiple smooth trending sections at different locations along the curved ridge (Curves 4–9, 12, 13, 15 and 16). This must mean the material properties or topographic conditions are changing along the curved ridges (Section 7.4). Curve 2 does not show any smooth trends.

In the following the constantly accelerating and decelerating sections and the sections of constant velocity are shown in detail. The velocity and topography plots of the curved ridges are presented in Appendix B.1 and the velocity statistics of each curved ridge in Region 1 are listed in Table B.1 in Appendix B.2. The graphs illustrating the measurements in the squared velocity plots and topography plots are in Appendix B.3.

7.1.1. Accelerating Velocity Sections

Curve 1 illustrates an example of a constantly accelerating curved ridge (Figure 7.3). From roughly 23 km to 30 km along the curved ridge the square of the velocity increases linearly. The velocity increase from ∼10 m/s to ∼26 m/s equates to an apparent acceleration of ∼0.04 m/s^2 when applying Equation 6.3.

Table 7.1 lists the measured values for the initial velocity v_i, the final velocity v_f, the travelled distance Δd and the corresponding acceleration a. For orientation, the approximate position from Rheasilvia's centre at which the measurement was taken P, is added. Furthermore, the predominant slope α, derived from the topography plot, is included. The method for deriving the acceleration and slope are described in Section 6.9.

The predominant slope was used to calculate the acceleration of a friction-free object sliding down this slope on Vesta. With Vesta's gravity g_V, this acceleration is given by $g_\mathrm{V} \sin(\alpha)$ and represents the maximum acceleration reachable on the current slope. The last column in Table 7.1 shows the ratio of the acceleration of the sliding friction-free object and the acceleration determined with the squared velocity plot. If the ratio is below one, the

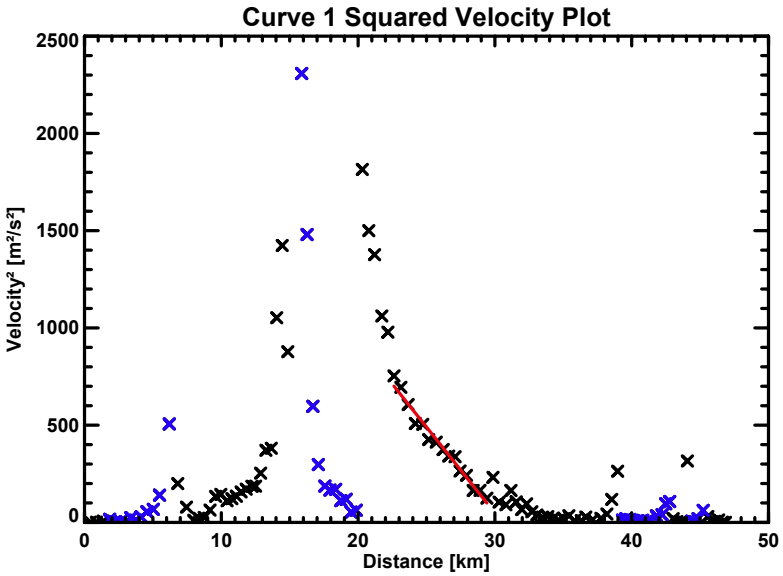

(a) Squared velocity plot Curve 1.

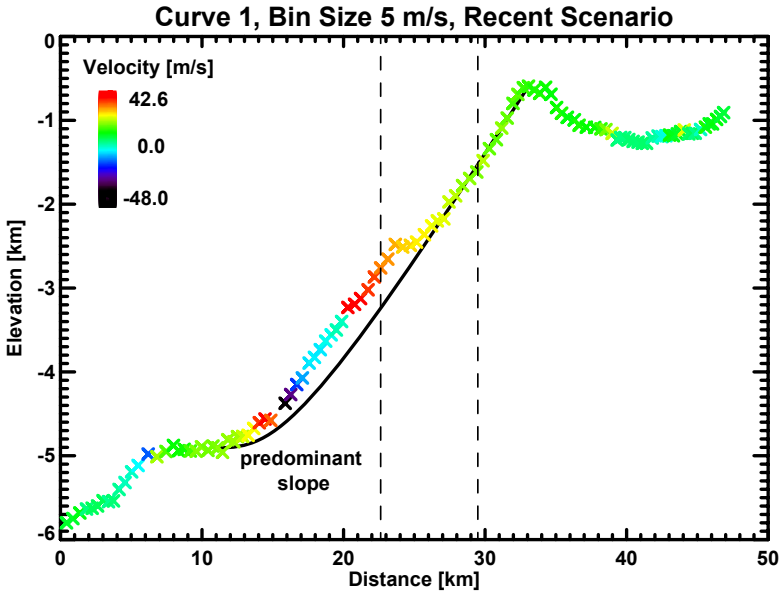

(b) Topography plot Curve 1.

Figure 7.3.: Curve 1, with an accelerating section between 22 km and 30 km. The mass motion occurred from right to left. (a) The blue points correspond to negative velocities and the accelerating trend is fit by the red line. (b) The predominant slope is sketched (black line) and the dashed lines mark where the measurement was taken.

Table 7.1.: Measurement parameters and derived values for the accelerating sections, from the squared velocity and topography plots in Region 1 (Appendix B.3). The superscript *IC* denotes the presence of an impact crater at the measurement location. The measurements in bold are reliable (see text) and were used to derive the material properties in Section 7.4.

Curve	v_i [m/s]	v_f [m/s]	Δd [km]	P [km]	α [°]	a [$\cdot 10^{-3}$ m/s^2]	$g_V \sin(\alpha)$ [$\cdot 10^{-3}$ m/s^2]	$\frac{a}{g_V \sin(\alpha)}$
1	**10.0**	**26.5**	**6.8**	**147**	**12.5**	**44.2 ±4.0**	**54.3 ±6.5**	**0.82 ±0.12**
5^{IC}	19.1	57.8	7.0	146	1.8	211.6 ±21.7	7.7 ±0.9	27.41 ±4.32
5	10.0	22.6	9.3	155	0.9	22.1 ±3.5	3.9 ±0.5	5.73 ±1.13
6	**37.7**	**41.6**	**11.8**	**192**	**7.0**	**13.2 ±3.9**	**30.4 ±3.6**	**0.43 ±0.14**
8	39.2	52.0	37.7	166	2.7	15.4 ±1.7	11.8 ±1.4	1.31 ±0.21
9	19.5	37.9	5.4	192	1.1	97.8 ±11.3	4.9 ±0.6	19.86 ±3.30
10	46.9	56.3	11.4	182	9.2	42.7 ±5.6	4.2 ±0.5	1.06 ±0.19
11^{IC}	101.5	173.5	21.4	174	4.0	462.6 ±22.7	17.5 ±2.1	26.50 ±3.43
11	43.9	97.7	21.6	207	8.7	176.3 ±20.4	37.9 ±4.6	4.65 ±0.77
12^{IC}	39.2	102.4	5.0	160	1.9	891.6 ±83.3	8.3 ±1.0	106.92 ±16.26
12	5.7	24.6	5.5	173	1.2	51.6 ±4.0	5.1 ±0.6	10.04 ±1.44
13	**2.8**	**18.0**	**14.9**	**198**	**11.2**	**10.5 ±0.9**	**48.5 ±5.8**	**0.22 ±0.03**
15	**20.8**	**24.0**	**5.0**	**174**	**4.3**	**14.5 ±5.5**	**18.8 ±2.3**	**0.77 ±0.31**

continues on page 93

Table 7.1 continued

16	20.4	64.5	12.2	175	12.3	152.8 ±16.4	53.1 ±6.4	2.88 ±0.46
16	11.4	29.4	12.4	228	0.9	29.5 ±2.6	3.9 ±0.5	7.55 ±1.12

measured acceleration is smaller than the friction-free sliding acceleration and physically possible on the current slope.

The relative errors of g_V and $g_V \sin(\alpha)$ are equivalent (12% [*Ermakov et al.*, 2014]) and the relative error of $\frac{a}{g_V \sin(\alpha)}$ is given by $\sqrt{(\frac{\Delta a}{a})^2 + (\frac{\Delta g_V}{g_V})^2}$ following standard error propagation, where Δ indicates the absolute error.

All calculated accelerations but two (derived from Curves 11 and 12) are below the gravitational acceleration of Vesta (0.25 ± 0.03 m/s^2). The impossibly large accelerations of Curves 11 and 12 can be explained by the presence of impact craters where the measurement was taken (cf. Figure 6.13(a)). The impacts have probably deformed the original structure of the curved ridges. Additionally, Curve 5 has a relatively large acceleration of ~85% of Vesta's gravity. Again the topography plot shows an impact crater where the measurement was taken. Consequently, the accelerations derived from Curves 5, 11 and 12 are not reliable.

The remaining measurements produce accelerations below ~71% of Vesta's gravity, which would be expected for masses moving under the influence of gravity.

The accelerations derived from Curves 1, 6, 13 and 15 are less than for a friction-free sliding object (Table 7.1). They are 82% ± 12%, 43% ± 14%, 22% ± 3% and 77% ± 31% of the maximum friction-free sliding acceleration, respectively. These accelerations indicate that gravity was able to induce, or continue, the mass motion on the current slope. The average of all positive velocities associated with Curves 1, 6, 13 and 15 is given by 22.1 ± 15.5 m/s and the maximum of all values does not exceed 99.3 m/s.

Nevertheless, in the remaining eight measurements not effected by impact cratering (Curves 5, 8–12, and 16), the calculated accelerations exceed those which would be reached by an object when sliding frictionless down the present slope (Table 7.1). It is therefore impossible that the slopes on which these accelerations appear are the slopes on which the masses moved. The acceleration of Curve 10 is however, only slightly larger than the acceleration of a friction-free sliding object and may be below the friction-free sliding acceleration within the measuring error.

The velocities associated with Curves 5, 8–12 and 16 are generally larger compared to those with accelerations below the friction-free sliding acceleration (Curves 1, 6, 13 and 15). Their average positive velocity is 34.1 ± 27.1 m/s and the maximum value is 177.1 m/s.

7.1.2. Decelerating Velocity Sections

Curves 3–9 and 13–15 show constantly decelerating trends along sections of the curved ridges. Figure 7.4 shows the squared velocity and topography plots of Curve 6 as an example. From roughly 40 km to 85 km along the curved ridge the velocity drops linearly from ∼39 m/s to ∼13 m/s in the squared velocity plot. This equates to a deceleration of ∼-0.015 m/s^2 (Equation 6.3). Table 7.2 shows the corresponding measurements from the remaining fourteen curved ridges based on the procedure described in Section 6.9.

Curve 8 exhibits a topographic mound near the basin floor where the deceleration was measured. This mound is indicative of subsequent mass wasting, non-parallel to the curved ridge (cf. Figure 6.13(b)). Curve 9 shows two sections of deceleration at an impact crater (cf. Figure 6.13(a)). Both processes probably have altered the original structure and hence the measurements are not reliable at these locations.

Generally, the mean positive velocities of the curved ridges with decelerating trends, with the exception of Curves 8 and 9, is 26.3 ± 18.9 m/s with an individual maximum of 123.8 m/s. The deceleration ranges between -(14.8 ± 1.3)·10^{-3} m/s^2 and -(181.0 ± 11.8)·10^{-3} m/s^2 (Table 7.2).

With the exception of Curves 8 and 9, all curved ridges show a step in the topographic slope where the decelerating section begins. In the topography plots, this appears as accumulated material on top of the predominant slope (Figure 7.4(b)).

7.1.3. Constant Velocity Sections

Curve 7 is an example of a curved ridge with a constant velocity section. Figure 7.5 shows that between roughly 24 km and 44 km from Rheasilvia's centre the velocity is ∼23 m/s. Comparing this section with the topography plot, it becomes clear that the constant velocity is associated with a plateau (Figure 7.5(b)). Shortly before reaching the plateau, a decelerating trend is evident in the velocity plot (Figure 7(a)).

Table 7.3 lists the measured values for all four curved ridges with constant velocity sections in Region 1. The constant velocities of Curves 4, 6, 7 and 10

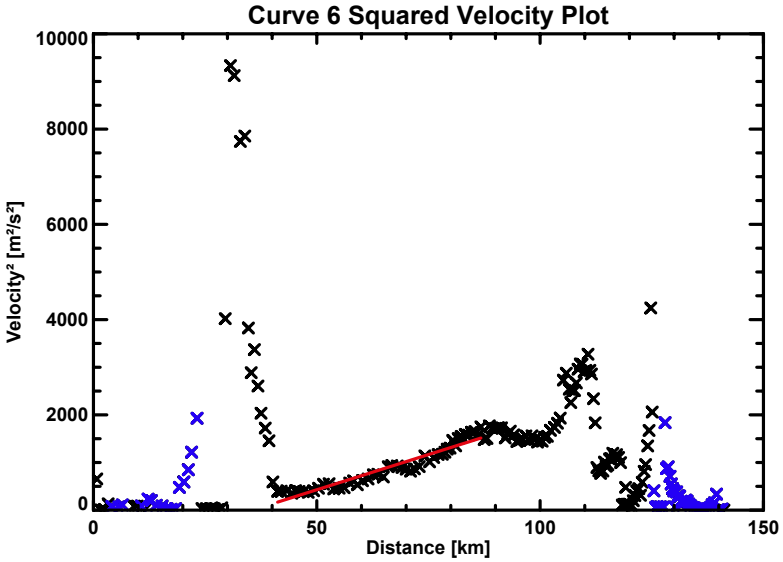

(a) Squared velocity plot Curve 6.

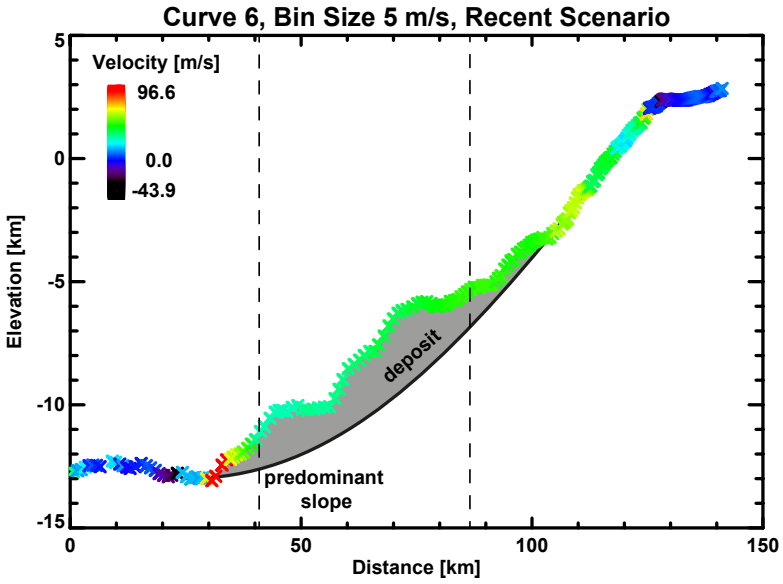

(b) Topography plot Curve 6.

Figure 7.4.: Curve 6, with a decelerating profile between 40 km and 87 km. The mass motion occurred from right to left. (a) The blue points correspond to negative velocities and the fit to the decelerating trend is illustrated by the red line. (b) A deposit (grey area) accumulated by the deceleration of material wasting on top of the predominant slope (black line). The dashed lines mark where the deceleration was measured. Similar depositional features are observed in Curves 3–7, 9, 13–15, 22 and 26.

Table 7.2.: Measurement parameters and derived values for the decelerating sections, from the squared velocity and topography plots in Region 1 (Appendix B.3). The superscripts *MW* and *IC* indicate subsequent mass wasting and the presence of impact craters at the measurement location, respectively. The measurements in bold are reliable (see text) and were used to derive the material properties in Section 7.4.

Curve	v_i [m/s]	v_f [m/s]	Δd [km]	P [km]	α [°]	a [$\cdot 10^{-3}$ m/s^2]
3	**58.7**	**35.4**	**29.1**	**176**	**7.7**	**-37.5 ±3.8**
4	**52.4**	**35.7**	**17.3**	**188**	**5.9**	**-42.5 ±3.3**
5	**54.1**	**27.7**	**14.3**	**174**	**12.2**	**-75.6 ±6.0**
6	**38.9**	**13.0**	**45.5**	**171**	**7.5**	**-14.8 ±1.3**
6	**56.6**	**37.5**	**10.3**	**198**	**10.7**	**-88.0 ±15.6**
7	**36.8**	**24.9**	**6.1**	**175**	**3.3**	**-60.0 ±7.5**
7	**74.6**	**44.9**	**9.8**	**183**	**5.0**	**-181.0 ±11.8**
8^{MW}	52.4	35.7	15.5	135	3.1	-72.7 ±6.8
9^{IC}	15.8	8.8	8.8	158	2.0	-9.8 ±2.6
9^{IC}	39.8	17.7	10.9	165	2.0	-58.1 ±4.6
9	**65.6**	**50.7**	**8.7**	**181**	**3.9**	**-100.0 ±6.3**
13	**24.5**	**3.4**	**15.7**	**138**	**4.1**	**-18.8 ±1.9**
14	**24.4**	**7.7**	**5.5**	**134**	**5.7**	**-48.6 ±6.7**
15	**27.9**	**10.1**	**9.0**	**123**	**3.9**	**-37.7 ±3.3**

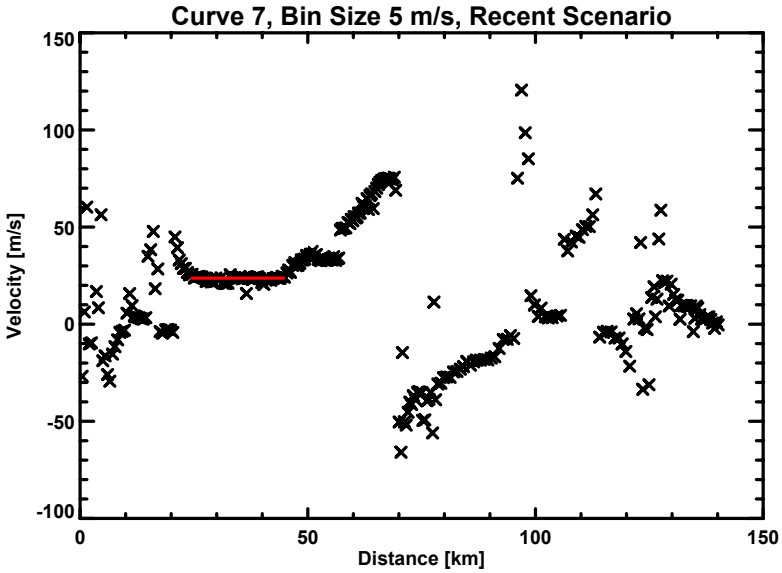

(a) Velocity plot Curve 7.

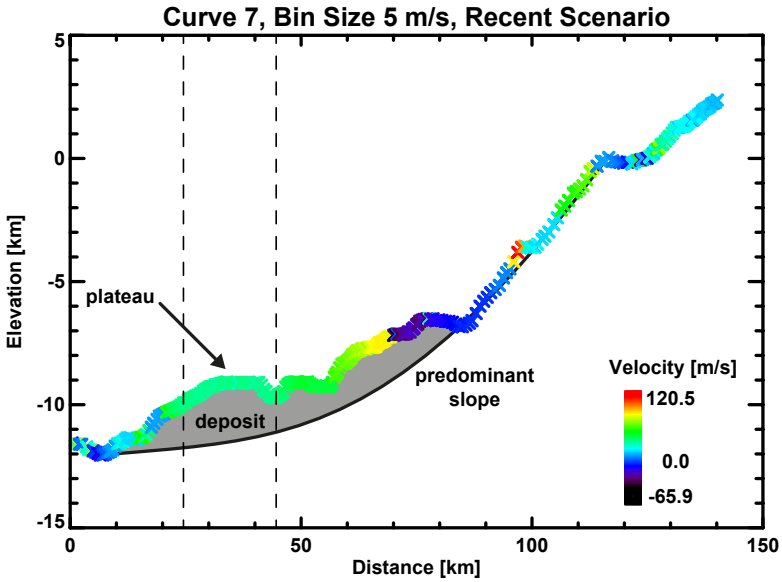

(b) Topography plot Curve 7.

Figure 7.5.: Curve 7, with an constant profile between 24 km and 44 km. The mass motion occurred from right to left. (a) The red line represents the fit to the constant velocity section. (b) A deposit (grey area) covers the predminant slope (black line) forming a plateau. The dashed lines mark where the constant velocity was measured. A plateau is also observed for Curves 20 and 24.

Table 7.3.: Measurement parameters for the constant velocity sections, from the velocity and topography plots in Region 1 (Appendix B.1). The measurements are reliable (see text) and were used to derive the material properties in Section 7.4.

Curve	v [m/s]	Δd [km]	P [km]	α [°]
4	**28.0 ±1.8**	**25.4**	**166**	**5.5**
6	**39.5 ±1.6**	**24.7**	**190**	**7.4**
7	**23.1 ±1.6**	**19.8**	**166**	**3.7**
10	**11.4 ±1.4**	**26.2**	**222**	**1.2**

range between 11.4 ± 1.4 m/s and 39.5 ± 1.6 m/s (Table 7.3). The average of all positive velocities of the curved ridges is 33.2 ± 23.2 m/s.

7.2. Region 2: The Rheasilvia and Veneneia Intersection

Eleven curved ridges (Curves 17–27) cover the area where Rheasilvia and Veneneia intersect. Figure 7.6 shows the curved ridges of Region 2 on a topographic map of Vesta's southern hemisphere. The derived average velocity is 12.6 ± 33.9 m/s (Table B.4). Neglecting negative velocities, which indicate an uphill motion away from the pole and thus are not physically explicable by the Coriolis Effect, the average velocity is 31.0 ± 25.3 m/s (Table B.4). These values are discussed in Section 8.2.

As with Region 1, the relatively large fluctuation in velocity can partly be explained by dynamic trends, including sections of constant acceleration (Curves 17, 19, 22, 24 and 25), constant deceleration (Curves 22, 24 and 26) and constant velocity (Curves 20 and 24). Figure 7.6 illustrates these sections by the gradual change and preservation of colour along the curved ridges.

Note that Curves 18, 21, 23 and 27 changed too randomly to allow smooth trends to be detected. Additionally, Curve 23 shows an increase in elevation towards Rheasilvia's centre, indicating that the curved ridge is located in an area of irregular topography.

The velocity and topography plots of the curved ridges are shown in

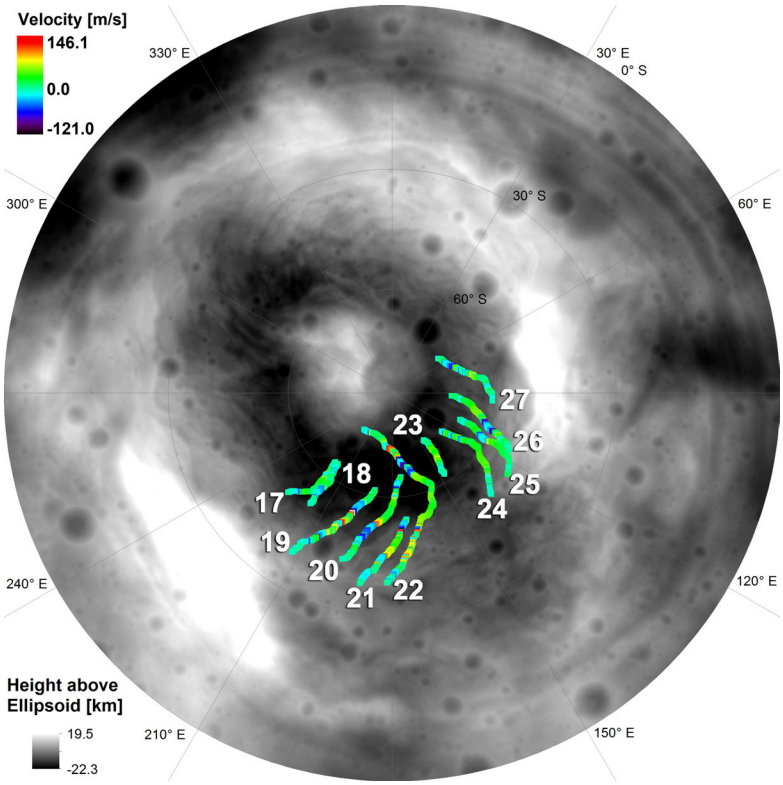

Figure 7.6.: The velocity distribution of the curved ridges in Region 2 on a stereographic topographic map of Vesta's southern hemisphere. The individual mapping points of the curved ridges are colour-coded according to their velocity with red indicating high, and dark purple low, values while the colour bar is linear. The average positive velocity of the illustrated mapping points is 31.0 ± 25.3 m/s.

Appendix B.1 and Table B.2 in Appendix B.2 lists the velocities of each curved ridge in Region 2. The graphs illustrating the measurements used in the squared velocity plots and topography plots are in Appendix B.3.

7.2.1. Accelerating Velocity Sections

There are six sections of accelerating velocities along curved ridges within Region 2 (Table 7.4). All accelerations are below the gravitational acceleration of Vesta with the maximum value being 41% of Vesta's gravity. Although these values agree with gravitationally accelerated mass motions on Vesta, only one acceleration (Curve 25) is lower than the maximum reachable acceleration of

Table 7.4.: Measurement parameters and derived values for the accelerating sections, from the squared velocity and topography plots in Region 2 (Appendix B.3). The superscript *IC* denotes an impact crater at the measurement location. The measurement in bold is reliable (see text) and was used to derive the material properties in Section 7.4.

Curve	v_i [m/s]	v_f [m/s]	Δd [km]	P [km]	α [°]	a [$\cdot 10^{-3}$ m/s^2]	$g_V \sin(\alpha)$ [$\cdot 10^{-3}$ m/s^2]	$\frac{a}{g_V \sin(\alpha)}$
17^{IC}	8.0	40.4	11.7	139	-3.7	67.2 ±3.0	-16.3 ±2.0	-4.11 ±0.53
19	6.6	29.7	5.4	200	13.8	78.5 ±16.1	59.6 ±7.1	1.32 ±0.31
22	34.4	60.7	17.4	153	9.7	71.7 ±5.4	42.2 ±5.1	1.70 ±0.24
24	18.1	42.2	7.0	161	11.0	103.7 ±8.5	47.6 ±5.7	2.18 ±0.32
24^{IC}	24.3	32.0	10.1	174	1.4	21.4 ±3.5	6.2 ±0.7	3.43 ±0.70
25	**6.9**	**25.0**	**26.9**	**206**	**14.2**	**10.8 ±1.1**	**61.3 ±7.4**	**0.18 ±0.03**

a friction-free sliding object on the current slope ($g_V \sin(\alpha)$).

Curve 25 exhibits an accelerations of 18% ± 3% of the friction-free sliding acceleration on the current slope ($10.8 \cdot 10^{-3}$ m/s^2, Table 7.4). The average positive velocity is 22.8 ± 15.4 m/s with a maximum individual value of 79.3 m/s.

The accelerating section of Curve 17 (139 km from Rheasilvia's centre) and the second accelerating section of Curve 24 (174 km from Rheasilvia's centre) coincide with impact craters which are likely to have altered the topography and influenced the measurements (cf. Figure 6.13(a)). In the case of Curve 17, the impact crater has changed the local slope to a negative value. In other words the elevation locally increases towards the basin floor.

The remaining accelerating sections of Curves 19 and 22, as well as the first accelerating section of Curve 24, have accelerations above the friction-free sliding acceleration on the current slope (Table 7.4). Their average positive velocity of 37.8 ± 27.3 m/s and the maximum individual value of 146.1 m/s

Table 7.5.: Measurement parameters and derived values for the decelerating sections, from the squared velocity and topography plots in Region 2 (Appendix B.3). The superscript *IC* denotes an impact crater at the measurement location. The measurements in bold are reliable (see text) and were used to derive the material properties in Section 7.4.

Curve	v_i [m/s]	v_f [m/s]	Δd [km]	P [km]	α [°]	a [$\cdot 10^{-3}$ m/s^2]
22	**62.6**	**23.9**	**29.0**	**193**	**7.7**	**-57.7 ±1.9**
24^{IC}	44.5	27.5	9.5	182	1.4	-64.4 ±5.2
26	**53.5**	**29.4**	**8.5**	**152**	**8.3**	**-118.1 ±10.2**

are relatively large compared to those of Curve 25.

7.2.2. Decelerating Velocity Sections

Curves 22, 24 and 26 have sections of constantly decelerating mass motions.

From the topography plot, Curve 24 has an impact crater at the location of the deceleration (cf. Figure 6.13(a)), which possibly had an effect on the observed curvature.

Curves 22 and 26 have decelerations of -(57.7 ± 1.9)·10^{-3} m/s^2 and -(118.1 ± 10.2)·10^{-3} m/s^2, respectively (Table 7.5). As with Curve 6 in Section 7.1.2, the sections of deceleration are accompanied by a pile of material settled on top of the predominant slope (cf. Figure 7.4(b)). The average positive velocity of Curves 22 and 26 is 37.5 ± 25.3 m/s with a maximum individual value of 130.3 m/s (Table B.2).

7.2.3. Constant Velocity Sections

Curves 20 and 24 have sections of constant velocities of 22.5 ± 1.5 m/s and 45.8 ± 3.9 m/s, respectively. The average positive velocity of both curved ridges together is 29.6 ± 18.7 m/s and the maximum individual value is 105.5 m/s.

The topography plots show that the constant velocity sections of Curves 20 and 24 are located on plateaus similar to the case of Curve 7 (Figure 7.5(b)).

Table 7.6.: Measurement parameters for the constant velocity sections, from the velocity and topography plots in Region 2 (Appendix B.1). The measurements are reliable (see text) and were used to derive the material properties in Section 7.4.

Curve	v [m/s]	Δd [km]	P [km]	α [°]
20	**22.5 ±1.5**	**15.0**	**176**	**7.4**
24	**45.8 ±3.9**	**12.4**	**191**	**3.9**

A deceleration is evident in the velocity plots (Figures 20(a) and 24(a)) for both curved ridges prior to the constant velocity section.

7.3. Region 3: The Central Peak

Curves 28–32 cover the central peak region (Figure 7.7). These ridges curve in the opposite direction compared to Regions 1 and 2 as a result from moving away from the centre of Rheasilvia down the central peak, if the Coriolis force affected mass wasting here. Thus, their velocities are negative in the used system (Table B.3) and of blue to green colour in Figure 7.7. The average velocity is -7.3 ± 23.4 m/s, and neglecting positive velocities which cannot be generated by the Coriolis force here, the average velocity is -21.6 ± 16.2 m/s (Table B.4). These values are discussed in Section 8.3.

Curves 29 and 31 posses constantly accelerating sections and Curve 30 has a section of constant velocity. Curves 28 and 32 do not have any identifiable smooth trends. None of the curved ridges in Region 3 shows a constantly decelerating trend which might be due to the small number of curved ridges in this region.

Note that an increase in a negative velocity in the direction away from Rheasilvia's centre results in a positive acceleration. In other words, in analogy to Regions 1 and 2, the acceleration in the direction of gravity (downhill) is positive.

The velocity and topography plots of the curved ridges are presented in Appendix B.1 and Table B.3 in Appendix B.2 lists the velocities derived for each curved ridge in Region 3. The squared velocity and topography plots illustrating the measurements of the constantly accelerating sections are in

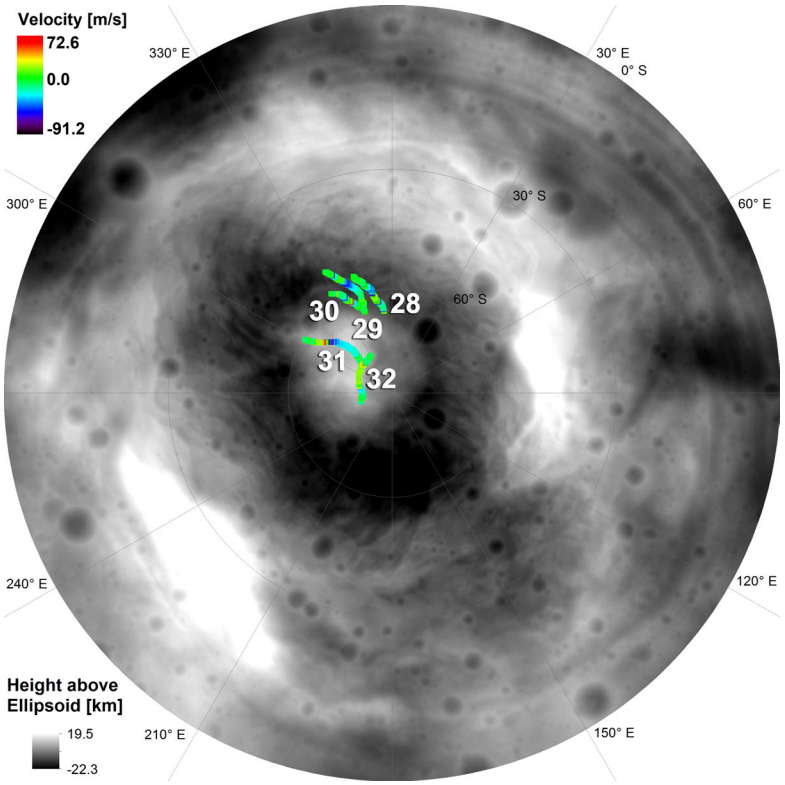

Figure 7.7.: The velocity distribution of the curved ridges in Region 3 on a stereographic topographic map of Vesta's southern hemisphere. The individual mapping points of the curved ridges are colour-coded according to their velocity with red indicating high, and dark purple low, values while the colour bar is linear. The average negative velocity of the illustrated mapping points is -25.9 ± 28.4 m/s.

Appendix B.3.

7.3.1. Accelerating Velocity Sections

The sections of constant acceleration of Curves 29 and 31 are below Vesta's gravity of 0.25 ± 0.03 m/s^2 (Table 7.7). However, the section of constant acceleration of Curve 29 coincides with a mound of non-parallel mass-wasting deposits near the Rheasilvia floor which probably altered the original structure (cf. Figure 6.13(b)). The acceleration of Curve 31 is 4.8% of Vesta's gravitational acceleration and 57% ± 9% of the friction-free sliding acceleration on the current slope. Thus, acceleration due to gravity is plausible. The

Table 7.7.: Measurement parameters and derived values for the accelerating sections, from the squared velocity and topography plots in Region 3 (Appendix B.3). The superscript *MW* denotes subsequent mass wasting at the measurement location. The measurement in bold is reliable (see text) and was used to derive the material properties in Section 7.4.

Curve	v_i [m/s]	v_f [m/s]	Δd [km]	P [km]	α [°]	a [$\cdot 10^{-3}$ m/s^2]	$g_V \sin(\alpha)$ [$\cdot 10^{-3}$ m/s^2]	$\frac{a}{g_V \sin(\alpha)}$
29^{MW}	6.5	17.4	8.5	87	3.1	15.3 ±2.1	13.5 ±1.6	1.13 ±0.21
31	**19.7**	**30.0**	**21.2**	**25**	**4.8**	**12.0 ±1.3**	**20.9 ±2.5**	**0.57 ±0.09**

Table 7.8.: Measurement parameters for the constant velocity sections, from the velocity and topography plots in Region 3 (Appendix B.1). The measurement is reliable (see text) and was to derive the material properties in Section 7.4.

Curve	v [m/s]	Δd [km]	P [km]	α [°]
30	**-8.9 ±1.2**	**8.0**	**83**	**4.4**

average negative velocity of Curve 31 is -26.6 ± 15.6 m/s with a maximum individual negative value of -91.2 m/s (Table B.3).

7.3.2. Constant Velocity Sections

Curve 30 has an average negative velocity of -14.9 ± 12.4 m/s with a minimum individual value of -53.3 m/s and has a section at a constant velocity of -8.9 ± 1.2 m/s (Table 7.8) at roughly 83 km from Rheasilvia's centre. Furthermore, the section of constant velocity coincides with a plateau in the slope (cf. Figure 7.5(b)). A relatively constant decrease in velocity shortly before reaching the plateau is evident in the velocity plot, however the section is too short to be listed as a constantly decelerating section.

7.4. Material Properties

7.4.1. Viscosity

As described in Section 3.1.3, acoustically fluidised material with high acoustic energy densities can be described by a Newtonian fluid, with an effective viscosity. The mass wasting of the Rheasilvia modification stage can be explained by such an acoustically fluidised motion (Section 3.1.7). Consequently the constant velocity sections identified earlier can be used to calculate the effective viscosity η_{eff} using Equation 3.6:

$$\eta_{\text{eff}} = \frac{g_{\text{V}} \rho \sin(\alpha) d^2}{3v}. \tag{3.6}$$

The thickness d of the flow was estimated to be 2.5 ± 1.0 km, corresponding to the approximate curved ridge height as described in Section 5.2. The curved ridges are representative of the curved structure produced during the Rheasilvia modification stage and the curved ridge height is therefore an appropriate measure of the vertical length scale of the mass motion. The density ρ was assumed to be 2000 ± 1000 kg/m^3, as suggested by *Collins and Melosh* [2003] and *Iverson* [1997]. The error of the viscosity propagates as follows:

$$\Delta\eta_{\text{eff}} = \eta_{\text{eff}} \sqrt{\left(\frac{\Delta g_{\text{V}}}{g_{\text{V}}}\right)^2 + \left(\frac{\Delta\rho}{\rho}\right)^2 + 2\left(\frac{\Delta d}{d}\right)^2 + \left(\frac{\Delta v}{v}\right)^2}, \tag{7.1}$$

where Δ indicates the absolute error of a value. The relative error on Vesta's gravity is 12% [*Ermakov et al.*, 2014]. There was no error assumed on the slope, as this is open to geologic interpretation and cannot be expressed as a statistical error (Section 6.9).

Table 7.9 lists the effective viscosities derived from the seven reliable sections of constant velocity in the three regions (Sections 7.1.3, 7.2.3 and 7.3.2). The viscosity ranges between 1.5·10^6 Pa·s and 9.0·10^6 Pa·s, with the largest value found in Region 3. The average viscosities of Regions 1 and 2 are (3.0 ± 0.8)·10^6 Pa·s and (3.8 ± 3.2)·10^6 Pa·s, respectively. Region 3 possesses only one reliable measurement ((9.0 ± 7.0)·10^6 Pa·s). Section 8.4 discusses these values with respect to expected values and the geologic region they occur in.

7.4.2. Coefficient of Friction

Alternatively, the mass wasting can be visualized as a body of debris sliding down the crater wall and central peak as described in Section 3.1.3 and

Table 7.9.: Measurement parameters, viscosities and coefficients of friction derived from constant velocity sections.

Curve	Region	v [m/s]	Δd [km]	P [km]	α [°]	η_{eff} [$\cdot 10^6$ Pa·s]	μ_{eff}
4	1	28.0 ±1.8	25.4	166	5.5	3.6 ±2.7	0.096
6	1	39.5 ±1.6	24.7	190	7.4	3.4 ±2.6	0.130
7	1	23.1 ±1.6	19.8	166	3.7	2.9 ±2.2	0.065
10	1	11.4 ±1.4	26.2	222	1.2	1.9 ±1.5	0.021
20	2	22.5 ±1.5	15.0	176	7.4	6.0 ±4.6	0.130
24	2	45.8 ±3.9	12.4	191	3.9	1.5 ±1.2	0.068
30	3	(-)8.9 ±1.2	8.0	83	4.4	9.0 ±7.0	0.077

Equation 3.7:

$$\mu_{\text{eff}} = \frac{a_{\text{FR}}}{g_{\text{V}} \cos(\alpha)} = \frac{a_{\text{FF}} - a}{g_{\text{V}} \cos(\alpha)} = \frac{g_{\text{V}} \sin(\alpha) - a}{g_{\text{V}} \cos(\alpha)}. \tag{3.7}$$

Only the measured acceleration a and gravity g_{V} (0.25 ± 0.03 m/s^2) introduce errors into the calculation. Following standard error propagation the absolute error of μ_{eff} can be calculated by:

$$\Delta\mu_{\text{eff}} = \frac{a}{g_{\text{V}} \cos(\alpha)} \sqrt{\left(\frac{\Delta g_{\text{V}}}{g_{\text{V}}}\right)^2 + \left(\frac{\Delta a}{a}\right)^2}, \tag{7.2}$$

where Δ indicates absolute errors.

Tables 7.10 and 7.11 list the coefficients of friction of the previously described reliable accelerating and decelerating curved ridge sections (Sections 7.1.1, 7.1.2, 7.2.1, 7.2.2 and 7.3.1). The coefficients of friction are also derived from the sections of constant velocity (Sections 7.1.3, 7.2.3 and 7.3.2). Here, the apparent acceleration is zero and consequently the friction-free

Table 7.10.: Measurement parameters and coefficients of friction derived from accelerating sections.

Curve	Region	P [km]	α [°]	a [$\cdot 10^{-3}$ m/s^2]	μ_{eff}
1	1	147	12.5	44.2 ±4.0	0.041 ±0.027
6	1	192	7.0	13.2 ±3.9	0.070 ±0.017
13	1	198	11.2	10.5 ±0.9	0.155 ±0.006
15	1	174	4.3	14.5 ±5.5	0.017 ±0.023
25	2	206	14.2	10.8 ±1.1	0.208 ±0.007
31	3	25	4.8	12.0 ±1.3	0.036 ±0.008

sliding acceleration and acceleration due to friction have the same magnitude. In other words, $\mu_{\text{eff}} = \tan(\alpha)$ (Table 7.9) and no error is introduced.

The coefficients of friction derived from the constantly accelerating, decelerating and constant velocity sections vary between 0.017 and 0.814. The highest coefficients of friction are observed for the constantly decelerating sections 0.369 ± 0.192. The constantly accelerating sections and sections of constant velocity have similar average coefficients of friction of 0.088 ± 0.076 and 0.084 ± 0.039, respectively. Nevertheless, the values are in agreement within their errors.

Considering the regions separately, Regions 1 and 2 have similar average coefficients of friction of 0.250 ± 0.208 and 0.279 ± 0.222, respectively. Region 3 has an average coefficient of friction of 0.082 ± 0.048. Although these values agree within their errors, the total number of measurements varies significantly between the regions (twenty, five and two measurements in Regions 1, 2 and 3, respectively) and hence this comparison needs to be considered with caution.

Section 8.4 discusses the measured coefficients of friction with respect to values which may be expected, the trends from which they are derived and the geologic region in which they occur.

Table 7.11.: Measurement parameters and coefficients of friction derived from decelerating sections.

Curve	Region	P [km]	α [°]	a [$\cdot 10^{-3}$ m/s^2]	μ_{eff}
3	1	176	7.7	-37.5 ±3.8	0.287 ±0.024
4	1	188	5.9	-42.5 ±3.3	0.274 ±0.024
5	1	174	12.2	-75.6 ±6.0	0.526 ±0.045
6	1	171	7.5	-14.8 ±1.3	0.191 ±0.009
6	1	198	10.7	-88.0 ±15.6	0.547 ±0.077
7	1	175	3.3	-60.0 ±7.5	0.298 ±0.042
7	1	183	5.0	-181.0 ±11.8	0.814 ±0.099
8	1	135	3.1	-71.7 ±6.8	0.341 ±0.044
9	1	181	3.9	-100.0 ±6.3	0.469 ±0.054
13	1	138	4.1	-18.8 ±1.9	0.147 ±0.012
14	1	134	5.7	-48.6 ±6.7	0.295 ±0.036
15	1	123	3.9	-37.7 ±3.3	0.219 ±0.022
22	2	193	7.7	-57.7 ±1.9	0.368 ±0.029
26	2	152	8.3	-118.1 ±10.2	0.623 ±0.071
31	3	25	4.8	-12.0 ±1.3	0.132 ±0.008

8. Discussion

In the previous chapter, the velocities along the 32 curved ridges within three geologically distinct regions of the Rheasilvia basin were introduced and evaluated. Furthermore, effective viscosities and coefficients of friction were derived from the data. The following sections first discuss whether the Coriolis force is a plausible candidate to have caused the curved ridges in the three regions. Implications for dynamics, crater shape and material properties will then be derived for the modification stage of the Rheasilvia impact event and related to values from the literature.

8.1. Region 1: 270°E to 360°E

The mean positive velocity of all the curved ridges of Region 1 (31.2 ± 26.8 m/s, Table B.4) agrees well with numerically simulated mass motion velocities during the Rheasilvia modification stage (Section 3.1.7). *Jutzi et al.* [2013] derived a typical mass motion velocity of 50 m/s, which is within the velocity range of most individual curved ridges investigated in this region. Curve 1, with a maximum value of 42.2 m/s (Table B.1), is the only curved ridge whose velocity range does not include 50 m/s. Not only do the separate curved ridges have average positive velocities of around 50 m/s (Table B.1), but also the sections of constant velocity (11.4–39.5 m/s, Table 7.3) agree with the predicted value within the same order of magnitude. The fact that the velocities derived independently from the curved ridges by assuming they were caused by the Coriolis Effect, agree with the predicted mass motion velocity from *Jutzi et al.* [2013], is strong evidence that the Coriolis force was indeed responsible for the curvature.

Furthermore, it is expected that the velocity within the basin increases from low values near the origin of the motion and decreases again near the basin floor where the motion comes to a halt. In Figure 7.2 this trend is evident as the blue to green to blue colour change of the curved ridges. This gradual increase and decrease of the mass-wasting velocities along the curved ridges is another good indication that the curved structure of the ridges does not contradict formation by the the Coriolis Effect.

The transient crater at the beginning of the modification stage was approximately 82 km deep and had a radius of 132 km [*Ivanov and Melosh*, 2013].

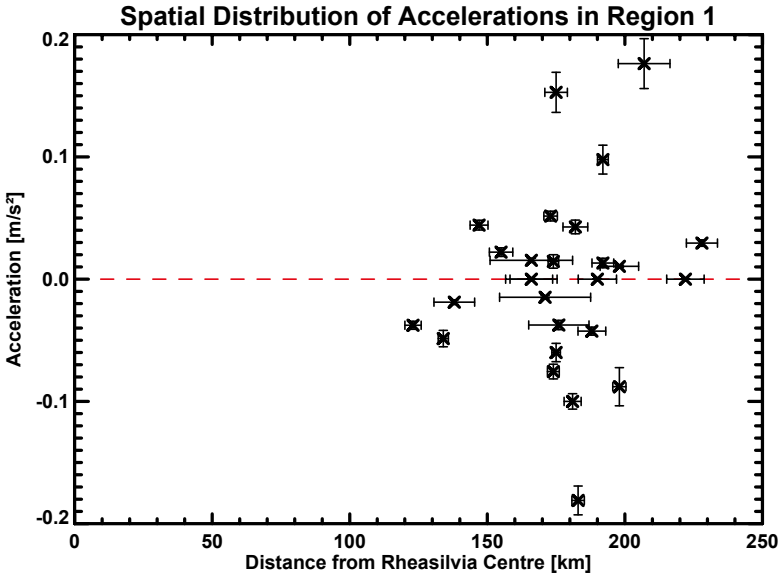

Figure 8.1.: The spatial distribution of accelerations derived for Region 1. The red dashed line indicates zero acceleration. Values above, below and on this line are accelerating, decelerating and moving with constant velocity, respectively. The bars on the distance describe the distance over which the acceleration, deceleration or velocity was constant (Δd) while the error bars on the acceleration illustrate the 1-σ uncertainty of the measurement.

Today Rheasilvia is about 19 km deep and has a radius of 250 km [*Jaumann et al.*, 2012]. The central peak has a diameter of roughly 180 km. The mass motions of the modification stage must have occurred during the transition between these two extreme crater shapes.

However, it is most probable that the curved ridges developed towards the end of the modification stage, because they would otherwise be overrun by large amounts of subsequent mass-wasting material, potentially hiding their curved structures. In agreement with this, the majority of curved ridges within Region 1 (eleven out of sixteen) originate beyond 200 km from Rheasilvia's centre. This indicates that the mass motion occurred at a time during the modification stage when the crater had grown to at least this size.

Masses moving down the transient crater wall of Rheasilvia are affected by Vesta's gravity. However, depending on the frictional forces, the masses may accelerate, decelerate or move with a constant velocity.

During the modification stage, masses wasted downhill from both the crater wall and central peak, towards the basin floor [*Melosh*, 1989]. Consequently,

the crater floor is filled with this material. In the Rheasilvia basin, most debris must have collected at radii of between roughly 90 km and 120 km from the centre, at the foot of the central peak. In this area the converging mass-wasting material should produce large variations in velocities, preventing the formation of the uniform conditions necessary for sections of constant acceleration, deceleration and constant velocity. The fact that distances up to 120 km from Rheasilvia's centre do not show any such sections (Figure 8.1) agrees with this expectation.

Figure 8.1 illustrates where sections of constantly accelerating and decelerating masses, and masses moving with constant velocity, were measured. The distances cluster between 120 km and 240 km from Rheasilvia's centre and the accelerations cover a range of ± 0.2 m/s^2. The range may be related to alteration of the curved ridges after their formation (e.g. impact cratering or further mass wasting, Section 6.8), heterogeneities in material properties or asymmetries in the crater shape and slopes. More precisely, heterogeneities within the pre-impact regolith or variations in acoustic energy during the modification stage may have resulted in variable internal friction within the wasting material, producing variable accelerations. Additionally, these heterogeneities may have created asymmetries in the crater shape, generating different downhill accelerating components ($g_V \sin(\alpha)$ varies). Nevertheless, all measured accelerations are below Vesta's gravitational acceleration of 0.25 ± 0.03 m/s^2 and therefore agree with expected values of masses moving under the influence of gravity.

Most accelerating sections (eight out of twelve sections) indicate that the mass motion was accelerated more than physically possible on the *current slope*. Their accelerations exceed the acceleration of a friction-free sliding object on the that slope. The slope on which they occurred must therefore have been steeper in order to produce such accelerations. This conclusion also independently arises from the theory of crater modification [*Ivanov and Melosh*, 2013] which states that the transient crater was deeper than the final crater, resulting in steeper slopes (Section 3.1.7). The remaining four accelerating sections for which the acceleration was below the frictionless sliding acceleration may have been produced on the current, or a steeper, slope. Consequently, the mass motion is likely to have taken place on steeper crater walls during the modification stage of Rheasilvia. The current slopes were produced by subsequent mass wasting covering the original trajectories. The original curved structure must therefore be in the regolith-covered subsurface.

However, it is not possible to predict how much steeper the slopes were because the ratio $a/g_V \sin(\alpha)$ is unknown, as is how it might change with distance from Rheasilvia's centre. As mentioned above, it is likely that the

Table 8.1.: Minimum slopes ($\alpha_{\min}$) calculated from the accelerating sections (Equations 8.1 and 8.2) whose measured acceleration (a) exceeds the acceleration of a friction-free sliding object ($g_V \sin(\alpha)$) on the current slope (α) in Region 1. P is the position of the accelerating sections within the Rheasilvia basin.

Curve	P [km]	α [°]	a [$\cdot 10^{-3}$ m/s^2]	$g_V \sin(\alpha)$ [$\cdot 10^{-3}$ m/s^2]	$\alpha_{\min}$ [°]
5	155	0.9	22.1 ±3.5	3.9 ±0.5	5.1 ±1.0
8	166	2.7	15.4 ±1.7	11.8 ±1.4	3.5 ±0.6
9	192	1.1	97.8 ±11.3	4.9 ±0.6	23.0 ±4.0
10	182	9.2	42.7 ±5.6	4.2 ±0.5	9.8 ±1.8
11	207	8.7	176.3 ±20.4	37.9 ±4.6	44.8 ±9.5
12	173	1.2	51.6 ±4.0	5.1 ±0.6	11.9 ±1.7
16	175	12.3	152.8 ±16.4	53.1 ±6.4	37.7 ±7.1
16	228	0.9	29.5 ±2.6	3.9 ±0.5	6.8 ±1.0

mass motion generating the curved structures occurred towards the end of the modification stage. Consequently, the slopes were possibly only slightly steeper than the observed ones today, although it cannot be excluded that locally the slopes may have been steeper at the end of the modification stage due to slumping or rim collapse [*Melosh*, 1989].

Table 8.1 lists the minimum slopes $\alpha_{\min}$ derived from the measured accelerations of Region 1. The minimum slope is given by the smallest slope necessary to produce the measured acceleration a, under Vesta's gravity g_V:

$$\alpha_{\min} = \arcsin\left(\frac{a}{g_V}\right). \tag{8.1}$$

The error (in radians) derives from standard error propagation, where Δ

indicates the absolute error of a value:

$$\Delta\alpha_{\min} = \frac{1}{\sqrt{g_V^2 - a^2}} \sqrt{\Delta a^2 + \left(\frac{a}{g_V}\Delta g_V\right)^2}. \tag{8.2}$$

Most accelerations (five out of eight) correspond to minimum slopes ranging between 3.5° and 11.9°, which are similar to the slopes observed today (0.9° to 12.3°).

However, some measured accelerations hint at much larger slopes at the time of the curved ridge formation. The measured acceleration of Curve 11 requires a minimum slope of 44.8° in order to be smaller than the acceleration of a frictionless sliding object. Although such steep slopes are rare today, they were probably present during the modification stage [*Ivanov and Melosh*, 2013] and may have been preserved locally until the late modification stage. For example, slumping and rim collapse (Section 5.1) may have locally and temporarily generated scarps with steep slopes [*Melosh*, 1989] which were subsequently covered by the mass wasting associated with the curved ridges. Thus the previously described scattering of accelerations (Figure 8.1) may have been induced by the earlier spatial variation of slopes on the crater wall.

Sections of decelerating mass motion indicate that the gravitational pull was exceeded by basal or internal friction, slowing the mass motion. A reduction in acoustic energy introduced by the thinning of the wasting avalanche, possibly towards the end of the modification stage, or the end of mass motion near the crater floor can cause such an increase in friction [*Collins and Melosh*, 2003]. It is expected that the masses slow down when reaching the basin floor and subsequently lose their acoustically fluidised low friction behaviour. Supporting this, the decelerating sections are mainly observed between 120 km and 200 km from Rheasilvia's centre (Figure 8.1) and cluster closer towards the centre compared to the accelerating (∼140–230 km) and constant velocity sections (∼160–230 km). Again this observation is in agreement with mass motion behaviour on the crater wall.

The debris of an avalanche is expected to pile up when masses start to decelerate. This creates a pile of material covering the slope. Indeed, with the exception of Curves 8 and 9, which are modified by mass wasting and impact craters, all decelerating sections of Region 1 show a step in the slope where the decelerating section begins. In the topography plots, this appears as accumulated material on top of the predominant slope (Figure 7.4(b)).

Furthermore, the sections of constant velocity are present on topographical plateaus and show sections of decelerating velocity shortly before reaching the plateau (Figure 7(a)). It is possible that the plateau was deposited by

the moving masses when reaching a constant velocity or that the plateau pre-existed and caused the decrease in velocity and subsequent constant velocity, agreeing with the expected relation between mass motion and topography.

The presence of such topographic features indicates that the mass motion occurred towards the end of the modification stage, because further large scale subsequent mass wasting in the modification stage would have covered these features.

The presented characteristics of the curved ridges in Region 1 including the velocity range, the increase and decrease of velocities along the curved ridges, the distribution of accelerations, the predicted crater shape with steeper slopes and the agreement of decelerations and topography strongly indicate that the curved ridges are correctly interpreted as having been formed by the effect of the Coriolis force on moving masses. The extent of the curved ridges and the presence of mass wasting associated topographic features hints at the formation of the curved ridges towards the end of the modification stage. Additionally, the accelerations exceeding the friction-free sliding acceleration support the theory that the slope on which particular mass motions occurred must have been steeper and spatially variable.

8.2. Region 2: The Rheasilvia and Veneneia Intersection

The average positive velocity obtained for the eleven curved ridges associated with Region 2 (31.0 ± 25.3 m/s, Table B.4) agrees well with the numerically simulated characteristic mass-wasting velocity of ∼50 m/s of the Rheasilvia modification stage [*Jutzi et al.*, 2013]. The constant mass-wasting velocities observed on Curves 20 and 24 (22.5–45.8 m/s, Table 7.6) also agree with the simulated value and the simulated value lies within the range of velocities of the separate curved ridges. These observations are all in agreement that the Coriolis force produced the curved ridges in Region 2.

As with Region 1, it is expected that masses moving down the crater wall first accelerate due to gravity and subsequently decelerate when reaching the basin floor, where the slopes flatten and friction becomes dominant. Although the curved ridges' velocity distributions in Region 2 are generally more undulating compared to those of Region 1, the velocity profiles show an overall velocity increase from low values near the crater rim and velocity decreases towards the basin floor. This is shown by the blue to green to blue colour trend in Figure 7.6. Outliers from this trend may be explained by alterations of the curved ridges after their formation, such as impact cratering or mass wasting. The Coriolis model therefore successfully describes the

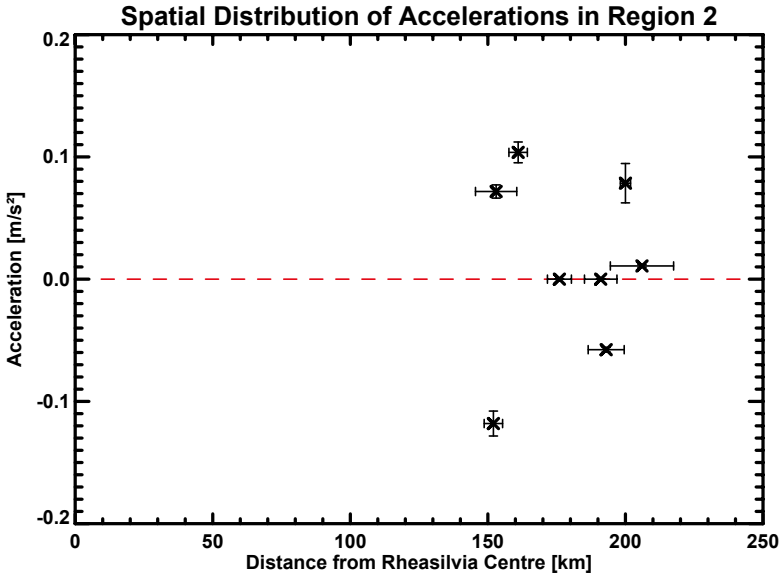

Figure 8.2.: The spatial distribution of accelerations derived for Region 2. The red dashed line indicates zero acceleration. Values above, below and on this line are accelerating, decelerating and moving with constant velocity, respectively. The bars on the distance describe the distance over which the acceleration, deceleration or velocity was constant (Δd) while the error bars on the acceleration illustrate the 1-σ uncertainty of the measurement.

expected dynamics of the curved ridges.

As explained in the previous section, the mass wasting must have occurred towards the end of the modification stage. Curved structures produced earlier in the modification stage were overrun by subsequent mass wasting of the later phase. Seven out of the eleven curved ridges of Region 2 originate near the crater rim of the current basin beyond 200 km from Rheasilvia's centre, as would be expected. Earlier in the modification stage the basin had not yet grown to this size, which would make a detection of curved ridges at the given locations impossible.

As with Region 1, Region 2 shows constant acceleration, deceleration and constant velocity sections along the curved ridges (Figure 8.2). The area near the central peak should not show such smooth trends, because the motion of merging masses from the central peak and crater wall result in an converging of material. In agreement, constant sections are only observed between 150 km and 220 km from Rheasilvia's centre on the crater wall (Figure 8.2).

Table 8.2.: Minimum slopes (α_{min}) calculated from the accelerating sections (Equations 8.1 and 8.2) whose measured acceleration (a) exceeds the acceleration of a friction-free sliding object ($g_V \sin(\alpha)$) on the current slope (α) in Region 2. P is the position of the accelerating sections within the Rheasilvia basin.

Curve	P [km]	α [°]	a [$\cdot 10^{-3}$ m/s^2]	$g_V \sin(\alpha)$ [$\cdot 10^{-3}$ m/s^2]	α_{min} [°]
19	200	13.8	78.5 ±16.1	59.6 ±7.1	18.3 ±4.5
22	153	9.7	71.7 ±5.4	42.2 ±5.1	16.7 ±2.4
24	161	11.0	103.7 ±8.5	47.6 ±5.7	24.5 ±3.8

Eight sections for which the acceleration, deceleration or velocity was constant were measured in Region 2 (Figure 8.2). The scattering of the values between ±0.13 m/s^2 can be explained by impact cratering or mass wasting which altered the curved ridges after their formation. Heterogeneities within the wasting material may also have caused variations in internal friction, resulting in different accelerations and asymmetries in the distribution of slopes at the formation stage of the curved ridges. These variations in slope would have generated variations in the downhill accelerating component of gravity ($g_V \sin(\alpha)$).

All measured accelerations are below that due to Vesta's surface gravity and it is therefore possible that the mass motion was driven by gravity. However, three out of four accelerating sections indicate that the current slope is not representative of the slope on which the masses moved during the modification stage, because the measured accelerations exceed the acceleration of a frictionless sliding object on the current slope.

The greater than friction-free sliding acceleration can only be explained if the slopes on which the masses moved during the modification stage were steeper than at present, resulting in larger downhill accelerations ($g_V \sin(\alpha)$). As previously mentioned, this requirement agrees with crater formation theory, which predicts steeper slopes during the modification stage [*Melosh*, 1989]. Assuming that the measured accelerations occurred frictionless, the minimum slopes (Equation 8.1) at the time of the mass motion must have varied between 16.7° and 24.5° (Table 8.2). These slopes are reasonable for

Rheasilvia towards the end of the modification stage [*Ivanov and Melosh*, 2013].

Region 2 exhibits two sections of decelerating mass motion suitable for analysis. As explained above, a decelerating debris avalanche will deform and pile up as a consequence of volume conservation. Just such, deposits were detected on top of both predominant slopes where the decelerations were measured (Figure 7.4(b)). Furthermore, the sections of constant velocity are associated with plateaus in the topography plots and a decrease in velocity shortly before reaching the plateaus. It is possible that the masses spread over the plateaus at constant velocities as a consequence of the change to flatter slopes or that the plateaus were deposited by the constantly moving masses. Thus the expected relation between mass motion and topography is evident in the velocity measurements and indicates a relatively late formation time in the modification stage as otherwise subsequent mass wasting would have covered these topographic features.

Region 2 is characterised by the intersection of the large basins Rheasilvia and Venenia (Section 2.4.3, Figure 2.11). Section 5.3 explains how curved structures may have been produced by the relaxation of Rheasilvia: the underlying Venenia basin may have reduced the brittle-ductile thickness ratio which may have generated spiral strike-slip faults [*Allemand and Thomas*, 1999]. However, the observations derived with the Coriolis model including the range of velocities, the increase and decrease of velocities along the motion, the distribution of accelerations, the predicted steeper crater walls and the agreement of decelerating mass motions with the topographic deposits strongly indicate that the curved ridges were formed by the Coriolis Effect. Furthermore, *Allemand and Thomas* [1999] predict the formation of the spiral strike-slip faults beyond the crater rim, however, the curved ridges do not expand beyond the crater rim. Consequently, the Coriolis Effect is found to be the preferred model for forming the curved ridges in Region 2.

8.3. Region 3: The Central Peak

Region 3 contains the five curved ridges on the central peak. The average negative velocity of all curved ridges (-21.6 ± 16.2 m/s, Table B.4) as well as the section of constant velocity measured within Curve 30 (-8.9 ± 1.2 m/s, Table 7.8) agree, within the order of magnitude, with an characteristic mass-wasting velocity of the modification stage (∼50 m/s) independently derived by *Jutzi et al.* [2013]. With exception of Curve 32 whose minimum value is -33.3 m/s (Table B.3), the range of velocities includes this simulated value.

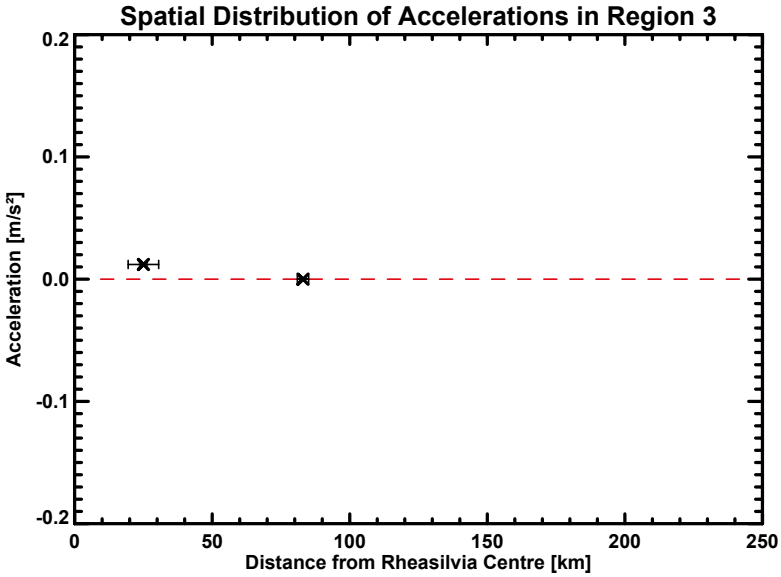

Figure 8.3.: The spatial distribution of accelerations derived for Region 3. The red dashed line indicates zero acceleration. Values above and on this line are accelerating and moving with constant velocity, respectively. The bars on the distance describe the distance over which the acceleration, deceleration or velocity was constant (Δd) while the error bars on the acceleration illustrate the 1-σ uncertainty of the measurement.

Although the measured velocities occupy the lower end of the simulated velocities, the general agreement still supports the theory that the Coriolis Effect has influenced the curved ridges.

As in Regions 1 and 2, an expected increase and decrease in velocity, generated by the initial acceleration of the mass motion on the central peak and final deceleration near the crater floor, is evident along most curved ridges in Region 3 (four out of five). Figure 7.7 illustrates this as the green to blue to green colour change towards the basin floor. This observation shows that the Coriolis model used to derive the velocities reproduces the expected dynamics, indicating that the curved ridges were deflected by the Coriolis Effect.

The masses merging at the crater floor (between roughly 90 km and 120 km) from the central peak and crater wall are expected to have prevented any smooth velocity trends near this location. Indeed, the trends observed within Region 3 extend to at most 90 km from Rheasilvia's centre at the foot of the central peak (Figure 8.3). The part of the curved ridges extending into the

crater floor area do not show any smooth trends.

Unlike the crater walls, the slope of the central peak does not necessarily have to be steeper during the modification stage. The peak starts rising at the end of the excavation stage and settles into a stable form towards the end of the modification stage [*Osinski et al.*, 2011]. Although a rebound of Rheasilvia's central peak is possible, it has not been reported in the literature.

The acceleration found in Region 3 (Figure 8.3) is not only below Vesta's surface gravity, but it is also below the acceleration of an object sliding frictionless on the current slope. It is therefore possible that the slope of the central peak when the mass motion occurred was similar to the current slope. However, in contrast to Regions 1 and 2, a constraint on the formation time of the curved ridges in Region 3 cannot be derived from this observation. Instead, with only one constantly accelerating and one constant velocity section within Region 3, definite conclusions about the central peak formation are not possible.

The measured section of constant velocity is associated with a topographical plateau and a decrease in velocity is evident before reaching constant velocity. It is possible that the plateau was deposited or that it produced the constant velocity when the masses decelerated from moving downhill, agreeing with the expected relation between mass motion and topography.

Section 5.3 describes the effect of an oblique impact on the fracture and fault pattern of the central peak. *Scherler et al.* [2006] found that an oblique impact can cause bent imbrication structures similar to the curved ridges on Rheasilvia's central peak. However, the best indication of an oblique impact is the asymmetric ejecta distribution, which for Rheasilvia, may be related to an oblique impact but might also be caused by the compositionally heterogeneous target [*Schenk et al.*, 2012]. The velocities, the gradual increase and decrease of velocities towards the basin floor, as well as the distribution and magnitude of the accelerations strongly support the Coriolis force explanation for the curved ridges in Region 3 which is therefore the most applicable explanation for having generated the curved ridges. Nevertheless, the small number of curved ridges and measurements make it difficult to reach definite conclusions.

8.4. Material Properties

The mass motion of the three regions can adequately be described by the Coriolis model. Therefore the measured sections of acceleration, deceleration and constant velocity can be used to provide insight into the material properties of the wasting debris, including effective viscosities and effective

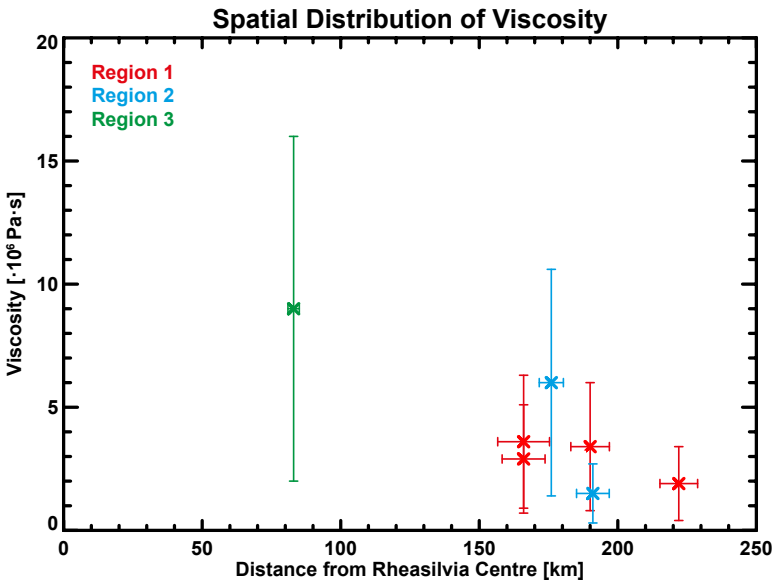

Figure 8.4.: The distribution of the effective viscosities along the extent of the Rheasilvia basin. The current crater floor covers the area between roughly 90 km and 120 km. The bars on the distance describe the distance over which the section was constant in velocity (Δd) while the error bars on the viscosity illustrate the 1-σ uncertainty of the measurement.

coefficients of friction (Section 7.4). The following paragraphs will discuss the derived properties with respect to the region in which they occur and the trend from which they derive.

8.4.1. Viscosity

The viscosity could be derived for seven sections of constant velocity (Table 7.9). All viscosities (1.5–9.0·10^6 Pa·s, comparable to basaltic lava flows [*Moore*, 1987]) agree with the estimates of acoustically fluidised material of 10^5–10^7 Pa·s [*Melosh*, 1986, 1979]) and agree within their errors. They are consistent with a constant viscosity of ∼2–3·10^6 Pa·s (Figure 8.4). The scatter in the calculated viscosities hints that variable conditions of acoustic fluidisation occurred within the Rheasilvia basin, generating fluctuations in the material properties. The large error bars are mainly introduced by uncertainties in debris density and flow thickness (Equation 7.1).

As discussed in Sections 8.1 and 8.2, the current slopes of Regions 1 and 2 are most probably shallower than the slopes on which the motion actually

occurred. Because the viscosity is proportional to $\sin(\alpha)$, this implies that the calculated viscosities are underestimated. The average measured current slopes of constant velocity sections in Regions 1 and 2 are 4.5° and 5.7°, respectively. The 'minimum' slopes derived from the comparison of the measured constant acceleration and the frictionless acceleration are 17.8° and 19.8° for Regions 1 and 2, respectively (Tables 8.1 and 8.2). Using the minimum slopes to calculate the viscosities with Equation 3.6, the viscosities would be larger by a factor of ∼4 and ∼3 in Regions 1 and 2, respectively (from $\sin(\alpha_{\min})/\sin(\alpha)$). Nevertheless, even with this correction, the viscosities agree with the expected range for acoustically fluidised material [*Melosh*, 1986, 1979].

8.4.2. Coefficient of Friction

In addition to the viscosity, the effective coefficients of friction were derived in the three regions for constantly accelerating, decelerating and constant velocity sections.

Coefficients of friction for dry material range between roughly 0.47 and 1.5 [*De Blasio*, 2011]. Vesta's surface rocks may be appropriately approximated as basalt (Section 2.4.2), with a coefficient of friction of ∼1.19 [*De Blasio*, 2011]. The dynamically derived coefficients of friction of constantly accelerating sections (0.088 ± 0.076) and constant velocity sections (0.084 ± 0.039) are well below these values (Tables 7.9 and 7.10). However, the mechanisms involved in the crater modification stage, e.g. acoustic fluidisation, temporarily reduce the effective coefficient of friction by an order of magnitude or more [*Collins and Melosh*, 2003; *Hsü*, 1975]. Thus, the coefficients of friction derived from the constantly accelerating sections and sections of constant velocity and their local slopes are in agreement with values derived from large acoustically fluidised landslides [*Legros*, 2002].

The coefficients of friction derived from the sections of constant deceleration (0.369 ± 0.192) are generally larger, which is as expected because a deceleration implies greater friction. The coefficients of friction approach the lower values of dry material (Table 7.11). This may hint at a smaller degree of acoustic fluidisation in sections where a deceleration was measured, possibly induced by heterogeneities within the energy density and involved material.

Figure 8.5 illustrates the distribution of the effective coefficients of friction with distance from Rheasilvia's centre for the three regions. The vertical scatter in the plot is probably related to spatially variable material properties induced by regolith heterogeneities or different degrees of acoustic fluidisation

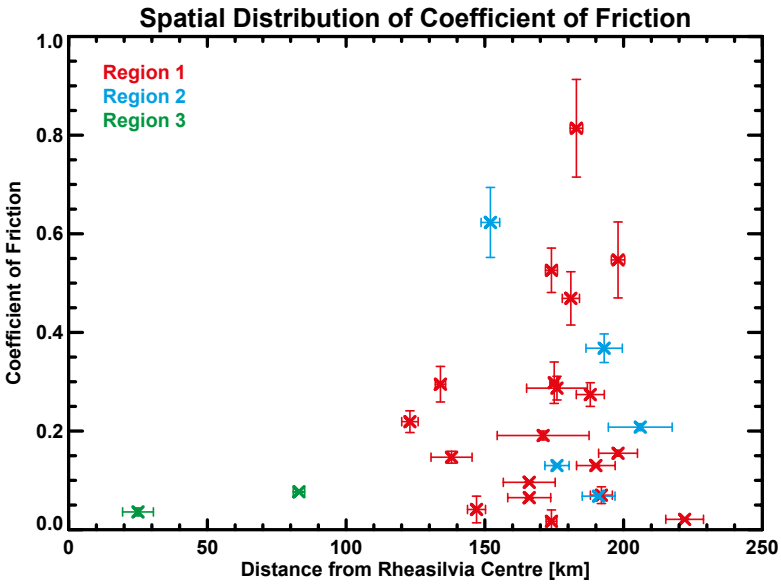

Figure 8.5.: The distribution of the effective coefficients of friction along the extent of the Rheasilvia basin. The current crater floor covers the area between roughly 90 km and 120 km. The bars on the distance describe the distance over which the section was constant in acceleration, deceleration or velocity (Δd) while the error bars on the coefficients of friction show the 1-σ uncertainty of the measurement.

[*Collins and Melosh*, 2003; *Melosh*, 1986]. Additionally, later mass wasting and impact cratering may have locally influenced the curvature and slopes, resulting in a wider range of coefficients of friction.

Alternatively, the variation of the effective coefficients of friction within the basin may be explained by self-sustaining acoustic fluidisation of the wasting material as observed in Struzstroms [*Collins and Melosh*, 2003]. The motion of the wasting material itself induces an acoustic energy field. This field may add to the acoustic energy embedded by the impact event and may further reduce the coefficient of friction when propagating downhill. Self-sustaining acoustic fluidisation is dependent on the volume of the wasting material and may therefore be more or less effective depending on the size of the wasting avalanche [*Collins and Melosh*, 2003; *Melosh*, 1986]. The local addition of such an acoustic energy field may contribute to a wider range of effective coefficients of friction.

The coefficients of friction in Regions 1 and 2 are similar (0.250 ± 0.208 and 0.279 ± 0.222, respectively), however Region 3 exhibits coefficients of friction

Table 8.3.: Comparison of dynamic measurements of the three geologically distinct regions within Rheasilvia.

Region	Acceleration Range [% of g_V]	Deceleration Range [$\cdot 10^{-3}$ m/s^2]	Constant Velocity Range [m/s]	Average Pos./Neg. Velocity [m/s]
1	4.2 – 70.5	-(14.8 – 181.0)	11.4 – 39.5	31.2 ± 26.8
2	4.3 – 41.5	-(57.7 – 118.1)	22.5 – 45.8	31.0 ± 25.3
3	4.8		-8.9	-21.6 ± 16.2

which are reduced by a factor of about 3 (0.082 ± 0.048). Note that this observation contradicts the higher viscosity found in Region 3 (Section 8.4.1). The low coefficients of friction also contradict the relatively small velocities in Region 3. However, the small number of measured coefficients of friction does not provide reliable statistics for Region 3. It may well be that the coefficients of friction are actually distributed in a similar manner to Regions 1 and 2 and agree with the measured velocities and viscosities in Region 3.

The effective coefficients of friction were derived on the current slopes. However, the earlier analysis suggests that steeper slopes in Regions 1 and 2 may have been present when the mass motion occurred. In general, the coefficients of friction determined with Equation 3.7 would be larger on steeper slopes, because the friction must compensate for the increased component of the gravitational acceleration downhill on the steeper slope. Consequently the derived coefficients of friction in Regions 1 and 2 represent the lower limit to the possible values.

8.5. Dynamical Comparison of the Regions

Regions 1 and 2 seem similar in terms of the dynamic properties such as the average velocity and the acceleration and deceleration of sections of the curved ridges (Table 8.3). Region 3, however, appears to differ.

For example, the magnitude of the average negative velocity in Region 3 is ∼70% less than the average positive velocities of Regions 1 and 2. The negative velocity in Region 3 is generated by the direction of motion away from the rotation axis. For comparison, the average positive velocities of Regions 1 and 2 vary by ∼1%. This observation is complemented by the relatively small value for the constant velocity section measured within Region 3. Here,

the magnitude of the constant velocity of 8.9 ±1.2 m/s is ∼19–78% of the velocities measured in Regions 1 and 2.

The range and distribution of accelerations in Regions 1 and 2 are relatively similar and reasonable for material moving under the influence of gravity. This may indicate similar conditions of acoustic fluidisation in Regions 1 and 2. The acceleration measured in Region 3 (4.8 m/s^2) is similar to the lowest values measured in Regions 1 and 2 (4.2 m/s^2 and 4.3 m/s^2, respectively).

The relatively large velocities and accelerations in Regions 1 and 2 may be explained by steeper slopes at the time of the mass wasting. The necessity for steeper slopes in Regions 1 and 2 is shown by the measurements of accelerations which exceed the acceleration of a friction-free sliding object on the current slope (Sections 7.1.1 and 7.2.1). In Region 3 the measured acceleration is 57% of the acceleration of a frictionless moving object and thus does not require a steeper slope (Sections 7.3.1). Hence, the larger gravitational component downhill in Regions 1 and 2 at the time of the mass wasting resulted in larger accelerations and velocities compared to Region 3, which may have had a similar slope to the current one.

With steeper slopes in Regions 1 and 2, the degree of acoustic fluidisation in all three regions is likely to have been similar when the mass motion occurred. This is supported by the similar viscosities in the three regions when considering the steeper slopes in Regions 1 and 2 (Section 8.4.1). Only the low coefficients of friction in Region 3 seem to contradict, however, the small number of measurements in Region 3 in combination with the large scatter of coefficients of friction in Regions 1 and 2 does not provide reliable statistics.

In Regions 1 and 2, some measured accelerations exceeded the acceleration of a friction-free sliding object. The measurements (Tables 8.1 and 8.2) show that the average minimum slopes of Region 1 (17.8° ± 15.8°) and Region 2 (19.8° ± 4.1°) are similar, but the scatter is much larger in Region 1. This may hint at the complex topography of a heterogeneous regolith layer before the Rheasilvia impact. Pre-existing target conditions may have resulted in an irregular rim collapse and a commensurate variation of slopes during Rheasilvia's modification stage in Region 1. In contrast, the creation of the underlying Veneneia basin in Region 2 may have smoothed the topography, thinned the regolith layer and loosened and created small regolith fragments, resulting in more homogeneous target properties. Thus, the subsequent Rheasilvia impact produced similar slopes during the modification stage in Region 2.

It is probable that the regolith in Region 2 is less consolidated compared to other regions within Rheaslivia because underlying Venenia loosened and

fragmented material prior to the Rheasilvia impact. This less consolidated regolith may explain the undulating velocity profiles in Region 2. Such material is more likely to be mobilized by seismic shaking of impact events after the curved ridges' formation and would therefore blur and alter the curved ridges, resulting in less smooth velocity distributions compared to areas with more consolidated regolith.

8.6. Comparision to Other Mass-Wasting Velocities

The mass wasting during the modification stage of the Rheasilvia impact can be compared to very large landslides which show similar mass-wasting behaviour to impact events [*Collins and Melosh*, 2003; *Melosh*, 1986]. In particular, so-called *sturzstroms* are described by acoustically fluidised debris and rock avalanches with extraordinary mobility and run-out lengths [*Collins and Melosh*, 2003].

In some cases it was possible to estimate the velocities of sturzstroms on Earth. For instance, *Jibson et al.* [2006] report mass-wasting velocities larger than 54 m/s triggered by the Denali Fault earthquake in 2002. The sturzstrom material consisted of a rock/ice mixture propagating ∼11 km on a glacial surface after a drop of ∼2 km. *Plafker et al.* [1971] reported a debris avalanche of rock, ice, snow and soil travelling 14.5 km after a drop of ∼3.5 km with an average wasting velocity of 80–90 m/s during the 1970 Peru earthquake. *Crosta et al.* [2001] estimate the general velocities of debris and rock avalanches to be 10–100 m/s.

Although these estimates are similar to the velocities of the Rheasilvia modification stage on Vesta derived in this work, they may result from different dynamics because of the different gravitational acceleration, the presence of an atmosphere, and water mixed within the avalanche body on Earth.

The much lower gravitational acceleration on Vesta reduces the potential energy of a mass by a factor of ∼40 compared to Earth. This is partly compensated by the higher drop heights on Vesta. For Rheasilvia, with a drop height $h = 19$ km, the approximate mass specific potential energy is $E_{\mathrm{pot}} = g_{\mathrm{V}} h = 5$ kJ/kg. For comparison, the Denali Fault drop of 2 km and the Peru avalanche drop of 3.5 km result in mass specific potential energies of ∼20 kJ/kg and ∼35 kJ/kg on Earth, respectively. However, the material properties of the avalanche will determine how much of the available energy is finally transferred into kinetic energy.

The measured mass-wasting velocities for the Rheasilvia modification stage,

the Denali Fault and the Peru earthquake avalanches are ∼30 m/s, ∼54 m/s and ∼85 m/s, respectively. These velocities result in kinetic energies per unit mass ($E_{\text{kin}} = \frac{1}{2}v^2$) of 0.5 kJ/kg, 1.5 kJ/kg and 3.6 kJ/kg, which are 10%, 8% and 10% of the maximal available potential energy of the Rheasilvia basin, the Denali Fault and the Peru earthquake avalanches, respectively. Although, this comparison is purely based on gravitational effects and does not consider any material differences, such as the presence of water as lubricant on Earth, the portions of potential energy transferred into kinetic energy for the three mass-wasting scenarios are in good agreement. This may mean that a common process, e.g. acoustic fluidisation, is involved, supporting the mobilization of the masses almost independently of the specific geologic conditions [*Collins and Melosh*, 2003].

9. Conclusions and Summary

9.1. Conclusions

Using the Coriolis model described in Chapter 6, it was possible to derive mass-wasting velocities during the Rheasilvia modification stage for 32 curved ridges distributed over three geologically distinct regions. These include the area between 270°E and 360°E (Region 1), the area where the Veneneia basin underlies Rheasilvia (Region 2) and the central peak (Region 3).

Based on the discussion in Chapter 8, the following scenario and conclusions of the Rheasilvia modification stage are supported by the Coriolis model:

1. Towards the end of the modification stage (approximately 30 minutes after impact [*Jutzi et al.*, 2013; *Ivanov and Melosh*, 2013]), downhill mass wasting was deflected by the Coriolis force, creating a curved pattern.

2. Masses wasted with a characteristic velocity of 29.6 ± 24.6 m/s. This velocity could be reached due to the temporarily reduction in internal friction by acoustic fluidisation. More precisely, the effective coefficients of friction were reduced to values ranging between 0.02 and 0.81 and the effective viscosities ranged between $1.9 \cdot 10^6$ Pa·s and $9.0 \cdot 10^6$ Pa·s.

   Region 1:
   The characteristic velocity was 31.2 ± 26.8 m/s.

   The pre-existing topography of a heterogeneous regolith layer induced the asymmetric rim collapse of temporarily steep slopes, on which the the mass-wasting material propagated.

   Region 2:
   The characteristic velocity was 31.0 ± 25.3 m/s.

   Mass wasting was influenced by the underlying Veneneia basin. The previous impact had smoothed the topography and homogenised the regolith layer, resulting in a similar distribution of slopes during the modification stage.

   Region 3:
   The characteristic velocity was 21.6 ± 16.2 m/s.

The mass motion occurred on probably similar slopes, compared to today's topography.

Regions 1 and 2:
The mass motion occurred on steeper crater walls, compared to today's topography.

Decelerating material on the crater wall, generated by a change in slope or friction, piled up and today appears as deposits on the predominant slope.

Regions 1, 2 and 3:
The moving masses accelerated due to Vesta's gravity near the crater rim and near the top of the central peak and decelerated when reaching the flatter slopes of the crater floor.

The wasting material from the central peak and crater wall merged at the foot of the central peak, where the convergence of masses prevented the formation of smooth velocity trends.

3. The mass wasting on Rheasilvia's wall and central peak attenuated at the end of the modification stage. Further alteration of the basin occurred in the form of mass wasting due to slope failure and impact cratering.

4. The isostatic adjustment of the giant basin to the equilibrium shape of Vesta stressed the crater shape. This stress was probably released along the curved pattern created by the Coriolis-deflected mass wasting of the modification stage. Subsequently the curved ridges were formed by regolith aligning with the Coriolis pattern.

9.2. Summary

This work investigates the formation process of the large south polar Rheasilvia basin on asteroid (4) Vesta. The Rheasilvia basin is a 500 km diameter impact basin whose centre nearly coincides with Vesta's rotation axis. This situation makes Rheasilvia unique in terms of the Coriolis Effect.

The Dawn spacecraft orbited Vesta in 2011 and 2012, providing image data of Vesta's surface at resolutions of up to 20 m/pixel. This data and a digital terrain model derived from stereo images (at resolution of ∼90 m/pixel) were used to investigate the Coriolis Effect on mass-wasting features related to the Rheailvia basin.

Most mass-wasting processes, such as slumping and landslides, are not visibly affected by the Coriolis force, primarily due to their small linear extents, however, on Vesta there are distinctive curved radial ridges within Rheasilvia which are probably representatives of the modification stage of the impact event when the Coriolis force deflected masses moving towards the basin floor.

A method to determine mass-wasting velocities along 32 prominent curved radial ridges within the Rheasilvia basin was developed. Located on Vesta's best fit ellipsoid, a set of inertial circles was fitted to each mapping point along a curved ridge. Using the inertial radii, the angular velocity of Vesta and the geodetic latitude of the mapping point, a set of mass-wasting velocities was inferred for each mapping point. Finally, the most commonly occurring velocity was determined with the help of a histogram and a velocity profile for each curved ridge was derived.

The curved ridges of three geologically distinct regions were analysed with this method. The regions are: the area between 270°E and 360°E (Region 1), the area where Rheasilvia and another large basin, Veneneia, intersect (Region 2) and the area of the central peak (Region 3). The average velocities in these regions are 31.2 ± 26.8 m/s (Region 1), 31.0 ± 25.3 m/s (Region 2) and 26.6 ± 16.2 m/s (Region 3).

Numerous aspects of the velocity profiles in the three regions support the theory that the Coriolis force caused the curved ridges. These include: the agreement of Coriolis-derived velocities with computer-based simulated mass-wasting velocities of ∼50 m/s, the increase and subsequent decrease of velocities along the curved ridges, the independent requirement of steeper crater walls during the modification stage, the absence of smooth velocity trends near the crater floor and the deposited material associated with decelerating velocity trends.

Some sections along the curved ridges showed constantly accelerating and decelerating velocities, as well as constant velocity. This behaviour enabled the determination of effective viscosities and coefficients of friction for the acoustically fluidised material during the Rheasilvia modification stage. The viscosities (derived from sections of constant velocity, the slope, and assumptions regarding the debris density and flow height) range between $1.9–9.0 \cdot 10^6$ Pa·s. Coefficients of friction (derived from the slope and sections of constant acceleration, deceleration and velocity) range between 0.017 and 0.814.

The geologically distinct regions show different behaviour during the modification stage. Regions 1 and 2 are similar in dynamic properties, however the mass motion must have occurred on steeper slopes compared to the cur-

rent topography. Mass wasting on the central peak exhibits lower velocities and accelerations which were probably caused by flatter slopes compared to Regions 1 and 2 at time of the mass wasting.

The Rheasilvia basin on Vesta provided a unique opportunity to investigate the dynamical and physical processes of the formation of large impact craters during the modification stage. In the case of Rheasilvia, the current morphology enabled the mass-wasting processes to be reconstructed based on the current structure of the curved ridges. A detailed geophysical analysis of these features yielded quantitative constraints on velocities, as well as on material properties and transport during and after the modification stage. This approach is unique, as no other methods have so far dynamically reconstructed an impact event purely based on observations. In addition, this thesis demonstrated for the first time that the Coriolis force can strongly affect the crater formation process on rapidly rotating objects.

References

Allemand, P. and Thomas, P. (1999). Small-Scale Models of Multiring Basins. *Journal of Geophysical Research: Planets*, 104(E7):16501–16514, doi:10.1029/1999JE900008.

Ammannito, E., De Sanctis, M. C., Capaccioni, F., Teresa Capria, M., Carraro, F., Combe, J.-P., Fonte, S., Frigeri, A., Joy, S. P., Longobardo, A., Magni, G., Marchi, S., McCord, T. B., McFadden, L. A., McSween, H. Y., Palomba, E., Pieters, C. M., Polanskey, C. A., Raymond, C. A., Sunshine, J. M., Tosi, F., Zambon, F., and Russell, C. T. (2013a). Vestan Lithologies Mapped by the Visual and Infrared Spectrometer on Dawn. *Meteoritics and Planetary Science*, 48(11):2185–2198, doi:10.1111/maps.12192.

Ammannito, E., De Sanctis, M. C., Palomba, E., Longobardo, A., Mittlefehldt, D. W., McSween, H. Y., Marchi, S., Capria, M. T., Capaccioni, F., Frigeri, A., Pieters, C. M., Ruesch, O., Tosi, F., Zambon, F., Carraro, F., Fonte, S., Hiesinger, H., Magni, G., McFadden, L. A., Raymond, C. A., Russell, C. T., and Sunshine, J. M. (2013b). Olivine in an Unexpected Location on Vesta's Surface. *Nature*, 504(7478):122–125, doi:10.1038/nature12665.

Archinal, B. A., Acton, C. H., A'Hearn, M. F., Conrad, A., Consolmagno, G. J., Duxbury, T., Hestroffer, D., Hilton, J. L., Jorda, L., Kirk, R., Klioner, S., McCarthy, D., Meech, K., Oberst, J., Ping, J., Seidelmann, P. K., Tholen, D. J., Thomas, P. C., and Williams, I. P. (2013). Recommended Coordinate System for (4) Vesta. *The IAU Working Group on Cartographic Coordinates and Rotational Elements (WGCCRE)*. http://astrogeology.usgs.gov/groups/IAU-WGCCRE.

Binzel, R. P. and Xu, S. (1993). Chips off of Asteroid 4 Vesta – Evidence for the Parent Body of Basaltic Achondrite Meteorites. *Science*, 260(5105):186–191, doi:10.1126/science.260.5105.186.

Bottke, W. F., Nolan, M. C., Greenberg, R., and Kolvoord, R. A. (1994). Velocity Distributions among Colliding Asteroids. *Icarus*, 107(2):255–268, doi:10.1006/icar.1994.1021.

Bottke, W. F., Rubincam, D. P., and Burns, J. A. (2000). Dynamical Evolution of Main Belt Meteoroids: Numerical Simulations Incorporating Planetary Perturbations and Yarkovsky Thermal Forces. *Icarus*, 145(2):301–331, doi:10.1006/icar.2000.6361.

Bottke, W. F., Vokrouhlicky, D., Rubincam, D. P., and Broz, M. (2002). The Effect of Yarkovsky Thermal Forces on the Dynamical Evolution of Asteroids and Meteoroids. In Bottke, W. F., Cellino, A., Paolicchi, P., and Binzel, R. P., editors, *Asteroids III*, pages 395–408. The University of Arizona Press, Tucson, AZ, USA, ISBN 978-0-8165-2281-1.

Bowling, T. J., Johnson, B. C., Melosh, H. J., Ivanov, B. A., O'Brien, D. P., Gaskell, R., and Marchi, S. (2013). Antipodal Terrains Created by the Rheasilvia Basin Forming Impact on Asteroid 4 Vesta. *Journal of Geophysical Research: Planets*, 118(9):1821–1834, doi:10.1002/jgre.20123.

Breiter, S., Rożek, A., and Vokrouhlický, D. (2012). Stress Field and Spin Axis Relaxation for Inelastic Triaxial Ellipsoids. *Monthly Notices of the Royal Astronomical Society*, 427(1):755–769, doi:10.1111/j.1365-2966.2012.21970.x.

Britt, D. T., Colsolmagno, B. G., and Lebofsky, L. (2007). Main-Belt Asteroids. In McFadden, L.-A., Weissmann, P. R., and Johnson, T. V., editors, *Encyclopedia of the Solar System*, pages 349–364. Elsevier, London, UK, ISBN 978-0-1208-8589-3.

Britt, D. T., Yeomans, D., Housen, K., and Consolmagno, G. (2002). Asteroid Density, Porosity, and Structure. In Bottke, W. F., Cellino, A., Paolicchi, P., and Binzel, R. P., editors, *Asteroids III*, pages 485–500. The University of Arizona Press, Tucson, AZ, USA, ISBN 978-0-8165-2281-1.

Buczkowski, D. L., Wyrick, D. Y., Iyer, K. A., Kahn, E. G., Scully, J. E. C., Nathues, A., Gaskell, R. W., Roatsch, T., Preusker, F., Schenk, P. M., Le Corre, L., Reddy, V., Yingst, R. A., Mest, S., Williams, D. A., Garry, W. B., Barnouin, O. S., Jaumann, R., Raymond, C. A., and Russell, C. T. (2012). Large-Scale Troughs on Vesta: A Signature of Planetary Tectonics. *Geophysical Research Letters*, 39(L18205):1–6, doi:10.1029/2012GL052959.

Buczkowski, D. L., Wyrick, D. Y., Toplis, M., Yingst, R. A., Williams, D. A., Garry, W. B., Mest, S., Kneissl, T., Scully, J. E. C., Nathues, A., De Sanctis, M. C., LeCorre, L., Reddy, V., Hoffmann, M., Ammannito,

E., Frigeri, A., Tosi, F., Preusker, F., Roatsch, T., Raymond, C. A., Jaumann, R., Pieters, C. M., and Russell, C. T. (2014). The Unique Geomorphology and Physical Properties of the Vestalia Terra Plateau. *Icarus*, 244:89–103, doi:10.1016/j.icarus.2014.03.035.

Burbine, T. H., Buchanan, P. C., Binzel, R. P., Bus, S. J., Hiroi, T., Hinrichs, J. L., Meibom, A., and Mccoy, T. J. (2001). Vesta, Vestoids, and the Howardite, Eeucrite, Diogenite Group: Relationships and the Origin of Spectral Differences. *Meteoritics and Planetary Science*, 36(6):761–781, doi:10.1111/j.1945-5100.2001.tb01915.x.

Burns, J. A., Safronov, V. S., and Gold, T. (1973). Asteroid Nutation Angles. *Monthly Notices of the Royal Astronomical Society*, 165(4):403–411, doi:10.1093/mnras/165.4.403.

Bus, S. J. and Binzel, R. P. (2002a). Phase II of the Small Main-Belt Asteroid Spectroscopic Survey: A Feature-Based Taxonomy. *Icarus*, 158(1):146–177, doi:10.1006/icar.2002.6856.

Bus, S. J. and Binzel, R. P. (2002b). Phase II of the Small Main-Belt Asteroid Spectroscopic Survey: The Observations. *Icarus*, 158(1):106–145, doi:10.1006/icar.2002.6857.

Bus, S. J., Vilas, F., and Barucci, M. A. (2002). Visible-Wavelength Spectroscopy of Asteroids. In Bottke, W. F., Cellino, A., Paolicchi, P., and Binzel, R. P., editors, *Asteroids III*, pages 169–182. The University of Arizona Press, Tucson, AZ, USA, ISBN 978-0-8165-2281-1.

Collins, G. S. and Melosh, H. J. (2003). Acoustic Fluidization and the Extraordinary Mobility of Sturzstroms. *Journal of Geophysical Research: Solid Earth*, 108(B10):1–14, doi:10.1029/2003JB002465.

Coradini, A., Turrini, D., Federico, C., and Magni, G. (2011). Vesta and Ceres: Crossing the History of the Solar System. *Space Science Reviews*, 163(1-4):25–40, doi:10.1007/s11214-011-9792-x.

Crosta, G., Calvetti, F., Imposimato, S., Rodeman, D., Fratini, P., and Agliardi, F. (2001). Granular Flows and Numerical Modelling of Landslides. Technical Report EVG1 - CT-1999-00007, DAMOCLES Project.

Cruikshank, D. P., Tholen, D. J., Hartmann, W. K., Bell, J. F., and Brown, R. H. (1991). Three Basaltic Earth-Approaching Asteroids and the

Source of the Basaltic Meteorites. *Icarus*, 89(1):1–13, doi:10.1016/0019-1035(91)90083-6.

De Blasio, F. V. (2011). *Introduction to the Physics of Landslides: Lecture Notes on the Dynamics of Mass Wasting*. Springer, Dordrecht, Heidelberg, London, New York, ISBN 978-9-4007-1122-8.

De Sanctis, M. C., Ammannito, E., Buczkowski, D., Raymond, C. A., Jaumann, R., Mittlefehldt, D. W., Capaccioni, F., Capria, M. T., Frigeri, A., Magni, G., Tosi, F., Zambon, F., and Russell, C. T. (2014). Compositional Evidence of Magmatic Activity on Vesta. *Geophysical Research Letters*, 41(9):3038–s3044, doi:10.1002/2014GL059646.

De Sanctis, M. C., Ammannito, E., Capria, M. T., Capaccioni, F., Combe, J.-P., Frigeri, A., Longobardo, A., Magni, G., Marchi, S., McCord, T. B., Palomba, E., Tosi, F., Zambon, F., Carraro, F., Fonte, S., Li, Y. J., McFadden, L. A., Mittlefehldt, D. W., Pieters, C. M., Jaumann, R., Stephan, K., Raymond, C. A., and Russell, C. T. (2013). Vesta's Mineralogical Composition as Revealed by the Visible and Infrared Spectrometer on Dawn. *Meteoritics and Planetary Science*, 48(11):2166–2184, doi:10.1111/maps.12138.

De Sanctis, M. C., Ammannito, E., Capria, M. T., Tosi, F., Capaccioni, F., Zambon, F., Carraro, F., Fonte, S., Frigeri, A., Jaumann, R., Magni, G., Marchi, S., McCord, T. B., McFadden, L. A., McSween, H. Y., Mittlefehldt, D. W., Nathues, A., Palomba, E., Pieters, C. M., Raymond, C. A., Russell, C. T., Toplis, M. J., and Turrini, D. (2012). Spectroscopic Characterization of Mineralogy and Its Diversity Across Vesta. *Science*, 336(6082):697–700, doi:10.1126/science.1219270.

De Sanctis, M. C., Coradini, A., Ammannito, E., Filacchione, G., Capria, M. T., Fonte, S., Magni, G., Barbis, A., Bini, A., Dami, M., Ficai-Veltroni, I., and Preti, G. (2010). The VIR Spectrometer. *Space Science Reviews*, 163(1-4):329–369, doi:10.1007/s11214-010-9668-5.

Dence, M. R., Grieve, R. A. F., and Robertson, P. B. (1977). Terrestrial Impact Structures: Principal Characteristics and Energy Considerations. In Roddy, D. J., Pepin, R. O., and Merrill, R. B., editors, *Impact and Explosion Cratering*, pages 247–275. Pergamon Press, New York, NY, USA, ISBN 978-0-0802-2050-5.

Denevi, B. W., Blewett, D. T., Buczkowski, D. L., Capaccioni, F., Capria, M. T., De Sanctis, M. C., Garry, W. B., Gaskell, R. W., Le Corre, L., Li, J.-Y., Marchi, S., McCoy, T. J., Nathues, A., O'Brien, D. P., Petro, N. E., Pieters, C. M., Preusker, F., Raymond, C. A., Reddy, V., Russell, C. T., Schenk, P., Scully, J. E. C., Sunshine, J. M., Tosi, F., Williams, D. A., and Wyrick, D. (2012). Pitted Terrain on Vesta and Implications for the Presence of Volatiles. *Science*, 338(6104):246–249, doi:10.1126/science.1225374.

Duke, M. B. and Silver, L. T. (1967). Petrology of Eucrites, Howardites and Mesosiderites. *Geochimica et Cosmochimica Acta*, 31(10):1637–1665, doi:10.1016/0016-7037(67)90112-3.

Durran, D. R. (1993). Is the Coriolis Force Really Responsible for the Inertial Oscillation? *Bulletin of the American Meteorological Society*, 74(11):2179–2184, doi:10.1175/1520-0477(1993)074<2179:ITCFRR>2.0.CO;2.

Efroimsky, M. (2001). Relaxation of Wobbling Asteroids and Comets - Theoretical Problems, Perspectives of Experimental Observation. *Planetary and Space Science*, 49(9):937–955, doi:10.1016/S0032-0633(01)00051-4.

Efroimsky, M. and Lazarian, A. (2000). Inelastic Dissipation in Wobbling Asteroids and Comets. *Monthly Notices of the Royal Astronomical Society*, 311(2):269–278, doi:10.1046/j.1365-8711.2000.03036.x.

Elbeshausen, D., Wünnemann, K., and Collins, G. S. (2009). Scaling of Oblique Impacts in Frictional Targets: Implications for Crater Size and Formation Mechanisms. *Icarus*, 204(2):716–731, doi:10.1016/j.icarus.2009.07.018.

Ermakov, A. I., Zuber, M. T., Smith, D. E., Raymond, C. A., Balmino, G., Fu, R. R., and Ivanov, B. A. (2014). Constraints on vesta's interior structure using gravity and shape models from the dawn mission. *Icarus*, 240:146–160, doi:10.1016/j.icarus.2014.05.015.

ESRI (2010). ArcMap 10.0. Environmental Systems Resource Institute, Redlands, CA, USA, http://www.esri.com.

Etling, D. (2008). *Theoretische Meteorologie: Eine Einführung*. Springer, Berlin, Heidelberg, New York, 3. edition, ISBN 978-3-5407-5978-2.

Farinella, P., Paolicchi, P., and Zappalà, V. (1982). The Asteroids as Outcomes of Catastrophic Collisions. *Icarus*, 52(3):409–433, doi:10.1016/0019-1035(82)90003-3.

Feierberg, M. A., Larson, H. P., and Chapman, C. R. (1982). Spectroscopic Evidence for Undifferentiated S-Type Asteroids. *Astrophysical Journal*, 257:361–372, doi:10.1086/159995.

Foderà Serio, G., Manara, A., and Sicoli, P. (2002). Giuseppe Piazzi and the Discovery of Ceres. In Bottke, W. F., Cellino, A., Paolicchi, P., and Binzel, R. P., editors, *Asteroids III*, pages 17–24. The University of Arizona Press, Tucson, AZ, USA, ISBN 978-0-8165-2281-1.

French, B. M. (1998). *Traces of Catastrophe: A Handbook of Shock-Metamorphic Effects in Terrestrial Meteorite Impact Structures*. LPI Contribution No. 954, Lunar and Planetary Institute, Houston, TX, USA.

Fu, R. R., Hager, B. H., Ermakov, A. I., and Zuber, M. T. (2014). Efficient Early Global Relaxation of Asteroid Vesta. *Icarus*, 240:133–145, doi:10.1016/j.icarus.2014.01.023.

Fujiwara, A., Kawaguchi, J., Yeomans, D. K., Abe, M., Mukai, T., Okada, T., Saito, J., Yano, H., Yoshikawa, M., Scheeres, D. J., Barnouin-Jha, O., Cheng, A. F., Demura, H., Gaskell, R. W., Hirata, N., Ikeda, H., Kominato, T., Miyamoto, H., Nakamura, A. M., Nakamura, R., Sasaki, S., and Uesugi, K. (2006). The Rubble-Pile Asteroid Itokawa as Observed by Hayabusa. *Science*, 312(5778):1330–1334, doi:10.1126/science.1125841.

Fujiwara, A. and Tsukamoto, A. (1981). Rotation of Fragments in Catastrophic Impact. *Icarus*, 48(2):329–334, doi:10.1016/0019-1035(81)90113-5.

Garlick, M. A. (1888). *The Asteroids, or Minor Planets Between Mars and Jupiter*. J. B. Lippincott Company, Philadelphia, PA, USA.

Garlick, M. A. (2003). *The Story of the Solar System*. Cambridge University Press, Cambridge, UK, ISBN 978-0-5218-0336-6.

Gault, D. E., Quaide, W. L., and Oberbeck, V. R. (1974). Impact Cratering Mechanics and Structures. In Greeley, R. and Schultz, P. H., editors, *A Primer in Lunar Geology*, pages 177–189.

Gomes, R., Levison, H. F., Tsiganis, K., and Morbidelli, A. (2005). Origin of the Cataclysmic Late Heavy Bombardment Period of the Terrestrial Planets. *Nature*, 435(7041):466–469, doi:10.1038/nature03676.

Gradie, J. and Tedesco, E. (1982). Compositional Structure of the Asteroid Belt. *Science*, 216(4553):1405–1407, doi:10.1126/science.216.4553.1405.

Gundlach, B. and Blum, J. (2013). A New Method to Determine the Grain Size of Planetary Regolith. *Icarus*, 223(1):479–492, doi:10.1016/j.icarus.2012.11.039.

Gwinner, K., Scholten, F., Preusker, F., Elgner, S., Roatsch, T., Spiegel, M., Schmidt, R., Oberst, J., Jaumann, R., and Heipke, C. (2010). Topography of mars from global mapping by hrsc high-resolution digital terrain models and orthoimages: Characteristics and performance. *Earth and Planetary Science Letters*, 294(3-4):506–519, doi:10.1016/j.epsl.2009.11.007.

Gwinner, K., Scholten, F., Spiegel, M., Schmidt, R., Giese, B., Oberst, J., Heipke, C., Jaumann, R., and Neukum, G. (2009). Derivation and Validation of High-Resolution Digital Terrain Models from Mars Express HRSC Data. *Photogrammetric Engineering and Remote Sensing*, 75(9):1127–1142.

Henych, T. and Pravec, P. (2013). Asteroid Rotation Excitation by Subcatastrophic Impacts. *Monthly Notices of the Royal Astronomical Society*, 432(2):1623–1631, doi:10.1093/mnras/stt581.

Hiroi, T., Pieters, C. M., and Takeda, H. (1994). Grain Size of the Surface Regolith of Asteroid 4 Vesta Estimated From Its Reflectance Spectrum in Comparison with HED Meteorites. *Meteoritics and Planetary Science*, 29(3):394–396, doi:10.1111/j.1945-5100.1994.tb00603.x.

Hsü, K. J. (1975). Catastrophic Debris Streams (Sturzstroms) Generated by Rockfalls. *Geological Society of America Bulletin*, 86(1):129–140, doi:10.1130/0016-7606(1975)86<129:CDSSGB>2.0.CO;2.

IDL (2012). IDL 8.2. Exelis Visual Information Solutions, Boulder, CO, USA, http://www.exelisvis.com.

Ivanov, B. A. and Melosh, H. J. (2013). Two-Dimensional Numerical Modeling of the Rheasilvia Impact Formation. *Journal of Geophysical Research: Planets*, 118(7):1545–1557, doi:10.1002/jgre.20108.

Iverson, R. M. (1997). The Physics of Debris Flows. *Reviews of Geophysics*, 35(3):245–296, doi:10.1029/97RG00426.

Jaumann, R., Nass, A., Otto, K., Krohn, K., Stephan, K., McCord, T. B., Williams, D. A., Raymond, C. A., Blewett, D. T., Hiesinger, H., Yingst, R. A., De Sanctis, M. C., Palomba, E., Roatsch, T., Matz, K. D., Preusker, F., Scholten, F., and Russell, C. T. (2014). The Geological Nature of Dark Material on Vesta and Implications for the Subsurface Structure. *Icarus*, 240:3–19, doi:10.1016/j.icarus.2014.04.035.

Jaumann, R., Williams, D. A., Buczkowski, D. L., Yingst, R. A., Preusker, F., Hiesinger, H., Schmedemann, N., Kneissl, T., Vincent, J. B., Blewett, D. T., Buratti, B. J., Carsenty, U., Denevi, B. W., De Sanctis, M. C., Garry, W. B., Keller, H. U., Kersten, E., Krohn, K., Li, J.-Y., Marchi, S., Matz, K. D., McCord, T. B., McSween, H. Y., Mest, S. C., Mittlefehldt, D. W., Mottola, S., Nathues, A., Neukum, G., O'Brien, D. P., Pieters, C. M., Prettyman, T. H., Raymond, C. A., Roatsch, T., Russell, C. T., Schenk, P., Schmidt, B. E., Scholten, F., Stephan, K., Sykes, M. V., Tricarico, P., Wagner, R., Zuber, M. T., and Sierks, H. (2012). Vesta's Shape and Morphology. *Science*, 336(6082):687–690, doi:10.1126/science.1219122.

Jibson, R. W., Harp, E. L., Schulz, W., and Keefer, D. K. (2006). Large Rock Avalanches Triggered by the M 7.9 Denali Fault, Alaska, Earthquake of 3 November 2002. *Engineering Geology*, 83(1-3):144–160, doi:10.1016/j.enggeo.2005.06.029.

Jutzi, M., Asphaug, E., Gillet, P., Barrat, J.-A., and Benz, W. (2013). The Structure of the Asteroid 4 Vesta as Revealed by Models of Planet-Scale Collisions. *Nature*, 494(7436):207–210, doi:10.1038/nature11892.

Keil, K. (2002). Geological History of Asteroid 4 Vesta: The "Smallest Terrestrial Planet". In Bottke, W. F., Cellino, A., Paolicchi, P., and Binzel, R. P., editors, *Asteroids III*, pages 573–584. The University of Arizona Press, Tucson, AZ, USA, ISBN 978-0-8165-2281-1.

Keller, L. P. and McKay, D. S. (1997). The Nature and Origin of Rims on Lunar Soil Grains. *Geochimica et Cosmochimica Acta*, 61(11):2331–2341, doi:10.1016/S0016-7037(97)00085-9.

Kenkmann, T. (2002). Folding within Seconds. *Geology*, 30(3):231–234, doi:10.1130/0091-7613(2002)030<0231:FWS>2.0.CO;2.

Kenkmann, T., Collins, G. S., and Wünnemann, K. (2013). The Modification Stage of Crater Formation. In *Impact Cratering: Processes and Products*, pages 60–75. John Wiley and Sons, Chichester, UK, ISBN 978-1-4051-9829-5.

Kenkmann, T. and Dalwigk, I. (2000). Radial Transpression Ridges: A New Structural Feature of Complex Impact Craters. *Meteoritics and Planetary Science*, 35(6):1189–1201, doi:10.1111/j.1945-5100.2000.tb01508.x.

Kleinhans, M. G., Markies, H., Vet, S. J. d., Veld, A. C. i. t., and Postema, F. N. (2011). Static and Dynamic Angles of Repose in Loose Granular Materials under Reduced Gravity. *Journal of Geophysical Research*, 116(E11004):1–13, doi:10.1029/2011JE003865.

Knauss, J. A. (1997). *Introduction to Physical Oceanography*. Prentice-Hall, Inc., Upper Saddle River, NJ, USA, ISBN 978-0-1323-8155-0.

Komarov, M. M. and Sazanov, V. V. (1994). Light Pressure Forces and Torques Exerted on an Asteroid of Arbitrary Shape. *Solar System Research*, 28:16–23.

Konopliv, A., Asmar, S., Park, R., Bills, B., Centinello, F., Chamberlin, A., Ermakov, A., Gaskell, R., Rambaux, N., Raymond, C., Russell, C., Smith, D., Tricarico, P., and Zuber, M. (2014). The Vesta Gravity Field, Spin Pole and Rotation Period, Landmark Positions, and Ephemeris from the Dawn Tracking and Optical Data. *Icarus*, 240:103–117, doi:10.1016/j.icarus.2013.09.005.

Konopliv, A. S., Asmar, S. W., Bills, B. G., Mastrodemos, N., Park, R. S., Raymond, C. A., Smith, D. E., and Zuber, M. T. (2011). The Dawn Gravity Investigation at Vesta and Ceres. *Space Science Reviews*, 163(1–4):461–486, doi:10.1007/s11214-011-9794-8.

Krasinsky, G. A., Pitjeva, E. V., Vasilyev, M. V., and Yagudina, E. I. (2002). Hidden Mass in the Asteroid Belt. *Icarus*, 158(1):98–105, doi:10.1006/icar.2002.6837.

Krohn, K., Jaumann, R., Elbeshausen, D., Kneissl, T., Schmedemann, N., Wagner, R., Voigt, J., Otto, K., Matz, K. D., Preusker, F., Roatsch, T., Stephan, K., Raymond, C. A., and Russell, C. T. (2014a). Asymmetric Craters on Vesta: Impact on Sloping Surfaces. *Planetary and Space Science*, doi:10.1016/j.pss.2014.04.011.

Krohn, K., Jaumann, R., Otto, K., Hoogenboom, T., Wagner, R., Buczkowski, D. L., Garry, B., Williams, D. A., Yingst, R. A., Scully, J., De Sanctis, M. C., Kneissl, T., Schmedemann, N., Kersten, E., Stephan, K., Matz, K. D., Pieters, C. M., Preusker, F., Roatsch, T., Schenk, P., Russell, C. T., and Raymond, C. A. (2014b). Mass Movement on Vesta at Steep Scarps and Crater Rims. *Icarus*, 244:120–132, doi:10.1016/j.icarus.2014.03.013.

Küppers, M., O'Rourke, L., Bockelée-Morvan, D., Zakharov, V., Lee, S., von Allmen, P., Carry, B., Teyssier, D., Marston, A., Müller, T., Crovisier, J., Barucci, M. A., and Moreno, R. (2014). Localized Sources of Water Vapour on the Dwarf Planet (1) Ceres. *Nature*, 505(7484):525–527, doi:10.1038/nature12918.

Legros, F. (2002). The Mobility of Long-Runout Landslides. *Engineering Geology*, 63(3-4):301–331, doi:10.1016/S0013-7952(01)00090-4.

Li, J.-Y. (2012). Body-Fixed Coordinate Systems for Asteroid (4) Vesta. sbn.psi.edu/archive/dawn/fc/DWNVFC2_1A/DOCUMENT/VESTA_COORDINATES/VESTA_COORDINATES_120918.PDF.

Li, J.-Y., Le Corre, L., Schröder, S. E., Reddy, V., Denevi, B. W., Buratti, B. J., Mottola, S., Hoffmann, M., Gutierrez-Marques, P., Nathues, A., Russell, C. T., and Raymond, C. A. (2013). Global Photometric Properties of Asteroid (4) Vesta Observed with Dawn Framing Camera. *Icarus*, 226(2):1252–1274, doi:10.1016/j.icarus.2013.08.011.

Li, J.-Y., Mittlefehldt, D. W., Pieters, C. M., De Sanctis, M. C., Schröder, S. E., Hiesinger, H., Blewett, D. T., Russell, C. T., Raymond, C. A., and Keller, H. U. (2012). Investigating the Origin of Bright Materials on Vesta: Synthesis, Conclusions, and Implications. *43th Lunar and Planetary Science Conference*, The Woodlands, TX, USA, #2381.

Lucas, A., Mangeney, A., and Ampuero, J. P. (2014). Frictional Velocity-Weakening in Landslides on Earth and on Other Planetary Bodies. *Nature Communications*, 5, doi:10.1038/ncomms4417.

McCord, T. B., Adams, J. B., and Johnson, T. V. (1970). Asteroid Vesta: Spectral Reflectivity and Compositional Implications. *Science*, 168(3938):1445–1447, doi:10.1126/science.168.3938.1445.

McCord, T. B., Li, J.-Y., Combe, J.-P., McSween, H. Y., Jaumann, R., Reddy, V., Tosi, F., Williams, D. A., Blewett, D. T., Turrini, D., Palomba, E.,

Pieters, C. M., Sanctis, M. C. D., Ammannito, E., Capria, M. T., Corre, L. L., Longobardo, A., Nathues, A., Mittlefehldt, D. W., Schröder, S. E., Hiesinger, H., Beck, A. W., Capaccioni, F., Carsenty, U., Keller, H. U., Denevi, B. W., Sunshine, J. M., Raymond, C. A., and Russell, C. T. (2012). Dark Material on Vesta from the Infall of Carbonaceous Volatile-Rich Material. *Nature*, 491(7422):83–86, doi:10.1038/nature11561.

McCoy, T. J., Mittlefehldt, D. W., and Wilson, L. (2006). Asteroid Differentiation. In Lauretta, D. S. and McSween, H. Y., editors, *Meteorites and the Early Solar System II*, pages 733–745. The University of Arizona Press, Tucson, AZ, USA, ISBN 978-0-8165-2562-1.

McKinnon, W. B. (1978). An Investigation Into the Role of Plastic Failure in Crater Modification. In *Lunar and Planetary Science Conference Proceedings*, volume 9, pages 3965–3973.

McSween, H. Y., Ammannito, E., Reddy, V., Prettyman, T. H., Beck, A. W., Cristina De Sanctis, M., Nathues, A., Corre, L. L., O'Brien, D. P., Yamashita, N., McCoy, T. J., Mittlefehldt, D. W., Toplis, M. J., Schenk, P., Palomba, E., Turrini, D., Tosi, F., Zambon, F., Longobardo, A., Capaccioni, F., Raymond, C. A., and Russell, C. T. (2013a). Composition of the Rheasilvia Basin, a Window into Vesta's Interior. *Journal of Geophysical Research: Planets*, 118(2):335–346, doi:10.1002/jgre.20057.

McSween, H. Y., Binzel, R. P., De Sanctis, M. C., Ammannito, E., Prettyman, T. H., Beck, A. W., Reddy, V., Le Corre, L., Gaffey, M. J., McCord, T. B., Raymond, C. A., Russell, C. T., and the Dawn Science Team (2013b). Dawn; the Vesta–HED Connection; and the Geologic Context for Eucrites, Diogenites, and Howardites. *Meteoritics and Planetary Science*, 48(11):2090–2104, doi:10.1111/maps.12108.

McSween, H. Y., Ghosh, A., Grimm, R. E., Wilson, L., and Young, E. D. (2002). Thermal Evolution Models of Asteroids. In Bottke, W. F., Cellino, A., Paolicchi, P., and Binzel, R. P., editors, *Asteroids III*, pages 559–571. The University of Arizona Press, Tucson, AZ, USA, ISBN 978-0-8165-2281-1.

McSween, H. Y., Mittlefehldt, D. W., Beck, A. W., Mayne, R. G., and McCoy, T. J. (2011). HED Meteorites and Their Relationship to the Geology of Vesta and the Dawn Mission. *Space Science Reviews*, 163(1-4):141–174, doi:10.1007/s11214-010-9637-z.

Melosh, H. J. (1979). Acoustic Fluidization: A New Geologic Process? *Journal of Geophysical Research: Solid Earth*, 84(B13):7513–7520, doi:10.1029/JB084iB13p07513.

Melosh, H. J. (1984). Impact Ejection, Spallation, and the Origin of Meteorites. *Icarus*, 59(2):234–260, doi:10.1016/0019-1035(84)90026-5.

Melosh, H. J. (1986). The Physics of Very Large Landslides. *Acta mechanica*, 64(1):89–99.

Melosh, H. J. (1989). *Impact Cratering: A Geologic Process*. Oxford University Press, New York, NY, USA, ISBN 978-0-1951-0463-9.

Melosh, H. J. (2013). The Contact and Compression Stage of Impact Cratering. In *Impact Cratering: Processes and Products*, pages 32–42. John Wiley and Sons, Chichester, UK, ISBN 978-1-4051-9829-5.

Melosh, H. J. and Ivanov, B. A. (1999). Impact Crater Collapse. *Annual Review of Earth and Planetary Sciences*, 27(1):385–415, doi:10.1146/annurev.earth.27.1.385.

Michel, P., Benz, W., Tanga, P., and Richardson, D. C. (2001). Collisions and Gravitational Reaccumulation: Forming Asteroid Families and Satellites. *Science*, 294(5547):1696–1700, doi:10.1126/science.1065189.

Migliorini, F., Morbidelli, A., Zappalà, V., Gladman, B. J., Bailey, M. E., and Cellino, A. (1997). Vesta Fragments from v6 and 3:1 Resonances: Implications for V-type Near-Earth Asteroids and Howardite, Eucrite and Diogenite Meteorites. *Meteoritics and Planetary Science*, 32(6):903–916, doi:10.1111/j.1945-5100.1997.tb01580.x.

Minton, D. A. and Malhotra, R. (2010). Dynamical Erosion of the Asteroid Belt and Implications for Large Impacts in the Inner Solar System. *Icarus*, 207(2):744–757, doi:10.1016/j.icarus.2009.12.008.

Mittlefehldt, D. W., Li, J.-Y., Pieters, C. M., De Sanctis, M. C., Schröder, S. E., Hiesinger, H., Blewett, D. T., Russell, C. T., Raymond, C. A., and Yingst, R. A. (2012). Types and Distribution of Bright Materials on 4 Vesta. *43th Lunar and Planetary Science Conference*, The Woodlands, TX, USA, #1680.

Moore, H. J. (1987). The 1984 Mauna Loa Eruption and Planetary Geology. Reports of Planetary Geology and Geophysics Program 19870014048, U.S. Geological Survey, Menlo Park, CA, USA.

Morbidelli, A., Levison, H. F., Tsiganis, K., and Gomes, R. (2005). Chaotic Capture of Jupiter's Trojan Asteroids in the Early Solar System. *Nature*, 435(7041):462–465, doi:10.1038/nature03540.

Morbidelli, A., Marchi, S., Bottke, W. F., and Kring, D. A. (2012). A Sawtooth-Like Timeline for the First Billion Years of Lunar Bombardment. *Earth and Planetary Science Letters*, 355–356:144–151, doi:10.1016/j.epsl.2012.07.037.

Neukum, G. (1984). Meteorite Bombardment and Dating of Planetary Surfaces. Dissertation on attaining Venia Legendi. Report Number: NASA-TM-77558, Translation into English of "Meteoritenbombardement und Datierung Planetarer Oberflächen" Munich, Feb. 1983, pages 1–186.

Neukum, G., Ivanov, B. A., and Hartmann, W. K. (2001). Cratering Records in the Inner Solar System in Relation to the Lunar Reference System. *Space Science Reviews*, 96(1-4):55–86, doi:10.1023/A:1011989004263.

Noguchi, T., Nakamura, T., Kimura, M., Zolensky, M. E., Tanaka, M., Hashimoto, T., Konno, M., Nakato, A., Ogami, T., Fujimura, A., Abe, M., Yada, T., Mukai, T., Ueno, M., Okada, T., Shirai, K., Ishibashi, Y., and Okazaki, R. (2011). Incipient Space Weathering Observed on the Surface of Itokawa Dust Particles. *Science*, 333(6046):1121–1125, doi:10.1126/science.1207794.

O'Brien, D. P., Marchi, S., Morbidelli, A., Bottke, W. F., Schenk, P. M., Russell, C. T., and Raymond, C. A. (2014). Constraining the Cratering Chronology of Vesta. *Planetary and Space Science*, 103:131–142, doi:10.1016/j.pss.2014.05.013.

O'Brien, D. P. and Sykes, M. V. (2011). The Origin and Evolution of the Asteroid Belt — Implications for Vesta and Ceres. *Space Science Reviews*, 163(1-4):41–61, doi:10.1007/s11214-011-9808-6.

Osinski, G. R. and Pierazzo, E. (2013). Impact Cratering: Processes and Products. In *Impact Cratering: Processes and Products*, pages 1–20. John Wiley and Sons, Chichester, UK, ISBN 978-1-4051-9829-5.

Osinski, G. R., Tornabene, L. L., and Grieve, R. A. F. (2011). Impact Ejecta Emplacement on Terrestrial Planets. *Earth and Planetary Science Letters*, 310(3-4):167–181, doi:10.1016/j.epsl.2011.08.012.

Otto, K. A., Jaumann, R., Krohn, K., Matz, K.-D., Preusker, F., Roatsch, T., Schenk, P., Scholten, F., Stephan, K., Raymond, C. A., and Russell, C. T. (2013). Mass-Wasting Features and Processes in Vesta's South Polar Basin Rheasilvia. *Journal of Geophysical Research: Planets*, 118(11):2279–2294, doi:10.1002/2013JE004333.

Paldor, N. and Sigalov, A. (2001). The Mechanics of Inertial Motion on the Earth and on a Rotating Sphere. *Physica D: Nonlinear Phenomena*, 160(1):29–53.

Paolicchi, P., Burns, J. A., and Weidenschilling, S. J. (2002). Side Effects of Collsions: Spin Rate Changes, Tumbling Rotation Rates, and Binary Asteroids. In Bottke, W. F., Cellino, A., Paolicchi, P., and Binzel, R. P., editors, *Asteroids III*, pages 517–526. The University of Arizona Press, Tucson, AZ, USA, ISBN 978-0-8165-2281-1.

Papaloizou, J. C. B., Nelson, R. P., Kley, W., Masset, F. S., and Artymowicz, P. (2006). Disk-Planet Interactions during Planet Formation. In Reipurth, B., Jewitt, D., and Keil, K., editors, *Protostars and Planets V*, pages 655–668. The University of Arizona Press, Tucson, AZ, USA, ISBN 978-0-8165-2654-3.

Perna, D., Kaňuchová, Z., Ieva, S., Fornasier, S., Barucci, M. A., Lantz, C., Dotto, E., and Strazzulla, G. (2015). Short-Term Variability on the Surface of (1) Ceres: A Changing Amount of Water Ice? *Astronomy and Astrophysics*, 575(L1):1–6, doi:10.1051/0004-6361/201425304.

Pierazzo, E. and Melosh, H. J. (2000). Understanding Oblique Impacts from Experiments, Observations, and Modeling. *Annual Review of Earth and Planetary Sciences*, 28(1):141–167, doi:10.1146/annurev.earth.28.1.141.

Pieters, C. M., Ammannito, E., Blewett, D. T., Denevi, B. W., De Sanctis, M. C., Gaffey, M. J., Le Corre, L., Li, J.-Y., Marchi, S., McCord, T. B., McFadden, L. A., Mittlefehldt, D. W., Nathues, A., Palmer, E., Reddy, V., Raymond, C. A., and Russell, C. T. (2012). Distinctive Space Weathering on Vesta from Regolith Mixing Processes. *Nature*, 491(7422):79–82, doi:10.1038/nature11534.

Plafker, G., Ericksen, G. E., and Concha, J. F. (1971). Geological Aspects of the May 31, 1970, Perú Earthquake. *Bulletin of the Seismological Society of America*, 61(3):543–578.

Pravec, P. and Harris, A. W. (2000). Fast and Slow Rotation of Asteroids. *Icarus*, 148(1):12–20, doi:10.1006/icar.2000.6482.

Pravec, P., Harris, A. W., and Michalowski, T. (2002). Asteroid Rotations. In Bottke, W. F., Cellino, A., Paolicchi, P., and Binzel, R. P., editors, *Asteroids III*, pages 113–122. The University of Arizona Press, Tucson, AZ, USA, ISBN 978-0-8165-2281-1.

Press, W. H., Teukolsky, S. A., Vetterling, W. T., and Flannery, B. P. (1992). *Numerical Recipes in C: The Art of Scientific Computing*. Cambridge University Press, Cambridge, NY, USA, 2nd edition, ISBN 978-0-5214-3108-8.

Prettyman, T. H., Feldman, W. C., McSween, H. Y., Dingler, R. D., Enemark, D. C., Patrick, D. E., Storms, S. A., Hendricks, J. S., Morgenthaler, J. P., Pitman, K. M., and Reedy, R. C. (2011). Dawn's Gamma Ray and Neutron Detector. *Space Science Reviews*, 163(1-4):371–459, doi:10.1007/s11214-011-9862-0.

Prettyman, T. H., Mittlefehldt, D. W., Yamashita, N., Lawrence, D. J., Beck, A. W., Feldman, W. C., McCoy, T. J., McSween, H. Y., Toplis, M. J., Titus, T. N., Tricarico, P., Reedy, R. C., Hendricks, J. S., Forni, O., Corre, L. L., Li, J.-Y., Mizzon, H., Reddy, V., Raymond, C. A., and Russell, C. T. (2012). Elemental Mapping by Dawn Reveals Exogenic H in Vesta's Regolith. *Science*, 338(6104):242–246, doi:10.1126/science.1225354.

Preusker, F., Scholten, F., Knollenberg, J., Kührt, E., Matz, K.-D., Mottola, S., Roatsch, T., and Thomas, N. (2012a). The Northern Hemisphere of Asteroid (21) Lutetia - Topography and Orthoimages from Rosetta OSIRIS NAC Image Data. *Planetary and Space Science*, 66(1):54–63, doi:10.1016/j.pss.2012.01.008.

Preusker, F., Scholten, F., Matz, K.-D., Roatsch, T., Jaumann, R., Raymond, C. A., and Russell, C. T. (2012b). Topography of Vesta from Dawn FC Stereo Images. *7th European Planetary Science Congress 2012*, Madrid, Spain, #EPSC2012-428-1.

R. Greeley and R.M. Batson, editors (1990). *Planetary Mapping*. Cambridge University Press, New York, USA, ISBN 978-0-5213-0774-1.

Rayman, M. D., Fraschetti, T. C., Raymond, C. A., and Russell, C. T. (2006). Dawn: A Mission in Development for Exploration of Main

Belt Asteroids Vesta and Ceres. *Acta Astronautica*, 58(11):605–616, doi:10.1016/j.actaastro.2006.01.014.

Raymond, C. A., Jaumann, R., Nathues, A., Sierks, H., Roatsch, T., Preusker, F., Scholten, F., Gaskell, R. W., Jorda, L., Keller, H.-U., Zuber, M. T., Smith, D. E., Mastrodemos, N., and Mottola, S. (2011). The Dawn Topography Investigation. *Space Science Reviews*, 163(1-4):487–510, doi:10.1007/s11214-011-9863-z.

Raymond, C. A., Park, R. S., Asmar, S. W., Konopliv, A. S., Buczkowski, D. L., De Sanctis, M. C., McSween, H. Y., Russell, C. T., Jaumann, R., and Preusker, F. (2013). Vestalia Terra: An Acient Mascon in the Southern Hemisphere of Vesta. *44th Lunar and Planetary Science Conference*, The Woodlands, TX, USA, #2882.

Reddy, V. (2011). Reddy Vesta Rotationally Resolved Near-Infrared Spectra V1.0. EAR-A-I0046-3-REDDYVESTA-V1.0. *NASA Planetary Data System*. http://sbn.psi.edu/pds/resource/reddyvesta.html.

Reddy, V., Le Corre, L., O'Brien, D. P., Nathues, A., Cloutis, E. A., Durda, D. D., Bottke, W. F., Bhatt, M. U., Nesvorny, D., Buczkowski, D., Scully, J. E., Palmer, E. M., Sierks, H., Mann, P. J., Becker, K. J., Beck, A. W., Mittlefehldt, D., Li, J.-Y., Gaskell, R., Russell, C. T., Gaffey, M. J., McSween, H. Y., McCord, T. B., Combe, J.-P., and Blewett, D. (2012a). Delivery of Dark Material to Vesta via Carbonaceous Chondritic Impacts. *Icarus*, 221(2):544–559, doi:10.1016/j.icarus.2012.08.011.

Reddy, V., Nathues, A., Le Corre, L., Sierks, H., Li, J.-Y., Gaskell, R., McCoy, T., Beck, A. W., Schroder, S. E., Pieters, C. M., Becker, K. J., Buratti, B. J., Denevi, B., Blewett, D. T., Christensen, U., Gaffey, M. J., Gutierrez-Marques, P., Hicks, M., Keller, H. U., Maue, T., Mottola, S., McFadden, L. A., McSween, H. Y., Mittlefehldt, D., O'Brien, D. P., Raymond, C., and Russell, C. (2012b). Color and Albedo Heterogeneity of Vesta from Dawn. *Science*, 336(6082):700–704, doi:10.1126/science.1219088.

Richardson, D. C., Leinhardt, Z. M., Melosh, H. J., Bottke, W. F., and Asphaug, E. (2002). Gravitational Aggregates: Evidence and Evolution. In Bottke, W. F., Cellino, A., Paolicchi, P., and Binzel, R. P., editors, *Asteroids III*, pages 501–515. The University of Arizona Press, Tucson, AZ, USA, ISBN 978-0-8165-2281-1.

Richardson, J. E., Melosh, H. J., and Greenberg, R. J. (2004). Impact-Induced Seismic Activity on Asteroid 433 Eros: A Surface Modification Process. *Science*, 306(5701):1526–1529, doi:10.1126/science.1104731.

Richardson, J., Melosh, H., Greenberg, R., and O'Brien, D. (2005). The Global Effects of Impact-Induced Seismic Activity on Fractured Asteroid Surface Morphology. *Icarus*, 179(2):325–349, doi:10.1016/j.icarus.2005.07.005.

Ripa, P. (1997). "Inertial" Oscillations and the β-Plane Approximation(s). *Journal of Physical Oceanography*, 27(5):633–647.

Roatsch, T., Kersten, E., Matz, K. D., Preusker, F., Scholten, F., Elgner, S., Jaumann, R., Raymond, C. A., and Russell, C. T. (2013). High-Resolution Vesta Low Altitude Mapping Orbit Atlas Derived from Dawn Framing Camera Images. *Planetary and Space Science*, 85:293–298, doi:10.1016/j.pss.2013.06.024.

Roatsch, T., Kersten, E., Matz, K.-D., Preusker, F., Scholten, F., Jaumann, R., Raymond, C., and Russell, C. (2012). High Resolution Vesta High Altitude Mapping Orbit (HAMO) Atlas Derived from Dawn Framing Camera Images. *Planetary and Space Science*, 73(1):283–286, doi:10.1016/j.pss.2012.08.021.

Rubincam, D. P. (2000). Radiative Spin-up and Spin-down of Small Asteroids. *Icarus*, 148(1):2–11, doi:10.1006/icar.2000.6485.

Ruesch, O., Hiesinger, H., Blewett, D. T., Williams, D. A., Buczkowski, D., Scully, J., Yingst, R. A., Roatsch, T., Preusker, F., Jaumann, R., Russell, C. T., and Raymond, C. A. (2014a). Geologic Map of the Northern Hemisphere of Vesta based on Dawn Framing Camera (FC) Images. *Icarus*, 244:41–59, doi:10.1016/j.icarus.2014.01.035.

Ruesch, O., Hiesinger, H., De Sanctis, M. C., Ammannito, E., Palomba, E., Longobardo, A., Zambon, F., Tosi, F., Capria, M. T., Capaccioni, F., Frigeri, A., Fonte, S., Magni, G., Raymond, C. A., and Russell, C. T. (2014b). Detections and Geologic Context of Local Enrichments in Olivine on Vesta with VIR/Dawn Data. *Journal of Geophysical Research: Planets*, 119(9):2078–2108, doi:10.1002/2014JE004625.

Russell, C. T., Coradini, A., Christensen, U., De Sanctis, M. C., Feldman, W. C., Jaumann, R., Keller, H. U., Konopliv, A. S., McCord, T. B., McFadden, L. A., McSween, H. Y., Mottola, S., Neukum, G., Pieters,

C. M., Prettyman, T. H., Raymond, C. A., Smith, D. E., Sykes, M. V., Williams, B. G., Wise, J., and Zuber, M. T. (2004). Dawn: A Journey in Space and Time. *Planetary and Space Science*, 52(5–6):465–489, doi:10.1016/j.pss.2003.06.013.

Russell, C. T. and Raymond, C. A. (2011). The Dawn Mission to Vesta and Ceres. *Space Science Reviews*, 163(1-4):3–23, doi:10.1007/s11214-011-9836-2.

Russell, C. T., Raymond, C. A., Coradini, A., McSween, H. Y., Zuber, M. T., Nathues, A., De Sanctis, M. C., Jaumann, R., Konopliv, A. S., Preusker, F., Asmar, S. W., Park, R. S., Gaskell, R., Keller, H. U., Mottola, S., Roatsch, T., Scully, J. E. C., Smith, D. E., Tricarico, P., Toplis, M. J., Christensen, U. R., Feldman, W. C., Lawrence, D. J., McCoy, T. J., Prettyman, T. H., Reedy, R. C., Sykes, M. E., and Titus, T. N. (2012). Dawn at Vesta: Testing the Protoplanetary Paradigm. *Science*, 336(6082):684–686, doi:10.1126/science.1219381.

Russell, C. T., Raymond, C. A., Jaumann, R., McSween, H. Y., De Sanctis, M. C., Nathues, A., Prettyman, T. H., Ammannito, E., Reddy, V., Preusker, F., O'Brien, D. P., Marchi, S., Denevi, B. W., Buczkowski, D. L., Pieters, C. M., McCord, T. B., Li, J.-Y., Mittlefehldt, D. W., Combe, J.-P., Williams, D. A., Hiesinger, H., Yingst, R. A., Polanskey, C. A., and Joy, S. P. (2013). Dawn Completes Its Mission at 4 Vesta. *Meteoritics and Planetary Science*, pages 1–14, doi:10.1111/maps.12091.

Russell, C. T., Raymond, C. A., Nathues, A., Gutierrez-Marquez, P., Sanctis, M. C. D., Ammannito, E., Prettyman, T. H., Konopliv, A., Park, R., McSween, H. Y., Jaumann, R., Joy, S., Polanskey, C. A., Rayman, M., and the Dawn Science Team (2015). Dawn Arrives at Ceres: Better than Hubble Resolution. *46th Lunar and Planetary Science Conference*, The Woodlands, TX, USA, #1131.

Sazonov, V. V. (1994). Motion of an Asteroid about its Center of Mass Due to Torque from Light Pressure. *Solar System Research*, 28:152–162.

Scheeres, D. J., Ostro, S. J., Werner, R. A., Asphaug, E., and Hudson, R. S. (2000). Effects of Gravitational Interactions on Asteroid Spin States. *Icarus*, 147(1):106–118, doi:10.1006/icar.2000.6443.

Schenk, P., O'Brien, D. P., Marchi, S., Gaskell, R., Preusker, F., Roatsch, T., Jaumann, R., Buczkowski, D., McCord, T., McSween, H. Y., Williams,

D., Yingst, A., Raymond, C., and Russell, C. (2012). The Geologically Recent Giant Impact Basins at Vesta's South Pole. *Science*, 336(6082):694–697, doi:10.1126/science.1223272.

Scherler, D., Kenkmann, T., and Jahn, A. (2006). Structural Record of an Oblique Impact. *Earth and Planetary Science Letters*, 248(1-2):43–53, doi:10.1016/j.epsl.2006.05.002.

Schmedemann, N., Kneissl, T., Ivanov, B. A., Michael, G. G., Wagner, R. J., Neukum, G., Ruesch, O., Hiesinger, H., Krohn, K., Roatsch, T., Preusker, F., Sierks, H., Jaumann, R., Reddy, V., Nathues, A., Walter, S. H. G., Neesemann, A., Raymond, C. A., and Russell, C. T. (2014). The Cratering Record, Chronology and Surface Ages of (4) Vesta in Comparison to Smaller Asteroids and the Ages of HED Meteorites. *Planetary and Space Science*, 103:104–130, doi:10.1016/j.pss.2014.04.004.

Schröder, S. E., Mottola, S., Keller, H. U., Raymond, C. A., and Russell, C. T. (2013). Resolved Photometry of Vesta Reveals Physical Properties of Crater Regolith. *Planetary and Space Science*, 85:198–213, doi:10.1016/j.pss.2013.06.009.

Scott, R. F. (1967). Viscous Flow of Craters. *Icarus*, 7(1-3):139–148, doi:10.1016/0019-1035(67)90058-9.

Sharma, I., Burns, J. A., and Hui, C.-Y. (2005). Nutational Damping Times in Solids of Revolution. *Monthly Notices of the Royal Astronomical Society*, 359(1):79–92, doi:10.1111/j.1365-2966.2005.08864.x.

Sierks, H., Keller, H. U., Jaumann, R., Michalik, H., Behnke, T., Bubenhagen, F., Büttner, I., Carsenty, U., Christensen, U., Enge, R., Fiethe, B., Gutiérrez Marqués, P., Hartwig, H., Krüger, H., Kühne, W., Maue, T., Mottola, S., Nathues, A., Reiche, K.-U., Richards, M. L., Roatsch, T., Schröder, S. E., Szemerey, I., and Tschentscher, M. (2011). The Dawn Framing Camera. *Space Science Reviews*, 163(1-4):263–327, doi:10.1007/s11214-011-9745-4.

Singer, K. N., McKinnon, W. B., Schenk, P. M., and Moore, J. M. (2012). Massive Ice Avalanches on Iapetus Mobilized by Friction Reduction during Flash Heating. *Nature Geoscience*, 5(8):574–578, doi:10.1038/ngeo1526.

Smith, M. J., Paron, P., and Griffiths, J. S., editors (2011). *Geomorphological Mapping Methods and Applications*. Developments in Earth Surface Processes, 15. Elsevier, Oxford, UK, ISBN 978-0-4445-3446-0.

Snyder, J. P. (1987). Map Projections - A Working Manual. Professional Paper 1395, U.S. Geological Survey, Washington, D.C., USA.

Stephan, K., Jaumann, R., De Sanctis, M. C., Tosi, F., Ammannito, E., Krohn, K., Zambon, F., Marchi, S., Ruesch, O., Matz, K.-D., Preusker, F., Roatsch, T., Raymond, C. A., and Russell, C. T. (2014). Small Fresh Impact Craters on Asteroid 4 Vesta: A Compositional and Geological Fingerprint. *Journal of Geophysical Research: Planets*, 119(4):771–797, doi:10.1002/2013JE004388.

Stesky, R. M., Brace, W. F., Riley, D. K., and Robin, P.-Y. F. (1974). Friction in Faulted Rock at High Temperature and Pressure. *Tectonophysics*, 23(1-2):177–203, doi:10.1016/0040-1951(74)90119-X.

Stickle, A. M., Schultz, P. H., and Crawford, D. A. (2015). Subsurface Failure in Spherical Bodies: A Formation Scenario for Linear Troughs on Vesta's Surface. *Icarus*, 247:18–34, doi:10.1016/j.icarus.2014.10.002.

Takagi, D. (2010). Spreading of Viscous Fluids and Granular Materials on Slopes. Dissertation at the University of Cambridge, UK. Jun. 2010, pages 1–149, http://www.repository.cam.ac.uk/handle/1810/228707.

Thomas, P. C., Binzel, R. P., Gaffey, M. J., Storrs, A. D., Wells, E. N., and Zellner, B. H. (1997a). Impact Excavation on Asteroid (4) Vesta: Hubble Space Telescope Results. *Science*, 277(5331):1492–1495, doi:10.1126/science.277.5331.1492.

Thomas, P. C., Binzel, R. P., Gaffey, M. J., Zellner, B. H., Storrs, A. D., and Wells, E. (1997b). Vesta: Spin Pole, Size, and Shape from HST Images. *Icarus*, 128(1):88–94, doi:10.1006/icar.1997.5736.

Titley, S. R. (1966). Seismic Energy as an Agent of Morphologic Modification on the Moon. Technical Report N67-31943, U.S. Geological Survey, Flagstaff, AZ, USA.

Tsiganis, K., Gomes, R., Morbidelli, A., and Levison, H. F. (2005). Origin of the Orbital Architecture of the Giant Planets of the Solar System. *Nature*, 435(7041):459–461, doi:10.1038/nature03539.

Turrini, D., Combe, J. P., McCord, T. B., Oklay, N., Vincent, J. B., Prettyman, T. H., McSween, H. Y., Consolmagno, G. J., De Sanctis, M. C., Le Corre, L., Longobardo, A., Palomba, E., and Russell, C. T. (2014).

The Contamination of the Surface of Vesta by Impacts and the Delivery of the Dark Material. *Icarus*, 240:86–102, doi:10.1016/j.icarus.2014.02.021.

Turrini, D., Magni, G., and Coradini, A. (2011). Probing the History of Solar System through the Cratering Records on Vesta and Ceres. *Monthly Notices of the Royal Astronomical Society*, 413(4):2439–2466, doi:10.1111/j.1365-2966.2011.18316.x.

Wasson, J. T. (2013). Vesta and Extensively Melted Asteroids: Why HED Meteorites Are Probably Not from Vesta. *Earth and Planetary Science Letters*, 381:138–146, doi:10.1016/j.epsl.2013.09.002.

Weidenschilling, S. J. (1977). The Distribution of Mass in the Planetary System and Solar Nebula. *Astrophysics and Space Science*, 51(1):153–158, doi:10.1007/BF00642464.

Williams, D. A., Denevi, B. W., Mittlefehldt, D. W., Mest, S. C., Schenk, P. M., Yingst, R. A., Buczkowski, D. L., Scully, J. E. C., Garry, W. B., McCord, T. B., Combe, J.-P., Jaumann, R., Pieters, C. M., Nathues, A., Le Corre, L., Hoffmann, M., Reddy, V., Schäfer, M., Roatsch, T., Preusker, F., Marchi, S., Kneissl, T., Schmedemann, N., Neukum, G., Hiesinger, H., De Sanctis, M. C., Ammannito, E., Frigeri, A., Prettyman, T. H., Russell, C. T., and Raymond, C. A. (2014). The Geology of the Marcia Quadrangle of Asteroid Vesta: Assessing the Effects of Large, Young Craters. *Icarus*, 244:74–88, doi:10.1016/j.icarus.2014.01.033.

Williams, D. A., O'Brien, D. P., Schenk, P. M., Denevi, B. W., Carsenty, U., Marchi, S., Scully, J. E., Jaumann, R., De Sanctis, M. C., Palomba, E., Ammannito, E., Longobardo, A., Magni, G., Frigeri, A., Russell, C. T., Raymond, C. A., and Davison, T. M. (2013). Lobate and Flow-Like Features on Asteroid Vesta. *Planetary and Space Science*, doi:10.1016/j.pss.2013.06.017.

Wilson, L. and Keil, K. (1996). Volcanic Eruptions and Intrusions on the Asteroid 4 Vesta. *Journal of Geophysical Research: Planets*, 101(E8):18927–18940, doi:10.1029/96JE01390.

Wünnemann, K., Collins, G. S., and Osinski, G. R. (2008). Numerical Modelling of Impact Melt Production in Porous Rocks. *Earth and Planetary Science Letters*, 269(3–4):530–539, doi:10.1016/j.epsl.2008.03.007.

Yingst, R. A., Mest, S. C., Berman, D. C., Garry, W. B., Williams, D. A., Buczkowski, D., Jaumann, R., Pieters, C. M., De Sanctis, M. C., Frigeri,

A., Le Corre, L., Preusker, F., Raymond, C. A., Reddy, V., Russell, C. T., Roatsch, T., and Schenk, P. M. (2014). Geologic Mapping of Vesta. *Planetary and Space Science*, in press, doi:10.1016/j.pss.2013.12.014.

Zambon, F., De Sanctis, M. C., Schröder, S., Tosi, F., Longobardo, A., Ammannito, E., Blewett, D. T., Mittlefehldt, D. W., Li, J.-Y., Palomba, E., Capaccioni, F., Frigeri, A., Capria, M. T., Fonte, S., Nathues, A., Pieters, C. M., Russell, C. T., and Raymond, C. A. (2014). Spectral Analysis of the Bright Materials on the Asteroid Vesta. *Icarus*, 240:73–85, doi:10.1016/j.icarus.2014.04.037.

Appendices

A. IDL-Code Samples

A.1. Calculating the Velocity

```
;+
; :Name:
;  anaysis_velocity
;
; :Description:
;    This function calculates the velocity of each
;    point of a curved ridge. It projects the
;    neighbouring points in the tangent plane of the
;    centred point, determines radius and velocity
;    for each neighbour distance and finds the most
;    common radius by sorting radii in a histogram.
;
; :Parameters:
;    threeD:   three dimensional array containing
;              the x, y and z-coordinates of each
;              mapping point on the reference
;              ellipsoid derived with latlonTo3D
;    lat_lon:  two dimensional array containing
;              geocentric latitude and longitude of
;              each mapping point
;    binsize:  binsze for statistical derivation of
;              velocity, e.g. 5 m/s
;
; :Returns:
;    dis_vel:  two dimensional array containing the
;              distance from Rheasilvia's centre and
;              the velocity of each mapping point
;-
FUNCTION Anaysis_Velocity, threeD, lat_lon, binsize
; Constants describing Vesta's shape and rotation
; recent              ; ancient
a = 223800.           ; a = 236770.
b = 281550.           ; b = 277620.
omega = 0.000327      ; omega = 0.000348
length      = n_elements(threeD)/3-1
vel_distrib = 0.
```

```
vel_err     = 0.
velocity    = 0.
; Looping through all mapping points of a curved
   ridge
FOR i=1, length-1 DO BEGIN
    if i LT length/2. THEN pairs=i $
       ELSE pairs=length-i
    velocity=[0.]
; Looping through all neighbouring point pairs
    FOR j=1, pairs, increment DO BEGIN
        prev_point = threeD[*,i-j]
        post_point = threeD[*,i+j]
; Normal vector at threeD[*,i]
        norm_vec = [threeD[0,i]/b^2, $
                    threeD[1,i]/b^2, $
                    threeD[2,i]/a^2]
; Projecting the neighbouting point pair in the
   tangential plane
        prev_point_proj = prev_point -            $
           (((transpose(prev_point - threeD[*,i]) $
           # norm_vec) / (transpose(norm_vec)     $
           # norm_vec)) # norm_vec)
        post_point_proj = post_point -            $
           (((transpose(post_point - threeD[*,i]) $
           # norm_vec) / (transpose(norm_vec)     $
           # norm_vec)) # norm_vec)
; Reduce points to 2D with threeD[*,i]=[0,0],
   prev_point=[rPrev,0] and post_point=[xPost,yPost]
; Distance between prev_point_proj and threeD[*,i]
        rPrev = float(norm(prev_point_proj $
           - threeD[*,i]))
; Distance between post_point_proj and threeD[*,i]
        rPost = float(norm(post_point_proj $
           - threeD[*,i]))
; Testing direction of curvature
        dir_x = (transpose(prev_point_proj - $
           threeD[*,i]) # (post_point_proj - $
           threeD[*,i]) / (rprev*rpost))[0]
        dir_y = (transpose(norm_vec) #      $
           (crossp((prev_point_proj -       $
```

```
            threeD[*,i]), (post_point_proj - $
            threeD[*,i]) / (rprev*rpost))))[0]
         IF dir_x LT -1 THEN dir_x=-1
         IF dir_x GT  1 THEN dir_x= 1
; Angle between prev_point_proj and post_point_proj
         IF dir_y LT 0 THEN begin
            prevpostan = 2.*!pi - acos(dir_x)
         ENDIF ELSE BEGIN
            prevpostan = acos(dir_x)
         ENDELSE
; Calculating the 2D position of the post_point
         xPost = rPost*cos(prevpostan)
         yPost = rPost*sin(prevpostan)
; Determine circle through threeD[*,i], prev_point
   and post_point
         x = [rPrev,0.,xPost]
         y = [0.,0.,yPost]
         cir_3pnt, x, y, r, x0, y0
; Assigning direction of curvature
         IF dir_y LT 0 then r = -r
         IF float(prevpostan) EQ !pi then r = 0.
; Geodetic latitude
        lat_geodet = atan(tan(lat_lon[0,*] $
          *!pi/180.) / (1-((b-a)/b))^2)*180./!pi
; Determining the velocity
        velocity = [velocity,2.*omega*r* $
           sin(lat_geodet[i]*!pi/180.)]
    ENDFOR
    velocity=velocity[1:n_elements(velocity)-1]
; Extracting non-zero values
    null_num = where(velocity NE 0, nn)
    velocity_reduced = velocity[null_num]
; Testing if velocity has more than one value
    IF n_elements(velocity) EQ 1 THEN BEGIN
       vel_distrib=[vel_distrib, velocity]
       vel_err=[vel_err, 0.]
    ENDIF ELSE BEGIN
       IF nn GT 0 THEN BEGIN
; Producing a histogram
          his = histogram(velocity_reduced,     $
```

```
            omax=omax, omin=omin,                $
            location=binvals, binsize=binsize, $
            reverse_indices=ri)
; Finding the largest bin
         max_lok = where(max(his) EQ his)
; Storing values of largest bin
         values = 0.
         for k=0, n_elements(max_lok)-1 do begin
             values = [values, velocity_reduced $
                [ri[ri[max_lok[k]]:               $
                ri[max_lok[k]+1]-1]]]
         endfor
; Storing mean of largest bin in common array
         vel_distrib=[vel_distrib, mean(values $
            [1:n_elements(values)-1])]
         vel_err=[vel_err, stddev(values $
            [1:n_elements(values)-1])]
      ENDIF ELSE BEGIN
; Storing zero if there are no values in the
   histogram
        vel_distrib=[vel_distrib,0.]
        vel_err=[vel_err,0.]
      ENDELSE
    ENDELSE
ENDFOR
; Finding distance of mapping points for plotting
; recent              ; ancient
axis_lat=75.          ; axis_lat=74.
axis_lon=301.         ; axis_lon=293.
; Finding distance to Reasilvia's centre
distance_RS = 0.
lon_180 = lat_lon[1,*]
lat_geo_det = atan(tan(lat_lon[0,*]*!pi/180.) $
   / (1-((b-a)/b))^2)*180./!pi
lat_geo_det_RS = atan(tan(-axis_lat*!pi/180.) $
   / (1-((b-a)/b))^2)*180./!pi
FOR l=0, n_elements(lat_geo_det)-1 do begin
  ell_ll2rb, lon_180[l], -lat_geo_det[l], $
     axis_lon, lat_geo_det_RS, dist_RS, azi1, azi2
  distance_RS = [distance_RS, dist_RS]
```

```
ENDFOR
; Finding distance along curve
curve_len = fltarr(n_elements(lat_lon)/2)
lat_geo_det_first_point = atan(tan(lat_lon[0,0] $
   *!pi/180.)/(1-((b-a)/b))^2)*180./!pi
FOR l=1, n_elements(lat_lon)/2-1 do begin
  ell_ll2rb, lon_180[l-1], -lat_geo_det[l-1], $
  lon_180[l], -lat_geo_det[l], point_dist,    $
  azi1, azi2
  curve_len[l] = [curve_len[l-1] + point_dist]
ENDFOR
; Returning the distance from Rheasilvia's centre,
   the distance along the curve, the velocity and
   the standard deviation of of the velocity
dis_vel = transpose([[distance_RS[2:n_elements  $
   (distance_RS)-2]], [curve_len[1:n_elements   $
   (curve_len)-2]], [vel_distrib[1:n_elements   $
   (vel_distrib)-1]], [vel_err[1:n_elements     $
   (vel_distrib)-1]]])
RETURN, dis_vel
END
```

```
;+
; :Name:
;  latlonTo3D
;
; :Description:
;    This function converts latitude and longitude
;    in 3D coordinates (x,y,z) on the bi-axial
;    reference ellipsoid
;
; :Parameters:
;    lat_lon:  two dimensional array containing
;              geocentric latitude and longitude of
;              each mapping point
;
; :Returns:
;    threeD:   three dimensional array containing
;              the x, y and z-coordinates of each
;              mapping point on the reference
;              ellipsoid
;-
FUNCTION latlonTo3D, lat_lon
; Constants describing Vesta's shape
; recent              ; ancient
ab_ax = 281550.       ; ab_ax = 277620.
c_ax = 223800.        ; c_ax = 236770.
; Calculating the distance from the origin of the
   coordinate system
r = reform(ab_ax*c_ax/(sqrt(c_ax^2* $
   cos(lat_lon[0,*]*!pi/180.)^2 +   $
   ab_ax^2*sin(lat_lon[0,*]*!pi/180.)^2)))
; Calculating x, y and z
x = r*cos(lat_lon[1,*]*!pi/180.)* $
   cos(lat_lon[0,*]*!pi/180.)
y = r*sin(lat_lon[1,*]*!pi/180.)* $
   cos(lat_lon[0,*]*!pi/180.)
z = - sqrt(1. - (x^2+y^2)/ab_ax^2)*c_ax
threeD = reform([x,y,z],n_elements(x),3)
RETURN, transpose(threeD)
END
```

A.2. Ancient Vesta's Reference System

```
;+
; :Name:
;  shift_axis
;
; :Description:
;    This function calculates the latitude and
;    longitude of the mapping points with respect
;    to the ancient rotation axis which was shifted
;    by 3 degree. The function operates on a
;    spherical object and is followed by the
;    functions proj_off and latlonTo3D to complete
;    the transformation in to Vesta's ancient shape.
;
; :Parameters:
;    lat_lon:  two dimensional array containing
;              geocentric latitude and longitude of
;              each mapping point
;
; :Returns:
;    lat_lon_new: the new latitude and longitude
;              with respect to the shifted rotation
;              axis
;-
FUNCTION shift_axis, lat_lon
r = 1.
lat_lon_new = lat_lon
; x,y,z coordinates of mapping points
pnt_x = r*sin((90. - lat_lon_new[0,*])*!pi/180.)*
   cos(lat_lon_new[1,*]*!pi/180.)
pnt_y = r*sin((90. - lat_lon_new[0,*])*!pi/180.)*
   sin(lat_lon_new[1,*]*!pi/180.)
pnt_z = r*cos((90. - lat_lon_new[0,*])*!pi/180.)
; Position of axes after Fu et al. 2014
sh_lat_a = (90. - 2.9)   *!pi/180.
sh_lon_a = (17.3)        *!pi/180.
sh_lat_b = (90. + 0.8)   *!pi/180.
sh_lon_b = (107.3)       *!pi/180.
sh_lat_c = (90. - 87.)   *!pi/180.
```

```
sh_lon_c = (360. - 177.3)*!pi/180.
; Converting axes position to x,y,z coordinates
x_a = r*sin(sh_lat_a)*cos(sh_lon_a)
y_a = r*sin(sh_lat_a)*sin(sh_lon_a)
z_a = r*cos(sh_lat_a)
x_b = r*sin(sh_lat_b)*cos(sh_lon_b)
y_b = r*sin(sh_lat_b)*sin(sh_lon_b)
z_b = r*cos(sh_lat_b)
x_c = r*sin(sh_lat_c)*cos(sh_lon_c)
y_c = r*sin(sh_lat_c)*sin(sh_lon_c)
z_c = r*cos(sh_lat_c)
; Transferring into shifted system
basis_1 = [[1.,0.,0.], [0.,1.,0.], [0.,0.,1.]]
basis_2 = [[x_a,x_b,x_c], [y_a,y_b,y_c], $
   [z_a,z_b,z_c]]
pnt = transpose([pnt_x, pnt_y, pnt_z])
basis_tr = transpose(la_linear_equation(invert $
   (basis_2), basis_1))
pnt_nr = transpose(la_linear_equation(invert $
   (basis_tr), pnt))
; Converting to new latitude and longitude
lat_lon_new[0,*] = asin(pnt_nr[2,*]/r)*180./!pi
lat_lon_new[1,*] = atan(pnt_nr[1,*], pnt_nr[0,*]) $
   *180./!pi
; Converting negative longitudes
sh = where(lat_lon_new[1,*] LT 0, cnt)
IF cnt GT 0 THEN lat_lon_new[1,sh] = $
   360. + lat_lon_new[1,sh]
RETURN, lat_lon_new
END
```

```
;+
; :Name:
;  proj_off
;
; :Description:
;    This function calculates the latitude and
;    longitude of the mapping points with respect to
;    the ancient ellipsoid's origin which was offset
;    by 5.7 km.
;
; :Parameters:
;    lat_lon:  two dimensional array containing
;              geocentric latitude and longitude of
;              each mapping point
;
; :Returns:
;    lat_lon_new: the new latitude and longitude
;              with respect to the offset in origin
;-
FUNCTION proj_off, lat_lon
a = 277620.
b = 236770.
off = -5660.
m = tan(lat_lon[0,*]*!pi/180.)
x = (a^2*off*m - sqrt(a^4*b^2*m^2 + a^2*b^4 - $
   a^2*b^2*off^2)) / (a^2*m^2 + b^2)
y = sqrt(1 - x^2/a^2)*b
lat_new = atan(y/x)
lat_lon_new = lat_lon
lat_lon_new[0,*] = -lat_new*180./!pi
RETURN, lat_lon_new
END
```

B. Curve Plots and Statistics

B.1. Curve Plots

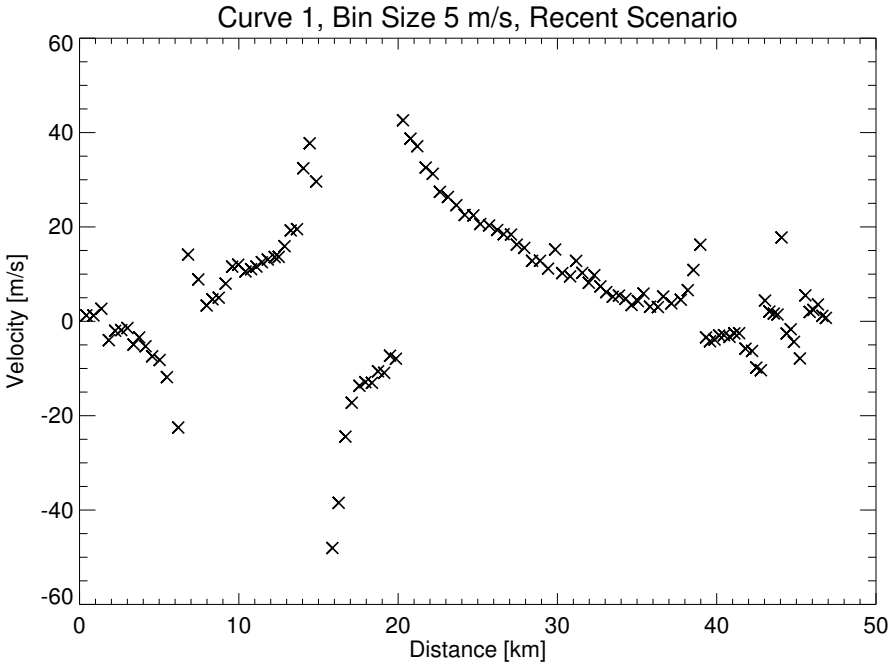

(a) Velocity plot Curve 1.

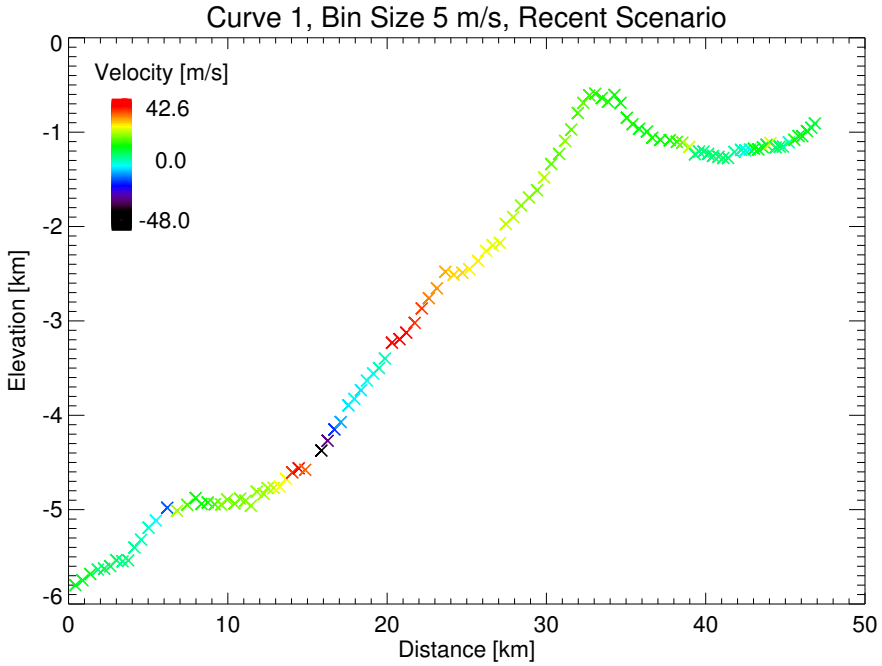

(b) Topography plot Curve 1.

Figure B.1.: Curve 1 evaluated with a bin size of 5 m/s with respect to Vesta's recent shape.

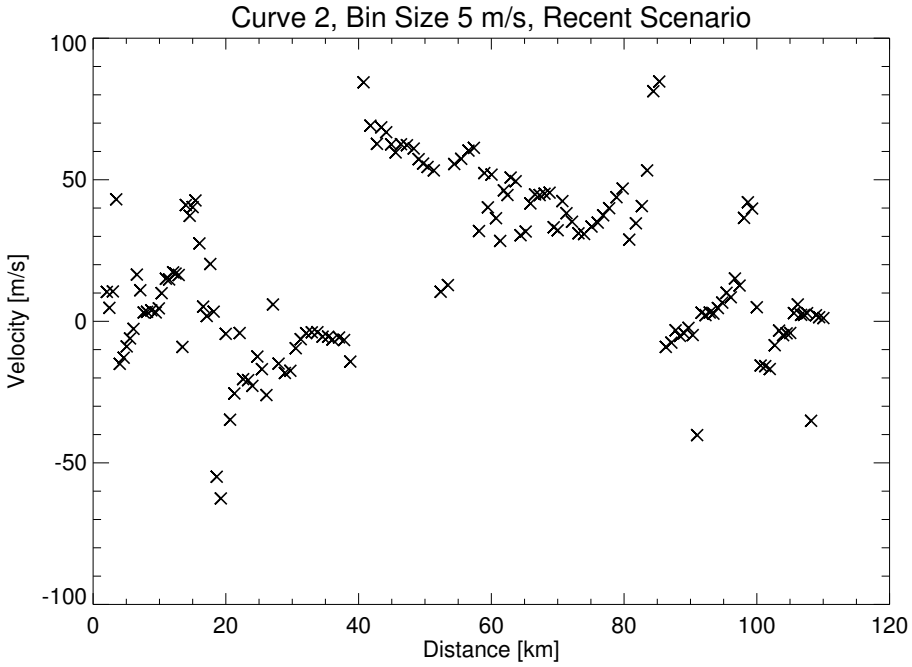

(a) Velocity plot Curve 2.

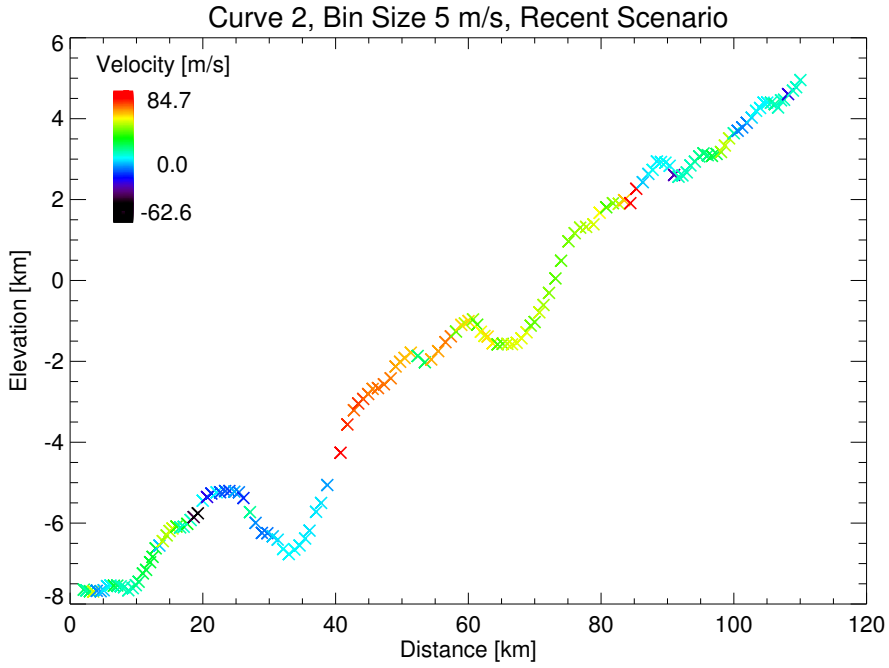

(b) Topography plot Curve 2.

Figure B.2.: Curve 2 evaluated with a bin size of 5 m/s with respect to Vesta's recent shape.

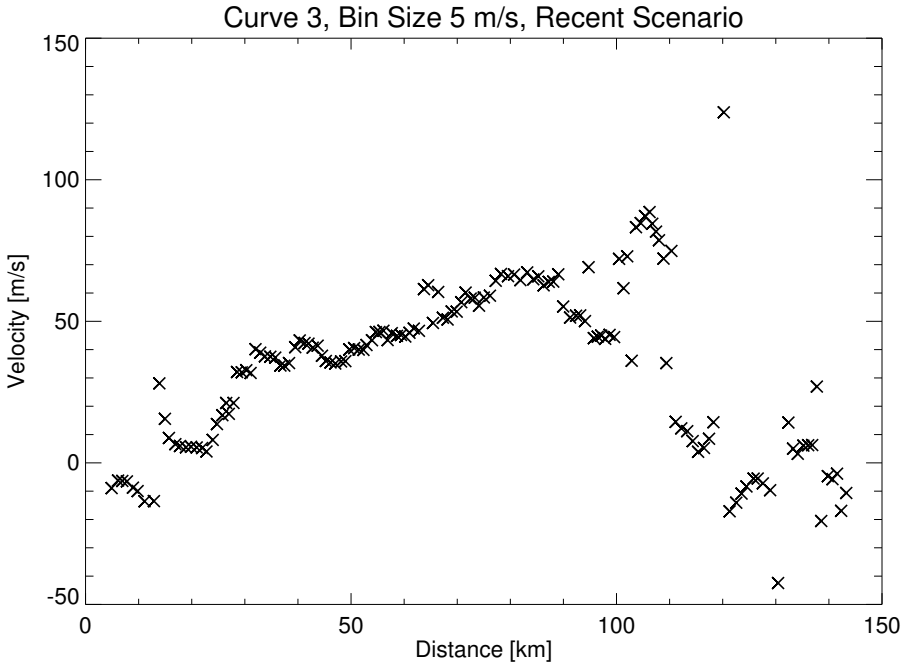

(a) Velocity plot Curve 3.

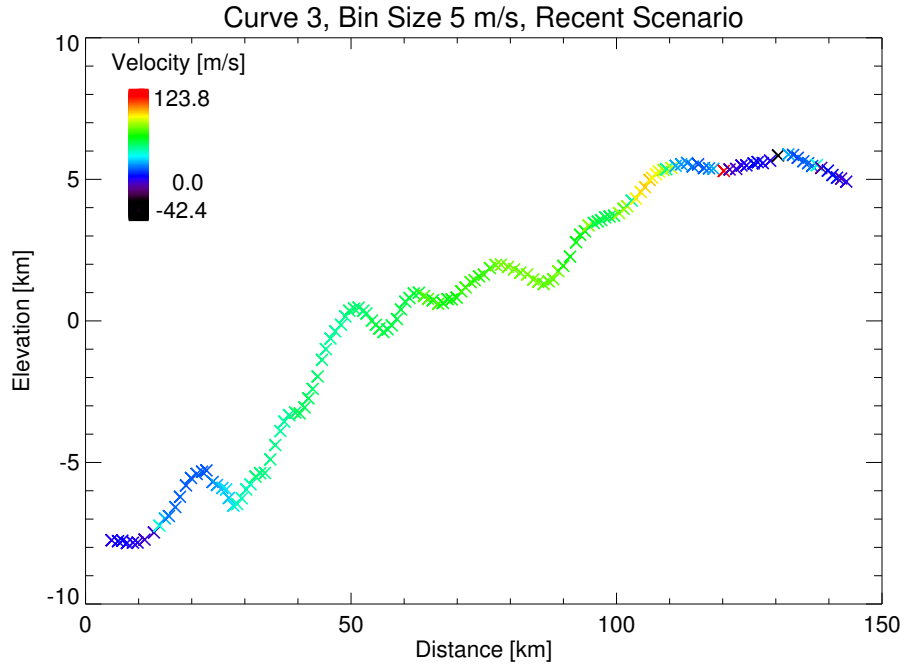

(b) Topography plot Curve 3.

Figure B.3.: Curve 3 evaluated with a bin size of 5 m/s with respect to Vesta's recent shape.

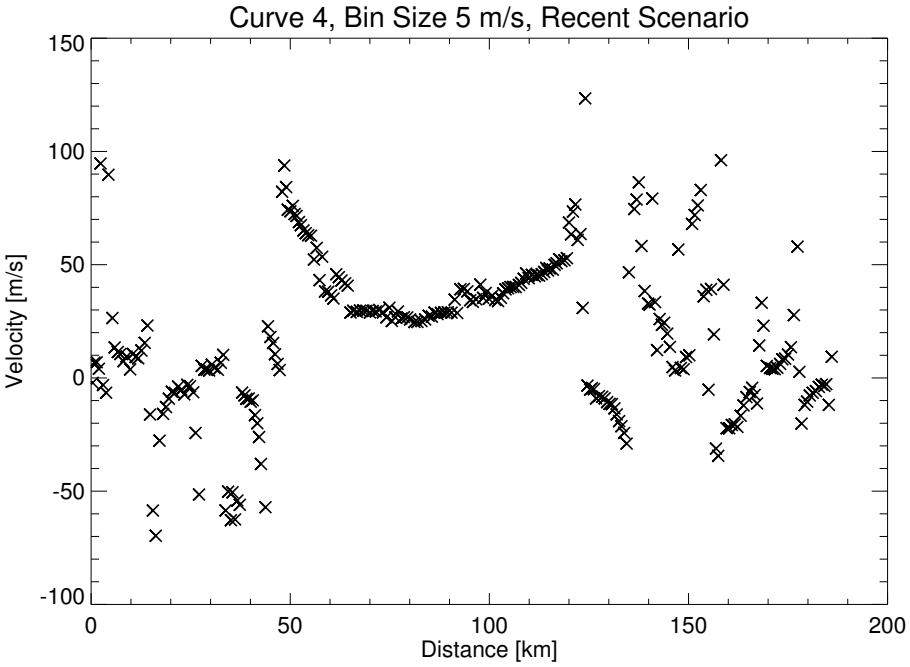

(a) Velocity plot Curve 4.

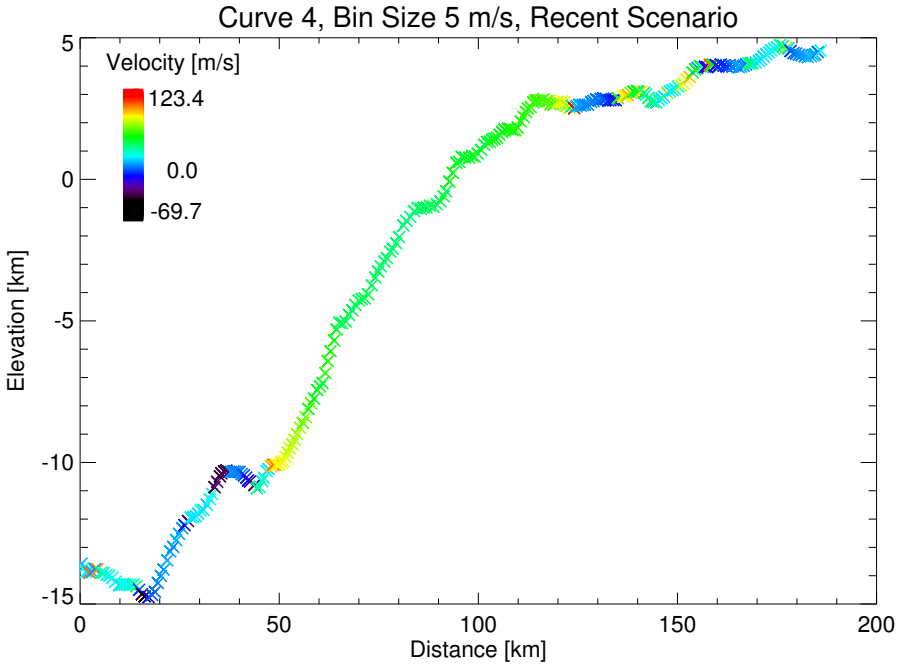

(b) Topography plot Curve 4.

Figure B.4.: Curve 4 evaluated with a bin size of 5 m/s with respect to Vesta's recent shape.

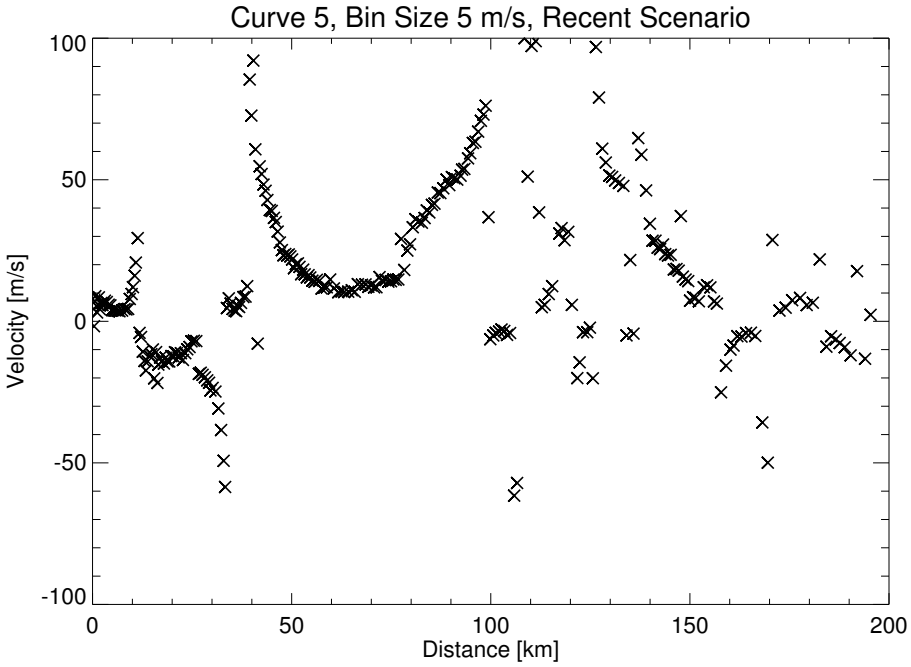

(a) Velocity plot Curve 5.

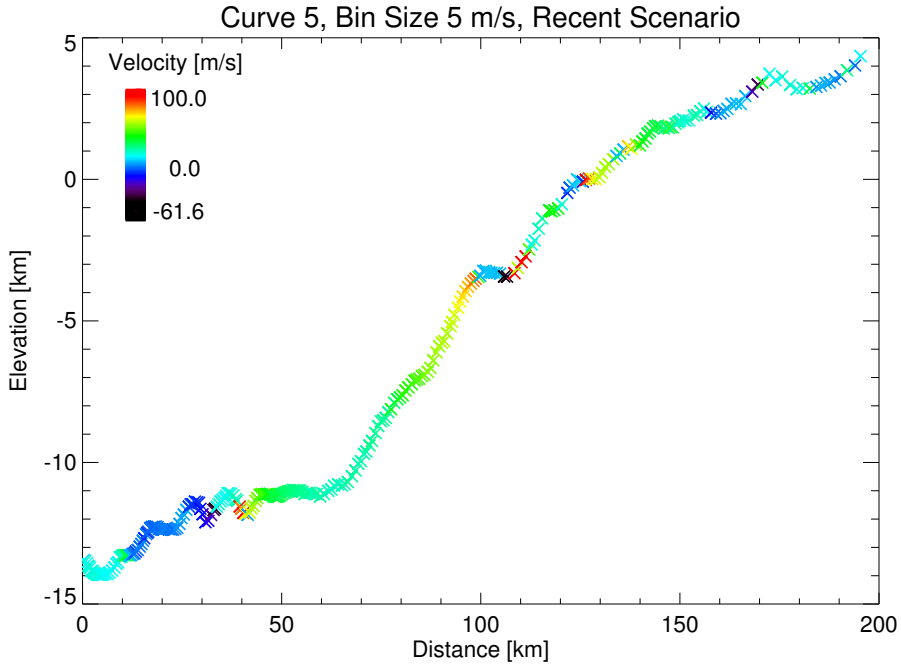

(b) Topography plot Curve 5.

Figure B.5.: Curve 5 evaluated with a bin size of 5 m/s with respect to Vesta's recent shape.

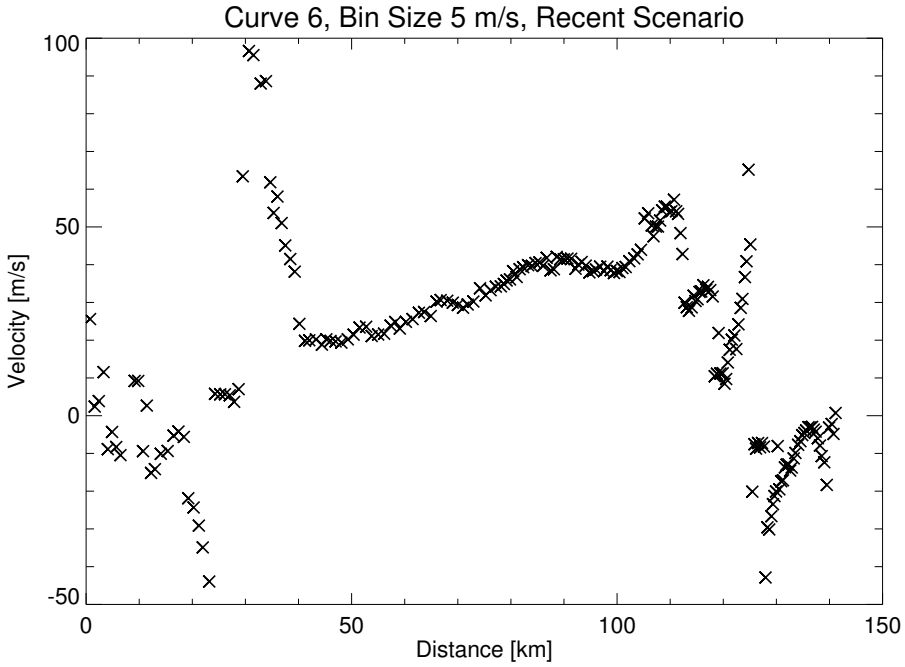

(a) Velocity plot Curve 6.

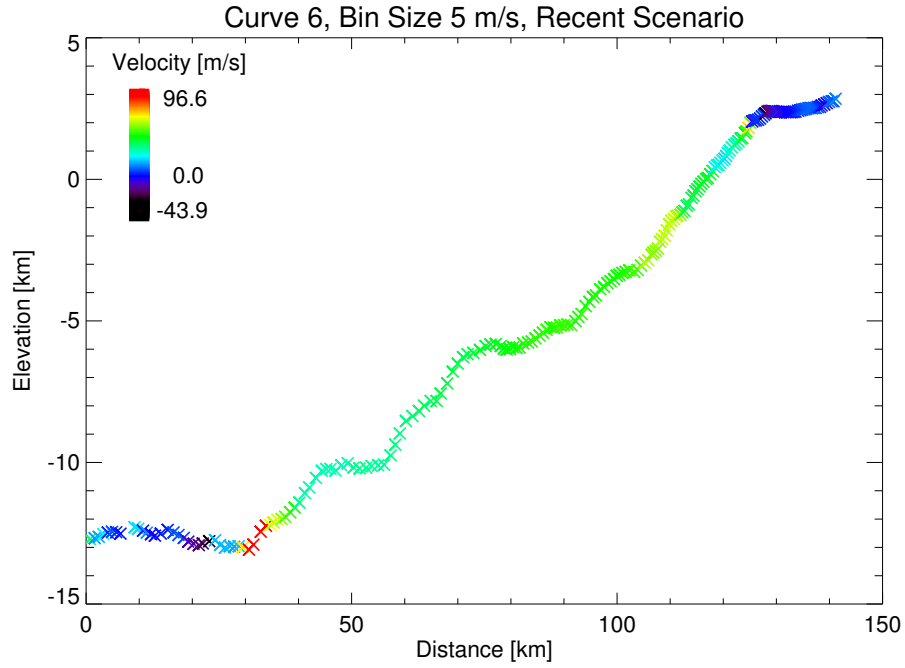

(b) Topography plot Curve 6.

Figure B.6.: Curve 6 evaluated with a bin size of 5 m/s with respect to Vesta's recent shape.

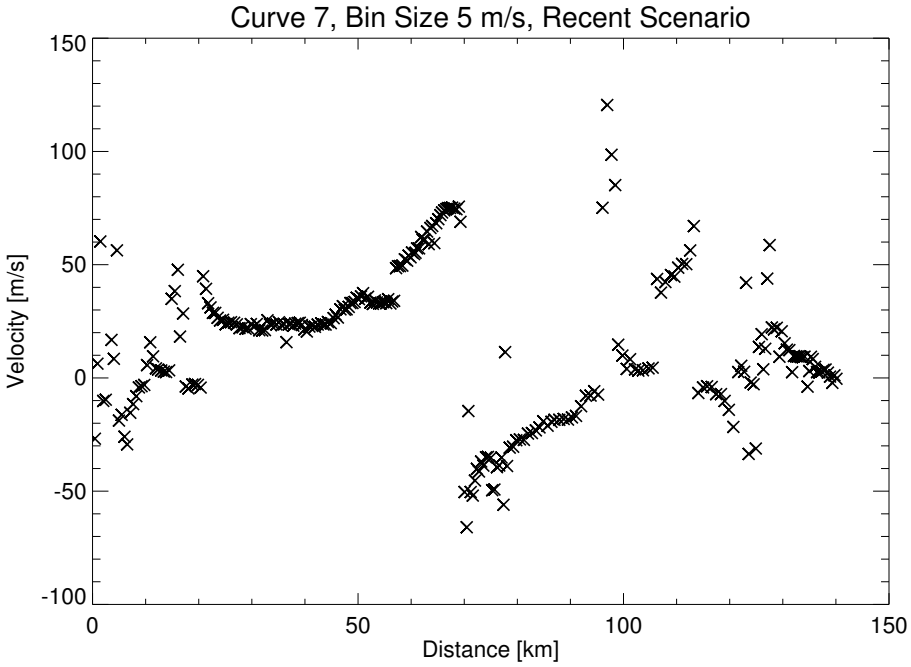

(a) Velocity plot Curve 7.

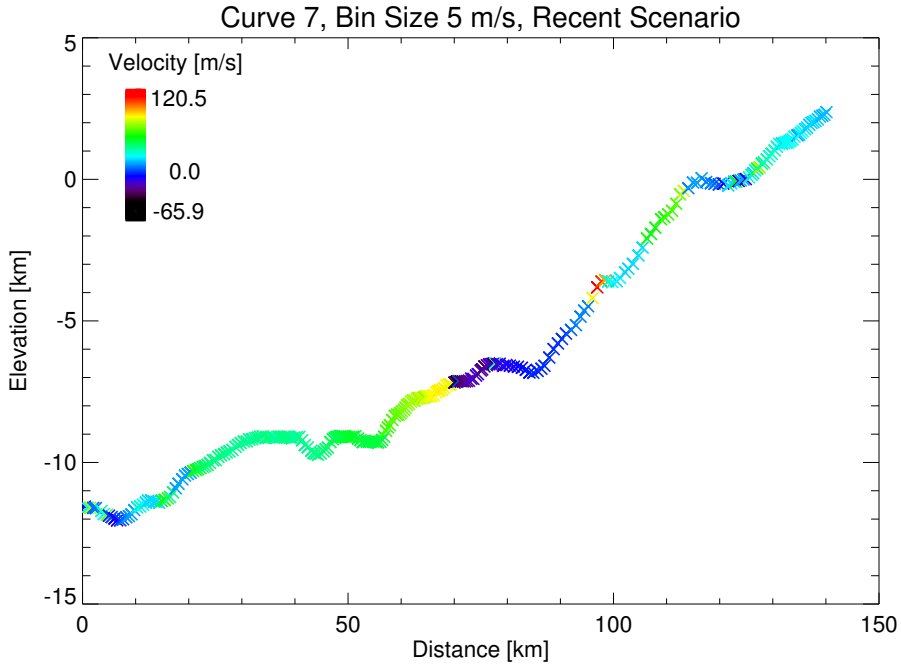

(b) Topography plot Curve 7.

Figure B.7.: Curve 7 evaluated with a bin size of 5 m/s with respect to Vesta's recent shape.

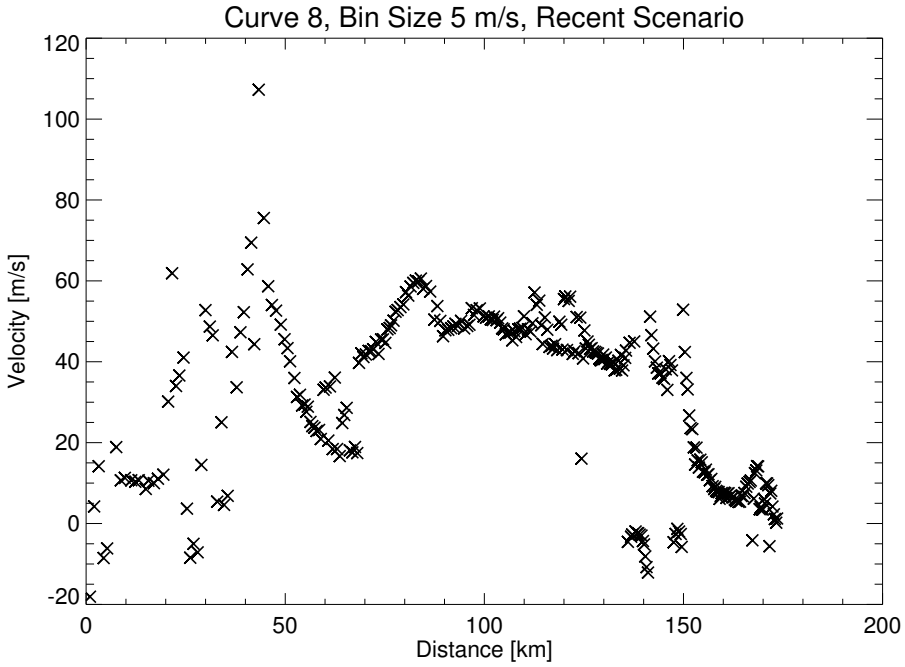

(a) Velocity plot Curve 8.

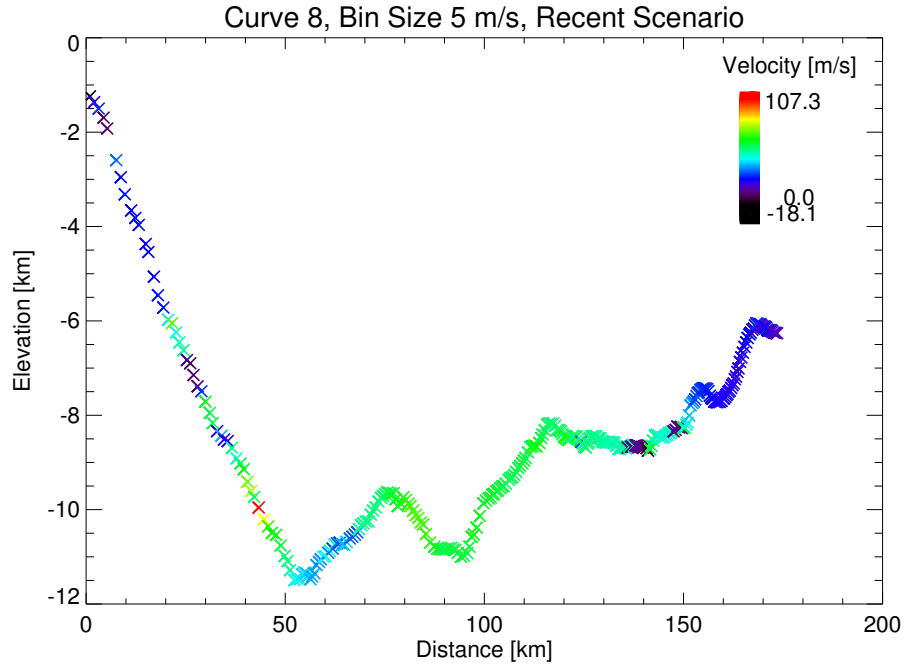

(b) Topography plot Curve 8.

Figure B.8.: Curve 8 evaluated with a bin size of 5 m/s with respect to Vesta's recent shape.

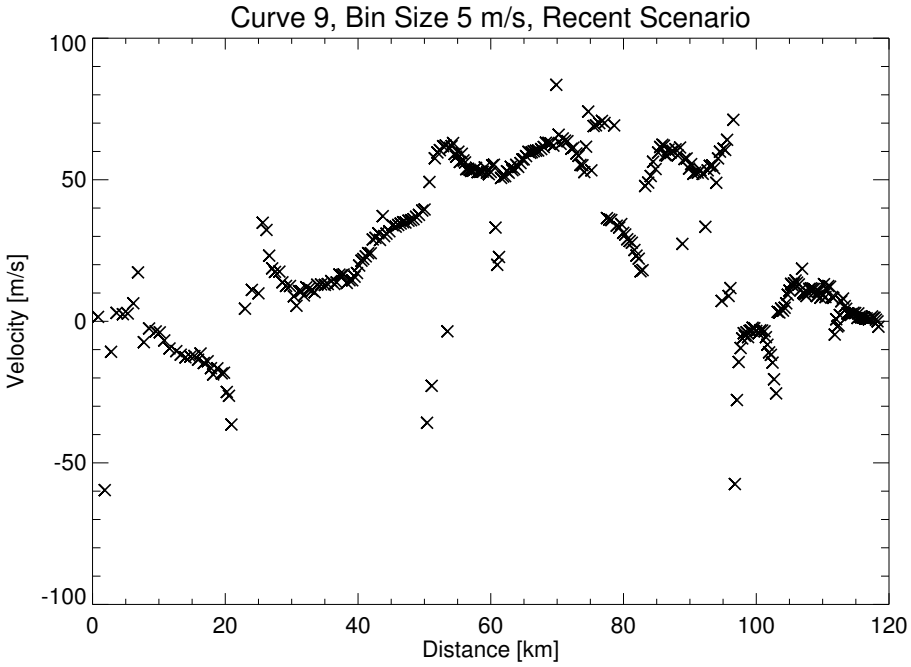

(a) Velocity plot Curve 9.

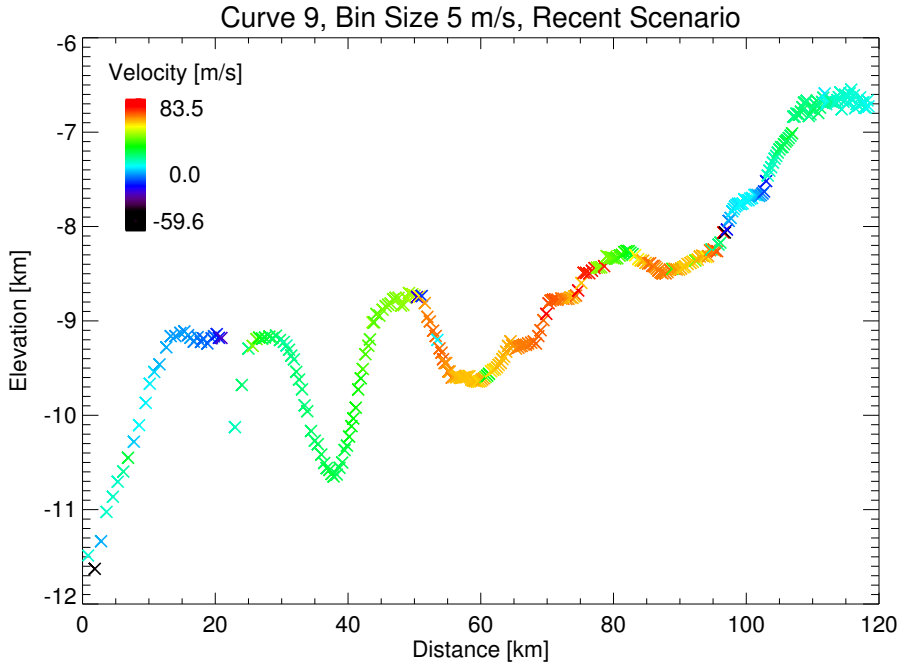

(b) Topography plot Curve 9.

Figure B.9.: Curve 9 evaluated with a bin size of 5 m/s with respect to Vesta's recent shape.

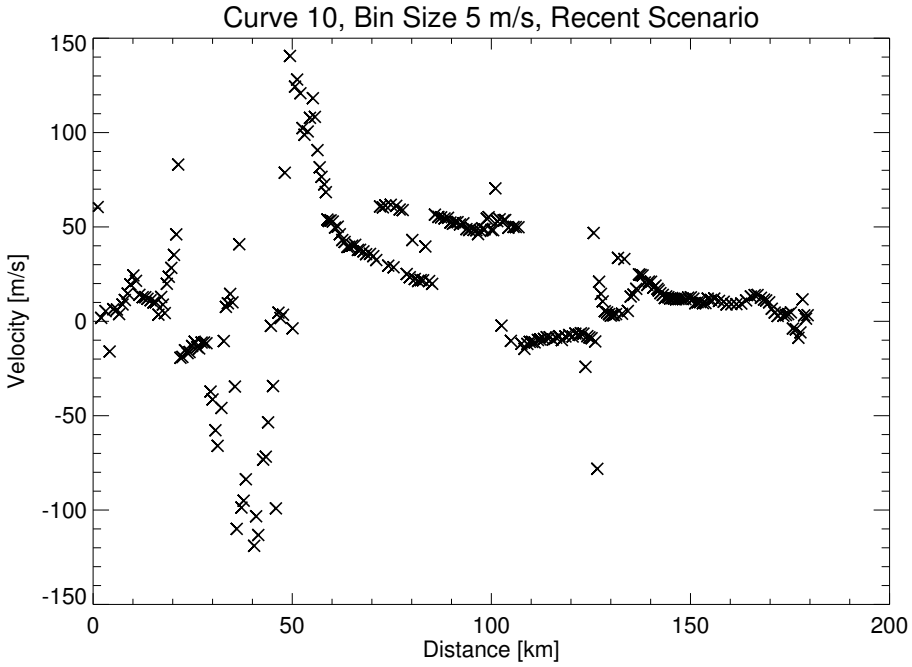

(a) Velocity plot Curve 10.

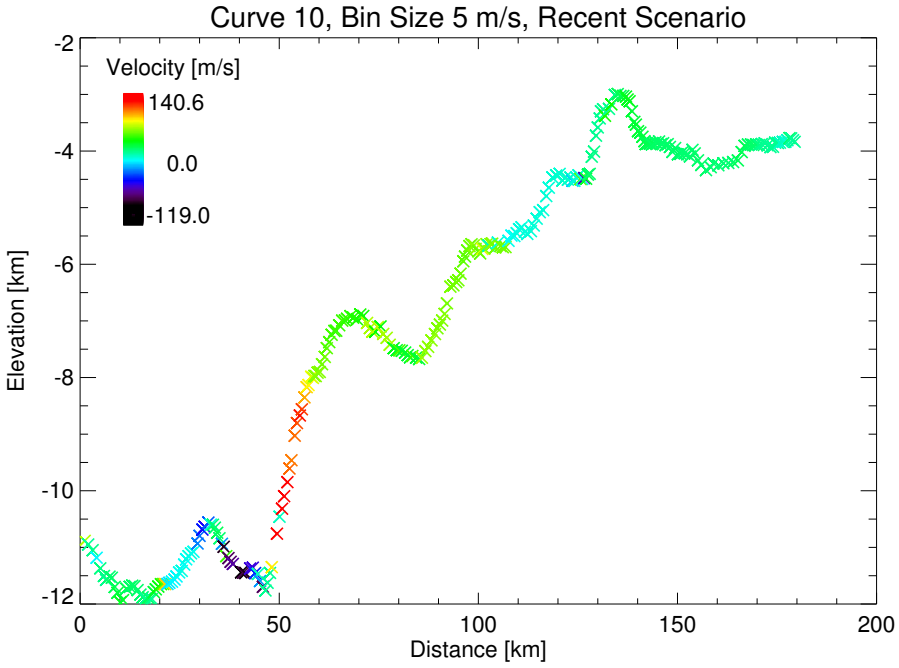

(b) Topography plot Curve 10.

Figure B.10.: Curve 10 evaluated with a bin size of 5 m/s with respect to Vesta's recent shape.

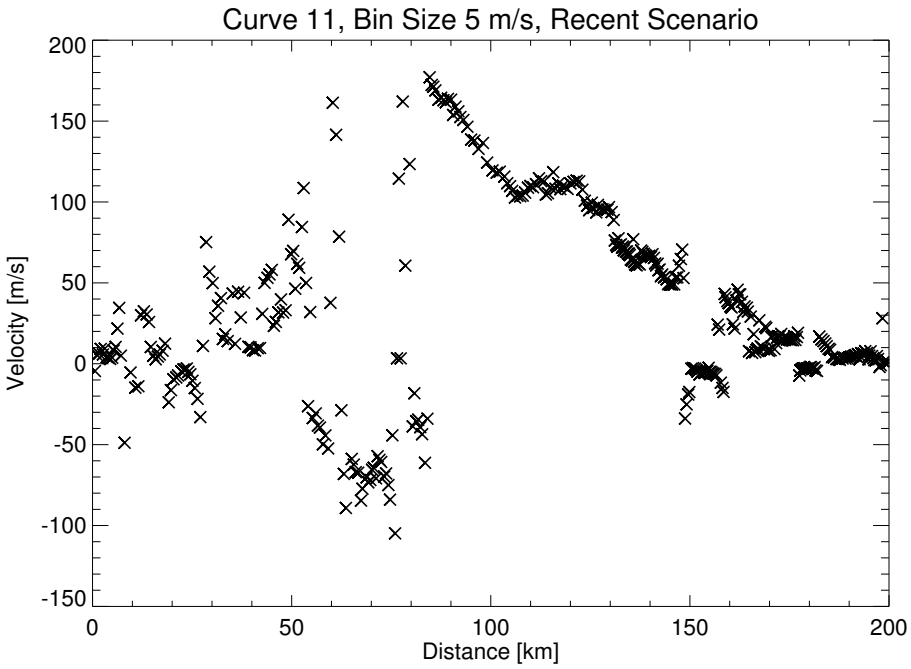

(a) Velocity plot Curve 11.

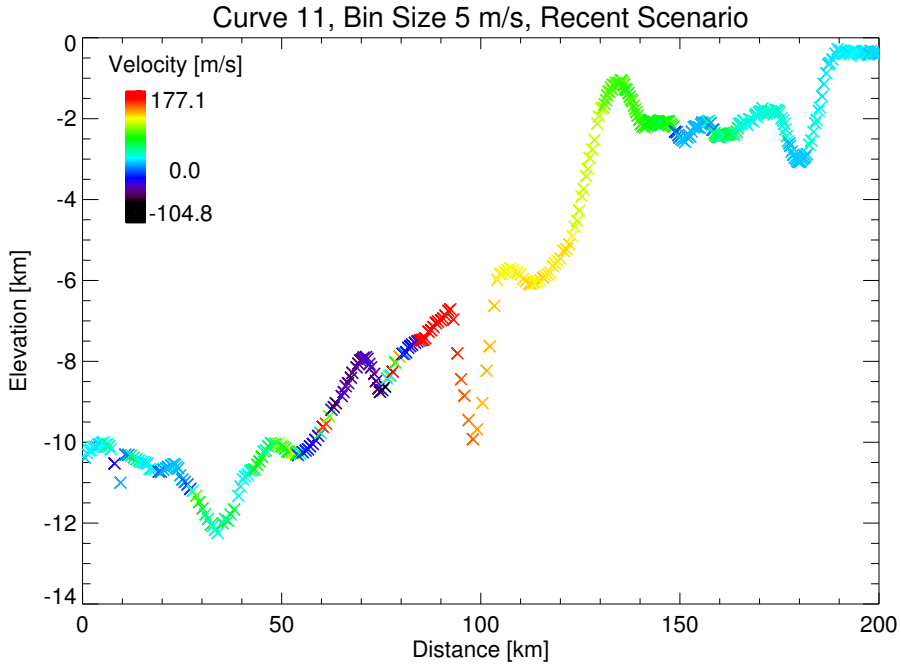

(b) Topography plot Curve 11.

Figure B.11.: Curve 11 evaluated with a bin size of 5 m/s with respect to Vesta's recent shape.

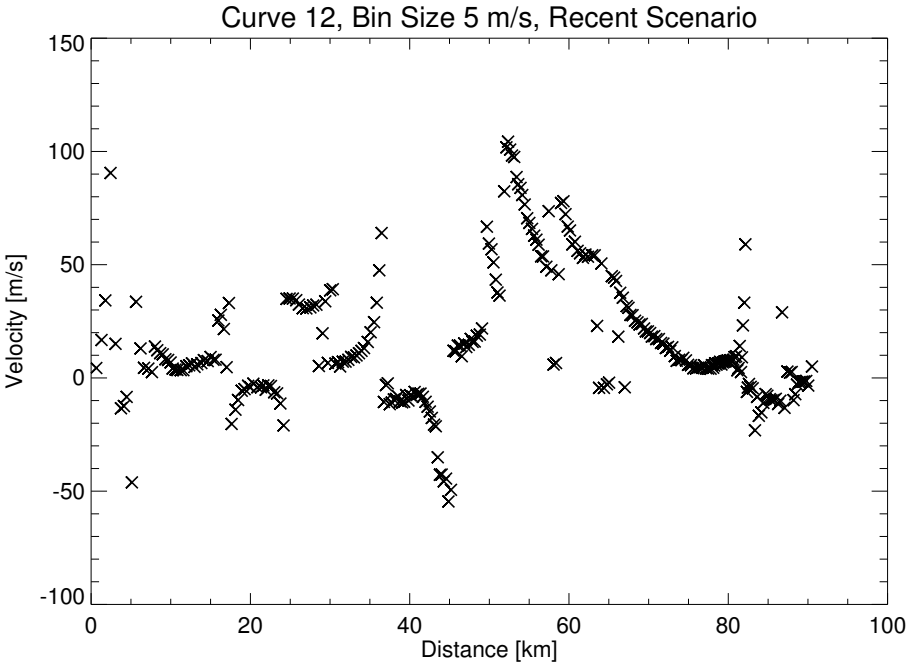

(a) Velocity plot Curve 12.

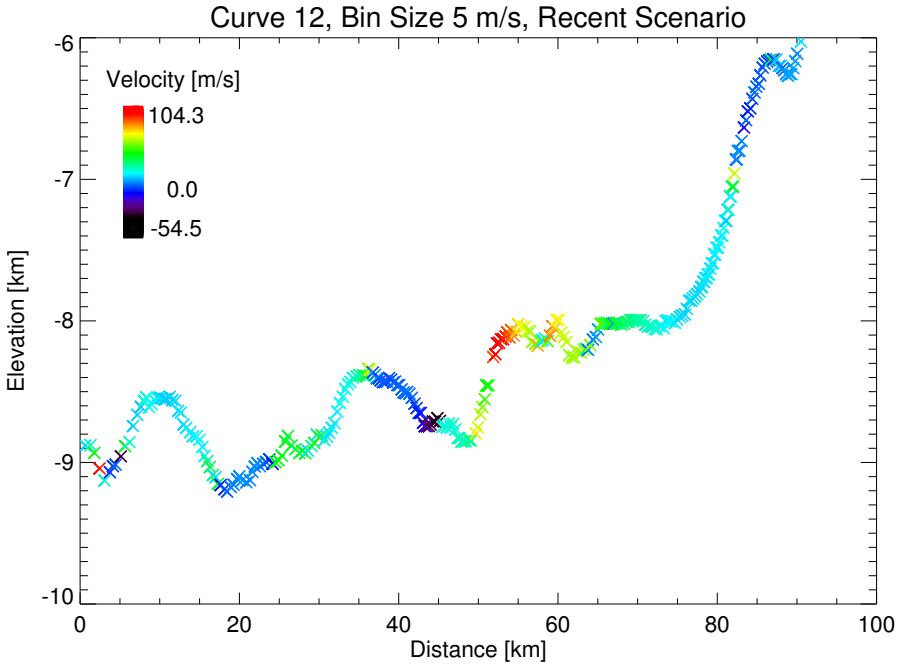

(b) Topography plot Curve 12.

Figure B.12.: Curve 12 evaluated with a bin size of 5 m/s with respect to Vesta's recent shape.

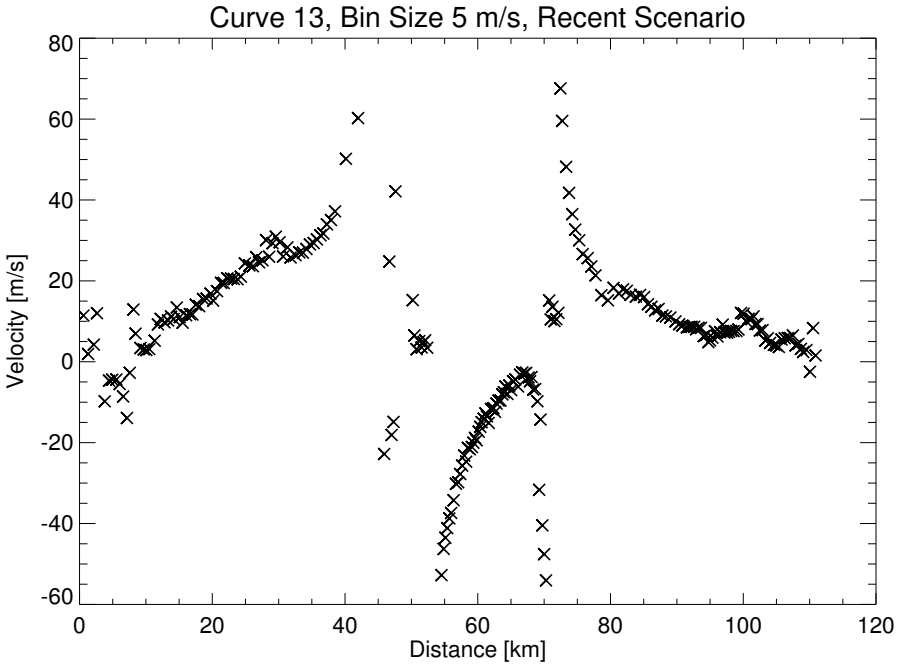

(a) Velocity plot Curve 13.

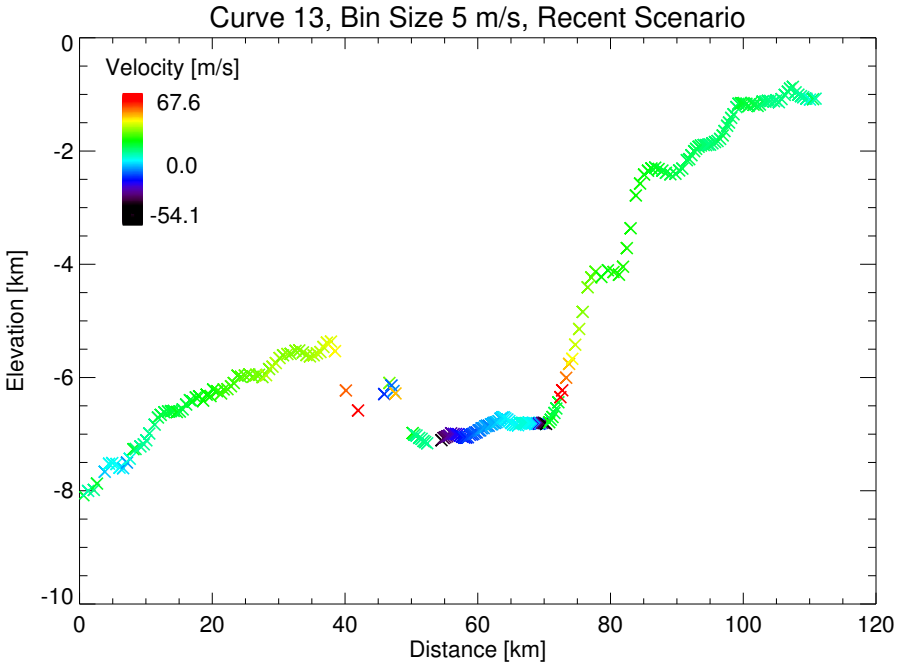

(b) Topography plot Curve 13.

Figure B.13.: Curve 13 evaluated with a bin size of 5 m/s with respect to Vesta's recent shape.

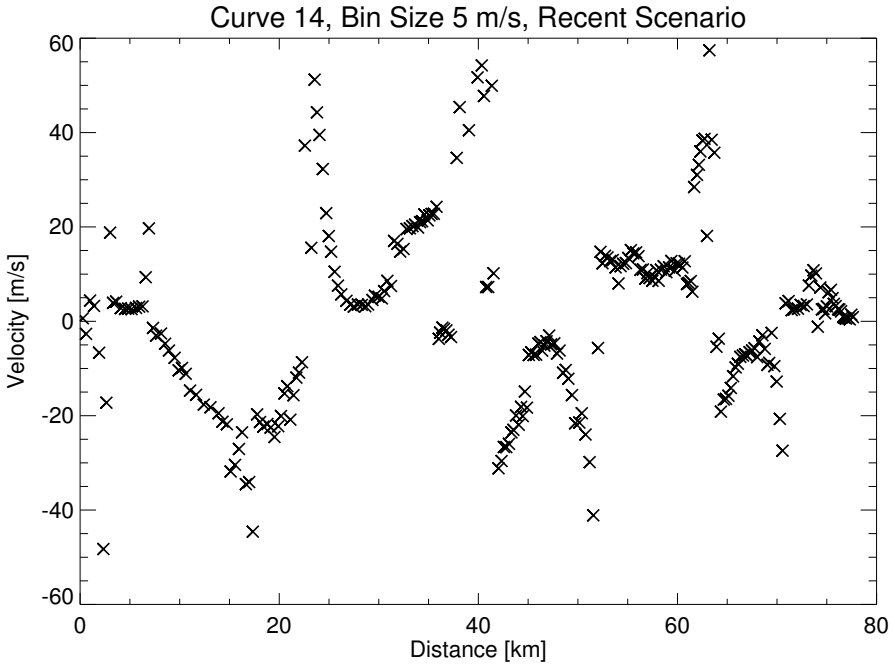

(a) Velocity plot Curve 14.

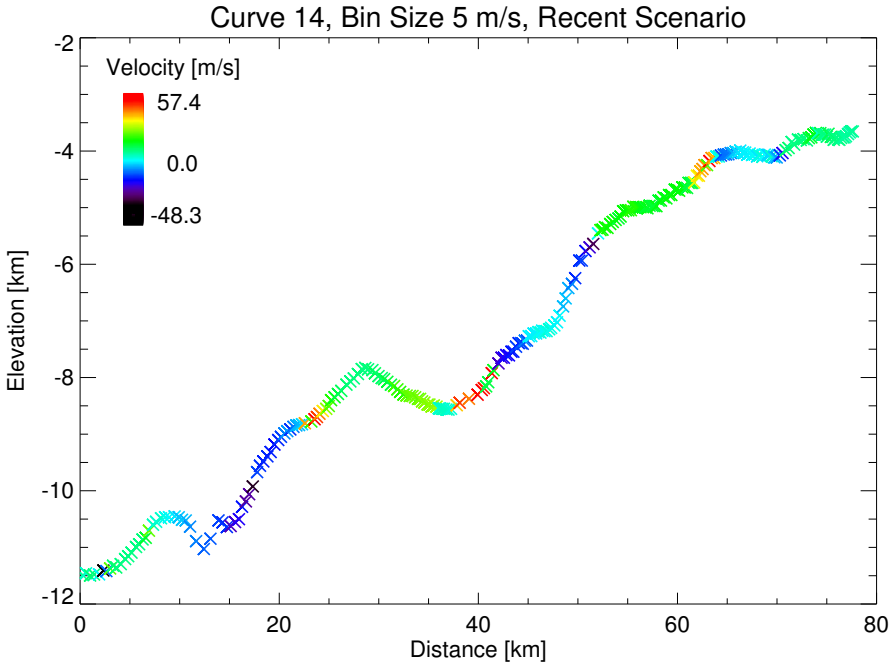

(b) Topography plot Curve 14.

Figure B.14.: Curve 14 evaluated with a bin size of 5 m/s with respect to Vesta's recent shape.

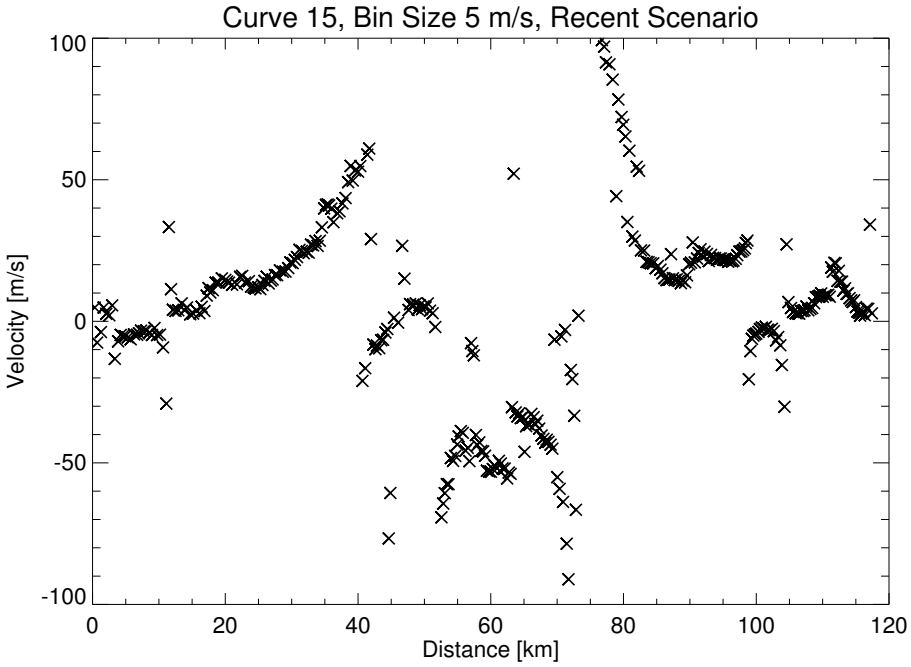

(a) Velocity plot Curve 15.

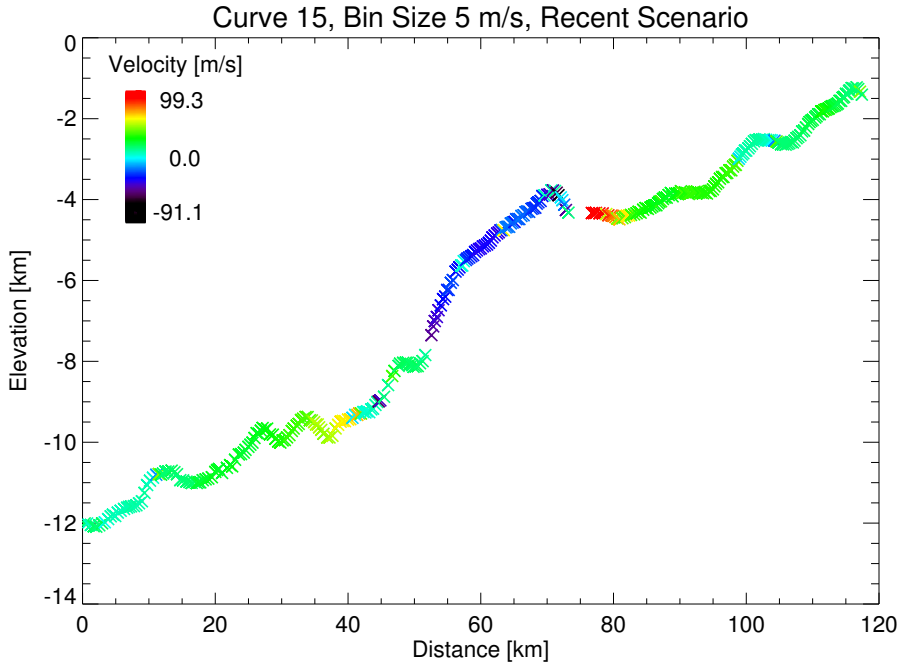

(b) Topography plot Curve 15.

Figure B.15.: Curve 15 evaluated with a bin size of 5 m/s with respect to Vesta's recent shape.

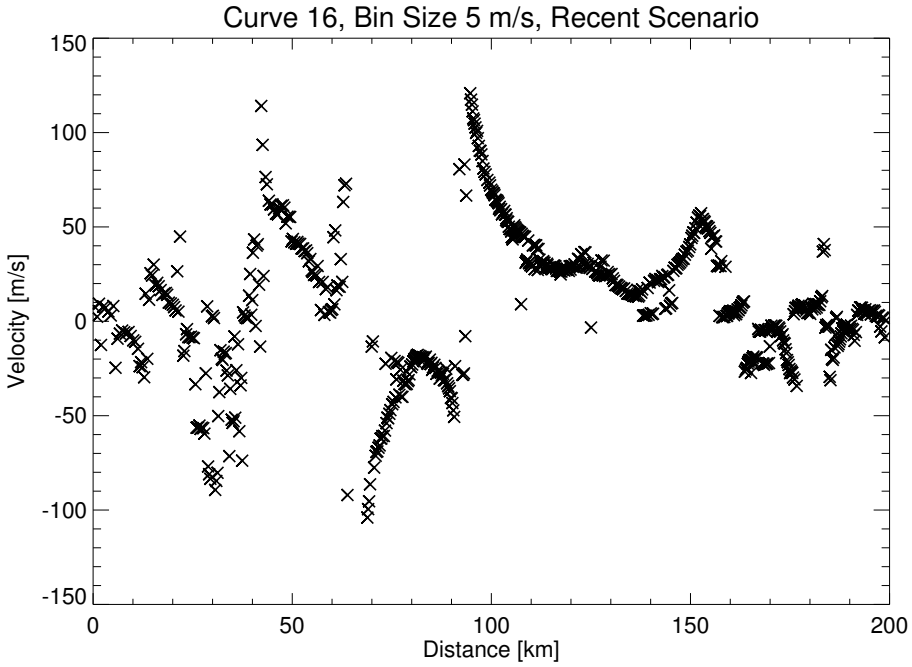

(a) Velocity plot Curve 16.

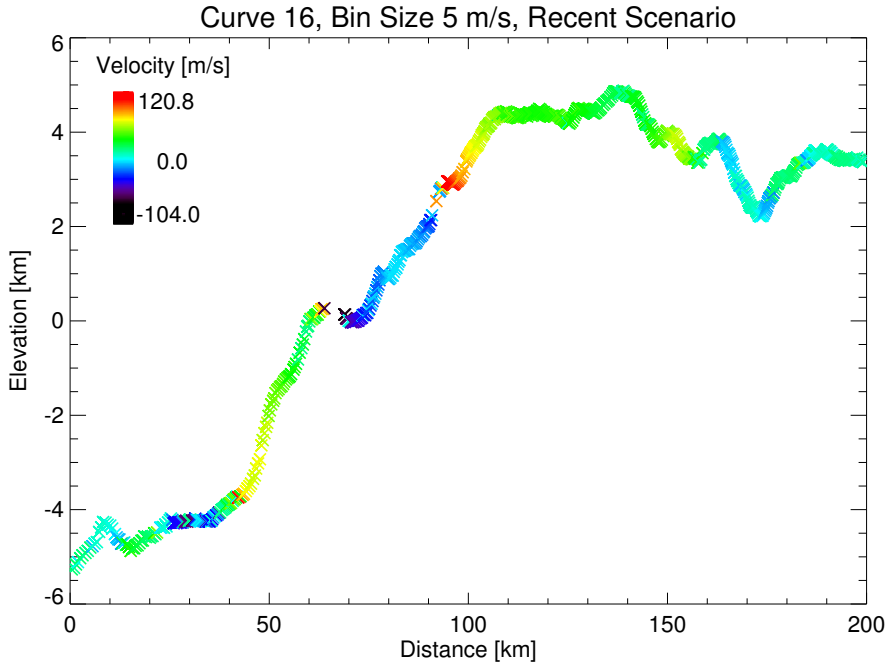

(b) Topography plot Curve 16.

Figure B.16.: Curve 16 evaluated with a bin size of 5 m/s with respect to Vesta's recent shape.

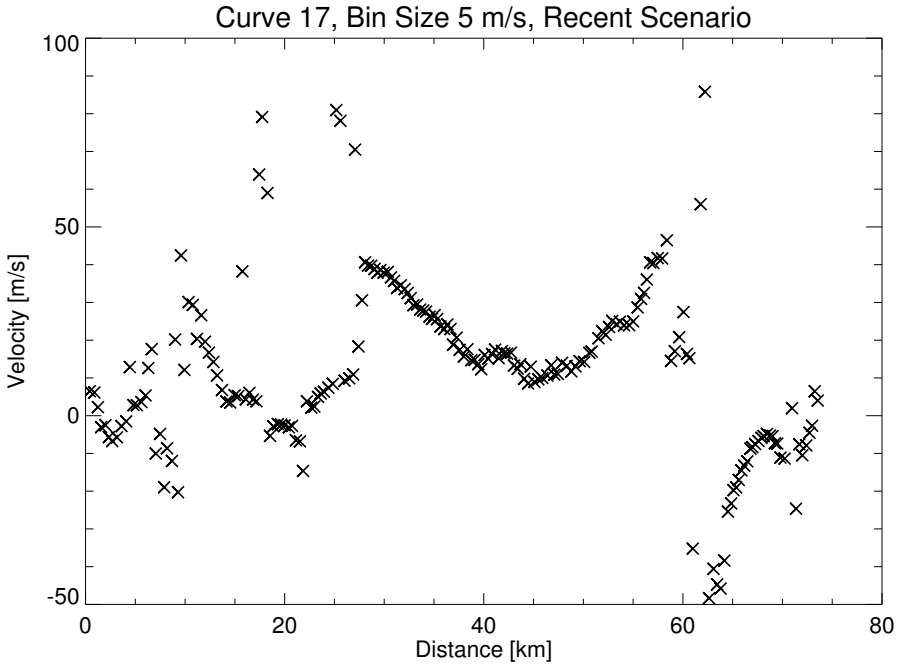

(a) Velocity plot Curve 17.

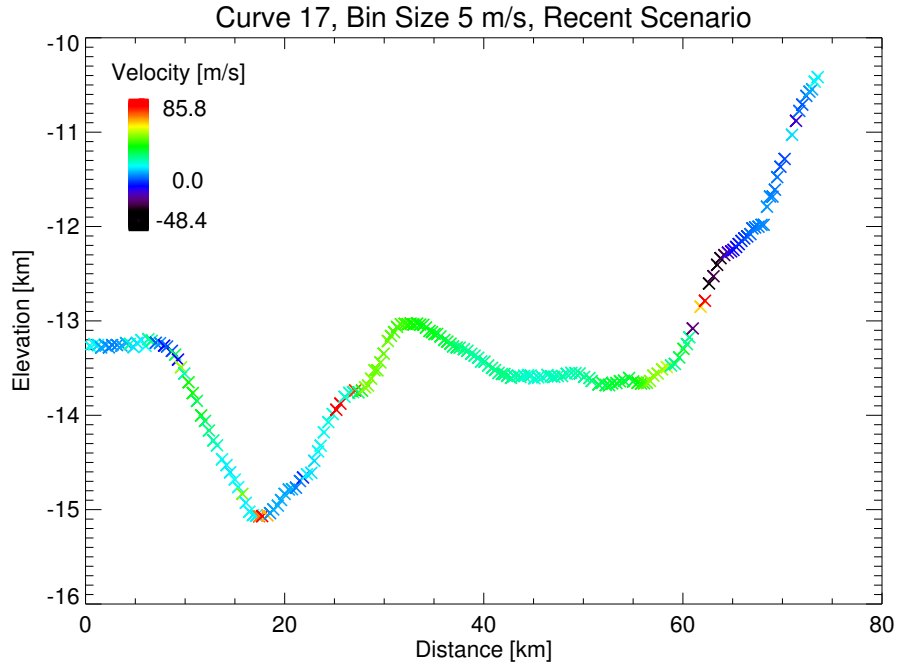

(b) Topography plot Curve 17.

Figure B.17.: Curve 17 evaluated with a bin size of 5 m/s with respect to Vesta's recent shape.

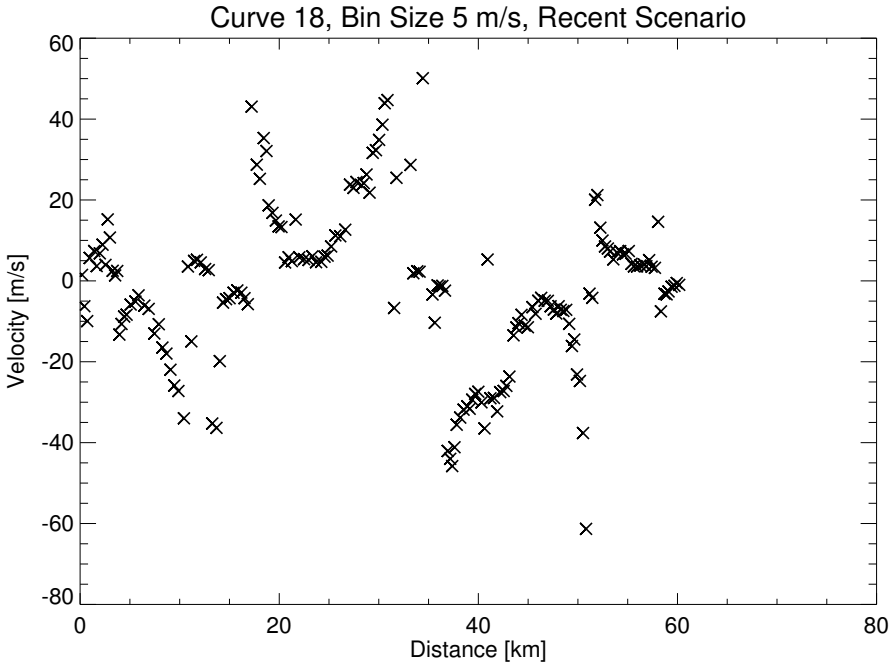

(a) Velocity plot Curve 18.

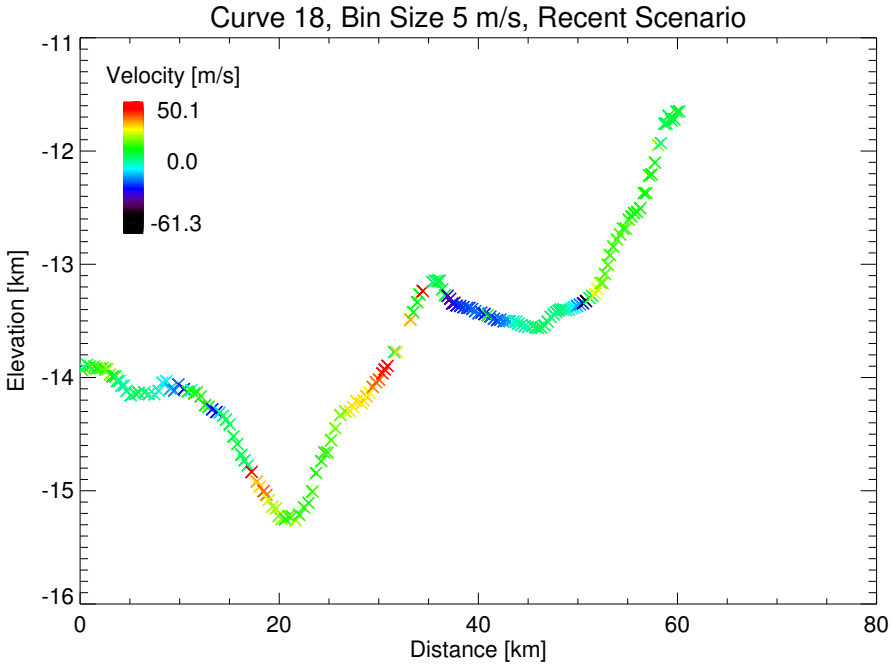

(b) Topography plot Curve 18.

Figure B.18.: Curve 18 evaluated with a bin size of 5 m/s with respect to Vesta's recent shape.

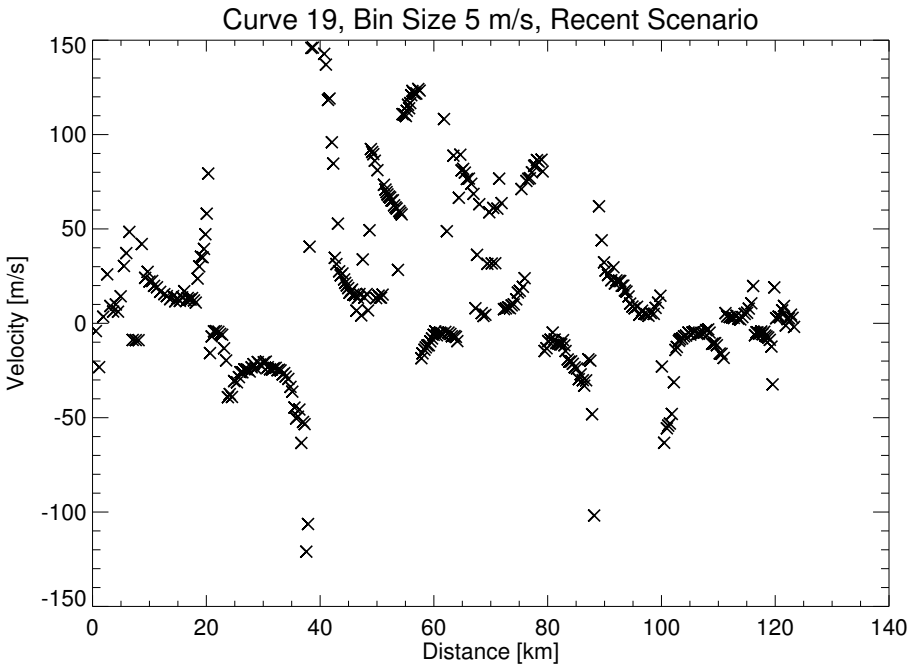

(a) Velocity plot Curve 19.

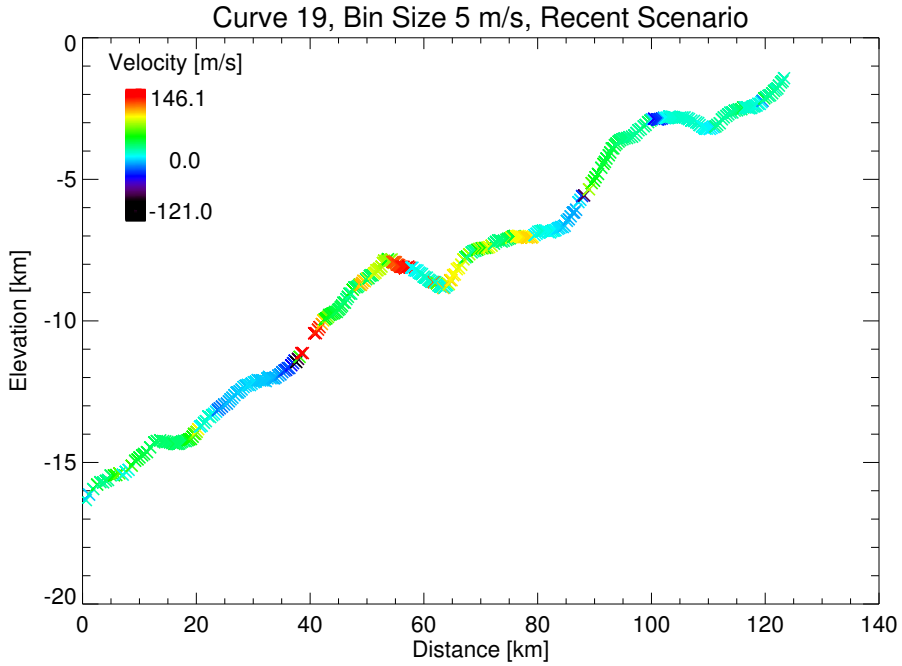

(b) Topography plot Curve 19.

Figure B.19.: Curve 19 evaluated with a bin size of 5 m/s with respect to Vesta's recent shape.

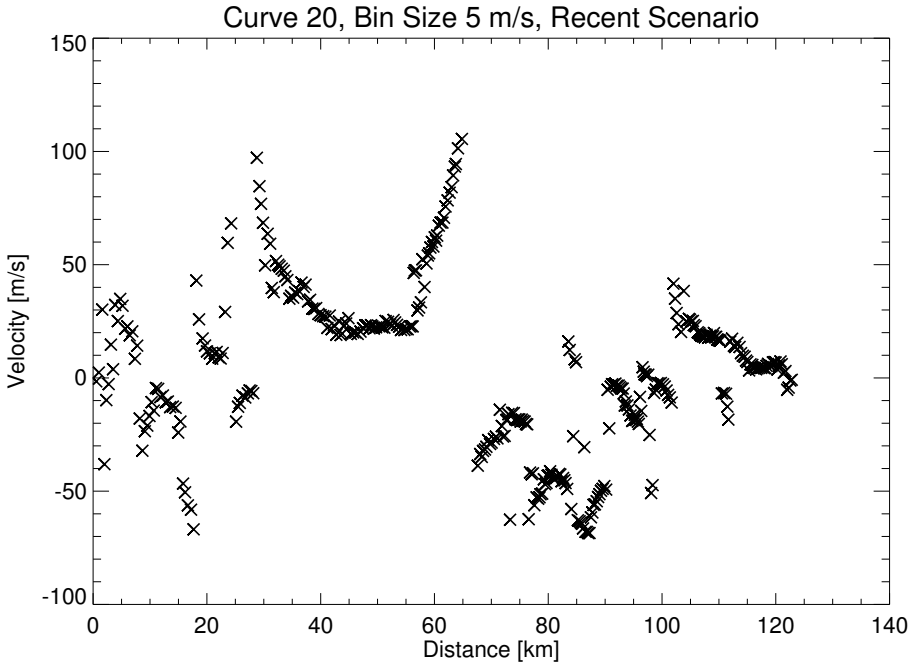

(a) Velocity plot Curve 20.

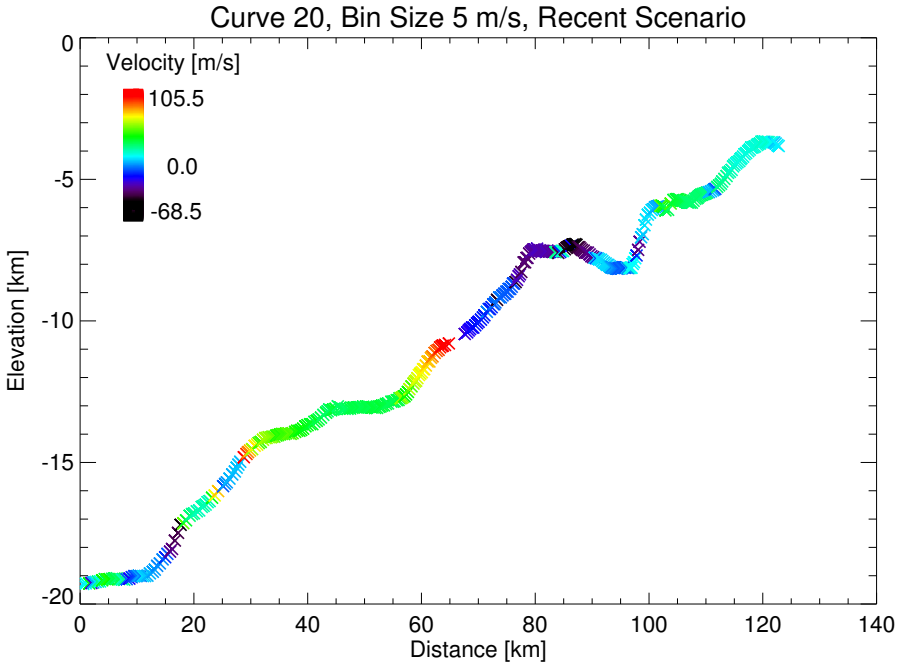

(b) Topography plot Curve 20.

Figure B.20.: Curve 20 evaluated with a bin size of 5 m/s with respect to Vesta's recent shape.

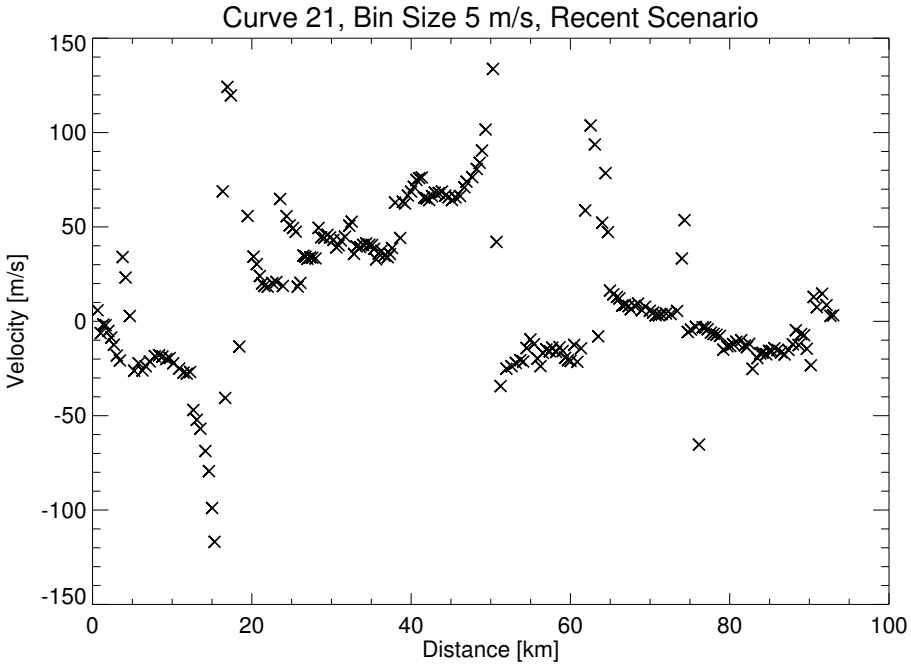

(a) Velocity plot Curve 21.

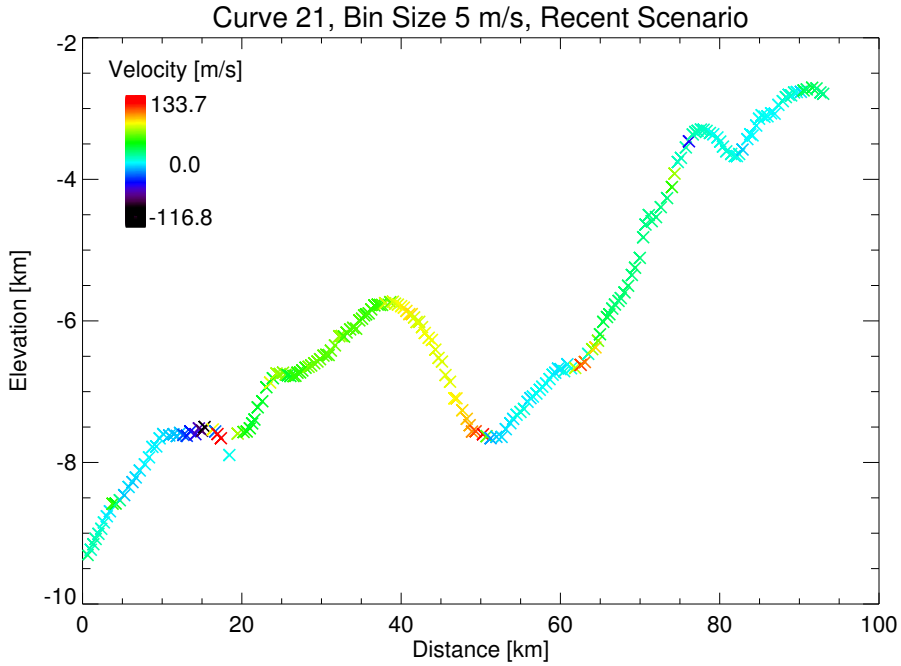

(b) Topography plot Curve 21.

Figure B.21.: Curve 21 evaluated with a bin size of 5 m/s with respect to Vesta's recent shape.

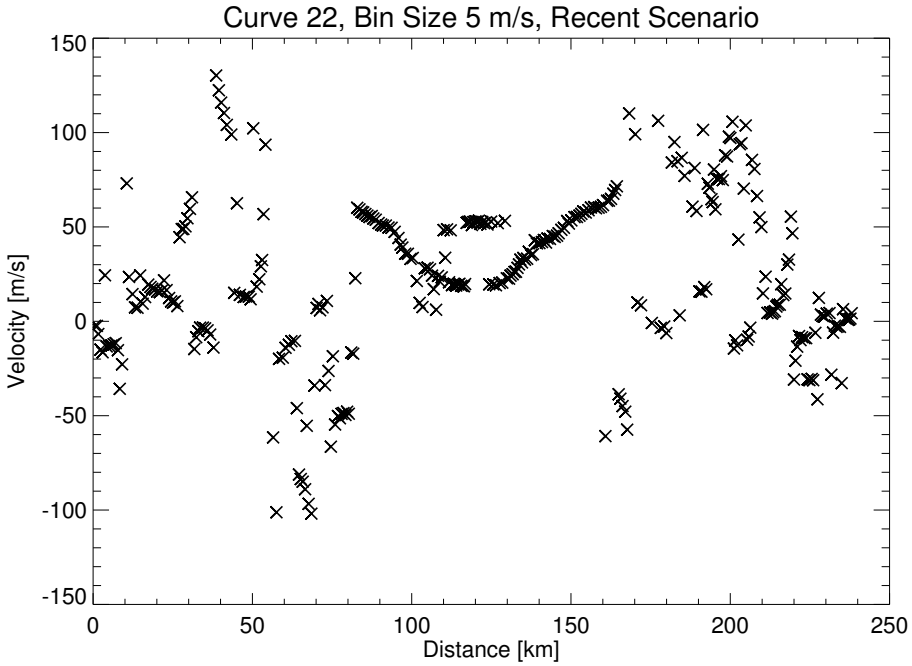

(a) Velocity plot Curve 22.

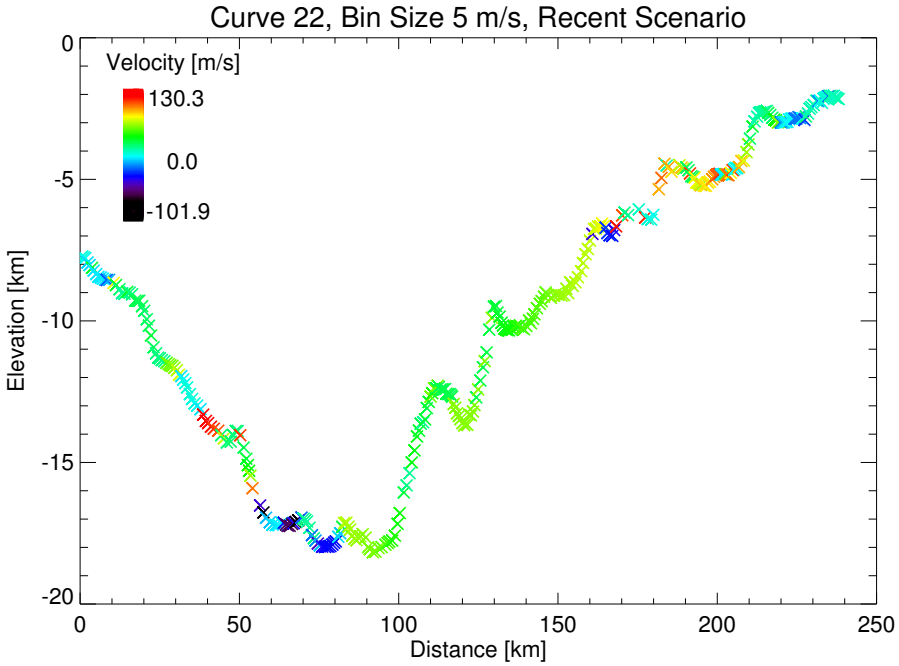

(b) Topography plot Curve 22.

Figure B.22.: Curve 22 evaluated with a bin size of 5 m/s with respect to Vesta's recent shape.

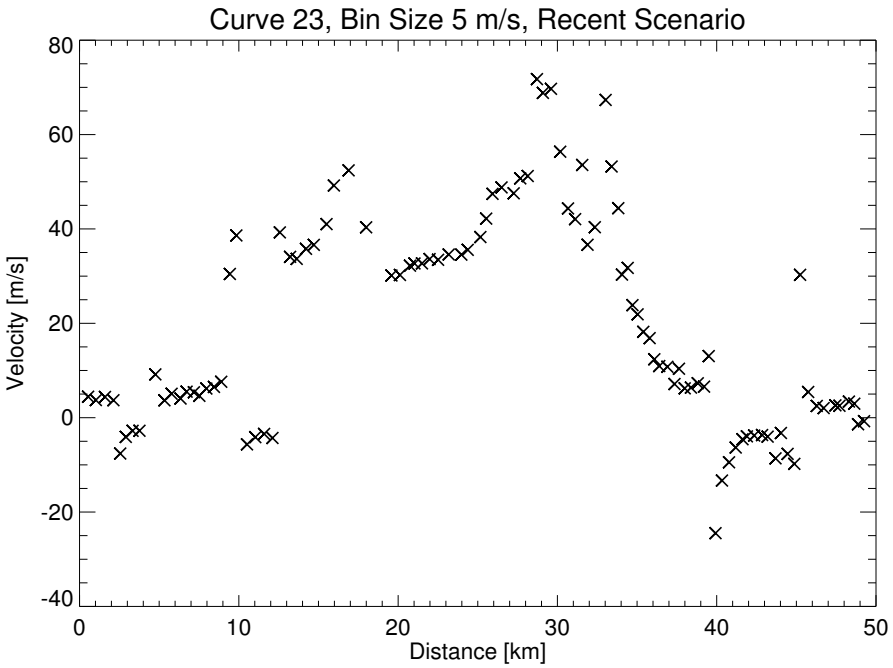

(a) Velocity plot Curve 23.

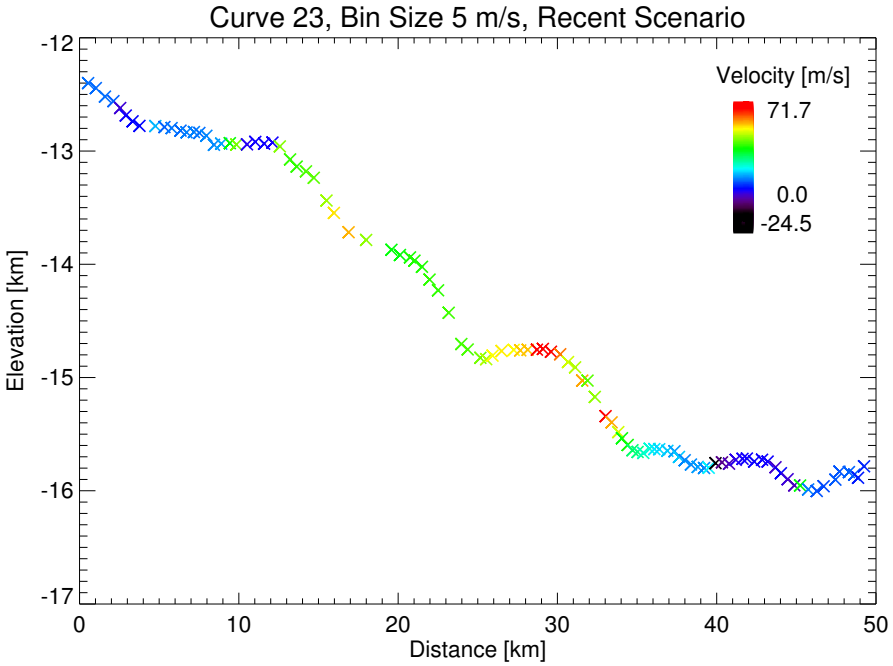

(b) Topography plot Curve 23.

Figure B.23.: Curve 23 evaluated with a bin size of 5 m/s with respect to Vesta's recent shape.

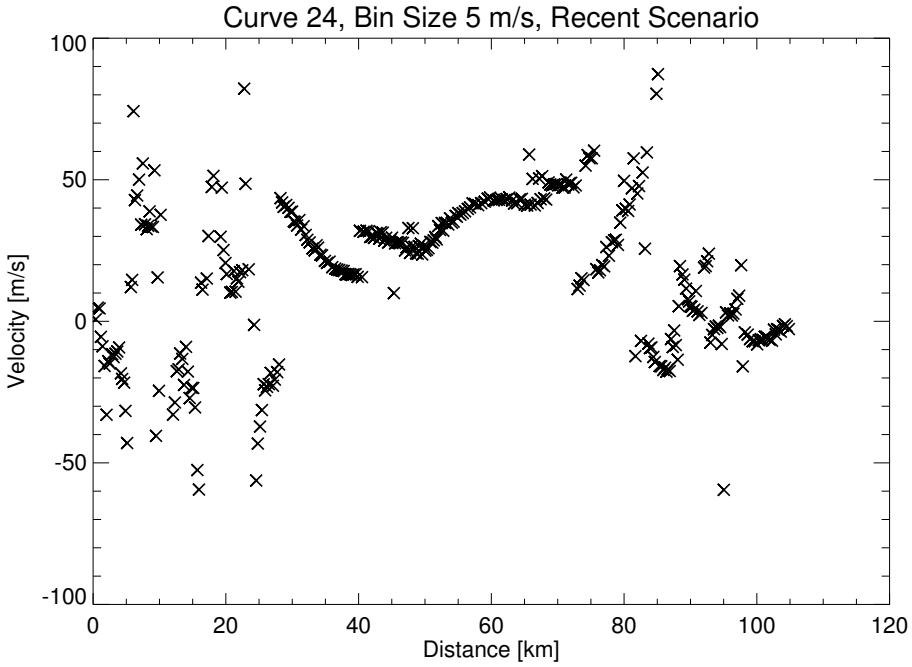

(a) Velocity plot Curve 24.

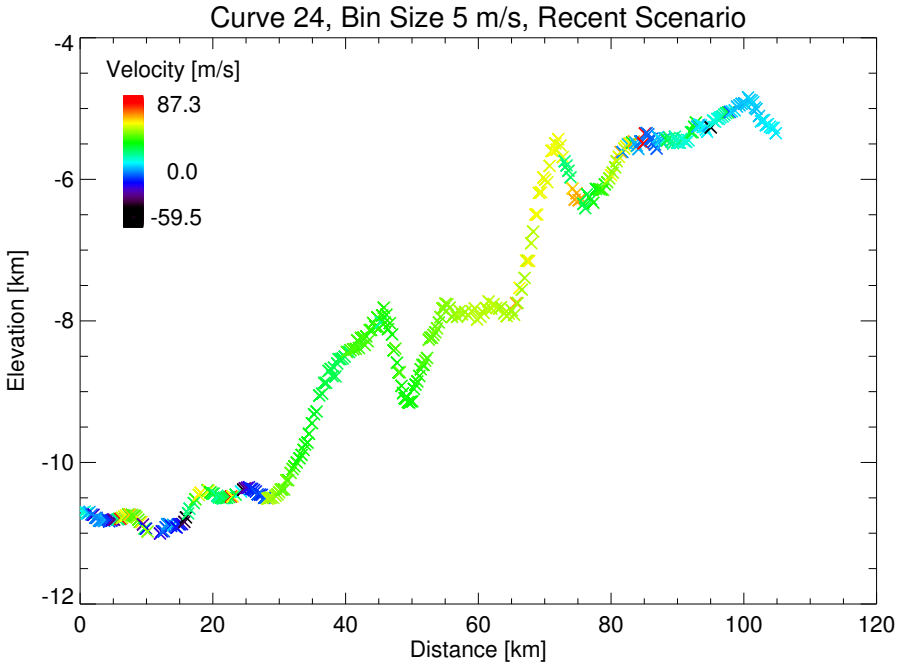

(b) Topography plot Curve 24.

Figure B.24.: Curve 24 evaluated with a bin size of 5 m/s with respect to Vesta's recent shape.

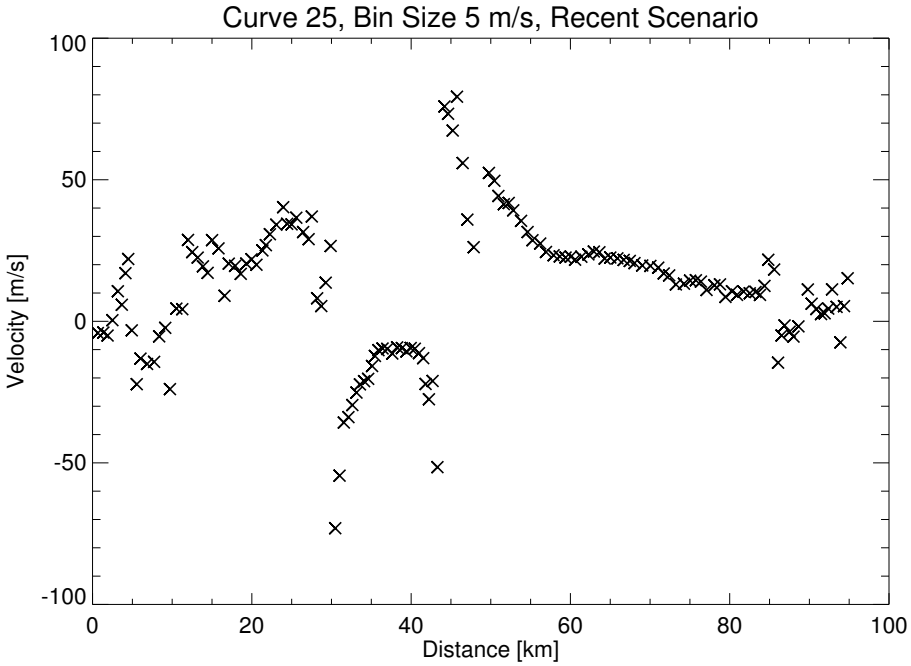

(a) Velocity plot Curve 25.

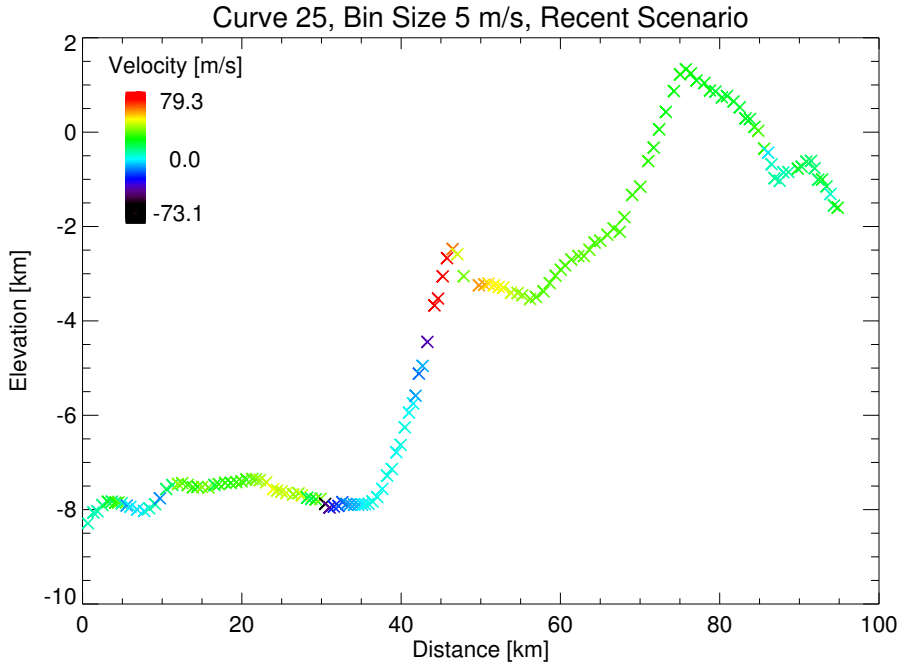

(b) Topography plot Curve 25.

Figure B.25.: Curve 25 evaluated with a bin size of 5 m/s with respect to Vesta's recent shape.

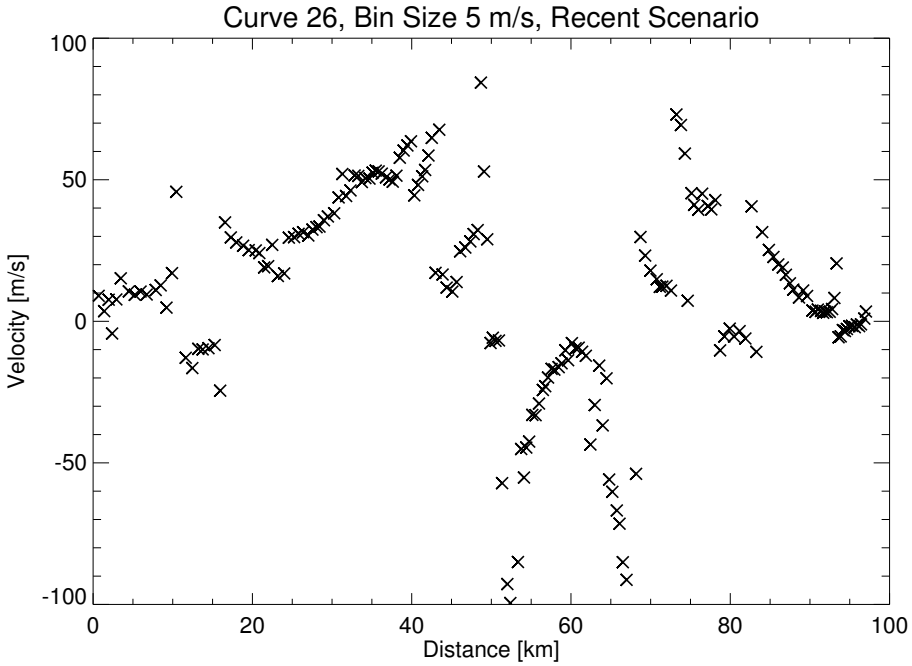

(a) Velocity plot Curve 26.

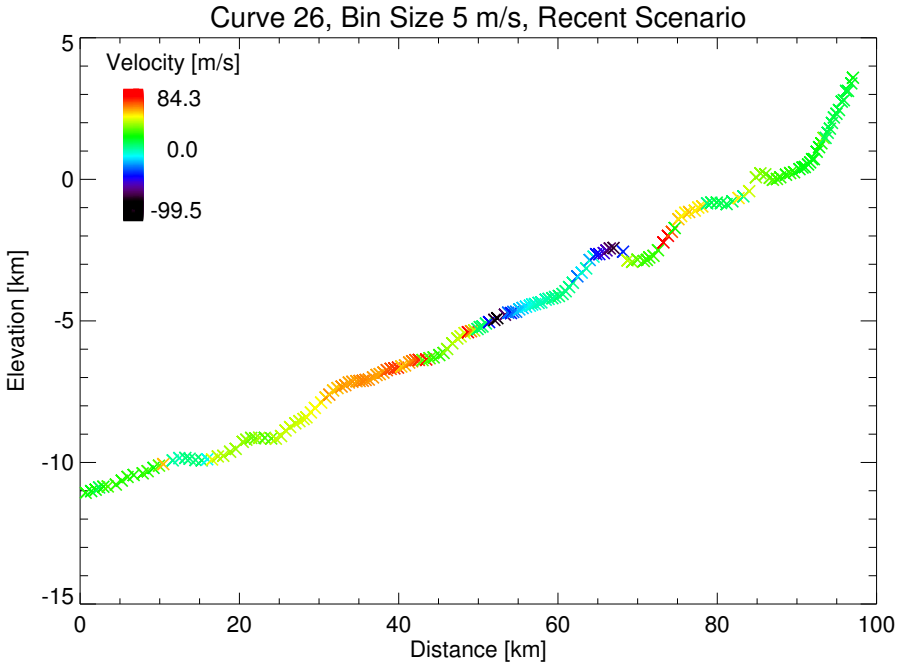

(b) Topography plot Curve 26.

Figure B.26.: Curve 26 evaluated with a bin size of 5 m/s with respect to Vesta's recent shape.

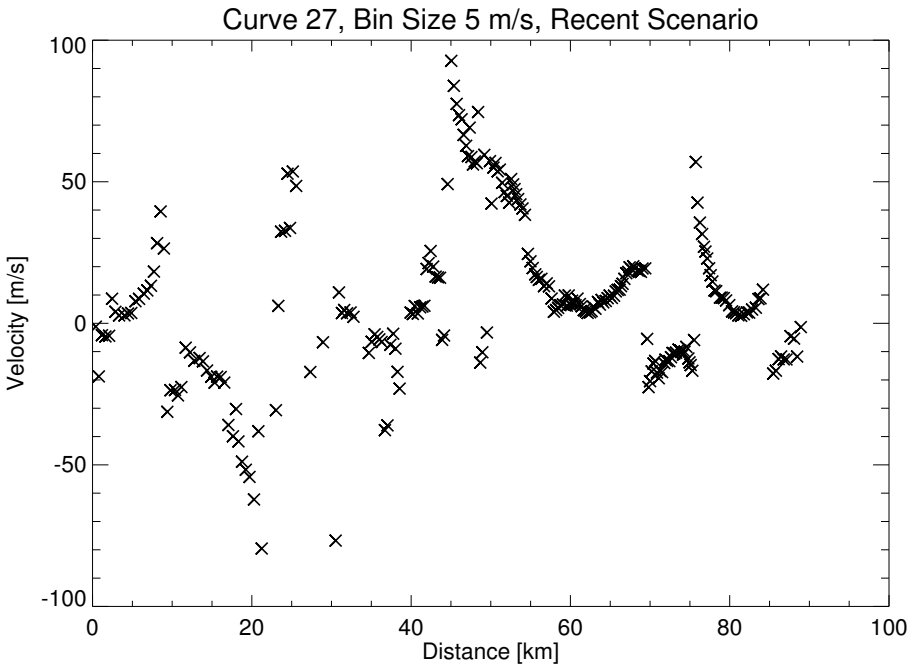

(a) Velocity plot Curve 27.

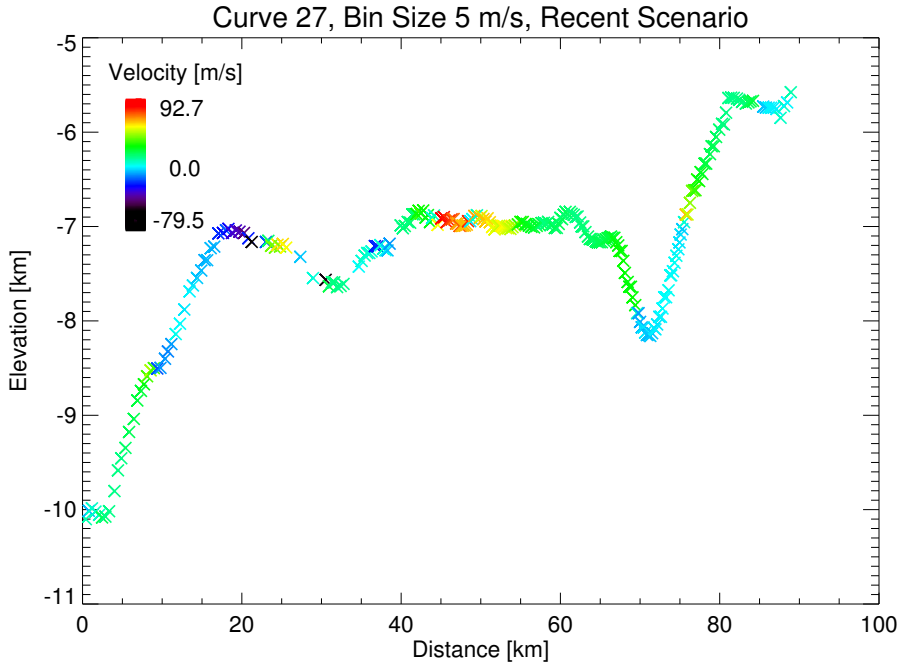

(b) Topography plot Curve 27.

Figure B.27.: Curve 27 evaluated with a bin size of 5 m/s with respect to Vesta's recent shape.

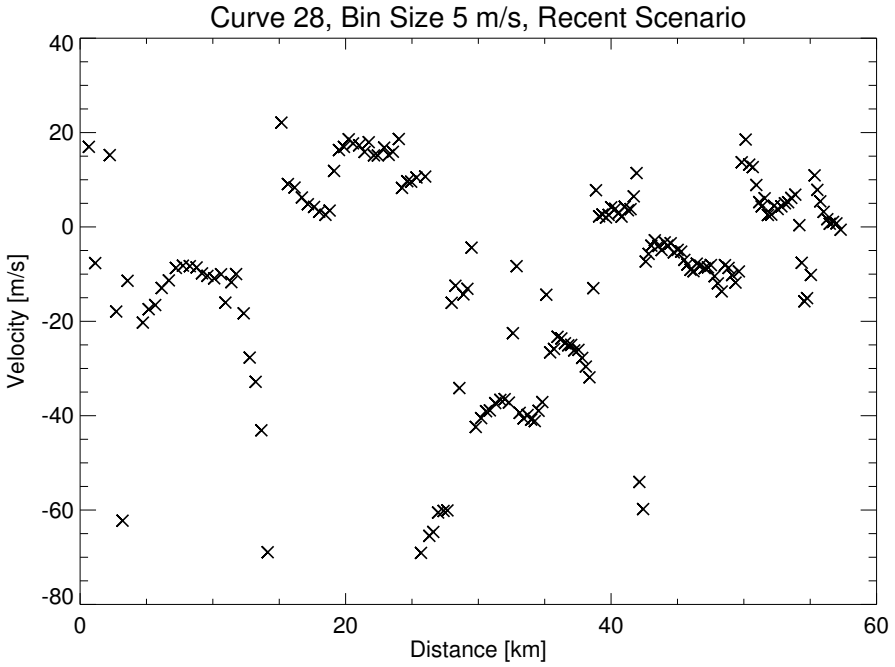

(a) Velocity plot Curve 28.

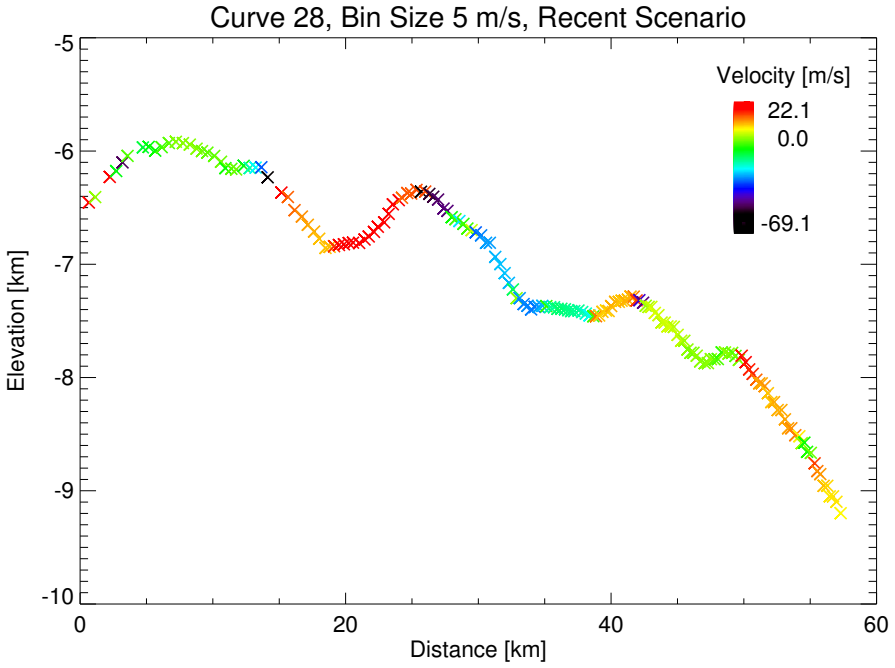

(b) Topography plot Curve 28.

Figure B.28.: Curve 28 evaluated with a bin size of 5 m/s with respect to Vesta's recent shape.

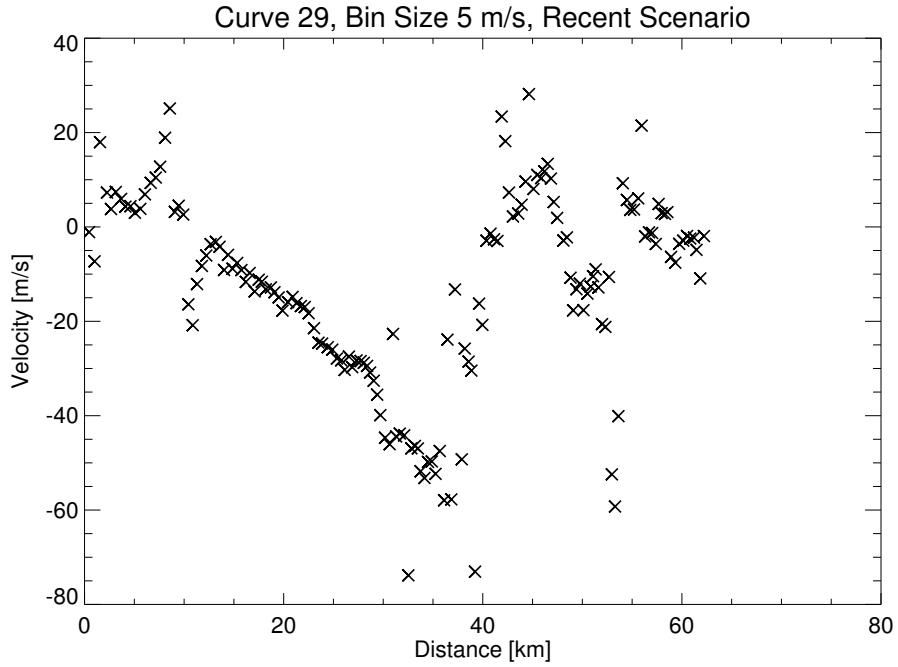

(a) Velocity plot Curve 29.

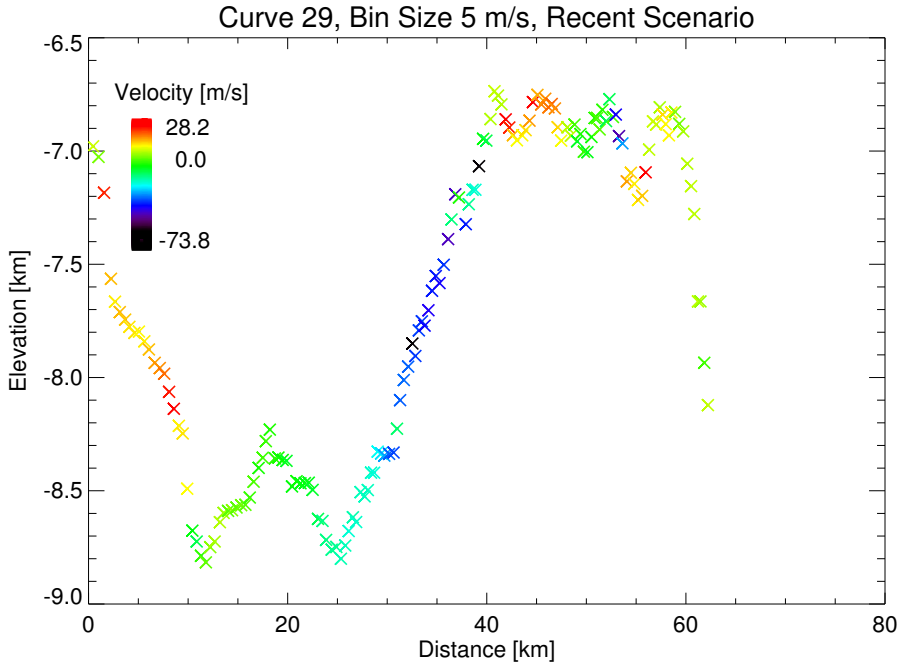

(b) Topography plot Curve 29.

Figure B.29.: Curve 29 evaluated with a bin size of 5 m/s with respect to Vesta's recent shape.

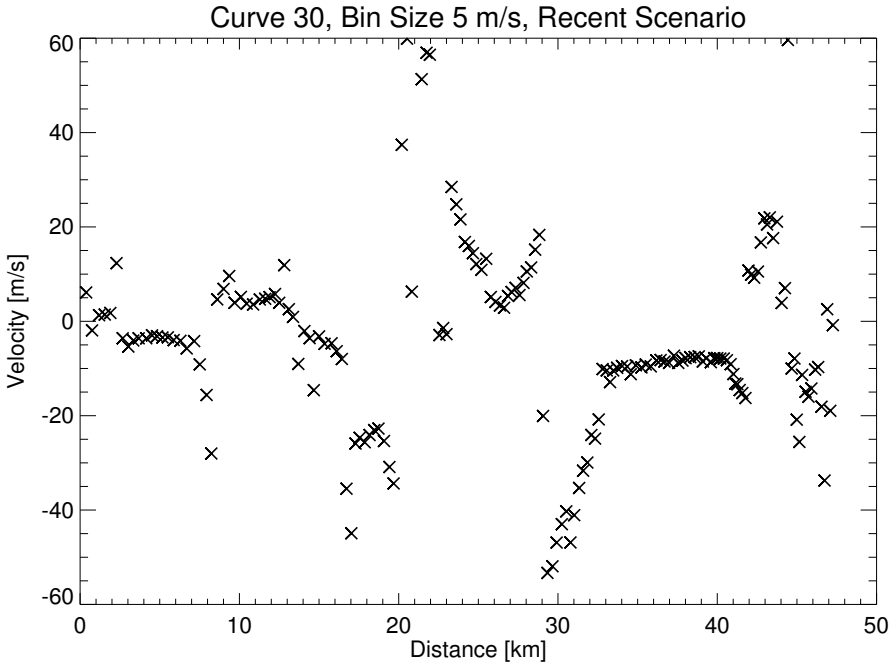

(a) Velocity plot Curve 30.

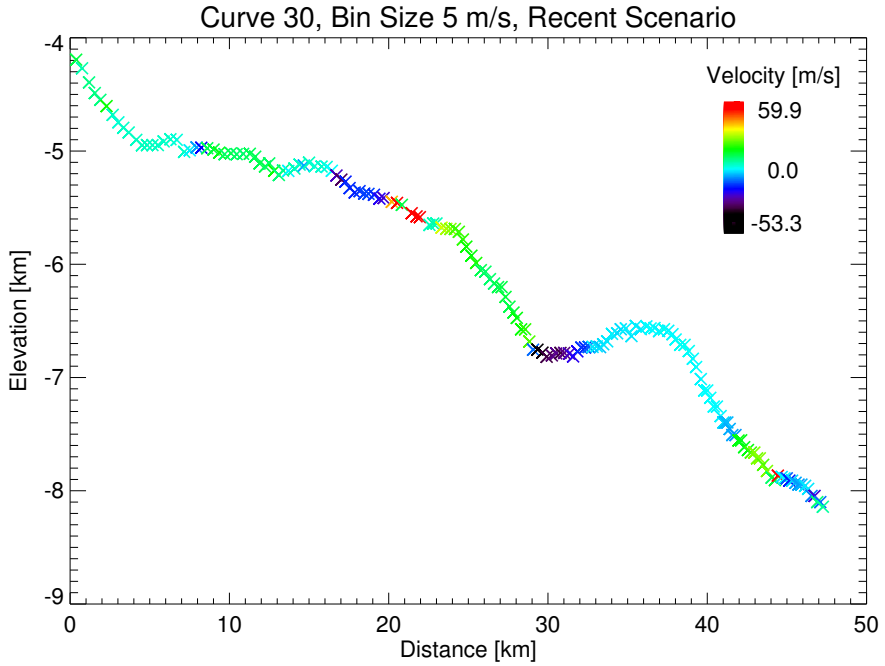

(b) Topography plot Curve 30.

Figure B.30.: Curve 30 evaluated with a bin size of 5 m/s with respect to Vesta's recent shape.

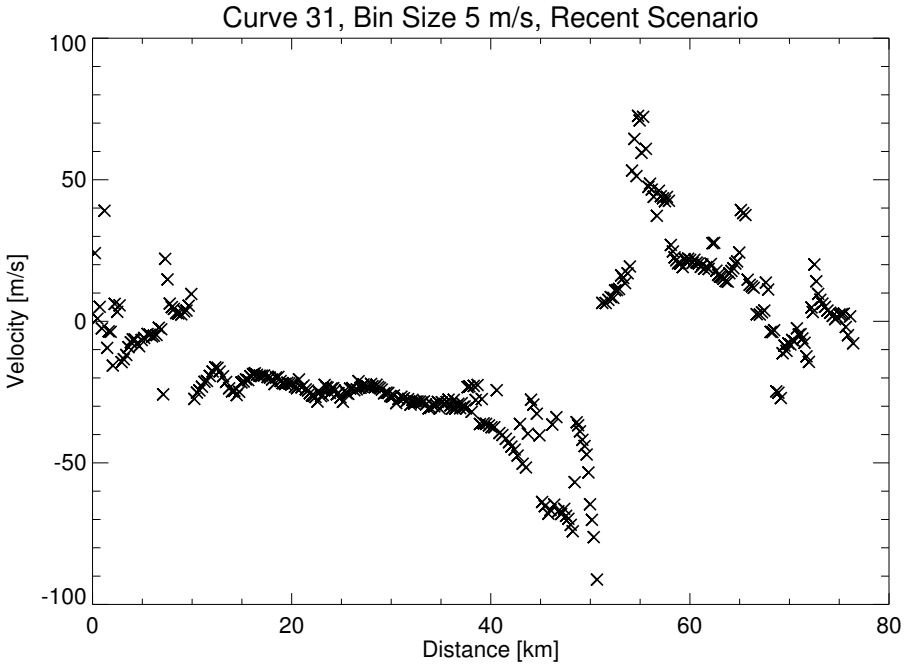

(a) Velocity plot Curve 31.

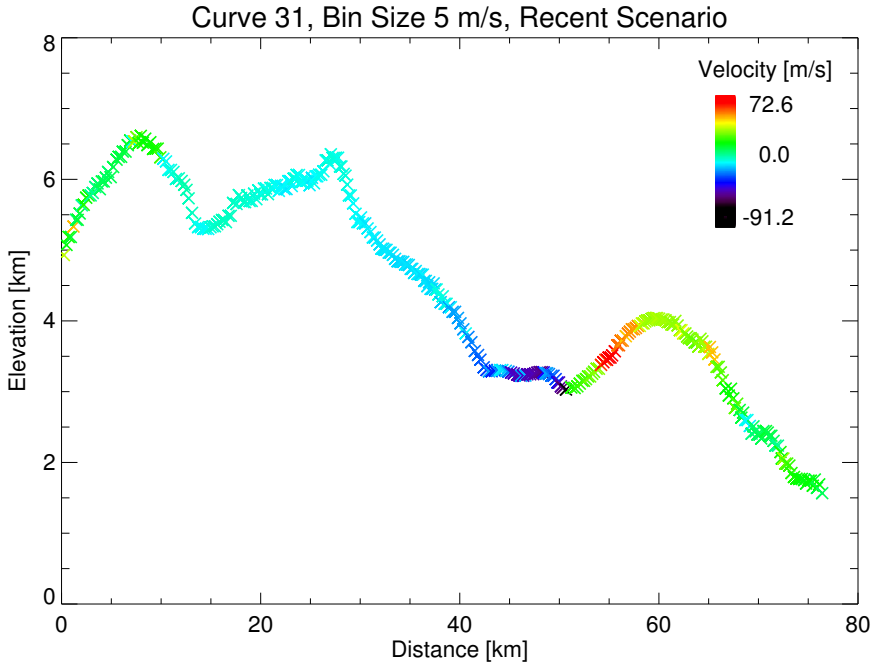

(b) Topography plot Curve 31.

Figure B.31.: Curve 31 evaluated with a bin size of 5 m/s with respect to Vesta's recent shape.

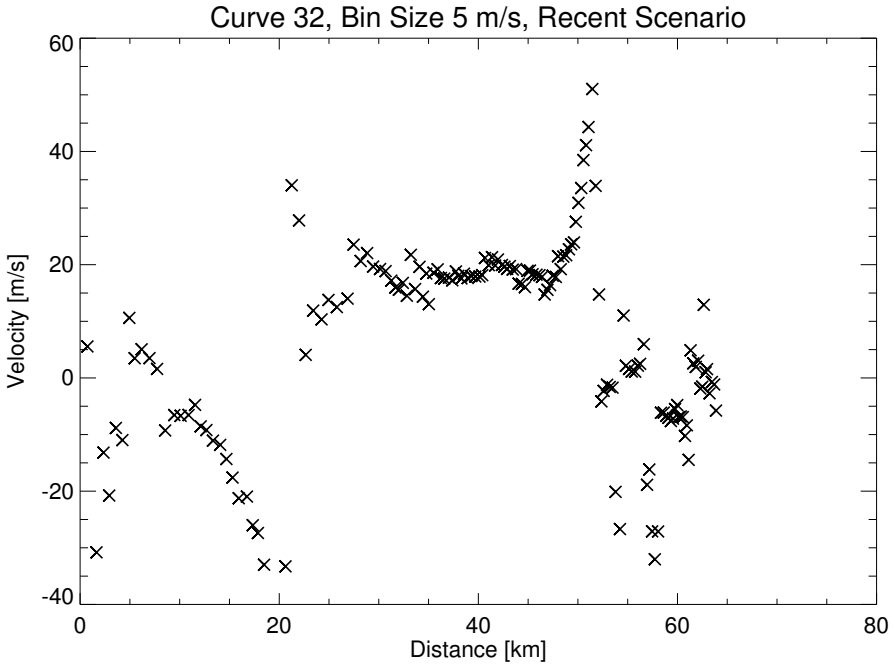

(a) Velocity plot Curve 32.

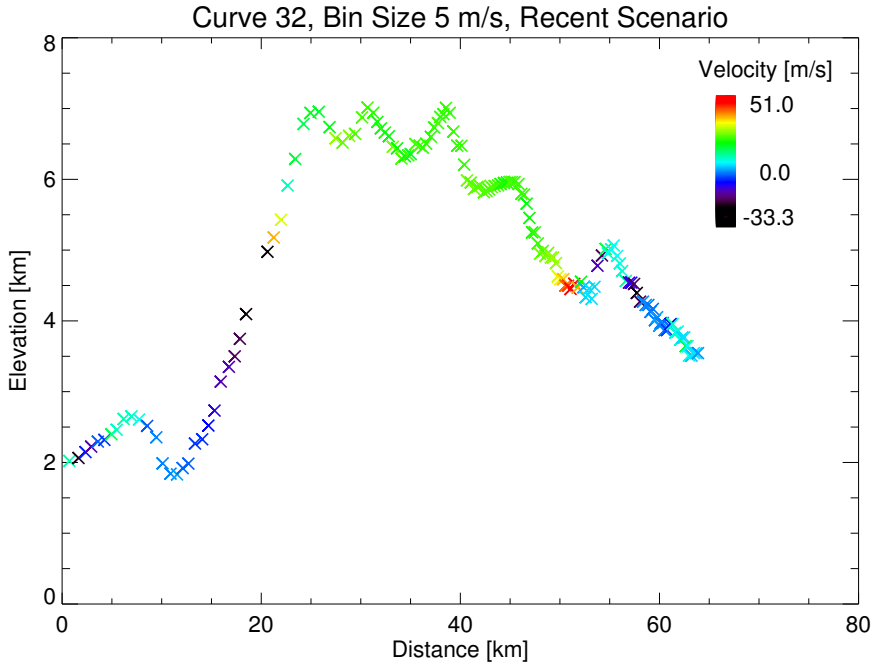

(b) Topography plot Curve 32.

Figure B.32.: Curve 32 evaluated with a bin size of 5 m/s with respect to Vesta's recent shape.

B.2. Curve Statistics

Table B.1.: Velocities of curved ridges of Region 1.

Curve	Number Mapping Points	Velocity Range [m/s]	Mean Velocity [m/s]	Mean Velocity Magnitude [m/s]	Mean Positive Velocity [m/s]
1	120	-48.0 ↔ 42.2	5.6 ±14.5	11.7 ±10.2	12.8 ±10.2
2	160	-62.6 ↔ 84.7	17.1 ±29.0	25.8 ±21.7	31.4 ±22.6
3	157	-42.4 ↔ 123.8	34.1 ±29.0	37.6 ±24.3	42.4 ±23.2
4	279	-69.7 ↔ 123.4	19.8 ±33.1	30.7 ±23.4	35.8 ±23.6
5	284	-61.6 ↔ 100.0	14.2 ±27.4	22.9 ±20.6	26.4 ±22.3
6	217	-43.9 ↔ 96.6	20.6 ±26.1	28.0 ±18.0	33.8 ±17.1
7	277	-65.9 ↔ 120.5	16.3 ±31.5	28.4 ±21.2	31.3 ±22.4
8	321	-18.1 ↔ 107.3	30.3 ±20.9	31.2 ±19.5	33.6 ±18.6
9	336	-59.6 ↔ 83.5	26.0 ±27.9	30.3 ±23.0	34.1 ±23.0
10	279	-119.0 ↔ 140.6	16.9 ±39.3	31.0 ±29.4	31.9 ±28.2
11	407	-104.8 ↔ 177.1	33.1 ±55.5	47.1 ±44.2	54.0 ±46.8
12	305	-54.5 ↔ 104.3	15.3 ±28.1	22.1 ±23.0	26.5 ±25.1
13	249	-54.1 ↔ 67.6	5.9 ±19.4	15.9 ±12.4	15.6 ±11.9
14	280	-48.2 ↔ 57.4	1.6 ±18.2	14.0 ±11.7	13.8 ±13.0
15	369	-91.1 ↔ 99.3	3.0 ±30.8	23.3 ±20.3	20.5 ±18.5
16	757	-104.0 ↔ 120.8	9.9 ±35.7	28.8 ±23.3	30.5 ±24.1

Table B.2.: Velocities of curved ridges of Region 2.

Curve	Number Mapping Points	Velocity Range [m/s]	Mean Velocity [m/s]	Mean Velocity Magnitude [m/s]	Mean Positive Velocity [m/s]
17	208	-48.4	12.5	19.4	22.0
		↔ 85.8	±21.8	±15.9	±16.5
18	191	-61.3	-1.8	14.3	13.1
		↔ 50.1	±19.1	±12.7	±11.9
19	380	-121.0	15.6	32.1	40.9
		↔ 146.1	±43.4	±33.1	±38.0
20	394	-68.5	3.8	27.9	28.4
		↔ 105.5	±34.9	±21.2	±22.0
21	223	-116.8	14.8	32.8	42.6
		↔ 133.7	±39.8	±26.9	±28.4
22	364	-101.9	23.6	38.0	41.7
		↔ 130.3	±41.1	±28.4	±28.4
23	105	-24.5	19.4	22.1	26.9
		↔ 71.7	±22.3	±19.6	±19.7
24	373	-59.5	17.9	26.6	30.9
		↔ 87.3	±25.6	±16.3	±15.3
25	149	-73.1	10.9	21.0	22.8
		↔ 79.3	±23.7	±15.5	±15.4
26	195	-99.5	10.4	27.9	29.7
		↔ 84.3	±34.1	±22.1	±19.4
27	283	-79.5	7.9	20.7	22.3
		↔ 92.7	±27.1	±19.2	±21.0

Table B.3.: Velocities of curved ridges of Region 3.

Curve	Number Mapping Points	Velocity Range [m/s]	Mean Velocity [m/s]	Mean Velocity Magnitude [m/s]	Mean Negative Velocity [m/s]
28	179	-69.1 ↔ 22.1	-9.8 ±20.6	16.6 ±15.7	-22.0 ±17.7
29	160	-73.8 ↔ 28.2	-13.2 ±20.6	18.1 ±16.4	-21.8 ±17.6
30	173	-53.3 ↔ 59.9	-4.2 ±19.3	14.5 ±13.3	-14.9 ±12.4
31	356	-91.2 ↔ 72.6	-11.2 ±27.2	24.4 ±16.4	-26.6 ±15.6
32	160	-33.3 ↔ 51.0	6.9 ±16.7	15.2 ±9.6	-12.0 ±9.5

Table B.4.: Joint velocities of curved ridges in the regions.

Region	Number Mapping Points	Velocity Range [m/s]	Mean Velocity [m/s]	Mean Magnitude Velocity [m/s]	Mean Pos./Neg. Velocity [m/s]
1	120	-119.0 ↔ 177.1	16.6 ±33.9	27.9 ±25.5	31.2 ±26.8
2	160	-121.0 ↔ 146.0	12.6 ±33.9	27.2 ±23.8	31.0 ±25.3
3	157	-91.2 ↔ 72.6	-7.3 ±23.4	19.0 ±15.4	-21.6 ±16.2
all	279	-121.0 ↔ 177.1	12.4 ±33.7	26.6 ±24.1	30.0/-20.3 ±25.9/18.8

B.3. Curve Measurements

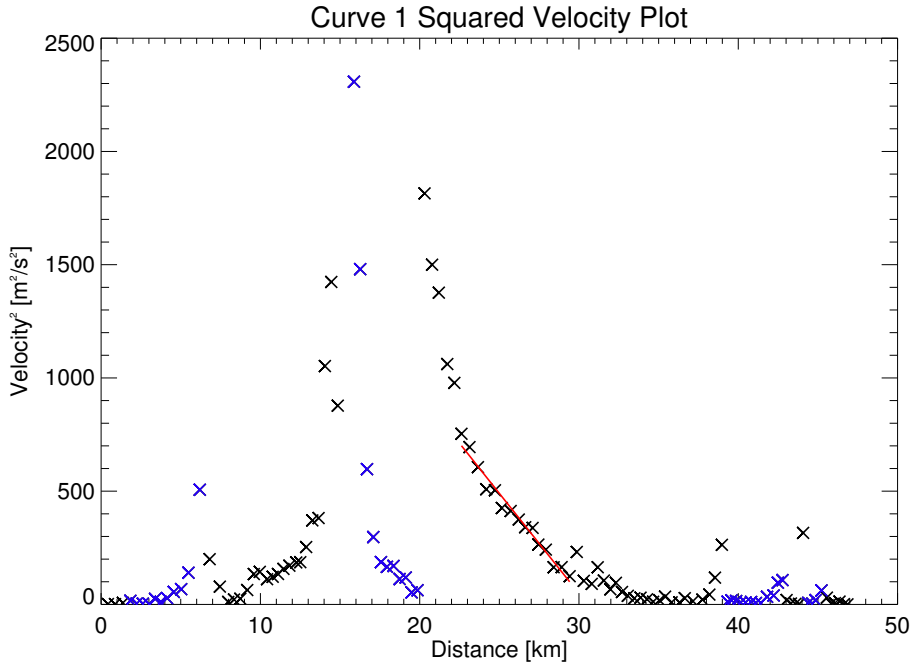

(a) Squared velocity plot Curve 1. Black and blue points are values derived from positive and negative velocities, respectively.

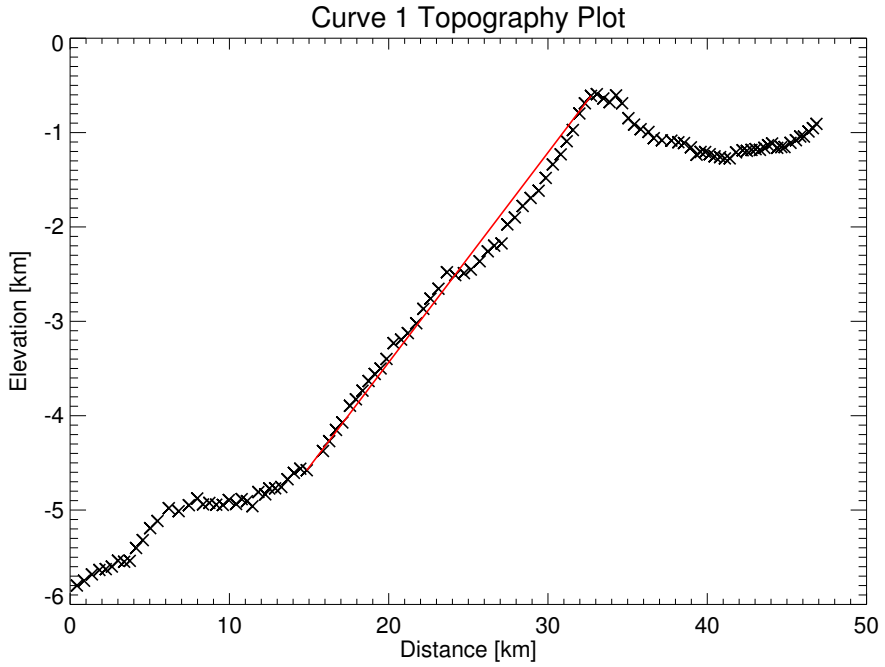

(b) Topography plot Curve 1.

Figure B.33.: Measurements (red line) derived from Curve 1 evaluated with a bin size of 5 m/s with respect to Vesta's recent shape.

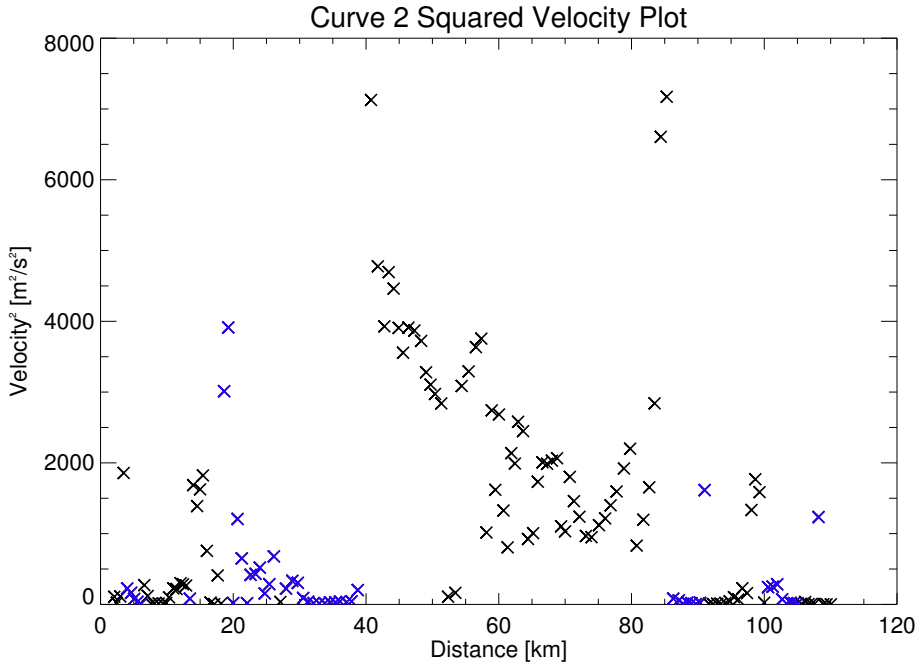

(a) Squared velocity plot Curve 2. Black and blue points are values derived from positive and negative velocities, respectively.

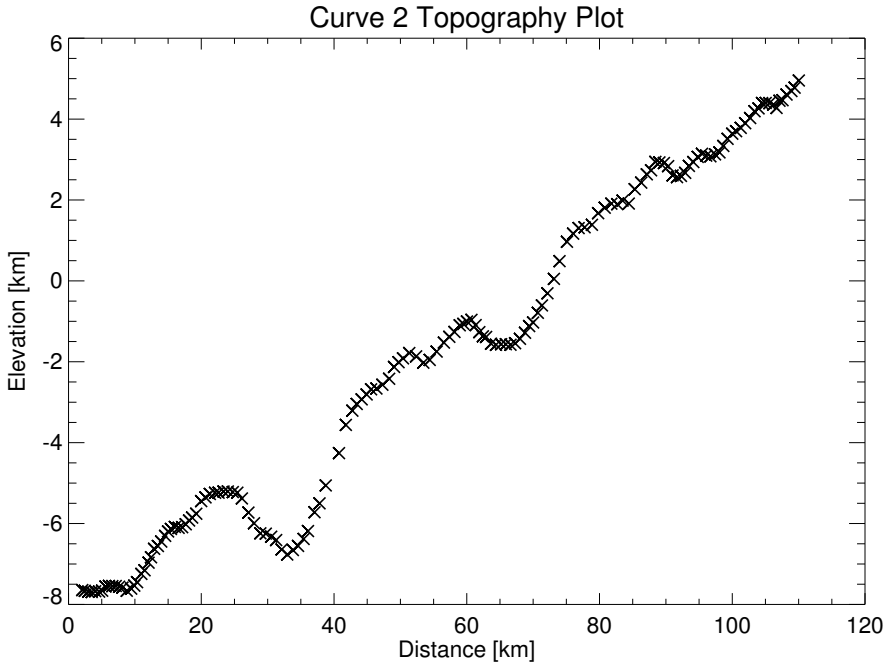

(b) Topography plot Curve 2.

Figure B.34.: Curve 2 evaluated with a bin size of 5 m/s with respect to Vesta's recent shape.

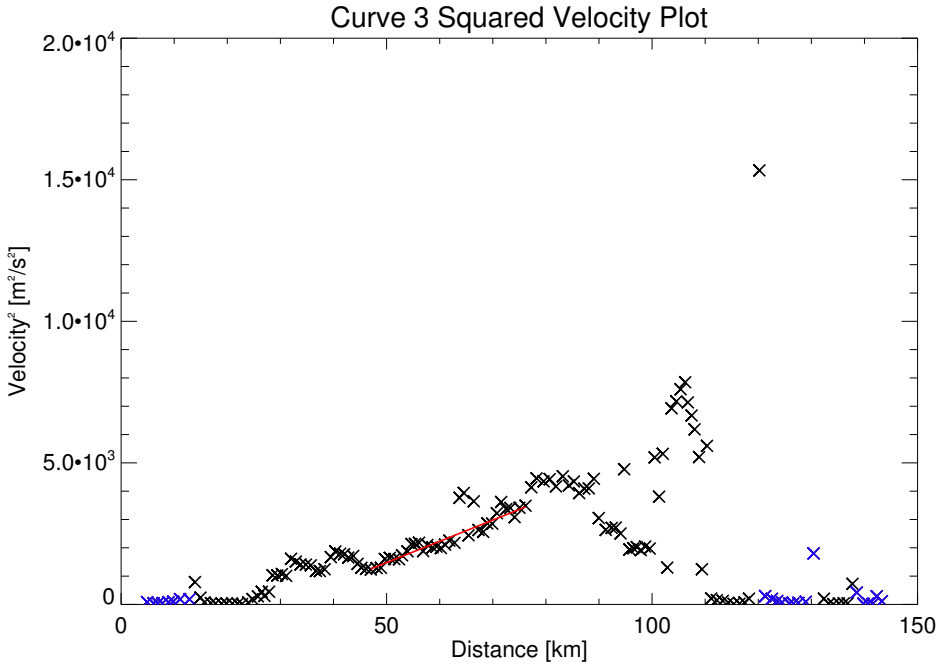

(a) Squared velocity plot Curve 3. Black and blue points are values derived from positive and negative velocities, respectively.

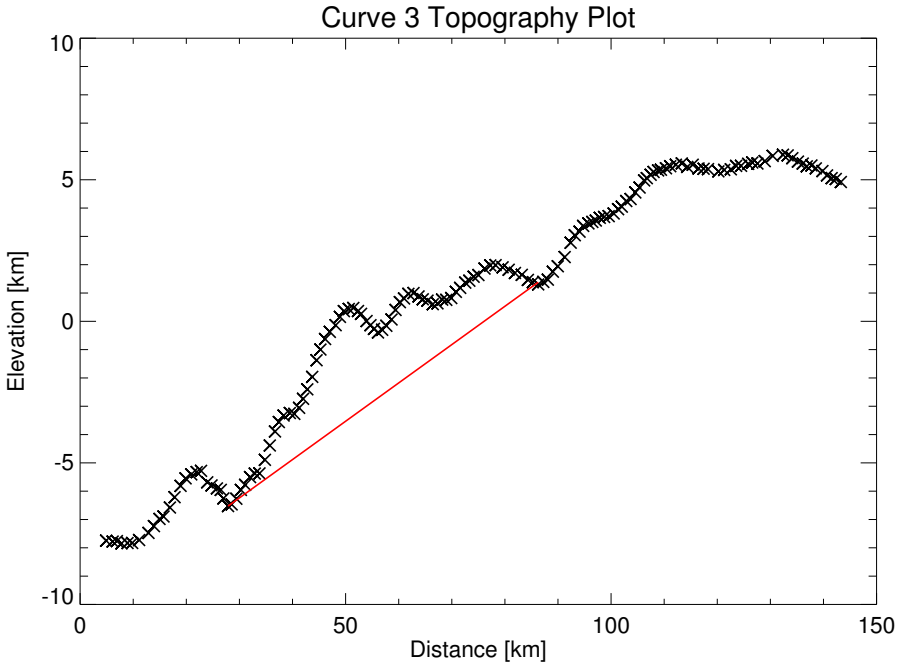

(b) Topography plot Curve 3.

Figure B.35.: Measurements (red line) derived from Curve 3 evaluated with a bin size of 5 m/s with respect to Vesta's recent shape.

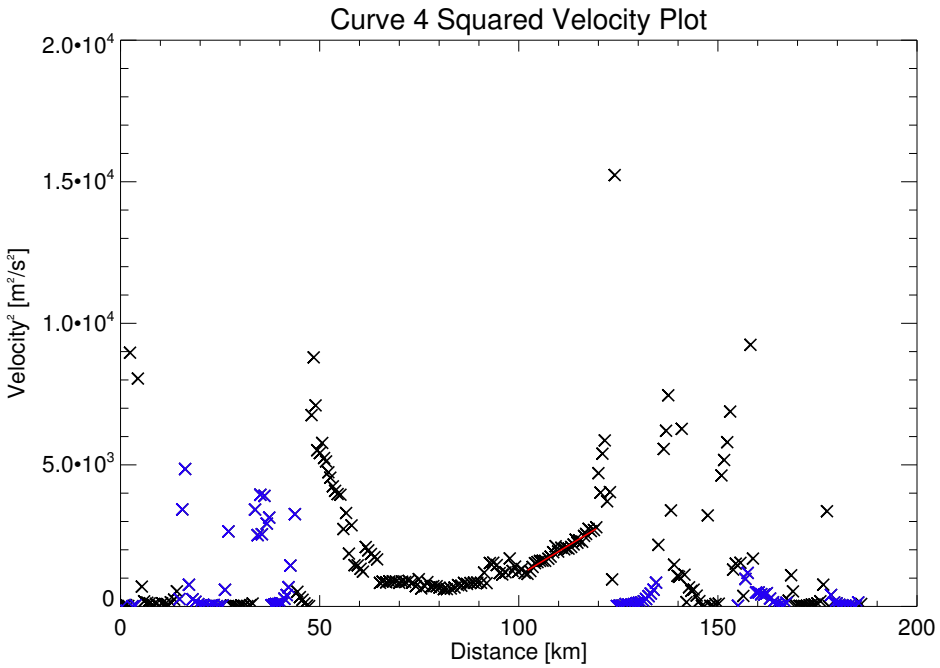

(a) Squared velocity plot Curve 4. Black and blue points are values derived from positive and negative velocities, respectively.

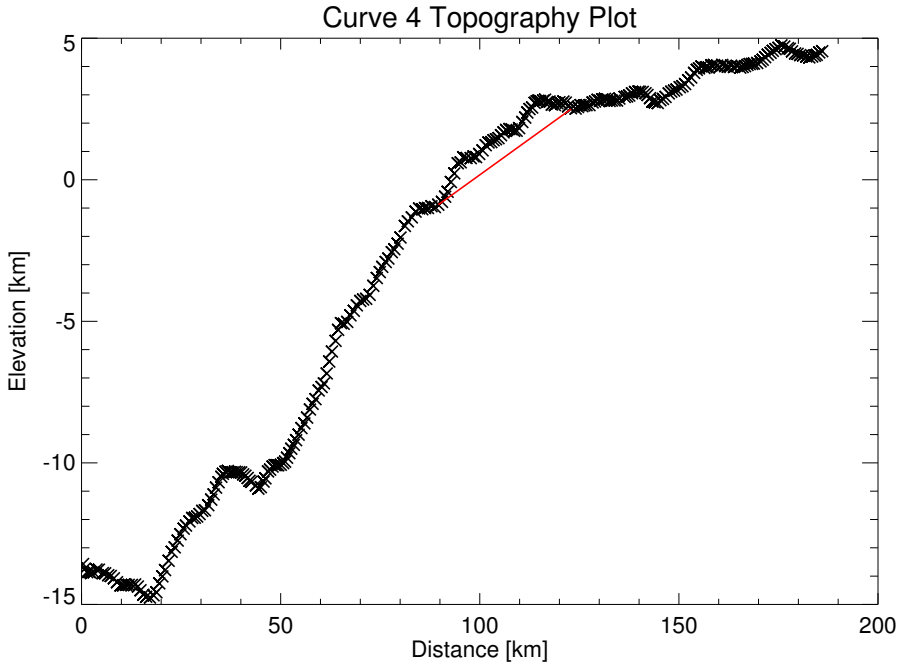

(b) Topography plot Curve 4.

Figure B.36.: Measurements (red line) derived from Curve 4 evaluated with a bin size of 5 m/s with respect to Vesta's recent shape.

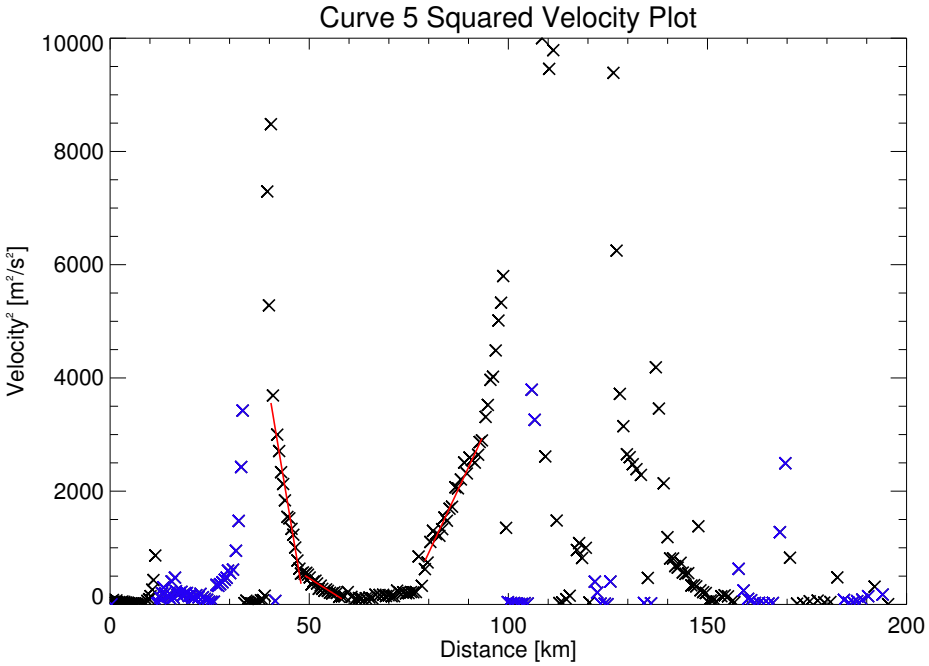

(a) Squared velocity plot Curve 5. Black and blue points are values derived from positive and negative velocities, respectively.

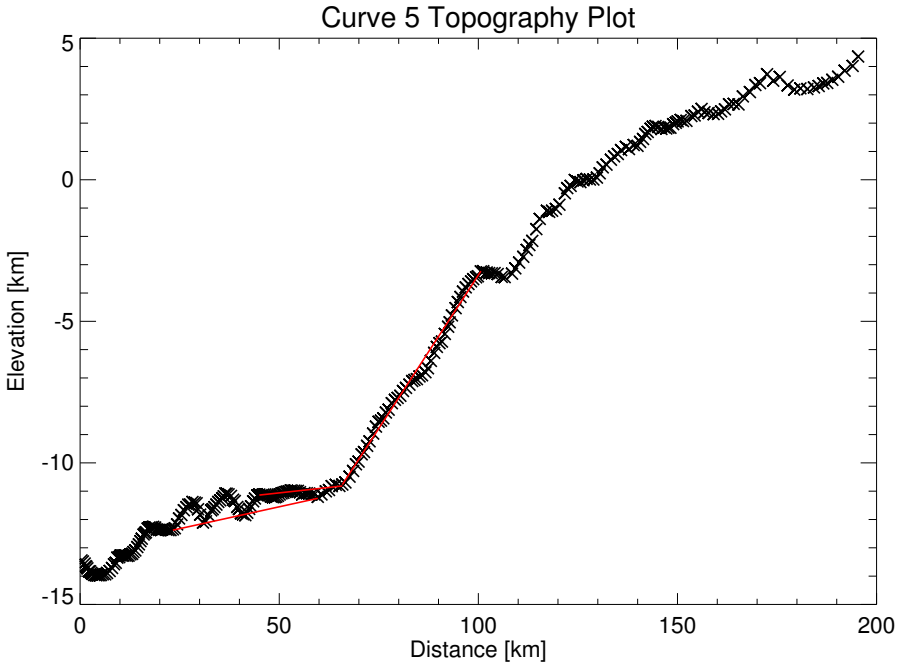

(b) Topography plot Curve 5.

Figure B.37.: Measurements (red line) derived from Curve 5 evaluated with a bin size of 5 m/s with respect to Vesta's recent shape.

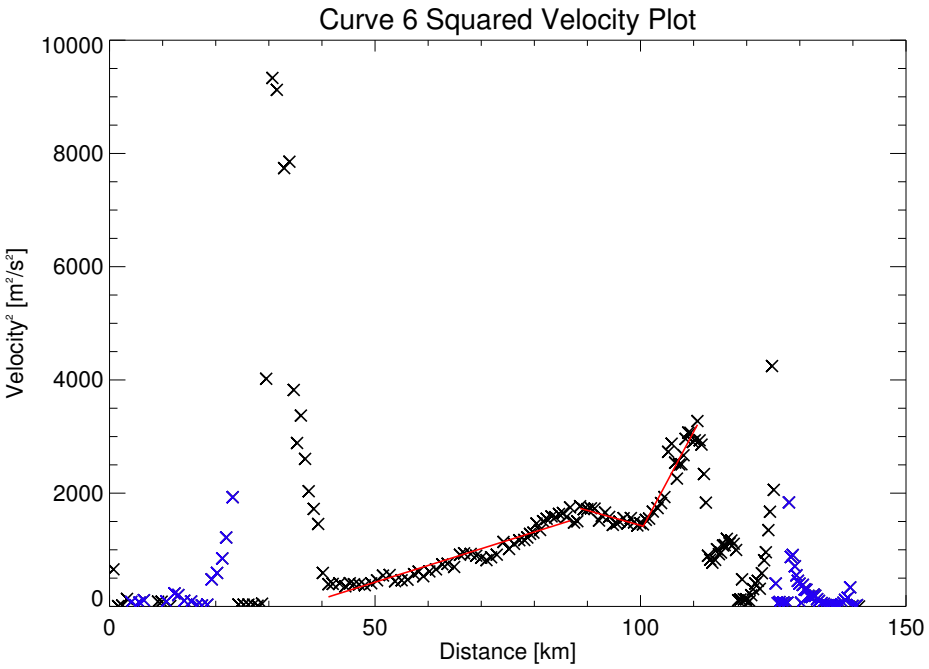

(a) Squared velocity plot Curve 6. Black and blue points are values derived from positive and negative velocities, respectively.

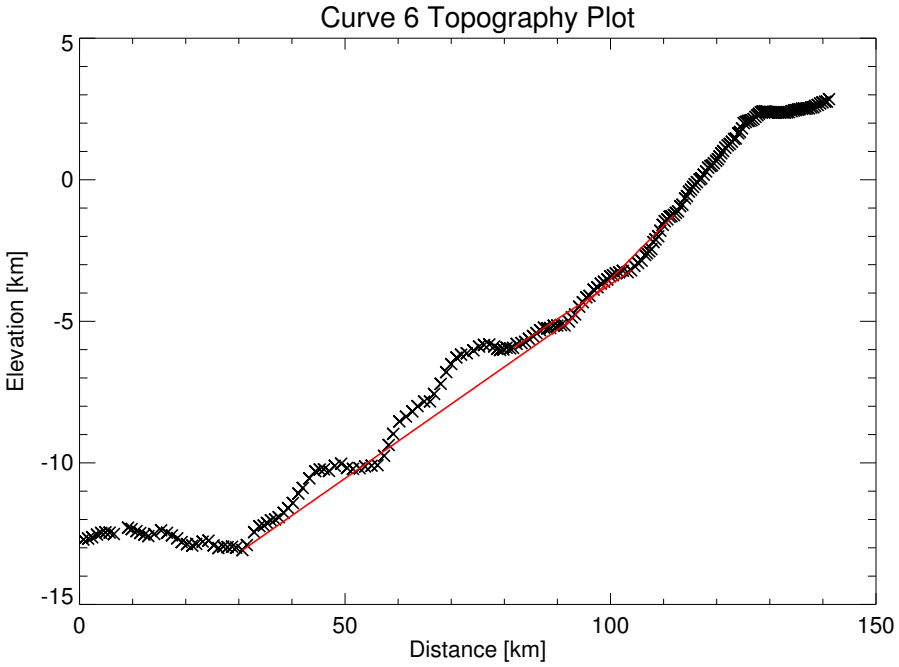

(b) Topography plot Curve 6.

Figure B.38.: Measurements (red line) derived from Curve 6 evaluated with a bin size of 5 m/s with respect to Vesta's recent shape.

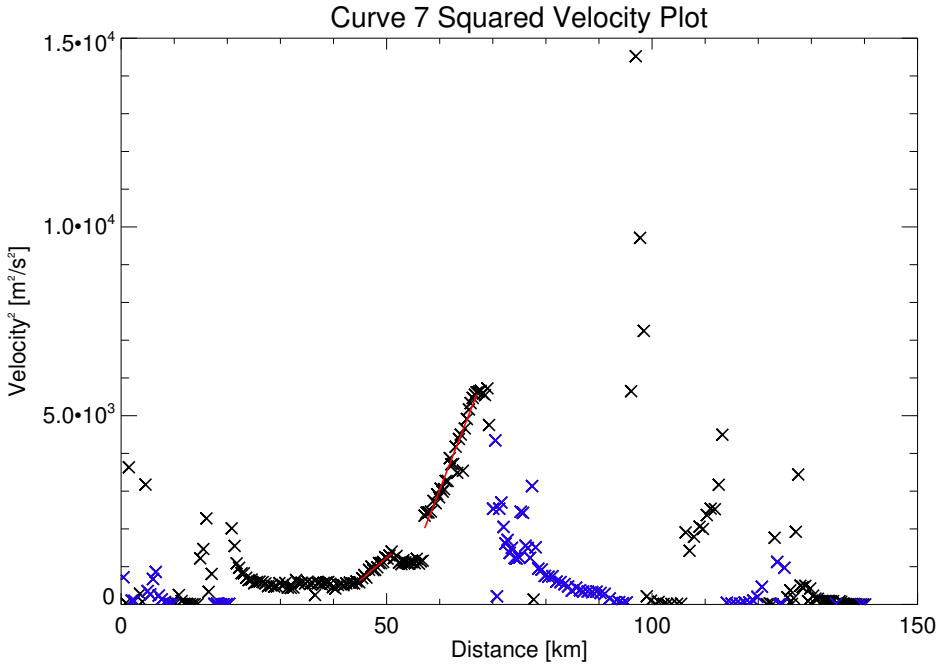

(a) Squared velocity plot Curve 7. Black and blue points are values derived from positive and negative velocities, respectively.

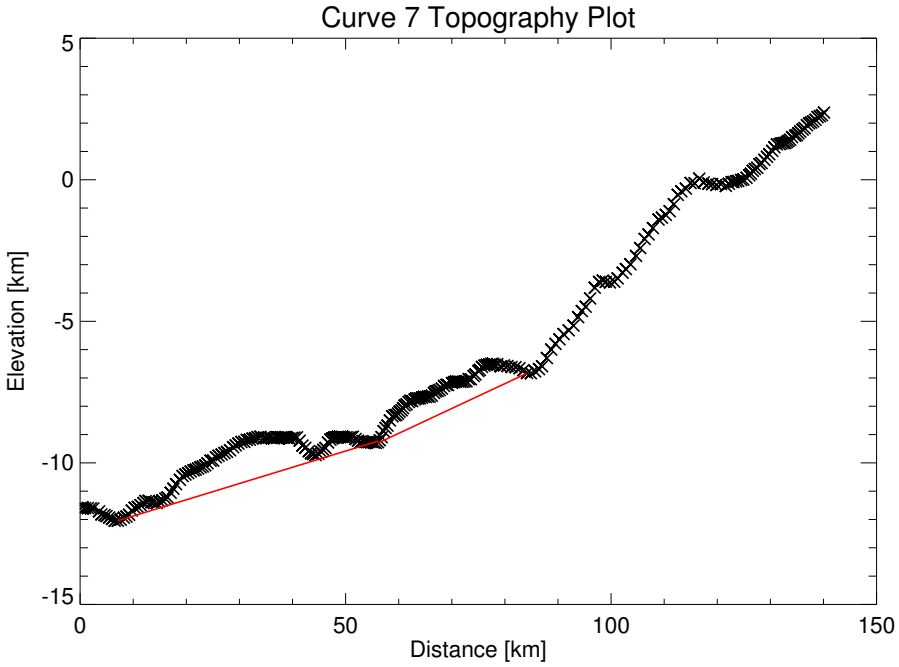

(b) Topography plot Curve 7.

Figure B.39.: Measurements (red line) derived from Curve 7 evaluated with a bin size of 5 m/s with respect to Vesta's recent shape.

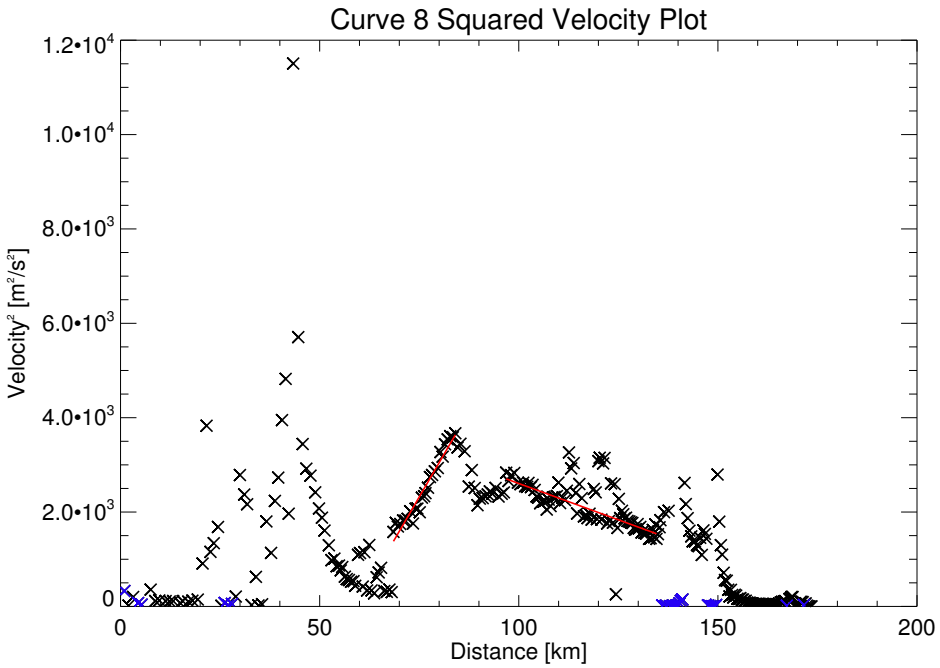

(a) Squared velocity plot Curve 8. Black and blue points are values derived from positive and negative velocities, respectively.

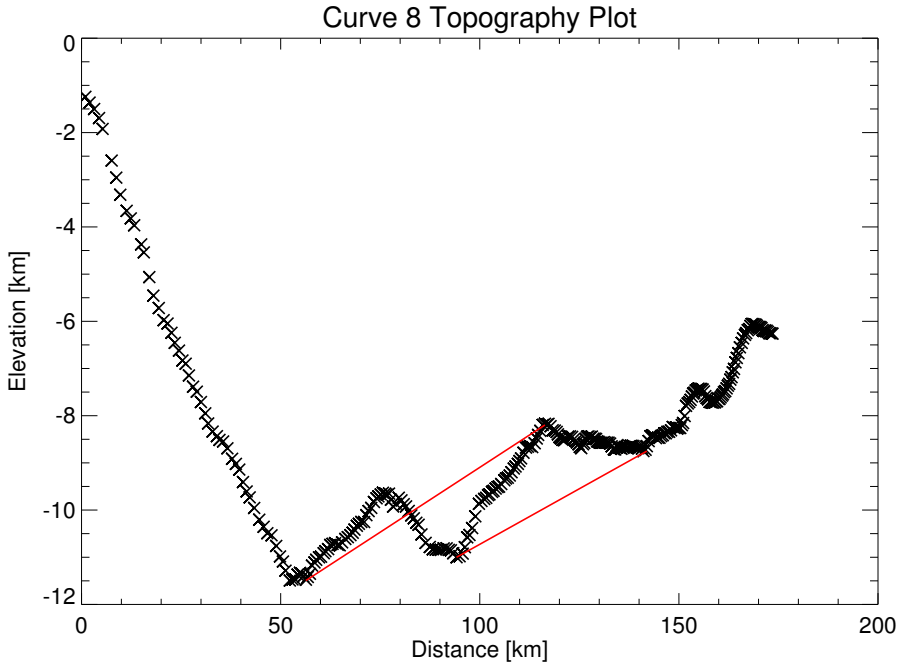

(b) Topography plot Curve 8.

Figure B.40.: Measurements (red line) derived from Curve 8 evaluated with a bin size of 5 m/s with respect to Vesta's recent shape.

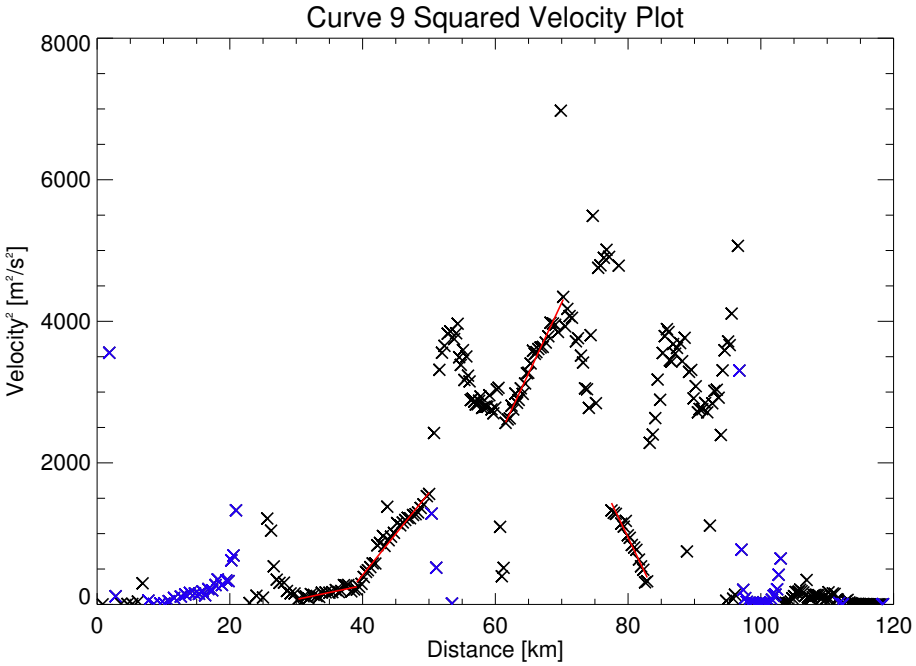

(a) Squared velocity plot Curve 9. Black and blue points are values derived from positive and negative velocities, respectively.

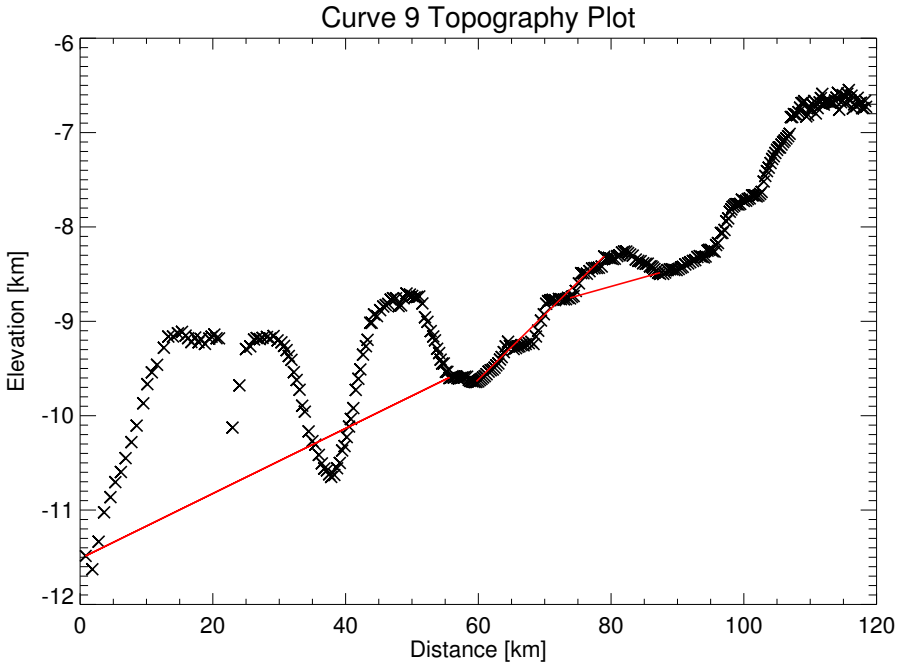

(b) Topography plot Curve 9.

Figure B.41.: Measurements (red line) derived from Curve 9 evaluated with a bin size of 5 m/s with respect to Vesta's recent shape.

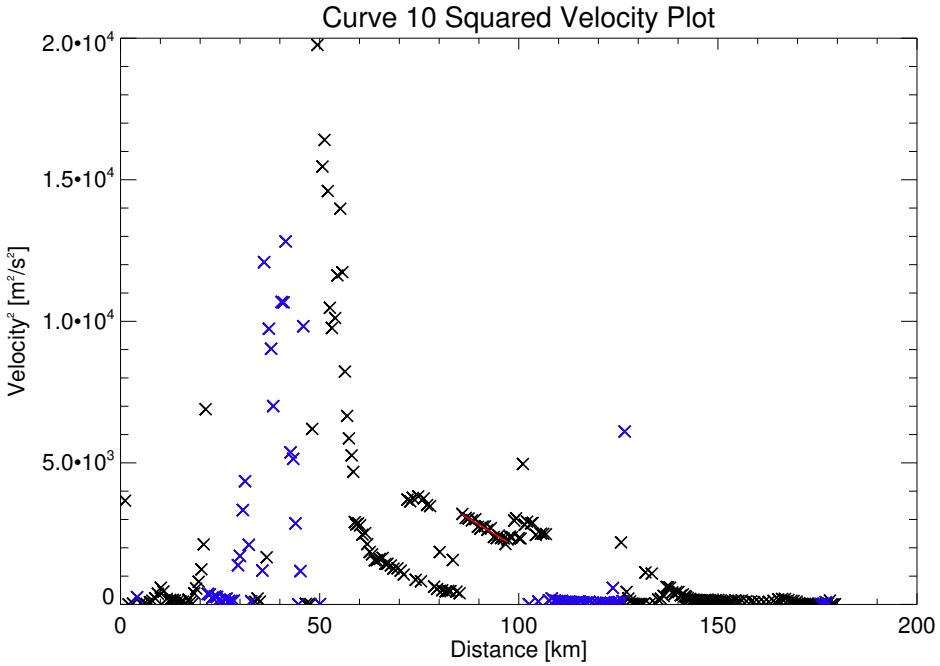

(a) Squared velocity plot Curve 10. Black and blue points are values derived from positive and negative velocities, respectively.

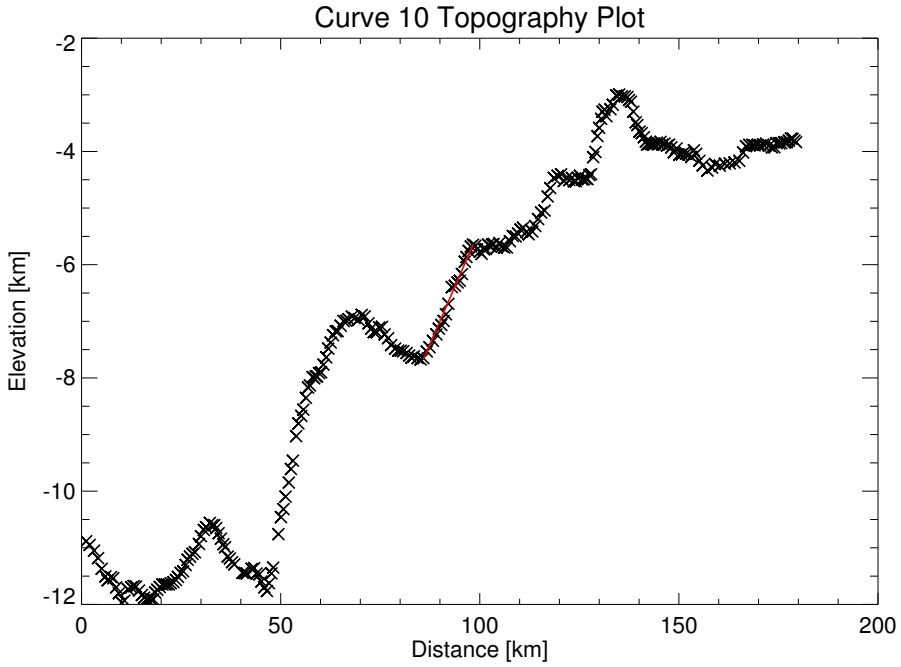

(b) Topography plot Curve 10.

Figure B.42.: Measurements (red line) derived from Curve 10 evaluated with a bin size of 5 m/s with respect to Vesta's recent shape.

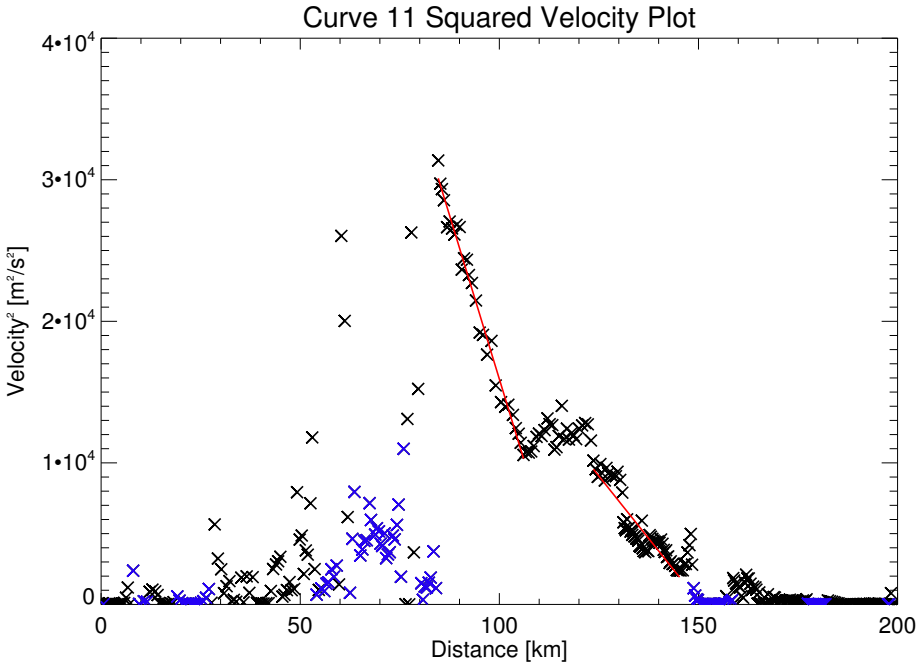

(a) Squared velocity plot Curve 11. Black and blue points are values derived from positive and negative velocities, respectively.

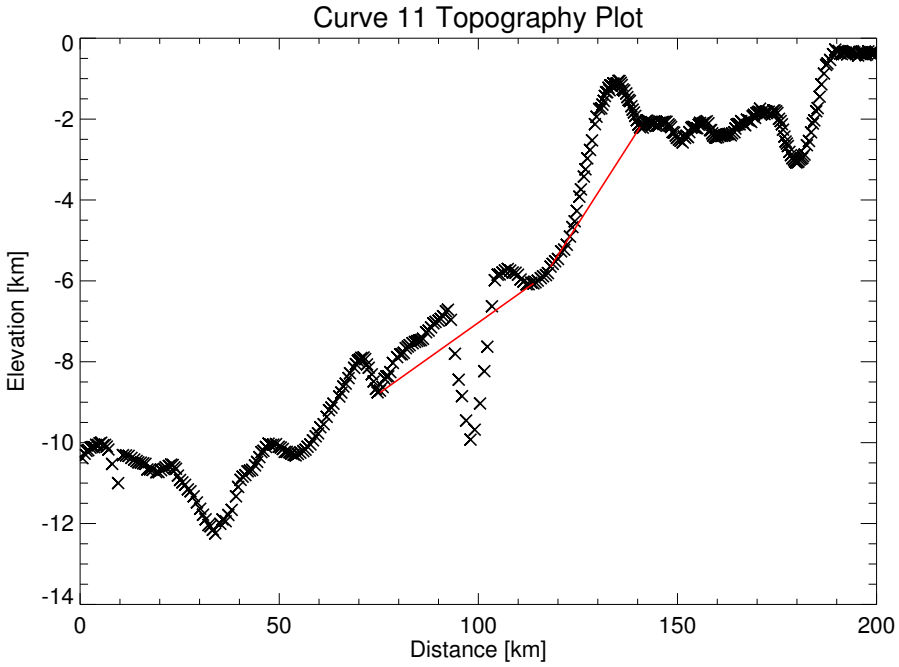

(b) Topography plot Curve 11.

Figure B.43.: Measurements (red line) derived from Curve 11 evaluated with a bin size of 5 m/s with respect to Vesta's recent shape.

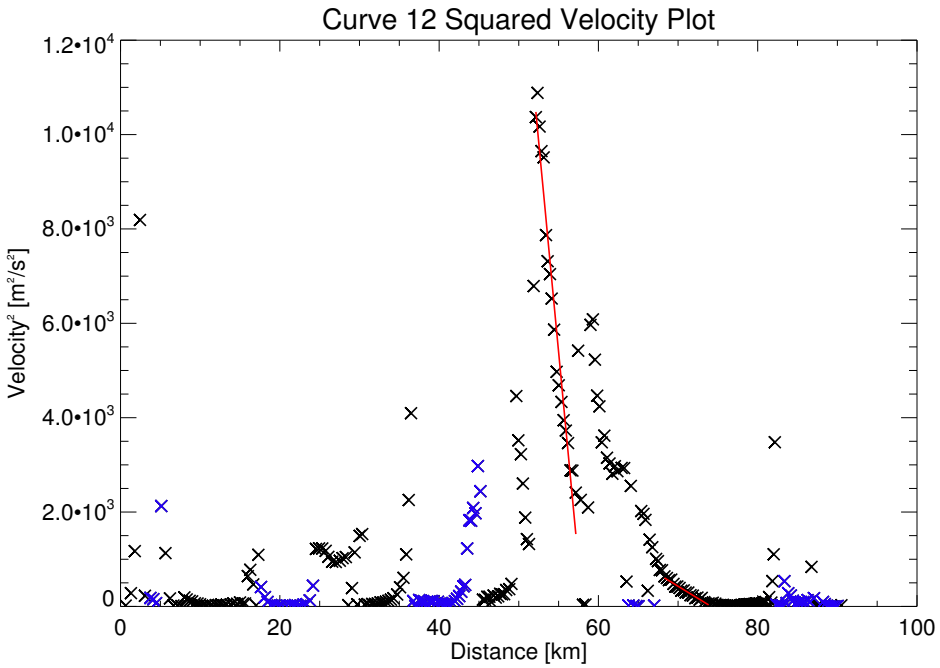

(a) Squared velocity plot Curve 12. Black and blue points are values derived from positive and negative velocities, respectively.

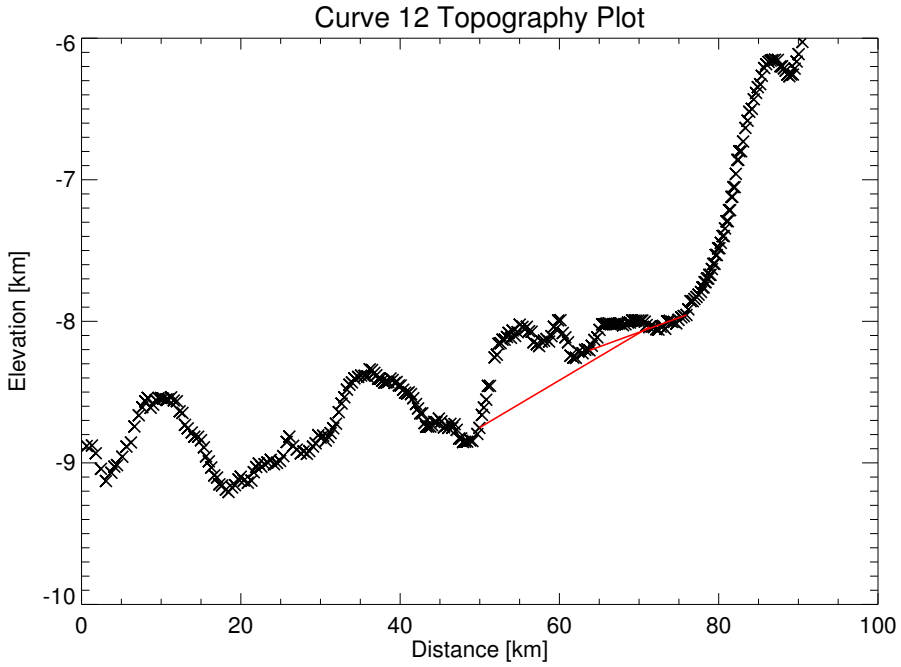

(b) Topography plot Curve 12.

Figure B.44.: Measurements (red line) derived from Curve 12 evaluated with a bin size of 5 m/s with respect to Vesta's recent shape.

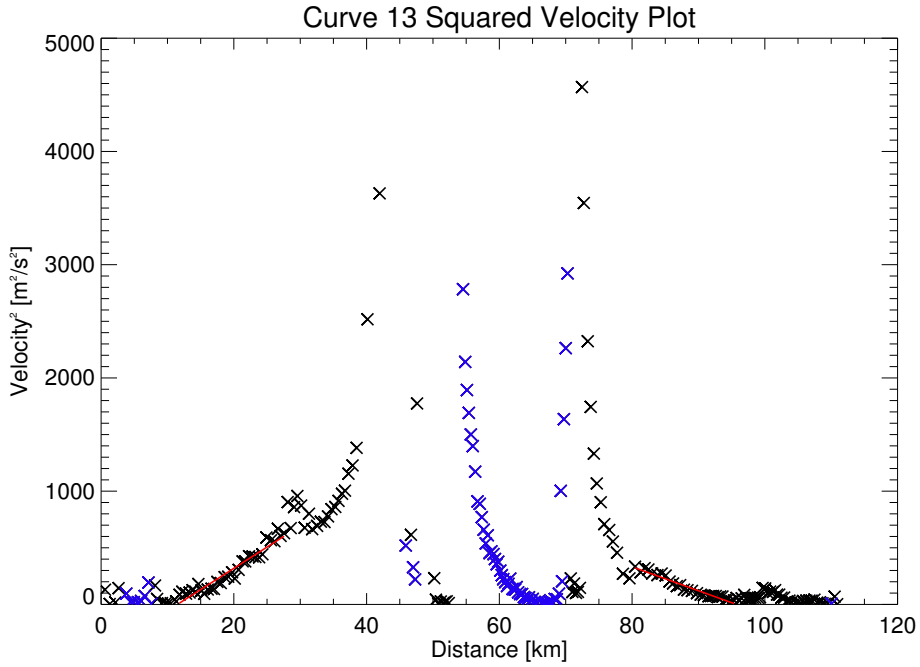

(a) Squared velocity plot Curve 13. Black and blue points are values derived from positive and negative velocities, respectively.

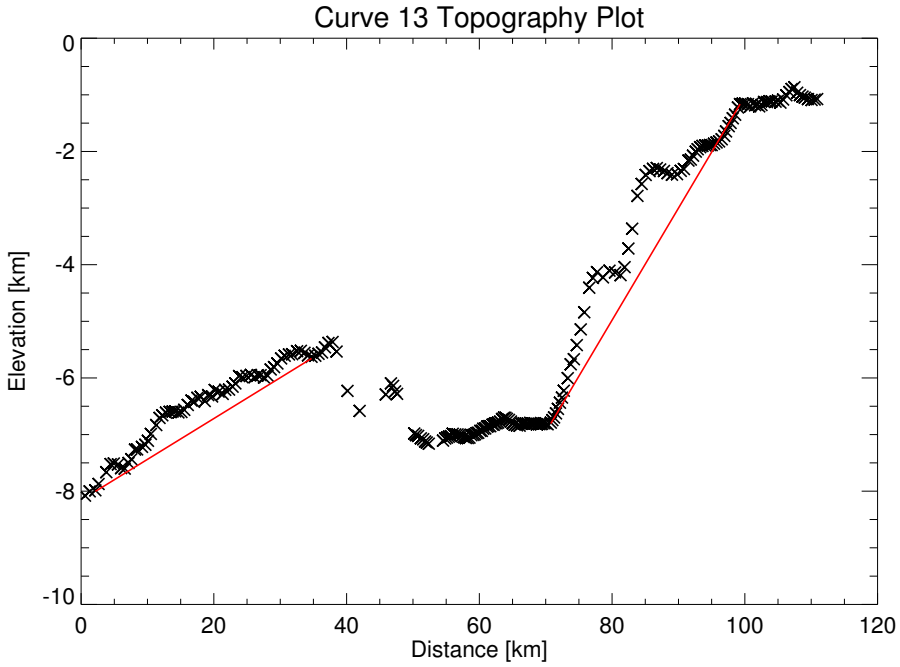

(b) Topography plot Curve 13.

Figure B.45.: Measurements (red line) derived from Curve 13 evaluated with a bin size of 5 m/s with respect to Vesta's recent shape.

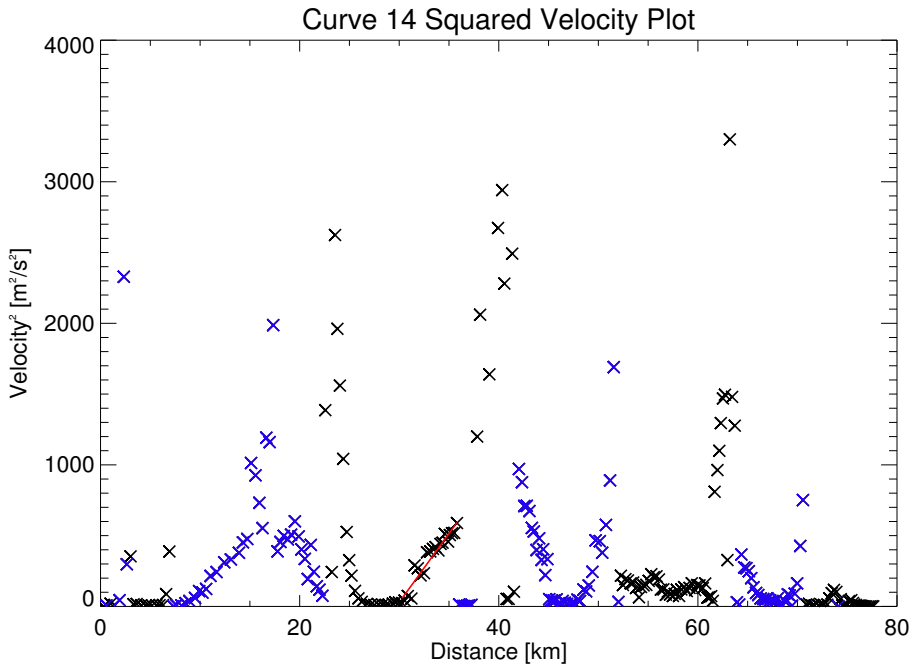

(a) Squared velocity plot Curve 14. Black and blue points are values derived from positive and negative velocities, respectively.

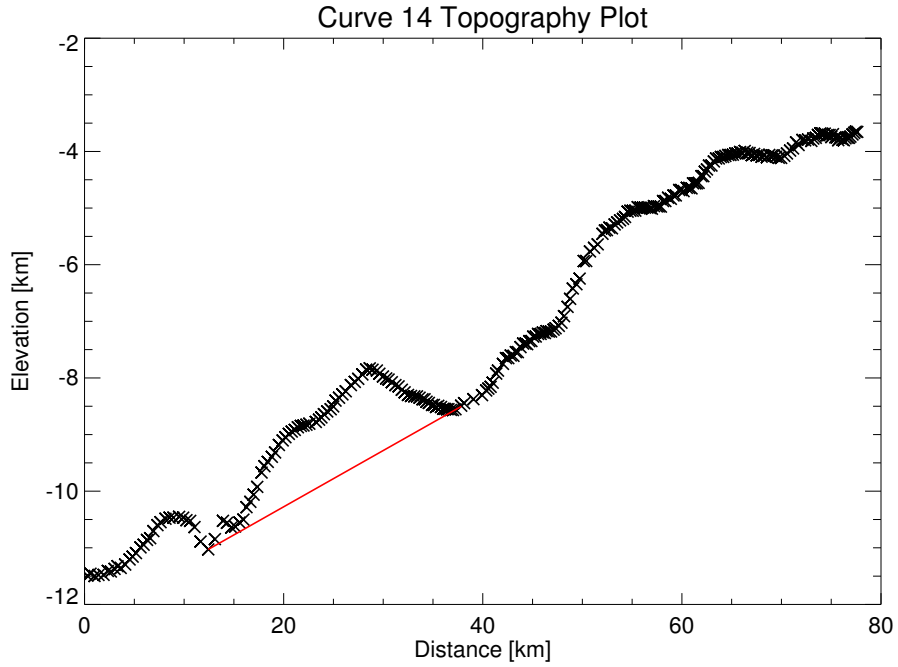

(b) Topography plot Curve 14.

Figure B.46.: Measurements (red line) derived from Curve 14 evaluated with a bin size of 5 m/s with respect to Vesta's recent shape.

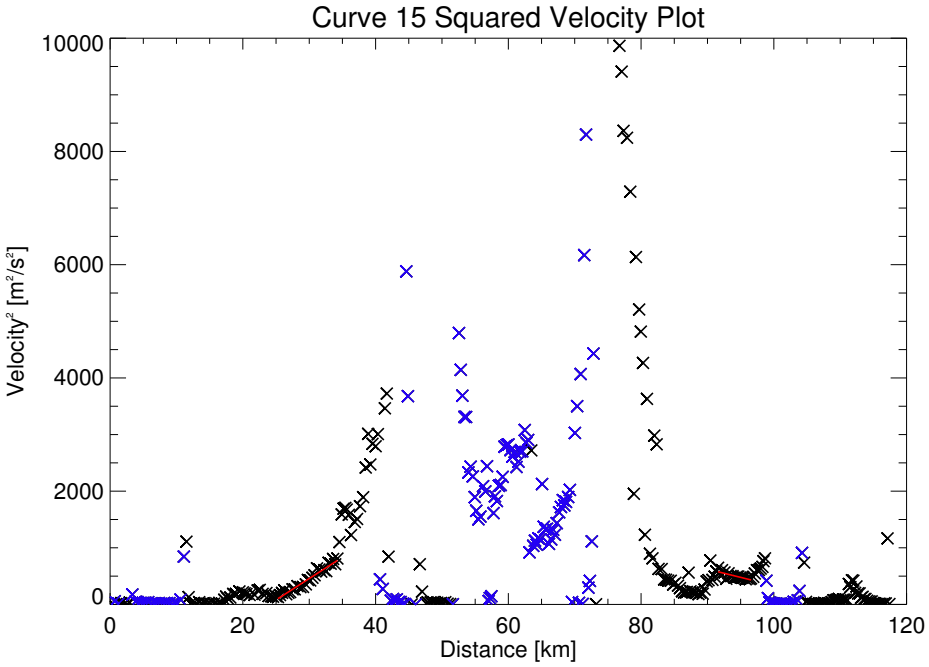

(a) Squared velocity plot Curve 15. Black and blue points are values derived from positive and negative velocities, respectively.

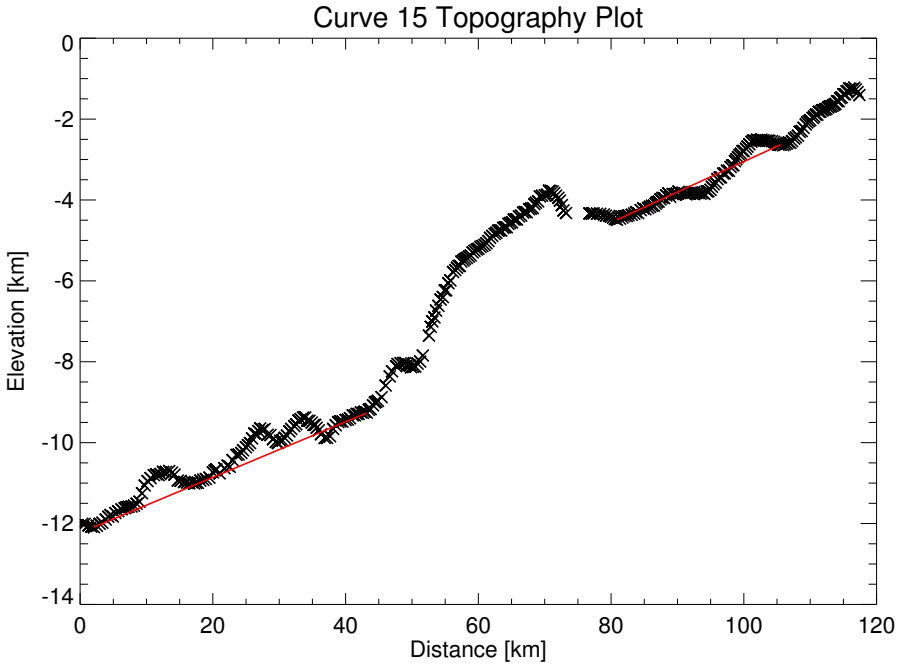

(b) Topography plot Curve 15.

Figure B.47.: Measurements (red line) derived from Curve 15 evaluated with a bin size of 5 m/s with respect to Vesta's recent shape.

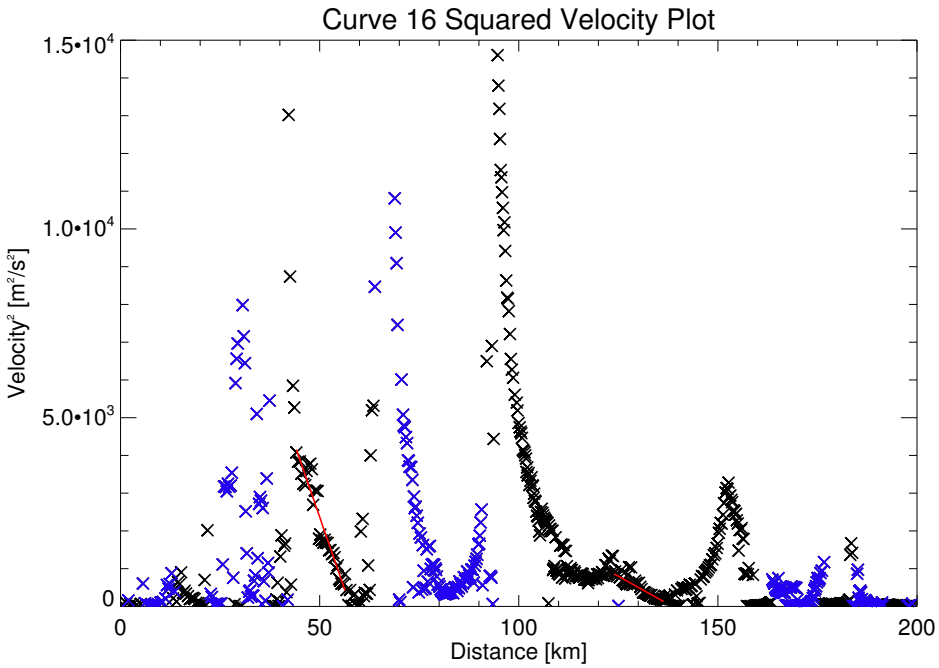

(a) Squared velocity plot Curve 16. Black and blue points are values derived from positive and negative velocities, respectively.

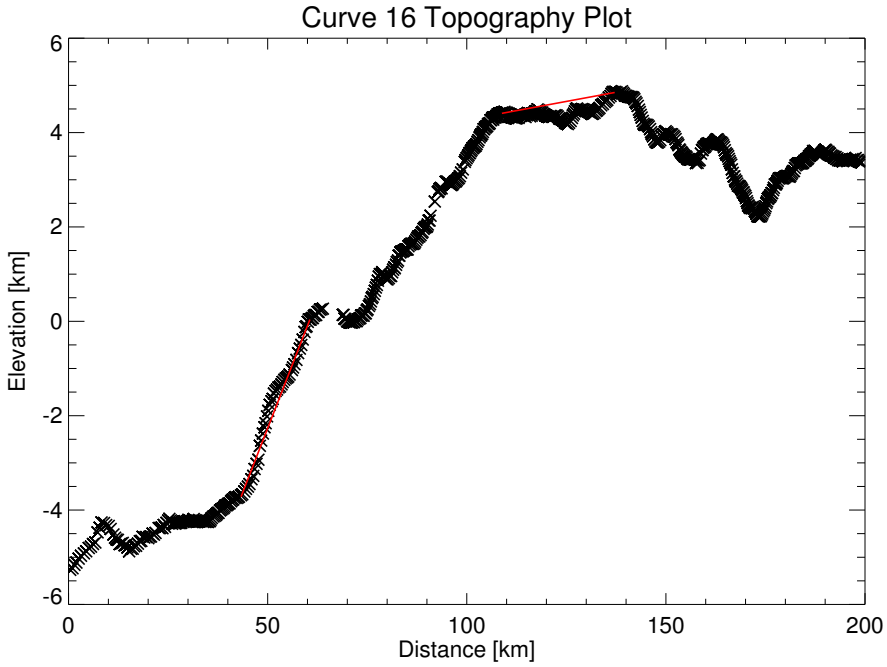

(b) Topography plot Curve 16.

Figure B.48.: Measurements (red line) derived from Curve 16 evaluated with a bin size of 5 m/s with respect to Vesta's recent shape.

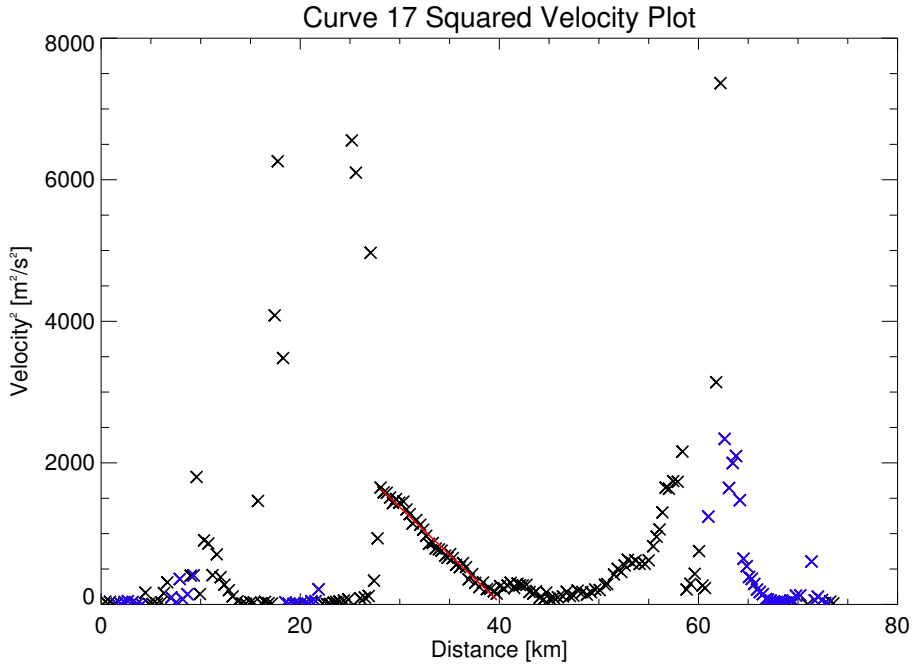

(a) Squared velocity plot Curve 17. Black and blue points are values derived from positive and negative velocities, respectively.

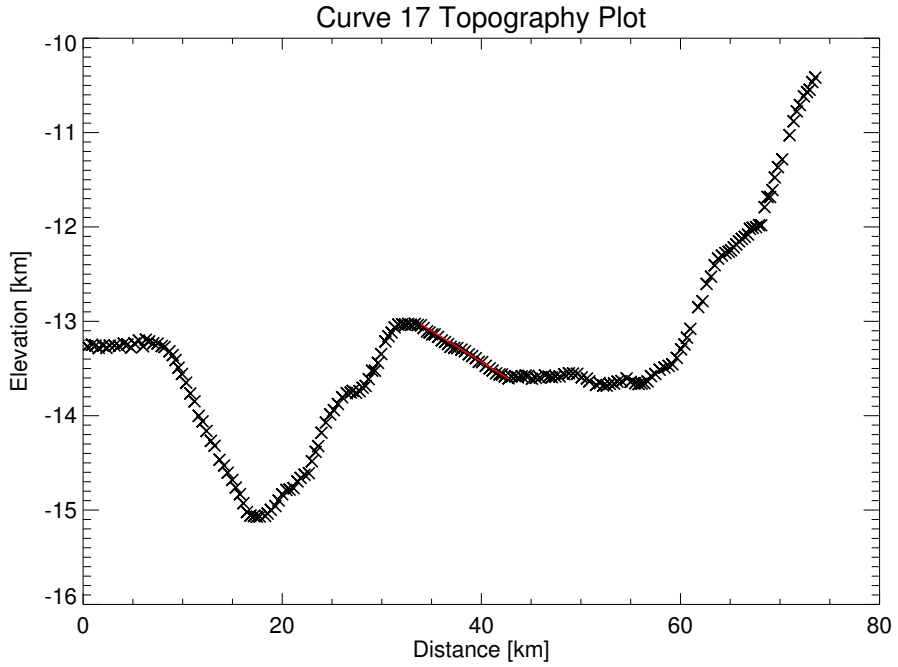

(b) Topography plot Curve 17.

Figure B.49.: Measurements (red line) derived from Curve 17 evaluated with a bin size of 5 m/s with respect to Vesta's recent shape.

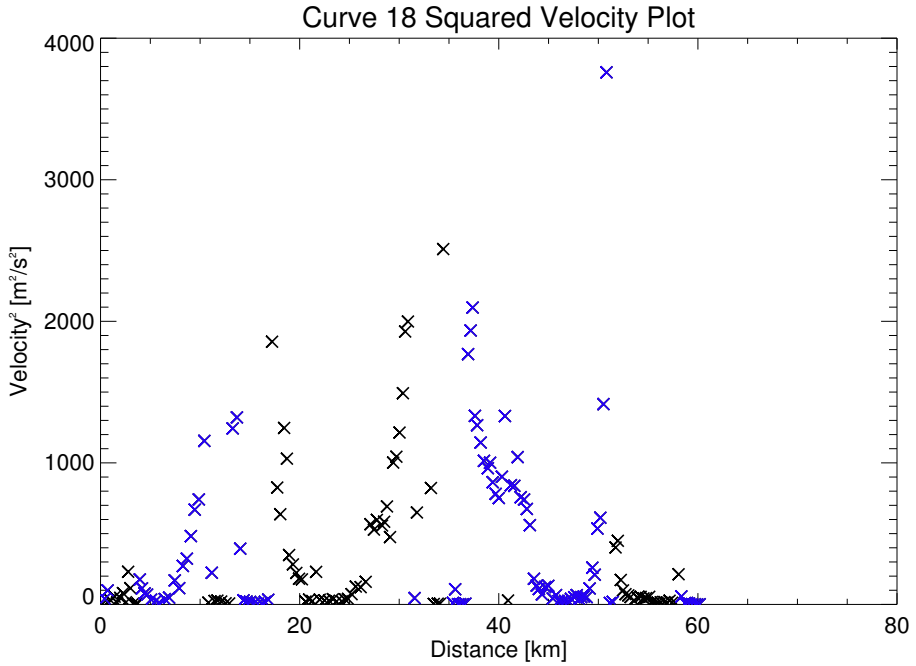

(a) Squared velocity plot Curve 18. Black and blue points are values derived from positive and negative velocities, respectively.

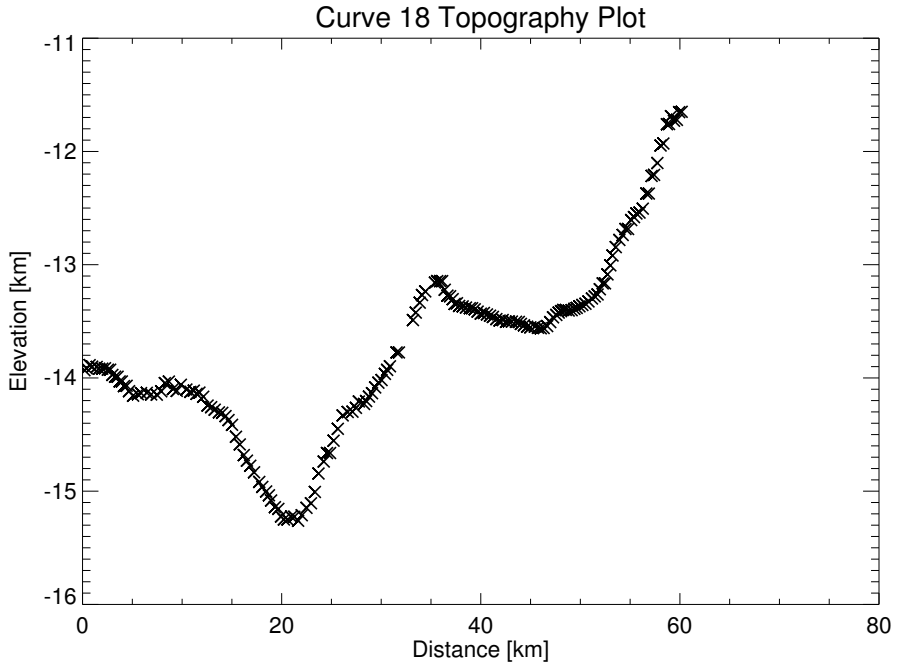

(b) Topography plot Curve 18.

Figure B.50.: Curve 18 evaluated with a bin size of 5 m/s with respect to Vesta's recent shape.

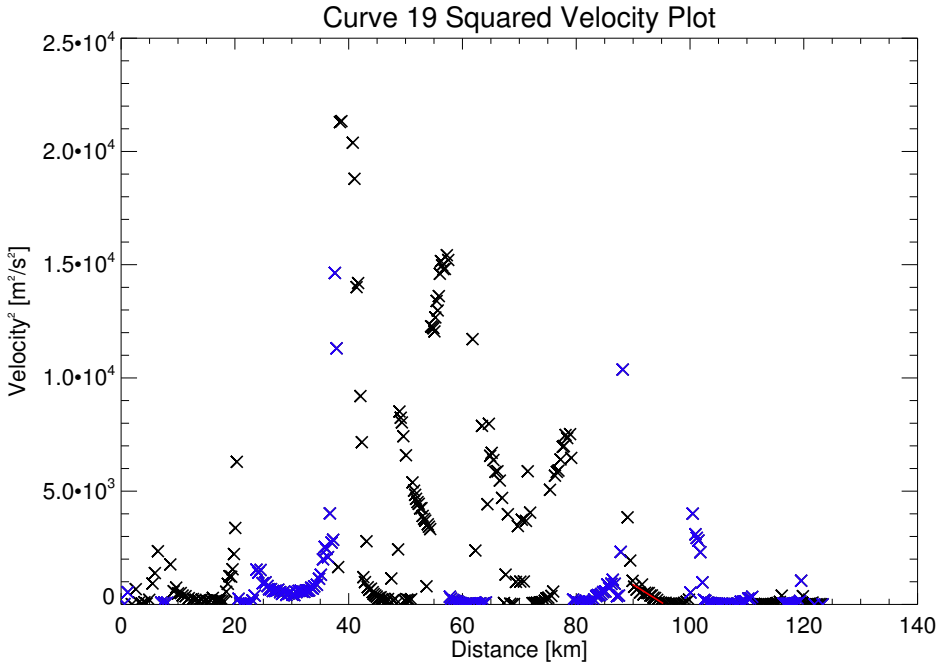

(a) Squared velocity plot Curve 19. Black and blue points are values derived from positive and negative velocities, respectively.

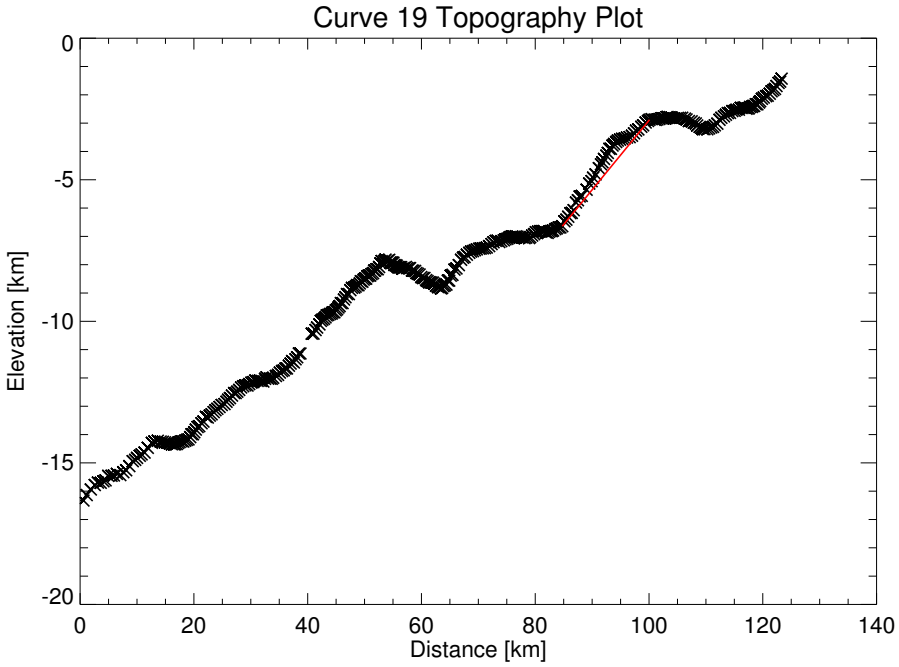

(b) Topography plot Curve 19.

Figure B.51.: Measurements (red line) derived from Curve 19 evaluated with a bin size of 5 m/s with respect to Vesta's recent shape.

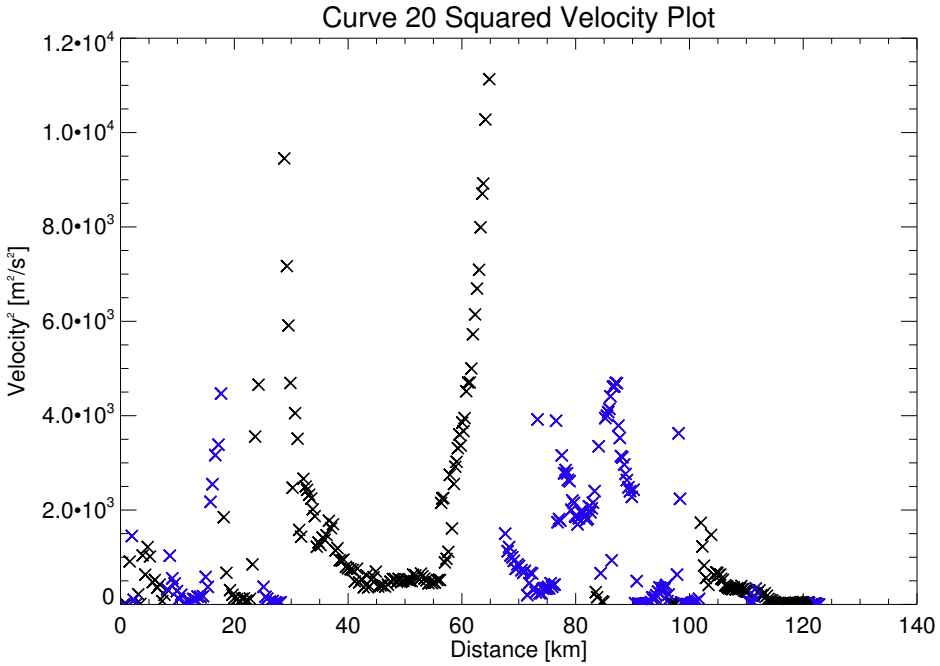

(a) Squared velocity plot Curve 20. Black and blue points are values derived from positive and negative velocities, respectively.

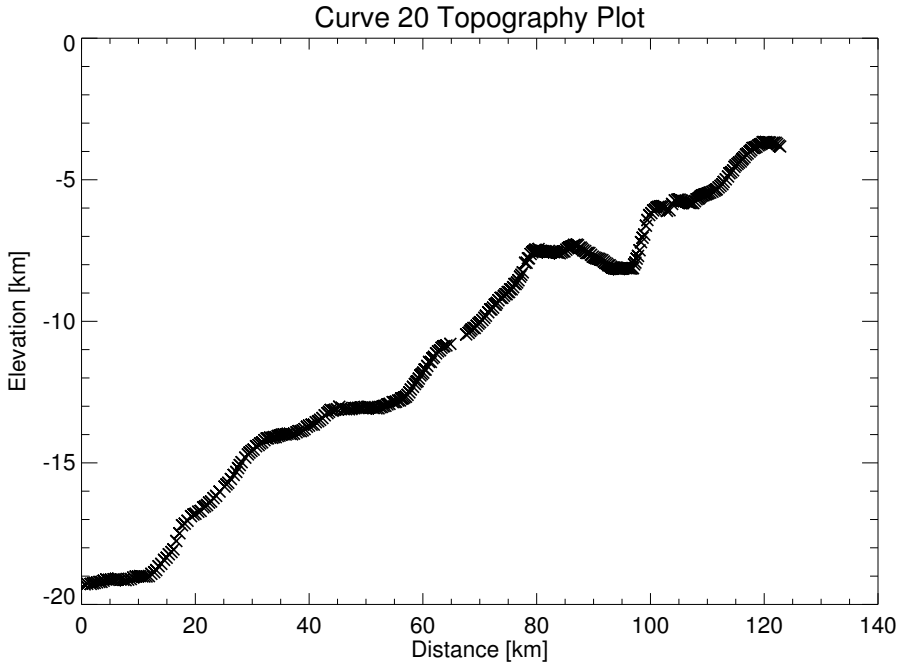

(b) Topography plot Curve 20.

Figure B.52.: Curve 20 evaluated with a bin size of 5 m/s with respect to Vesta's recent shape.

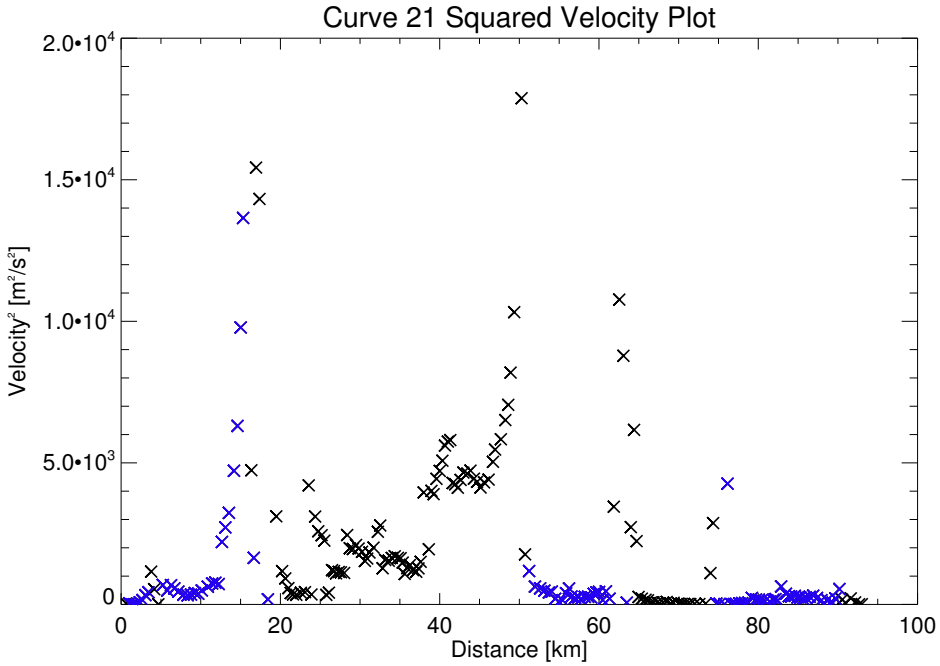

(a) Squared velocity plot Curve 21. Black and blue points are values derived from positive and negative velocities, respectively.

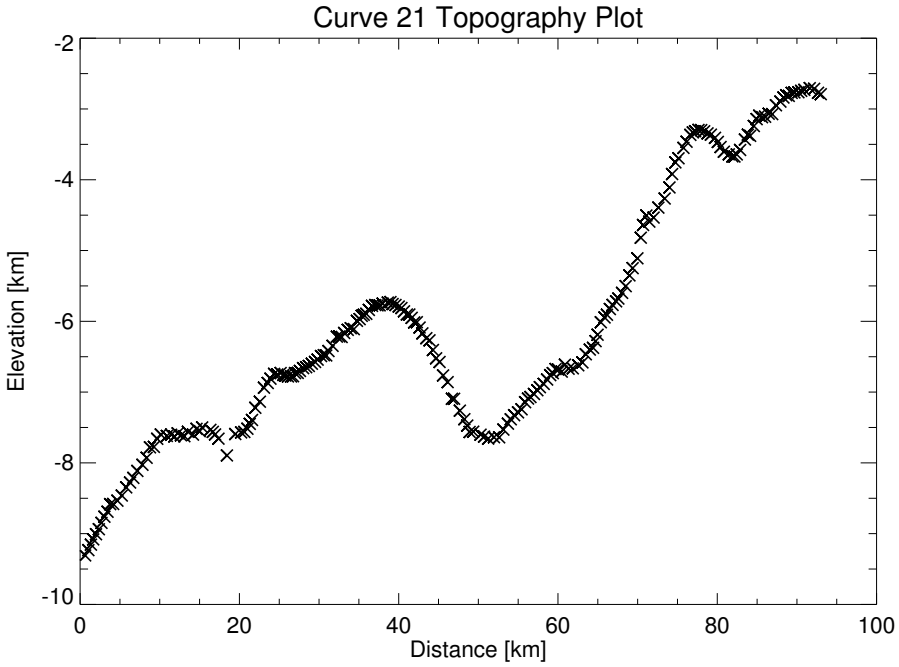

(b) Topography plot Curve 21.

Figure B.53.: Curve 21 evaluated with a bin size of 5 m/s with respect to Vesta's recent shape.

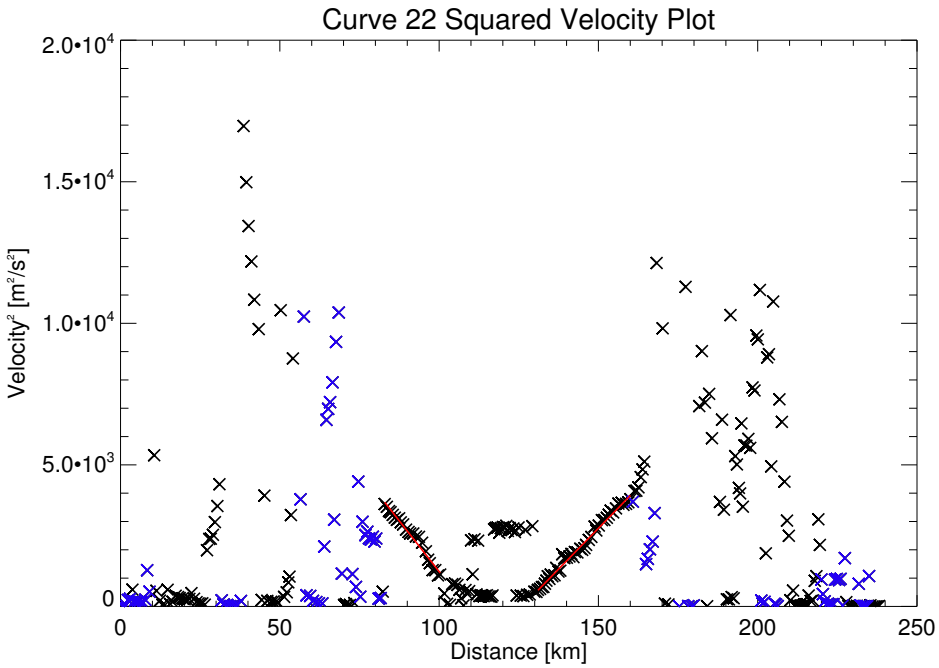

(a) Squared velocity plot Curve 22. Black and blue points are values derived from positive and negative velocities, respectively.

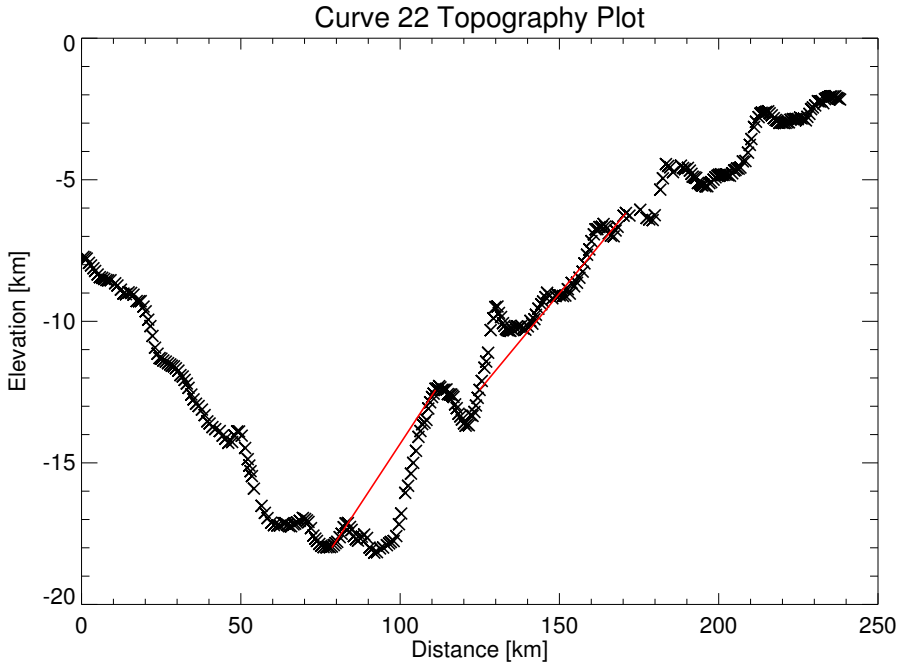

(b) Topography plot Curve 22.

Figure B.54.: Measurements (red line) derived from Curve 22 evaluated with a bin size of 5 m/s with respect to Vesta's recent shape.

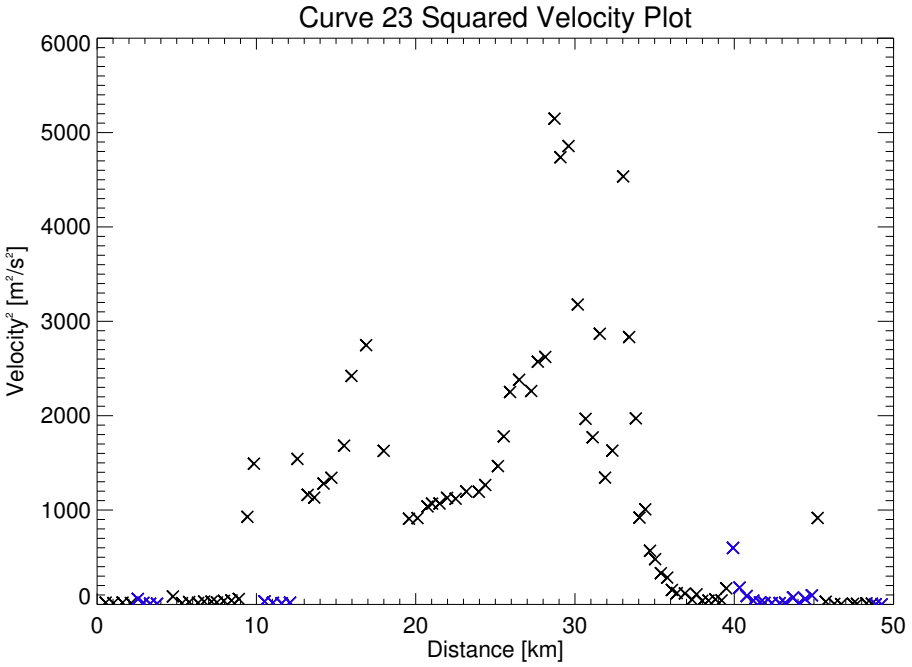

(a) Squared velocity plot Curve 23. Black and blue points are values derived from positive and negative velocities, respectively.

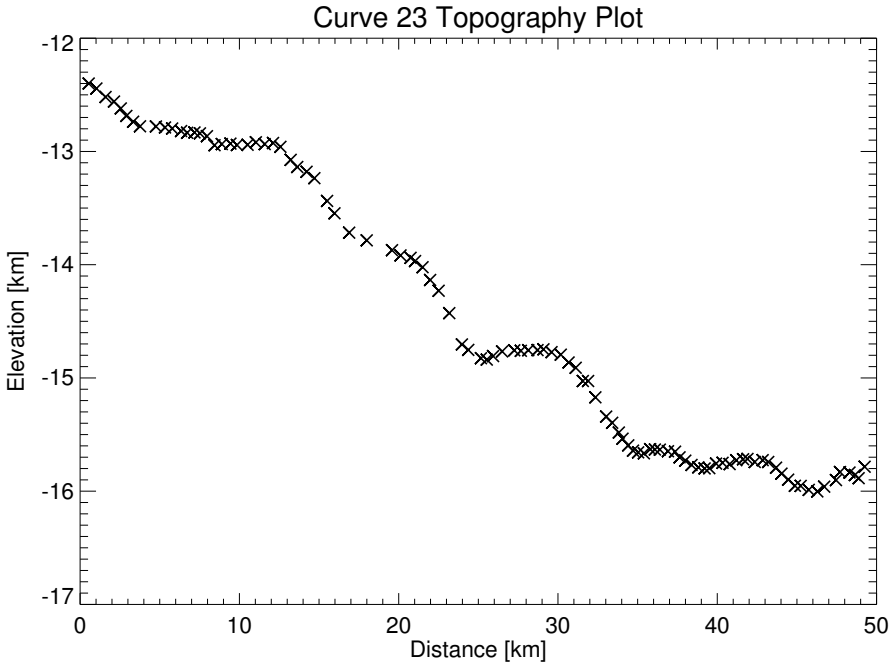

(b) Topography plot Curve 23.

Figure B.55.: Curve 23 evaluated with a bin size of 5 m/s with respect to Vesta's recent shape.

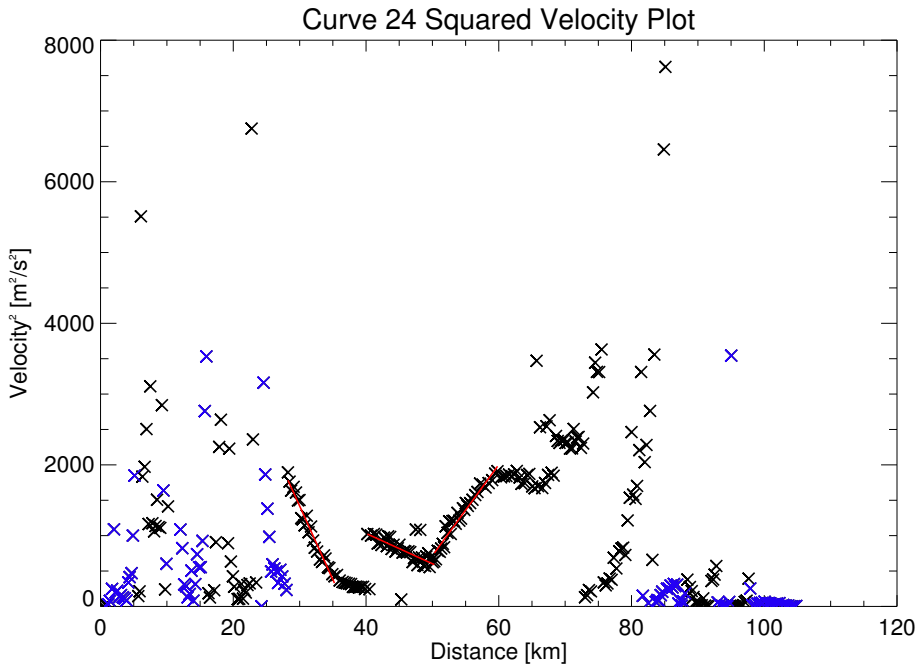

(a) Squared velocity plot Curve 24. Black and blue points are values derived from positive and negative velocities, respectively.

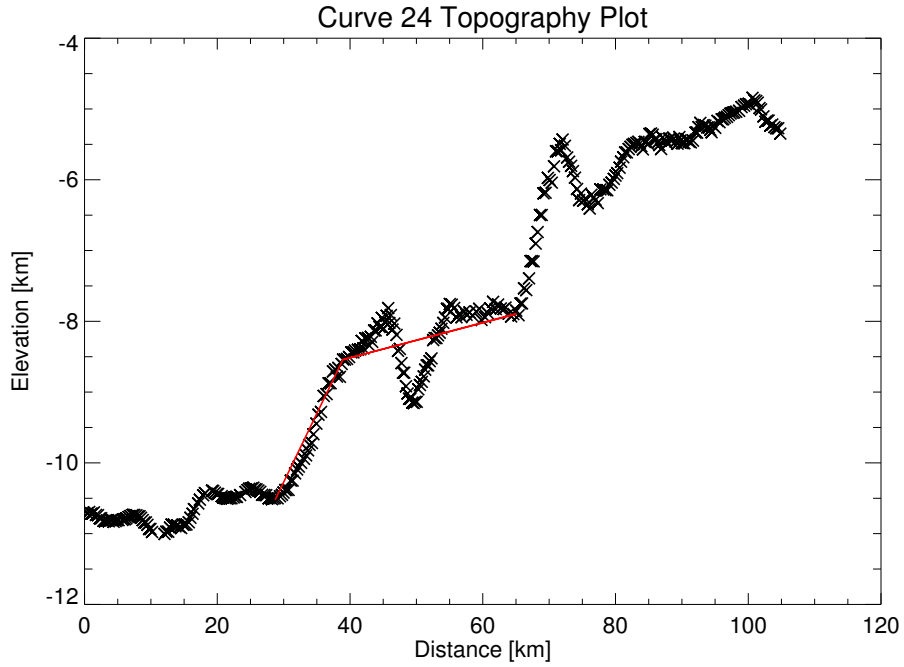

(b) Topography plot Curve 24.

Figure B.56.: Measurements (red line) derived from Curve 24 evaluated with a bin size of 5 m/s with respect to Vesta's recent shape.

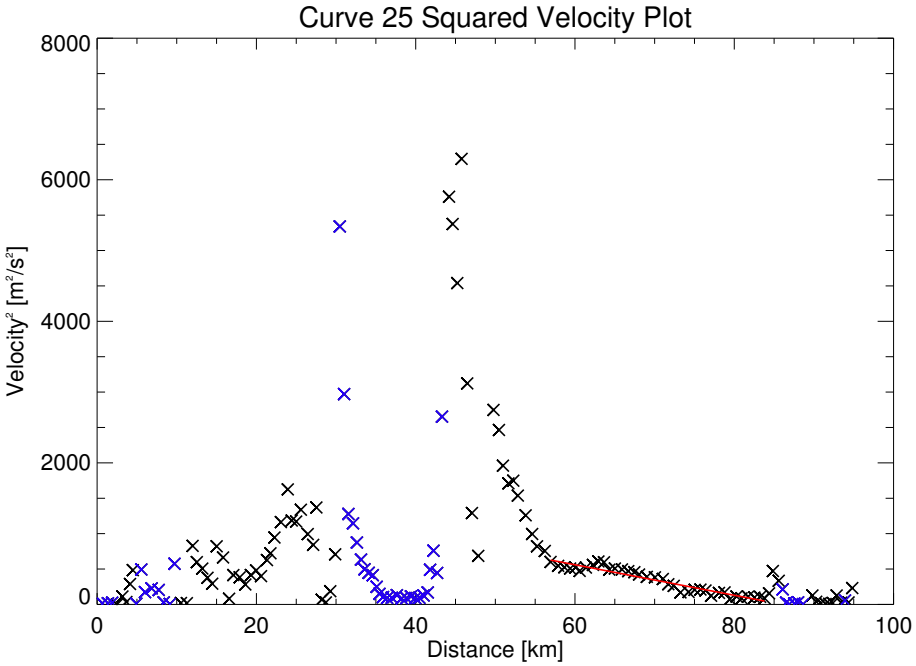

(a) Squared velocity plot Curve 25. Black and blue points are values derived from positive and negative velocities, respectively.

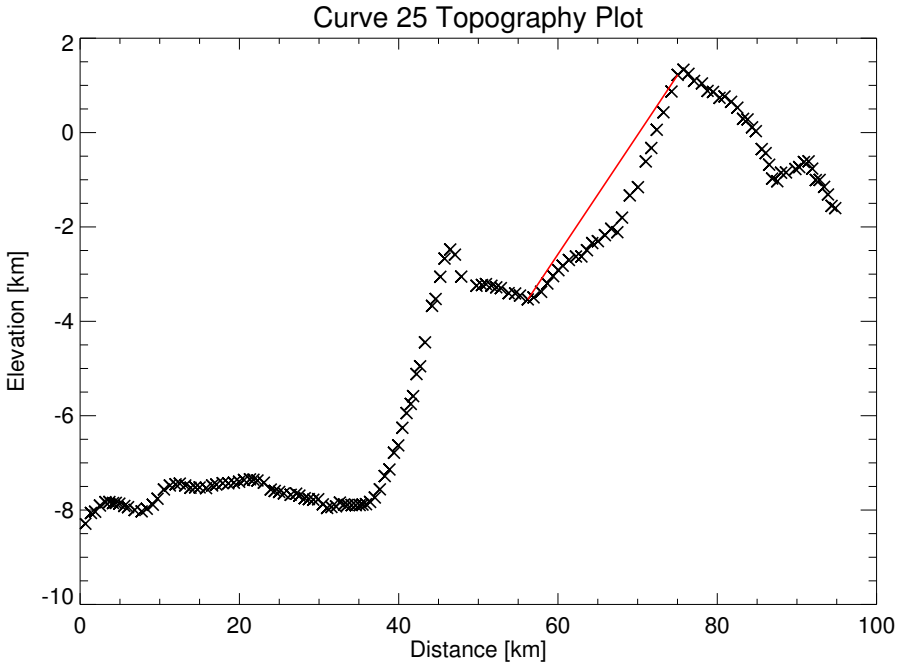

(b) Topography plot Curve 25.

Figure B.57.: Measurements (red line) derived from Curve 25 evaluated with a bin size of 5 m/s with respect to Vesta's recent shape.

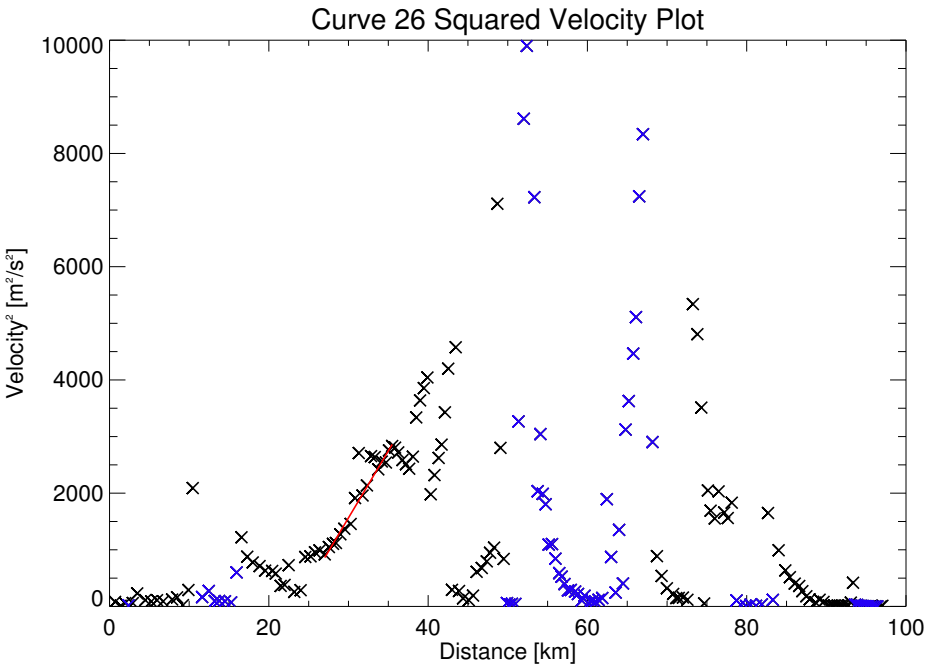

(a) Squared velocity plot Curve 26. Black and blue points are values derived from positive and negative velocities, respectively.

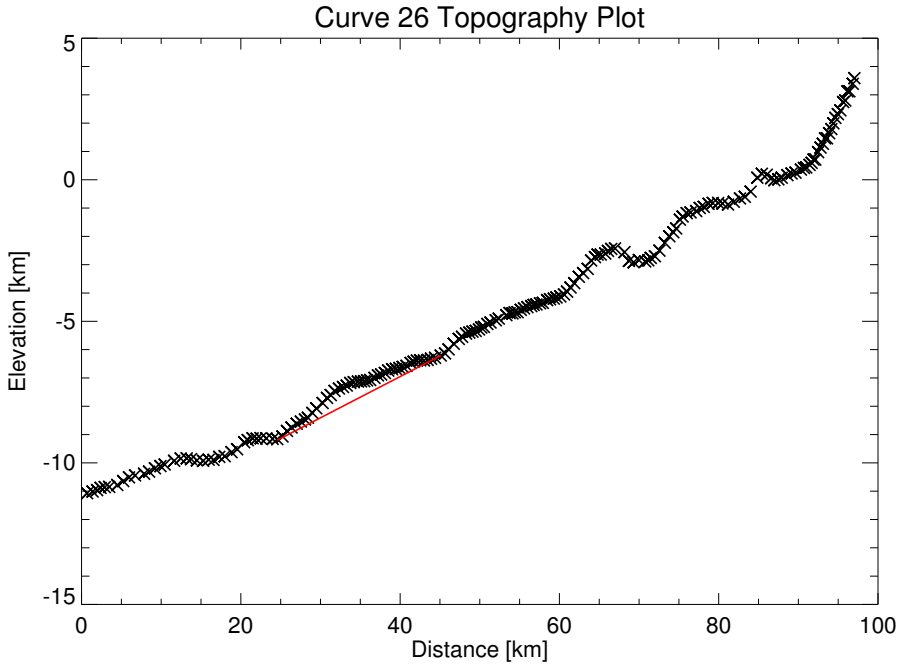

(b) Topography plot Curve 26.

Figure B.58.: Measurements (red line) derived from Curve 26 evaluated with a bin size of 5 m/s with respect to Vesta's recent shape.

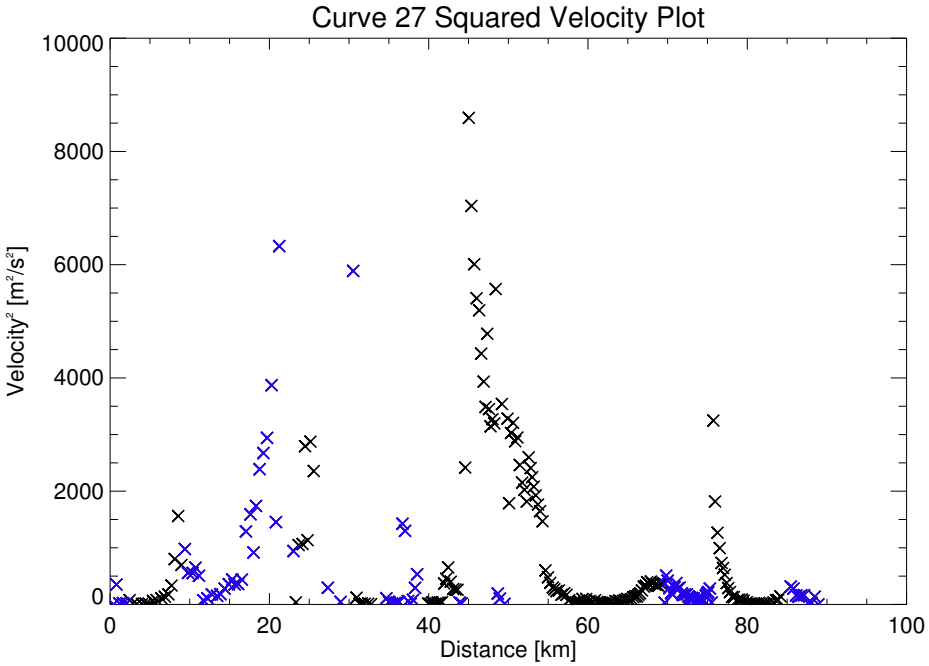

(a) Squared velocity plot Curve 27. Black and blue points are values derived from positive and negative velocities, respectively.

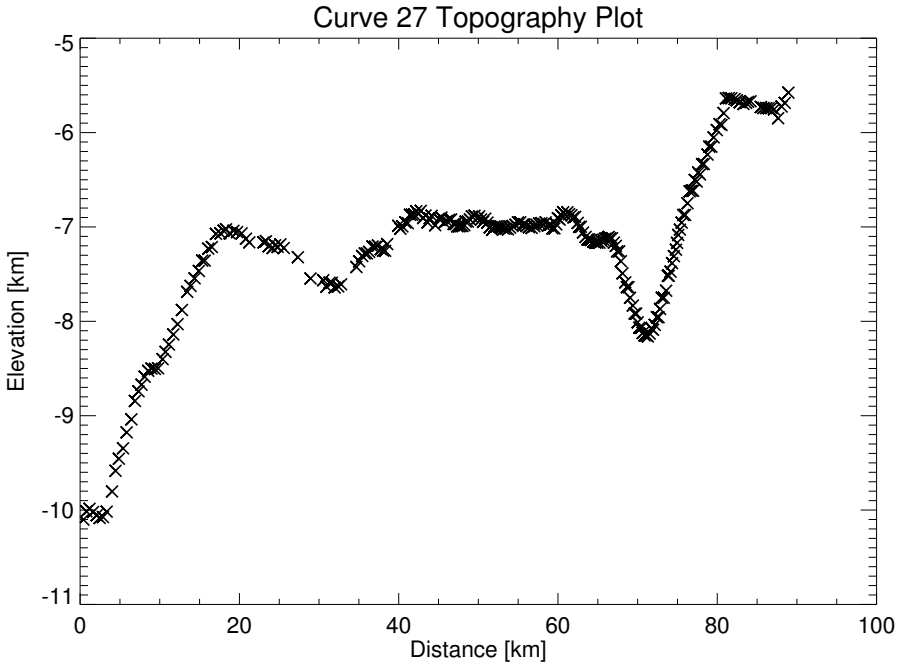

(b) Topography plot Curve 27.

Figure B.59.: Curve 27 evaluated with a bin size of 5 m/s with respect to Vesta's recent shape.

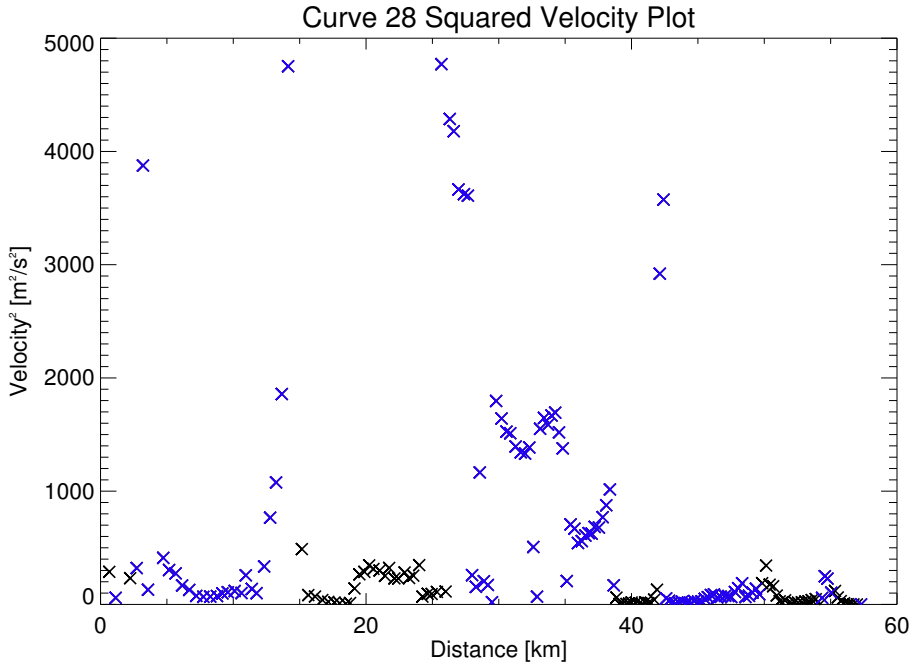

(a) Squared velocity plot Curve 28. Black and blue points are values derived from positive and negative velocities, respectively.

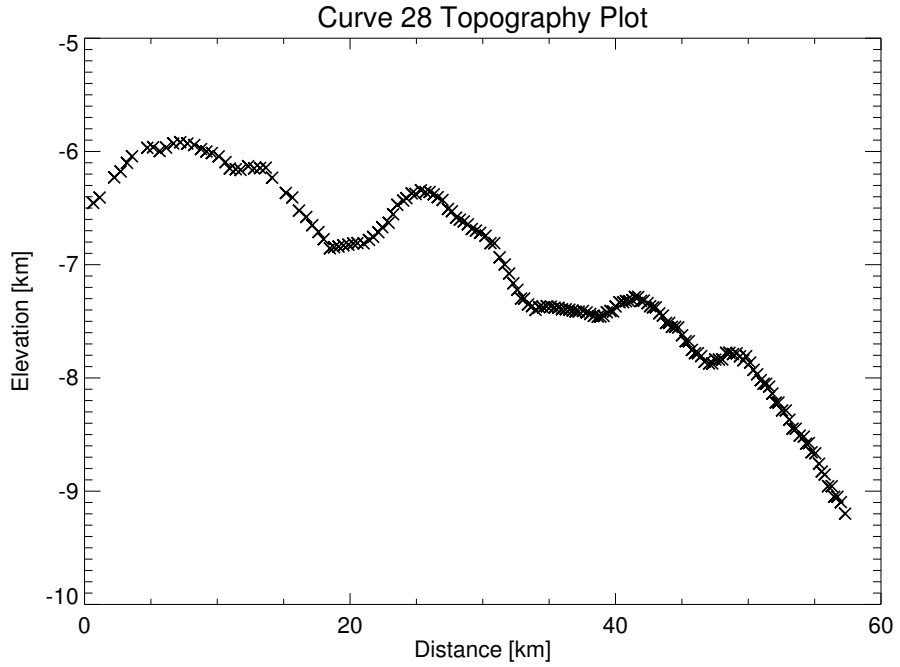

(b) Topography plot Curve 28.

Figure B.60.: Curve 28 evaluated with a bin size of 5 m/s with respect to Vesta's recent shape.

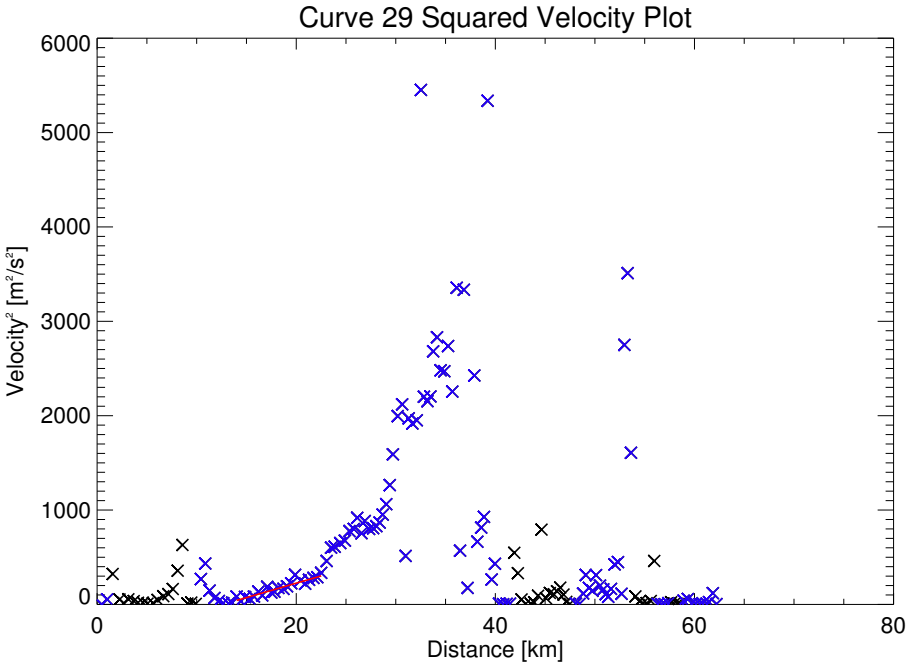

(a) Squared velocity plot Curve 29. Black and blue points are values derived from positive and negative velocities, respectively.

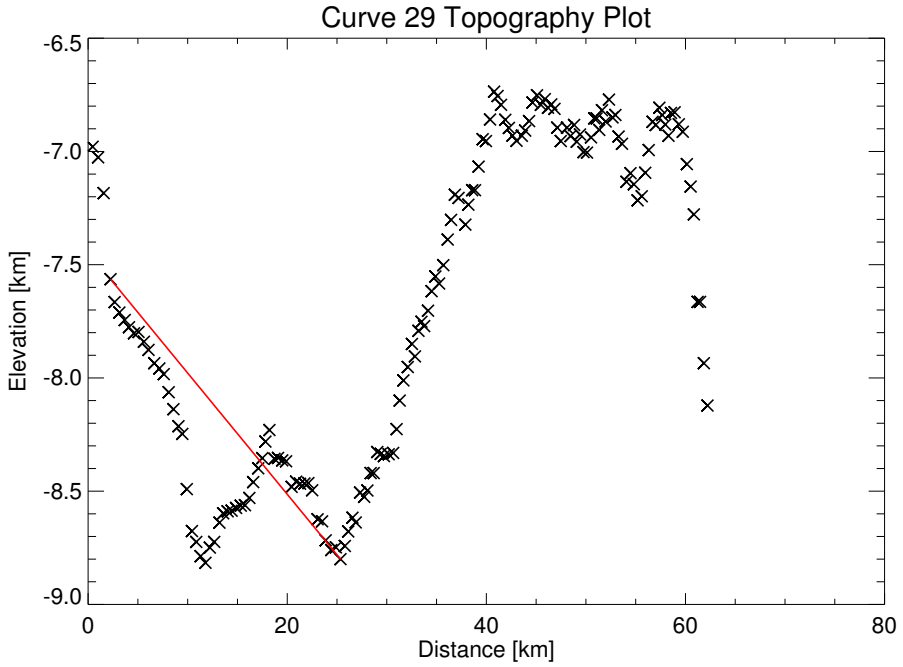

(b) Topography plot Curve 29.

Figure B.61.: Measurements (red line) derived from Curve 29 evaluated with a bin size of 5 m/s with respect to Vesta's recent shape.

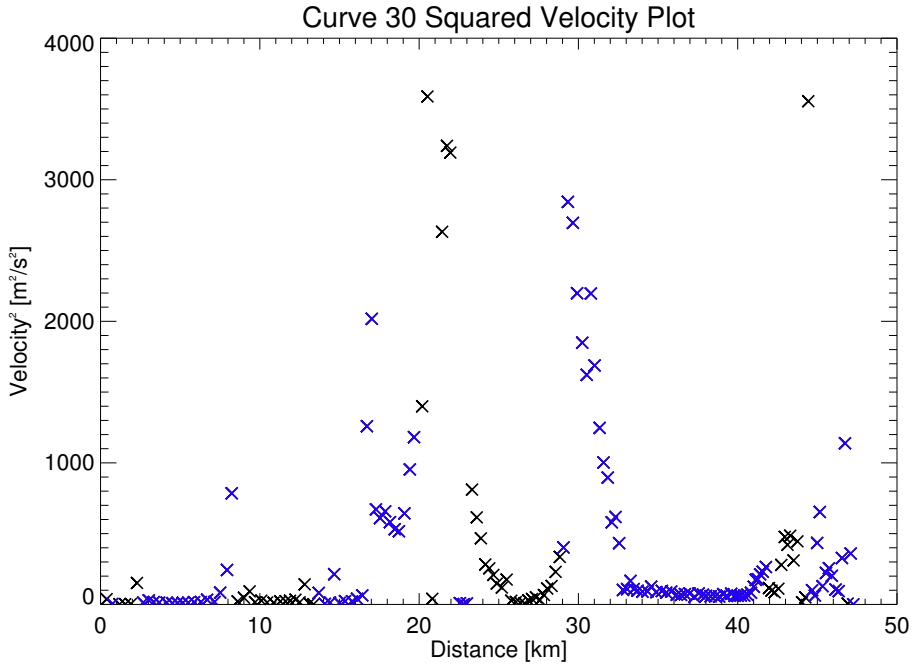

(a) Squared velocity plot Curve 30. Black and blue points are values derived from positive and negative velocities, respectively.

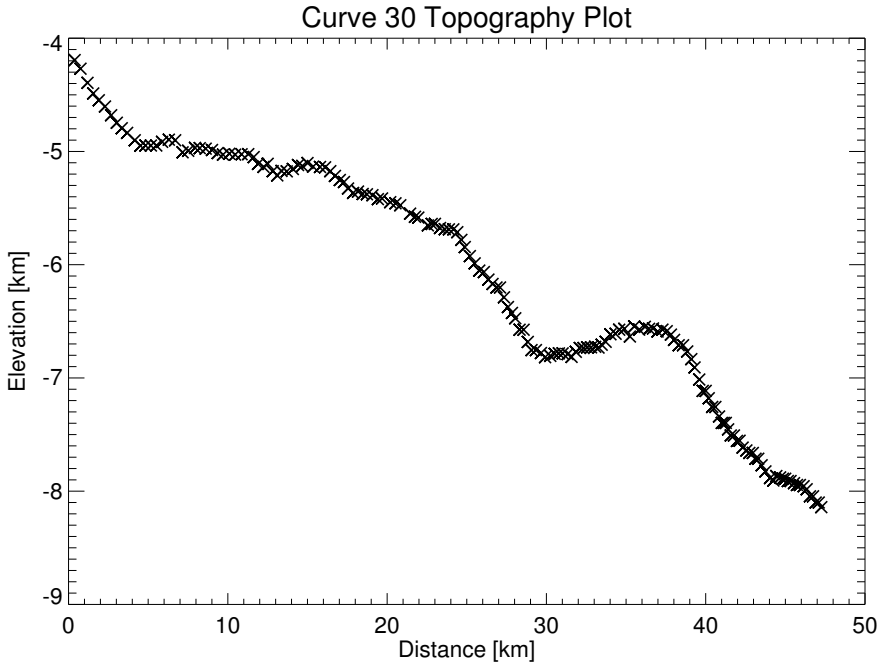

(b) Topography plot Curve 30.

Figure B.62.: Curve 30 evaluated with a bin size of 5 m/s with respect to Vesta's recent shape.

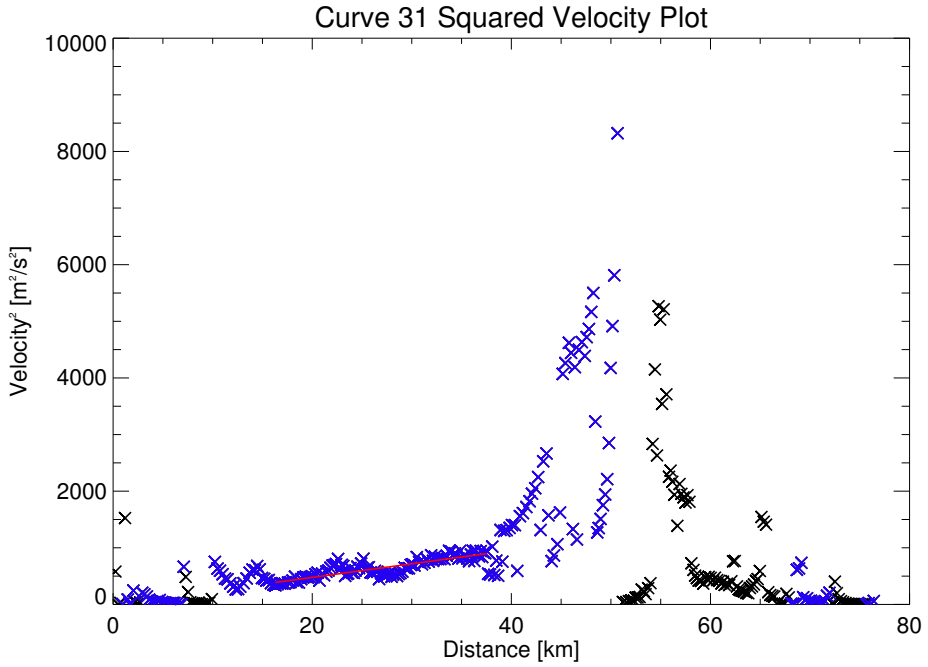

(a) Squared velocity plot Curve 31. Black and blue points are values derived from positive and negative velocities, respectively.

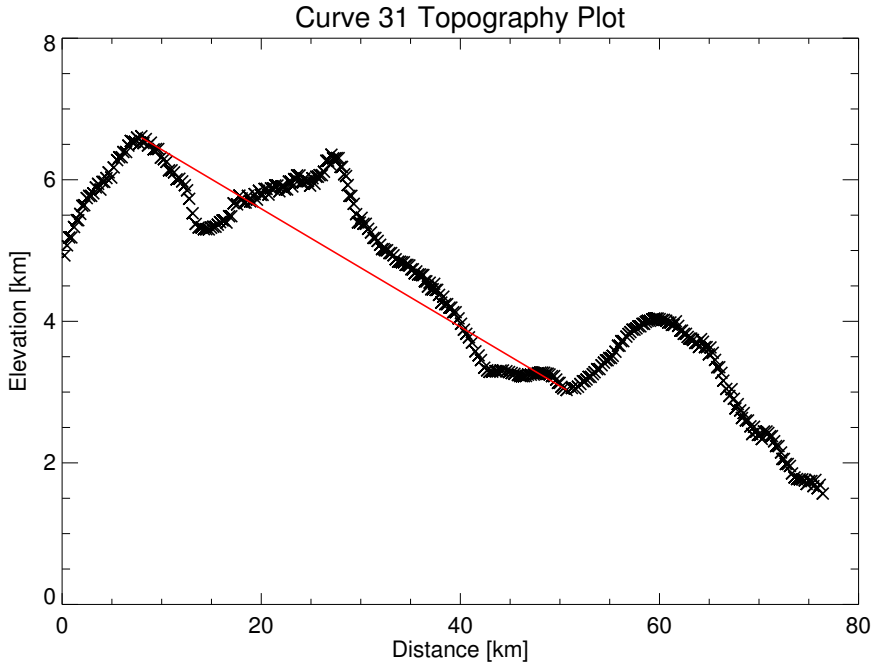

(b) Topography plot Curve 31.

Figure B.63.: Measurements (red line) derived from Curve 31 evaluated with a bin size of 5 m/s with respect to Vesta's recent shape.

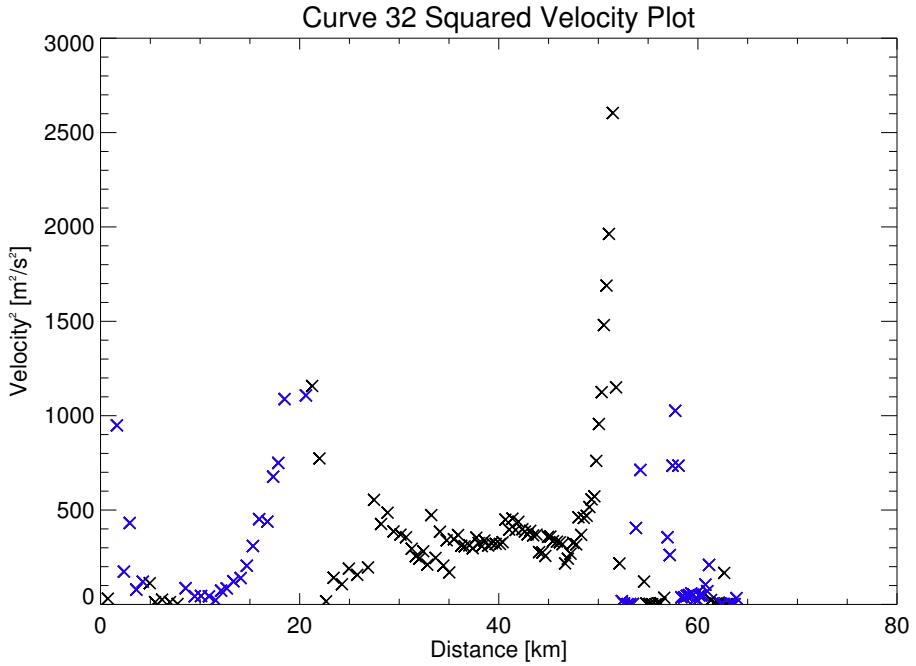

(a) Squared velocity plot Curve 32. Black and blue points are values derived from positive and negative velocities, respectively.

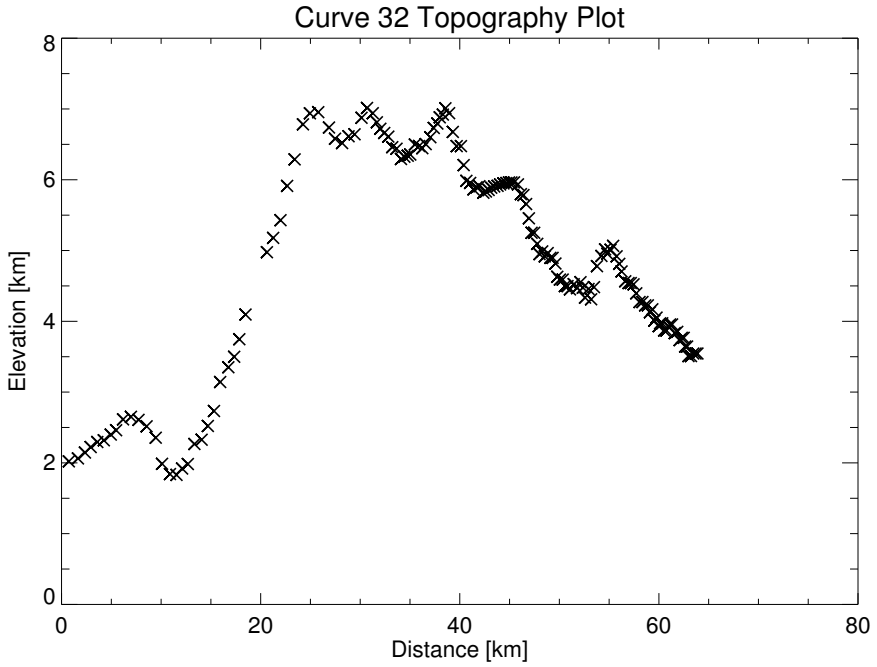

(b) Topography plot Curve 32.

Figure B.64.: Curve 32 evaluated with a bin size of 5 m/s with respect to Vesta's recent shape.

C. Mass-Wasting Features and Processes in Vesta's South Polar Basin Rheasilvia

The following work has been published as "Otto, K.A., Jaumann, R., Krohn, K., Matz, K.-D., Preusker, F., Roatsch, T., Schenk, P., Scholten, F., Stephan, K., Raymond, C.A. and Russell, C.T. (2013) Mass-Wasting Features and Processes in Vesta's South Polar Basin Rheasilvia. *Journal of Geophysical Research: Planets*, 118(11):2279–2294, doi:10.1002/2013JE004333".

JOURNAL OF GEOPHYSICAL RESEARCH: PLANETS, VOL. 118, 1–16, doi:10.1002/2013JE004333, 2013

Mass-wasting features and processes in Vesta's south polar basin Rheasilvia

Katharina A. Otto,[1] Ralf Jaumann,[1,2] Katrin Krohn,[1] Klaus-Dieter Matz,[1] Frank Preusker,[1] Thomas Roatsch,[1] Paul Schenk,[3] Frank Scholten,[1] Katrin Stephan,[1] Carol A. Raymond,[4] and Christopher T. Russell[5]

Received 25 January 2013; revised 4 October 2013; accepted 10 October 2013.

[1] The Rheasilvia crater is Vesta's largest impact basin. It is a 500 km diameter complex crater centered near the south pole and overlying the 400 km diameter impact basin Veneneia. Using Framing Camera (FC) data from the Dawn spacecraft's Low Altitude Mapping Orbit (20 m/pixel) and a digital terrain model derived from High Altitude Mapping Orbit stereo data, we identified various mass-wasting features within the south polar region. These features include intra-crater mass movements, flow-like and creep-like structures, slumping areas, landslides, and curved radial and concentric ridges. Intra-crater mass-wasting features are represented by lobate slides, talus material, dark patches on the crater wall, spurs along the crater rim and boulders. Slumping areas develop in compact material, whereas landslides form in relatively loose material. Both may be triggered by seismic shaking induced by impacts. Intra-crater mass wasting and slid and slumped materials are homogeneously distributed throughout the basin. Slumping and sliding processes have contributed most efficiently to basin degradation. Flow-like and creep-like features originate from granular material and cluster between 0°E and 90°E, an area exposing shocked and fractured material from the Rheasilvia impact event. The radial curved ridges are likely to be remnants of the early Rheasilvia collapse process, when radially moving masses were deflected by the Coriolis Effect. The concentric ridges are artifacts from the crater rim collapse. Curved ridges at the intersection of Rheasilvia and Veneneia, and on Rheasilvia's central peak, may also have been influenced by the Rheasilvia basin relaxation process, and an oblique impact, respectively.

Citation: Otto, K. A., et al. (2013), Mass-wasting features and processes in Vesta's south polar basin Rheasilvia, *J. Geophys. Res. Planets*, *118*, doi:10.1002/2013JE004333.

1. Introduction

[2] Asteroid (4) Vesta is important for understanding the early formation processes of terrestrial planetary objects. Not only is it the second most massive asteroid after (1) Ceres but it is also believed to be a surviving protoplanet [*Keil*, 2002; *McCord et al.*, 2006; *Russell et al.*, 2012]. Vesta is also thought to be the parent body of the Howardite Eucrite Diogenite (HED) meteorite family [*McCord et al.*, 1970; *Consolmagno and Drake*, 1977; *Binzel and Xu*, 1993], which originated from different layers of a differentiated body and that may have been ejected as a result of a large impact event [*Thomas et al.*, 1997; *Zuber et al.*, 2011]. However, until the NASA discovery mission Dawn visited Vesta, there had been no detailed data to aid in understanding the evolutionary processes of the protoplanet.

[3] The Dawn spacecraft orbited Vesta from August 2011 to September 2012 and collected surface data with three instruments [*Rayman et al.*, 2006; *Russell et al.*, 2004; *Russell and Raymond*, 2011]: the Visual and Infrared Spectrometer (VIR) which is able to detect surface mineralogical compositions through the analysis of spectral variations and the corresponding absorption features [*De Sanctis et al.*, 2010], the Gamma Ray and Neutron Detector (GRaND) which enables the evaluation of the isotopic composition of surface material [*Prettyman et al.*, 2011], and the Framing Camera (FC) which observes the surface in wavelengths ranging from visible to near infrared, while systematically changing observation geometries to provide multiple stereo coverage [*Raymond et al.*, 2011; *Preusker et al.*, 2012; *Jaumann et al.*, 2012]. In addition to a broadband clear filter, the FC is equipped with seven narrowband filters with effective wavelengths between 430 nm and 980 nm [*Sierks et al.*, 2011].

[1]German Aerospace Center, Berlin, Germany.
[2]Institute of Geosciences, Freie Universität Berlin, Berlin, Germany.
[3]Lunar and Planetary Science Institute, Houston, Texas, USA.
[4]California Institute of Technology, Jet Propulsion Laboratory, Pasadena, California, USA.
[5]Institute of Geophysics and Planetary Physics, University of California, Los Angeles, California, USA.

Corresponding author: K. A. Otto, German Aerospace Center, Rutherfordstraße 2, Berlin, DE-12489 Berlin, Germany. (katharina.otto@dlr.de)

2169-9097/13/10.1002/2013JE004333

[4] The Dawn mission allowed Vesta's morphology to be studied in detail. Here we concentrate on mass-wasting features in the southern hemisphere associated with the giant impact basin Rheasilvia. We identified and mapped various types of mass movements, the investigation of which aids in understanding the gravitational, structural and material properties of Vesta's surface as well as impact and surface degradation processes.

1.1. Gravitational Properties of Vesta

[5] Vesta is a triaxial ellipsoid with major axes of 286.3 km, 278.6 km, and 223.2 km and a mean radius of 262.7 km (± 0.1 km) [*Russell et al.*, 2012; *Jaumann et al.*, 2012]. With a mass of 2.59×10^{20} kg, the average surface gravity is 0.25 m/s^2. However, the density distribution as well as elevation differences generates variations in the local gravity field. Elevation differences vary the field by up to 20%. Density variations have an effect of about 1% [*Raymond et al.*, 2012], and centrifugal effects due to Vesta's relatively fast rotation of 5.3 h per revolution [*Russel et al.*, 2012] decrease the gravitational acceleration by at most 0.3%.

[6] Its low gravity means that Vesta preserves large variations in elevation. The elevation with respect to a 285 km by 229 km reference spheroid ranges from –22 km to +19 km [*Jaumann et al.*, 2012; *Preusker et al.*, 2012]. Most slopes have a gradient of 5° to 10°, although slopes as steep at 40° can be found on scarps of slumping material [*Jaumann et al.*, 2012]. Vesta's slopes are influenced by the low-gravity field on the surface, and two types of repose angles have to be considered. The static angle of repose influences the shape of scarps after the failure of material. This angle increases with decreasing gravity. The dynamic angle of repose is formed by depositions, such as landslide fans, and in contrast to the static case, the dynamic angle decreases with decreasing gravity [*Kleinhans et al.*, 2011]. Thus, scarps are steeper and deposits flatter in Vesta's gravity environment compared to more massive bodies such as the Moon.

1.2. The Giant Impact Basin Rheasilvia

[7] The giant south polar impact basin Rheasilvia was first observed by the Hubble Space Telescope [*Thomas et al.*, 1997]. The center of the 500 km ± 20 km diameter basin, located at 301°E and 75°S, almost coincides with the south pole [*Jaumann et al.*, 2012]. The elevation differences from the lowest region to the rim and central peak of the crater are about 35 km and 20 km, respectively. The excavation of vast amounts of material from Vesta's crust and upper mantle upon the impact that created Rheasilvia is likely to have changed Vesta's main moments of inertia, moving the rotation axis to its current position [*Thomas et al.*, 1997; *Zuber et al.*, 2011]. Centered at 170°E and 52°S with a diameter of 400 km ± 20 km, a second older impact basin, Veneneia, has been identified under the Rheasilvia impact basin [*Jaumann et al.*, 2012; *Schenk et al.*, 2012] (e.g., Figure 1). Ages estimated from crater density counts indicate that Rheasilvia and Veneneia are relatively young, with respect to Vesta's northern hemisphere [*Schenk et al.*, 2012; *Marchi et al.*, 2012].

[8] The rim of Rheasilvia is well preserved between 330°E and 120°E and between 200°E and 290°E. The rim between 120°E and 200°E is interrupted by the underlying Veneneia basin [*Jaumann et al.*, 2012], and thus, the material forming Rheasilvia's rim in this region lies within the Veneneia depression, resulting in a lower elevation when compared to areas with no underlying depression. Between 290°E and 330°E, opposite Veneneia in relation to Rheasilvia's center, the crater rim is also low. Such asymmetry in the crater shape and structure might be caused by preimpact topography, anisotropies in the target material [*Collins et al.*, 2008], or an oblique impact [*Poelchau and Kenkmann*, 2008].

2. Database

[9] The FC collected image data in clear and narrowband wavelengths from different orbital altitudes with pixel scales down to 20 m/pixel in the Low Altitude Mapping Orbit (LAMO). In the High Altitude Mapping Orbit (HAMO, 70 m/pixel), it obtained multiple images of the same area with different viewing geometries [*Raymond et al.*, 2011]. Based on this photogrammetric (stereo) data set, three-dimensional maps have been constructed on a reference spheroid of 285 km by 229 km. The resulting Digital Terrain Model (DTM) has a spatial resolution of ∼100 m/pixel (48 pixels/degree) and a vertical accuracy of ∼5 m [*Preusker et al.*, 2012]. The images were combined into a global mosaic for interpretation of morphologic structures, surface features, and stratigraphic relations [*Roatsch et al.*, 2013; *Jaumann et al.*, 2012].

[10] The maps in this work are presented in the "Claudia" coordinate system. This system is different from the coordinate system recommended by the International Astronomical Union (IAU) [*Archinal et al.*, 2011] as used to publish data in the Planetary Data System (PDS) [*Li*, 2012]. The Claudia longitude may be obtained from the IAU/PDS longitude by subtracting 150°.

3. Method

[11] FC images in LAMO resolution were used to analyze the morphology of mass-wasting features on Vesta's surface. The images were projected on a sphere of 255 km radius for large-scale mapping using a stereographic projection (equal angle). The elevation was taken into consideration using the DTM. A stereographic map of three narrowband ratios (749 nm/438 nm, 749 nm/917 nm, and 438 nm/749 nm) in HAMO resolution was applied for surface compositional interpretation. *Tompkins and Pieters* [1999] and *Pieters et al.* [2011] used these band ratios to define the Moon's mafic mineralogy; here Dawn HAMO images were used to calculate the same ratios for Vesta. The ratios indicate the depth of pyroxene absorption around 1000 nm (749 nm/917 nm) and the change of absorption between visible infrared and ultraviolet wavelengths (438 nm/749 nm).

4. Observed Types of Mass Wasting

[12] We identified six different types of mass-wasting features in the region inside of and around the Rheasilvia impact basin. These include intra-crater mass-wasting features associated with young craters, flow-like and creep-like patterns of shocked and fractured materials, slumps of compact material, landslides indicative of massive crater collapse mass wasting and curved ridges from the early formation stage of

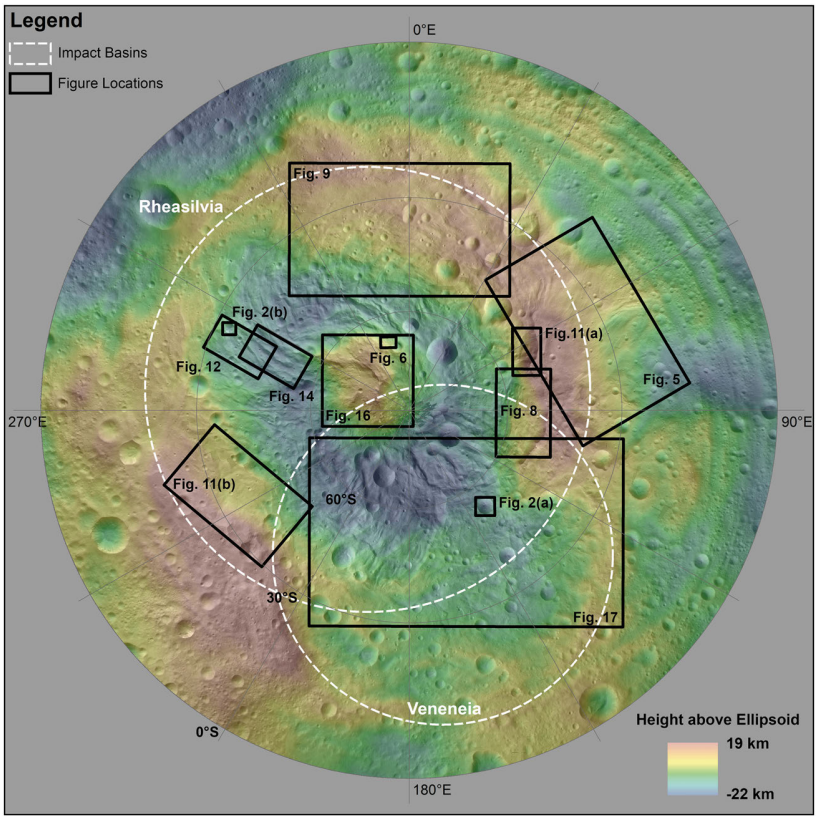

Figure 1. Context map showing the figure locations. The Rheasilvia and Veneneia basins are outlined. The map is a stereographic projection on a sphere of 255 km radius overlaid by a Digital Terrain Model (DTM) referenced to a 285 km by 229 km spheroid. All outlined figures are magnifications of this stereographic Low Altitude Mapping Orbit (LAMO) map.

Rheasilvia. In the following sections, we provide a description and detailed mapping of each type of feature. Figure 1 presents a context map of the illustrated features.

4.1. Intra-Crater Mass Wasting

[13] Mass wasting inside craters is part of the excavation and modification process of crater formation [*Melosh*, 1986] and even within craters in microgravity environments, such as the asteroid Itokawa or Mars' moon Phobos, this type of mass movement is observed [*Miyamoto et al.*, 2007; *Shingareva and Kuzmin*, 2001].

[14] After the excavation, the newly formed crater is not necessarily in a state of equilibrium. In the unstable condition when the slopes of the crater walls are higher than the angle of repose, debris will slide down into the crater [*Melosh*, 1989]. On Vesta, such debris slides can be observed on the crater floors as a pond of fine material or aprons along the crater wall in craters larger than 6 km [*Krohn et al.*, 2013]. Intra-crater landslides are often terraced concentrically due to downhill sliding. In some cases, the material bulges to form smaller hills on the crater floor, indicating the kinetic energy of the sliding mass was sufficient to pile up the material against gravity. Smaller landslides also form lobate tongues inside craters (Figure 2, arrow a).

[15] The debris aprons are sometimes associated with darker albedo bands at the transition from crater floor debris to crater wall (Figure 2, arrow c). These occur on slopes of about 25° to 30°. Above the low-albedo patches, the crater wall is generally smooth. Underneath the patches, toward the crater floor, the surface is more frequently cratered and appears to be older. The downslope motion of granular material causes inverse size segregation of the grains in the moving body by convection [*Khosropour et al.*, 1997] and kinetic sieving (the "Brazil Nut" effect). A reduction in shear forces allows the larger overlying particles to travel faster than the bulk of the material underneath [*De Blasio*, 2011]. Thus, the coarse-grained material exposes the finer material by traveling farther when the finer material has already settled. As a result, the smaller particles accumulate at the top of the apron. This size segregation may contribute to the formation of dark albedo patches along the crater wall. The craters which show the low-albedo patches are consequently often filled with larger boulders near the front of the landslide tongue where coarse-grained material is expected. These boulders may have segregated from the bulk of the landslide (Figure 2, arrow d). In subsequent mass-wasting processes, slides overrun the dark patches and form tongues. This albedo phenomenon occurs rarely and is thus likely to be dependent on material properties at the crater locations.

[16] Similar markings are seen on other asteroids such as Eros [*Thomas et al.*, 2002]. There, they are not necessarily associated with craters but are related to slopes larger than ∼25° and are an indicator for downslope movement.

[17] Some craters show spurs in the crater wall where larger blocks or crustal segments protrude from the crater

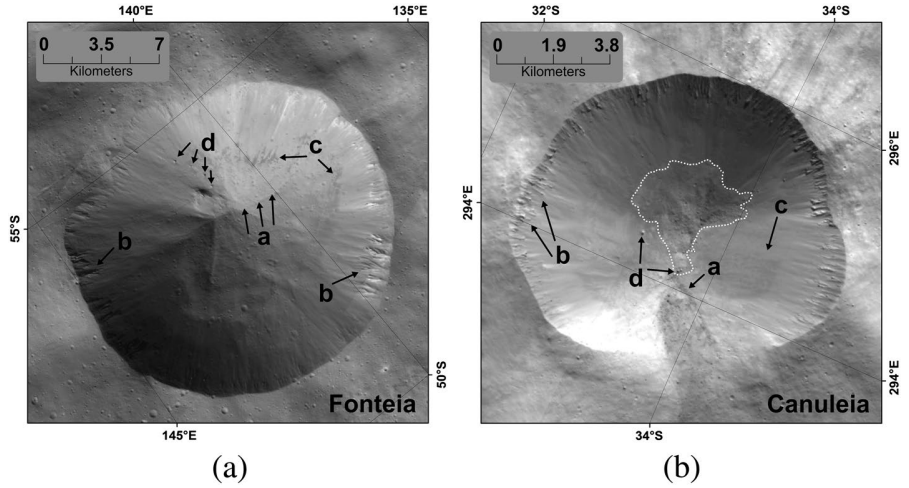

Figure 2. Examples of intra-crater mass-wasting features. (a) Crater Fonteia at 53°S and 141°E and (b) crater Canuleia at 34°S and 295°E. Note the different scales of the images. Both craters show lobate downslope movement (arrows a). In the case of Canuleia, a dark landslide emanates from the lower part of the image to the crater center. Spurs are present at the rims of the craters (arrows b). Fonteia shows dark patches overrun by brighter material (arrows c). Canuleia also exhibits low-albedo features but in a less prominent manner. Some larger boulders have gathered on the craters' floors and walls (arrows d). Also note the rocky block slightly above the center of Fonteia. Talus material is indicated by the dotted line inside crater Canuleia.

rim (Figure 2, arrow b). Larger boulders (up to 150 m across) often collect at the crater floor as a result of rock fall from these spur formations (Figure 2, arrow d). The spurs of all marked craters are similar in size, protruding 0.5 km to 3 km into the crater. The spur size is limited by the thickness of the compacted target material and varies between different crater locations.

[18] We also identified ponded talus material at the bottom of some craters. These ponds are filled by landslide material (Figure 2b, dashed line). The debris is often not flattened on the crater floor but is composed of lobes oriented toward the center of the crater. Vesta's relatively high mass means that seismic shaking does not flatten the debris in craters as efficiently as on smaller asteroids such as Eros [*Richardson et al.*, 2004].

[19] The distribution of intra-crater mass-wasting features is approximately homogeneous (Figure 3). This suggests that the material properties that cause these features are not localized but similar throughout the southern hemisphere.

[20] Intra-crater mass wasting is associated with young craters. A longer period of erosive activity, such as seismic shaking, might trigger landslides which fill a crater. Spurs might break off the crater rim and accumulate as boulders on the crater floor. Ejecta from later impacts in the vicinity of a crater, as well as intra-crater landslides, cover other intra-crater mass-wasting features including boulders and dark patches. Eventually, the crater is completely filled with talus material and no longer exhibits any other intra-crater mass-wasting features.

[21] The above described intra-crater mass-wasting features concern craters smaller than 50 km in diameter. Larger craters, such as Rheasilvia and Veneneia, exhibit different types of mass-wasting features. Here, spur formation and boulders occur only locally on the crater rims, where the impacts cut through compacted target material. Dark patches do not occur, but additional features, such as the flow-like and creep-like features, are present. Slides and slumping are the most common mass-wasting processes and are further described in the following sections.

4.2. Flow-Like Features

[22] The Rheasilvia basin exhibits flow-like mass movements, which show a flume-like pattern with striations parallel to the direction of travel and lobate scarps at the front of the features. The striations suggest fluid-like flow behavior, indicating that the frictional forces between the particles are small.

[23] A possible explanation for the low friction within a landslide was suggested by *Melosh* [1986] who introduced acoustic fluidization as a process to reduce friction within a very large landslide (more than 10^7 m^3) resulting in small height-to-distance ratios. The fluidization is generated by strong acoustic vibrations that temporarily reduce the pressure within the landslide. This allows the landslide to move under applied shear stresses that are below the threshold of motion for the given overburden.

[24] Flow-like features are most common on slopes of about 5° to 20° and cluster on the highest part of the Rheasilvia rim and on the central peak (Figure 4). Areas toward the Veneneia basin and lower elevated regions do not show such features. The surface of the flow-like features are smooth and based on the number of impact features on them, they appear to be younger in comparison to the surrounding area. The paths of the steepest slope do not generally coincide with the flow direction. This implies that the recent topography is formed by the deposit of the slide or that subsidence has taken place after the formation of the flow-like features.

[25] The outer crater rim of Rheasilvia along the Matronalia Rupes scarp (within the area of 20°S to 45°S and 35°E to 95°E) is dominated by a downslope flow-like mass-wasting feature (Figure 5). The fan of the flow is ∼100 km long

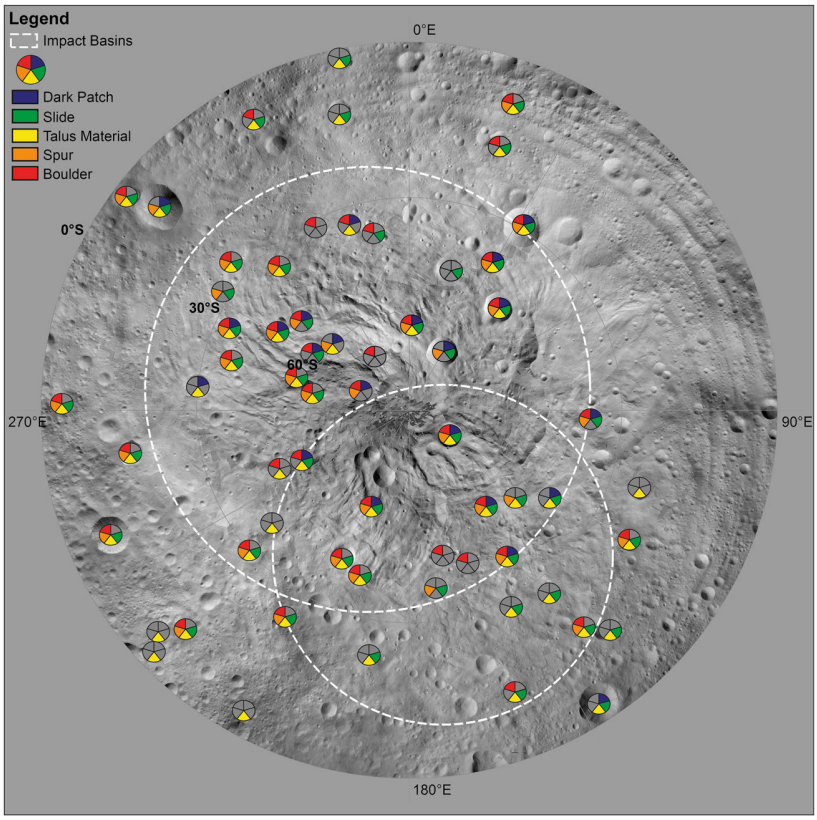

Figure 3. Distribution of intra-crater mass-wasting features including dark patches along the crater wall (blue), slides emanating into the crater bowl (green), talus material on the crater floor (yellow), spur formation along the crater rim (orange), and boulders (red). Only craters with non-eroded features are marked. The map is a stereographic LAMO projection on a sphere of 255 km radius.

extending over an elevation change of ∼7 km with slopes varying between 10° to 20°. This results in a height-to-distance ratio of 0.07 and thus can be classified as a long runout landslide. The relatively large volume of the landslide (∼6000 km^3) may have enabled acoustic fluidization to have reduced the internal friction.

[26] The flow-like feature originates from the edge of a plateau formed by the crater rim of Rheasilvia. Various parallel oriented striations with an angle of ∼30° to the slope direction (Figure 5, arrows) emerge downhill and form lobate slide fronts. Some of the material has subsided, forming depressed areas in front of the slide's toes, which might be due to compaction of a soft base or underlying topography.

[27] Another flow-like feature is located on the crater wall of Rheasilvia, directly opposite the previously described feature (within the area of 21°S to 33°S and 248°E to 265°E). The flow points toward Rheasilvia's center but again originates from the elevated crater rim. The central peak also exhibits flow-like downward movement of material, which suggests that the material forming Rheasilvia's rim and central peak differs from other surface materials within the crater, appearing to have lower internal friction. The formation of highly shocked and fractured materials on the crater wall and central peak during the impact process may explain the occurrence of flow-like features on elevated regions. Other possible formation processes include destabilization of fallback ejecta on steep flanks and impact melt flows. A combination of these effects would seem most plausible and a detailed study of the flow-like features can be found in *Williams et al.* [2013].

4.3. Creep-Like Features

[28] Other mass-wasting features occurring on Vesta's southern hemisphere are creep-like mounds on the regolith-covered surface. These mounds are elongated features with a straight or slightly curved shape. Their lengths vary from a few hundred meters to several kilometers and they often appear in clusters with a curved alignment perpendicular to the slope (Figure 6).

[29] The creep-like mounds are too small for their elevation to be inferred from the DTM; nevertheless, their shadows indicate their raised morphology. The length of a shadow cast by a nearby crater rim with measurable height in the DTM was used to determine the illumination angle and direction. With this information and considering the slope of the terrain, the typical heights of the creep-like mounds were estimated to be about 100 m to 150 m.

[30] The creep-like features occur on the inner and outer slopes of Rheasilvia's rim and on the central peak. They cluster in the region between 0°E and 90°E. On the opposite Rheasilvia crater rim, between 210°E and 240°E, further regions with creep-like features are evident. Other, much smaller creep-like regions are spread over the Rheasilvia basin, where they are often associated with the ejecta and

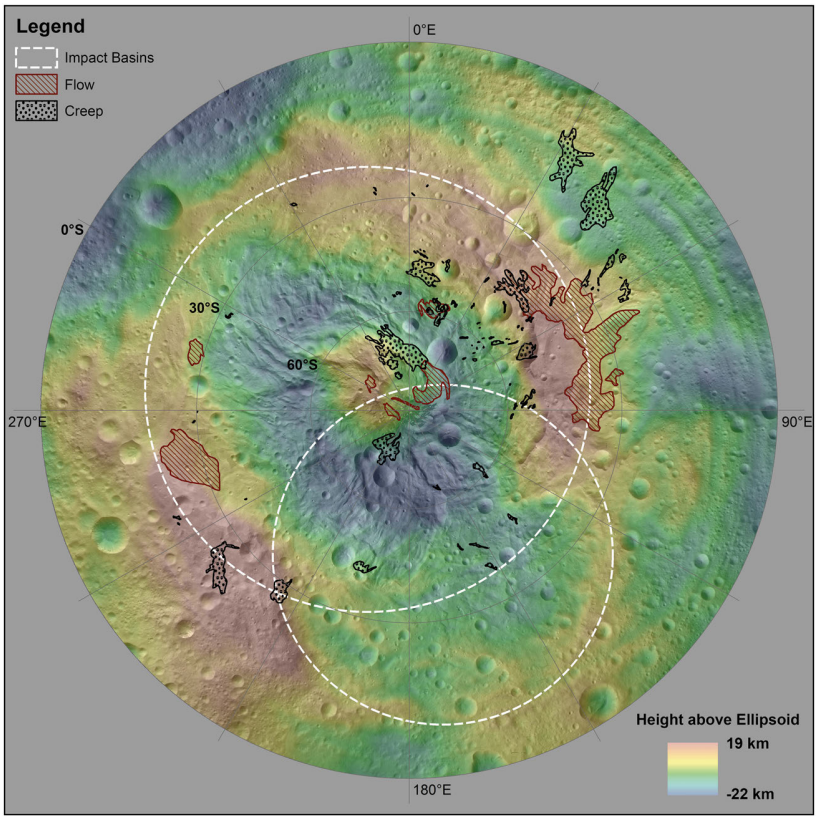

Figure 4. The distribution of flow-like (red) and creep-like features (black). The flow-like features are associated with elevated regions such as the Rheasilvia rim and the central peak. Flow-like and creep-like features cluster in the area between 0°E and 90°E. Further creep-like features occur in scattered regions within the Rheasilvia basin. The map is a stereographic projection on a sphere of 255 km radius overlaid by a DTM referenced to a 285 km by 229 km spheroid.

wall material of young craters. The clustering of regions with creep-like features on Rheasilvia's rim, central peak, and near young craters (Figure 4) indicates that material exhibiting creep-like features possesses the physical properties of highly shocked and fractured material.

[31] A possible explanation for the formation of the creep-like features is the local compaction of material due to seismic shaking from nearby impact events. Compaction and creeping can be a result of a pressure wave propagating through the regolith [*Titley*, 1966; *Schultz and Gault*, 1975], causing the material to pile up in small creep-like mounds. This phenomenon has already been observed on other asteroids [*Richardson Jr. et al.*, 2005].

4.4. Slumping

[32] Rotational slumping occurs on steep slopes, when the pressure of the slumping body exceeds the shear resistance of a sliding surface [*De Blasio*, 2011]. In a cohesive material (in which the main intra-material connection is provided by electrostatic bonds between the grains), the grains do not detach from each other to slide downhill, but a surface of rupture is formed by the shear stress of the overlying body. The body as a whole then slumps downward along the surface of rupture. This surface is hemispherical or spoon-like shaped, a result of the stress exerted on the material. As the center of mass of the sliding body does not coincide with the center of the circle formed by the surface of rupture, a torque is produced. Thus, the driving force of slumping originates from the torque produced by gravity on the center of mass.

[33] Features of rotational slumping include almost vertical scarps and heads that are tilted backward toward the scarp. Transverse cracks, ridges, and a toe feature at the front of the slide can often be observed (Figure 7). Within the Rheasilvia basin, these features are less prominent than the scarps and thus difficult to identify. They are eroded by subsequent impact cratering or local seismic shaking. In some places, the toes are still represented as slightly elevated terrains.

[34] The crater of the Rheasilvia impact has degraded due to slumping in various regions. Some slumping areas are heavily eroded while others are relatively well preserved. A prominent and relatively young area of rotational slumping blocks appears opposite the flow-like feature along the Matronalia Rupes scarp (section 4.2, Figure 5) toward the center of the Rheasilvia basin [*Krohn et al.*, 2013]. It is located within the area of 45°S to 65°S and 75°E to 115°E with the Matronalia Rupes scarp representing the main scarp of the slumping body (Figure 8). Numerous minor scarps of subsequent slumping, ridges, and the toe of the slumping body are evident.

[35] We identified three ancient relics of slumping blocks within the region of 35°S to 55°S and 165°E to 185°E, the area where Rheasilvia intersects Veneneia, within 20°S to

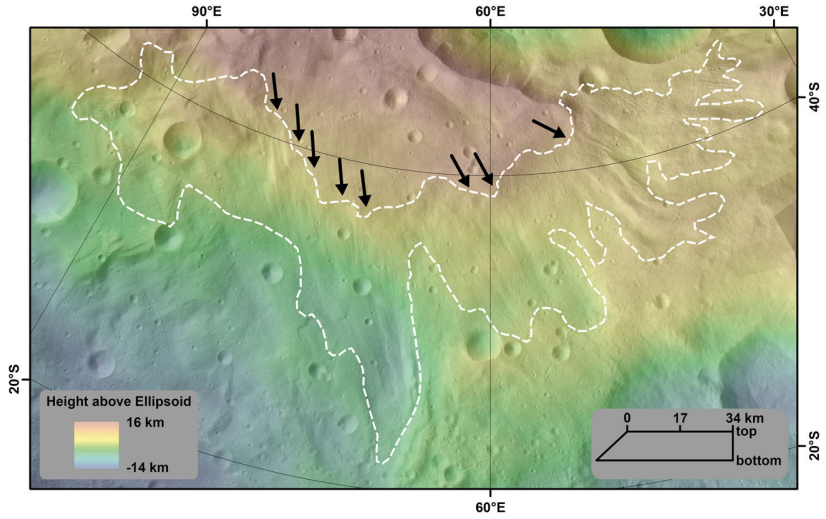

Figure 5. The flow-like feature north of the Matronalia Rupes scarp, within the area of 20°S to 45°S and 35°E to 95°E. The arrows indicate the origin of the flow, from which striations developed. The dashed line shows the extent of the feature. The image is in a stereographic projection with the scale bar applicable at the center of the image. It is overlaid by a DTM referenced to a 285 km by 229 km spheroid.

30°S and 290°E to 310°E, and within 25°S to 55°S and 320°E to 40°E (see Figure 9). Younger geologic activities, such as impact cratering or sliding of debris, eroded the original rotational slump scarps and heads, so that often only the upper parts of the slumping heads are visible as rounded elongated rims (see also section 4.6). The first two slumping areas have main scarps with an angle to the rim of Rheasilvia, indicating that the basin did not collapse concentrically in these regions. This might be due to varying material strengths and substructures within the Rheasilvia wall. The third slumping region's scarps are parallel to the crater rim following a concentric degradation of the Rheasilvia basin. The region includes an area of large craters with diameters up to 30 km (Figure 9) which possibly triggered the slumping process. The locations of the described slumping areas are sketched in Figure 10.

4.5. Slides

[36] Landslides are a form of avalanches which occur when the constituents of a material behave in a granular manner. The collapse of a previously stable slope of such material can be triggered by seismic shaking induced by nearby impact events [*Titley*, 1966; *Richardson Jr. et al.*, 2005]. The shock waves of these events briefly increase the shear stress and can trigger a slide when the slope does not return to a stable state. Once moving, the material converts potential energy into internal and kinetic energy. The motion is usually stopped by a topographic obstacle,

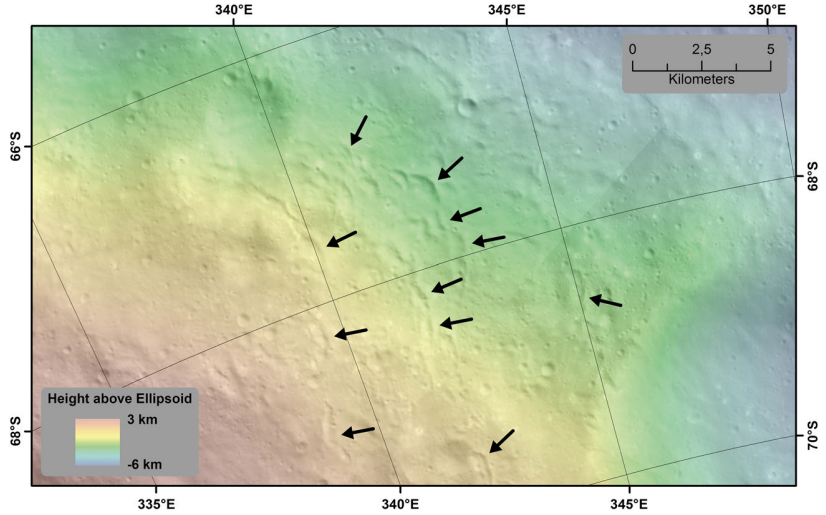

Figure 6. Creep-like features on Rheasilvia's central peak in the region centered at 68°S and 343°E. The arrows indicate examples of the elongated mounds. The creep-like mounds are parallel to the slope with a straight or slightly curved shape. The image is overlaid by a DTM referenced to a 285 km by 229 km spheroid. It is in a stereographic projection.

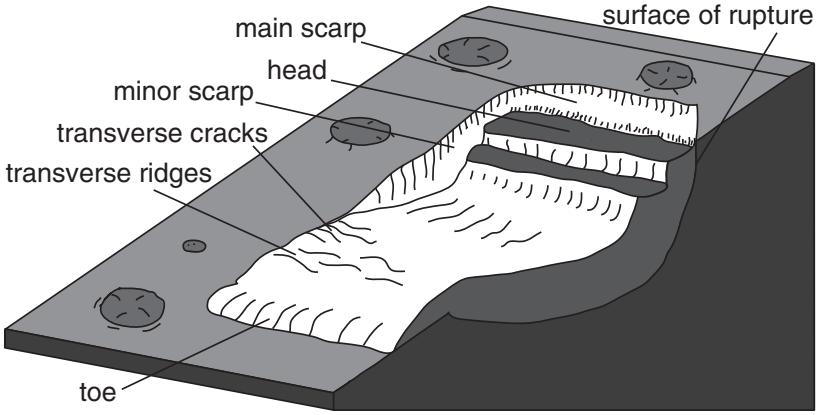

Figure 7. Schematics of a rotational slump. The rotational slump slides on a curved surface of rupture generating a main scarp and head feature. Further slumping results in minor scarps. The slumping body exhibits transverse cracks and ridges due to stretching and compression within the slumping body. The toe feature represents the front of the slump.

including reductions in slope which decrease slide momentum and provide a stable halting position.

[37] Boulders and smaller constituents of the slide collide during the movement, disintegrate, and distribute the momentum inside the slide in directions other than the downslope direction. This results in a spreading and widening of the landslide body where topography does not place constraints on the movement. This stretching is evident in landslides in the Rheasilvia basin (Figure 11).

[38] The Rheasilvia basin exhibits multiple ancient and recent landslides. The less eroded and younger landslides tend to be less massive in volume and runout length. The landslides migrated from the rim and central peak of Rheasilvia toward the basin floor. For most identified slides, an eroded scarp can be observed. The resting bodies of the slides consist of elongated lobes or widened fans of material.

[39] Figure 10 illustrates the distribution of landslides. The slides were separated into two categories, certain and possible, based upon the ease with which they could be identified. The landslides are almost evenly distributed along the crater rim and central peak. However, there is a region, identified above as a slumping area (section 4.4) between 10°E and 60°E in the Rheasilvia basin that is less populated with slides. The observed reduction in slides within the slumping area is consistent with other slumping areas, as slumping blocks consist of cohesive material that slides in blocks on the surface of rupture. Also, larger craters within the 10°E to 60°E area are likely to have altered the area so that slides are no longer identifiable.

[40] Some of the slides emanating from the rim of Rheasilvia tend to have a slightly curved runout. It is probable that they followed an underlying curved topography,

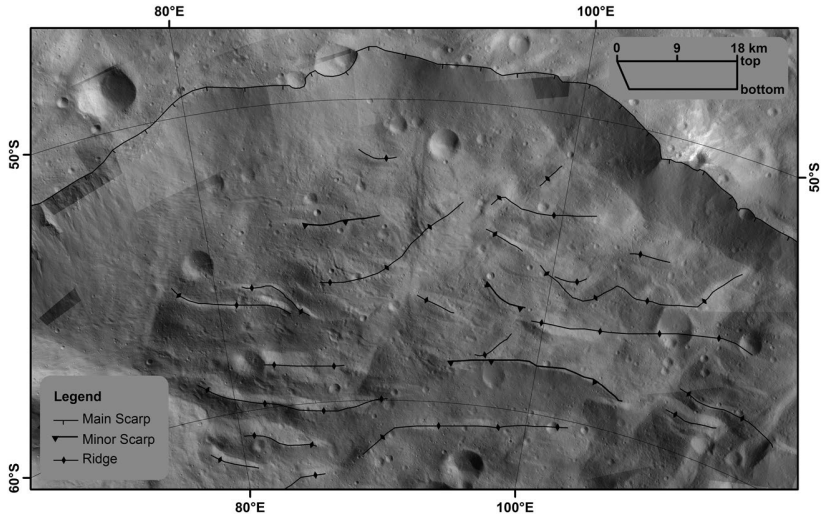

Figure 8. The youngest slumping area in the Rheasilvia basin along the scarp of Matronalia Rupes (main scarp), within the region of 45°S to 65°S and 75°E to 115°E. The minor scarp within the slumping body indicates slumping from previously wasted material, and ridges represent degraded scarps and material accumulations. The scarps and ridges were identified using the DTM and LAMO mosaic. The image is in a stereographic projection.

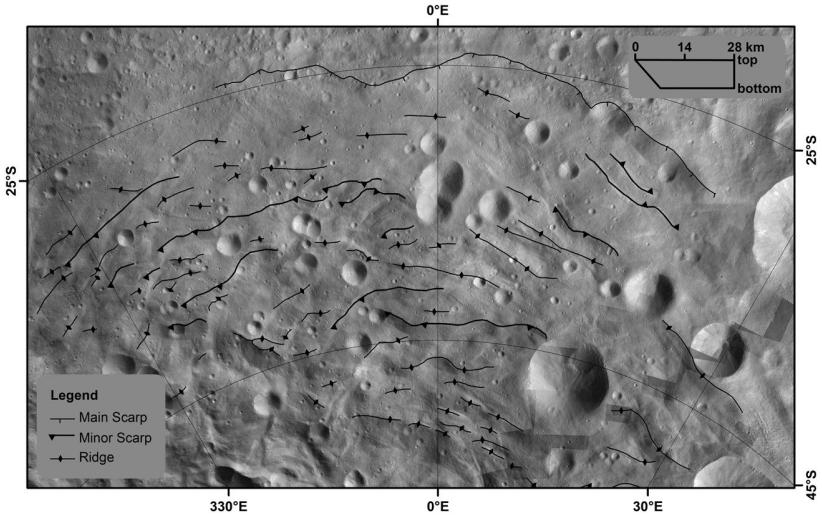

Figure 9. An ancient slumping body of Rheasilvia, within the area of 25°S to 55°S and 320°E to 40°E. The major scarp is the origin of the slumping block representing Rheasilvia's rim. Minor scarps within the slumping body indicate slumping from previously wasted material, and ridges represent degraded scarps and material accumulations. The larger impact craters were probably triggers for the slumping along scarps that they cross. The image is in a stereographic projection.

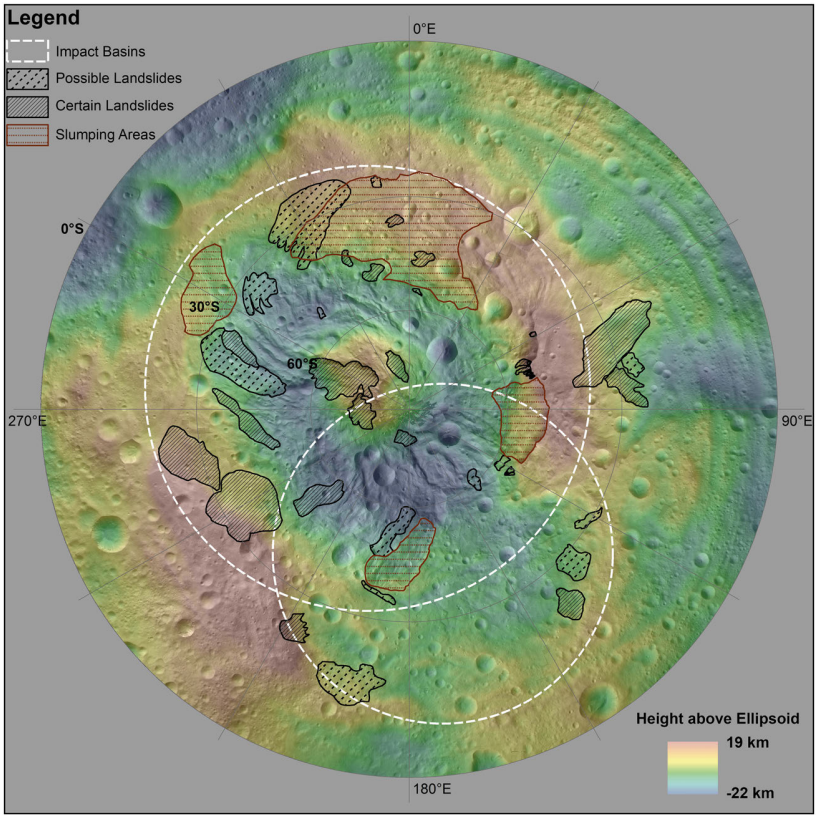

Figure 10. The distribution of landslides and slumping areas in the Rheasilvia and Veneneia area. Solid black lines represent reliable identification of landslides; dashed black lines mark possible landslides. Slumping areas are outlined in red. Landslides are distributed approximately homogeneously along the crater rim and on the central peak of Rheasilvia. Sliding and slumping areas are predominantly mutually exclusive with the exception of some small landslides within old slumping areas. The map is a stereographic projection on a sphere of 255 km radius overlaid by a DTM referenced to a 285 km by 229 km spheroid.

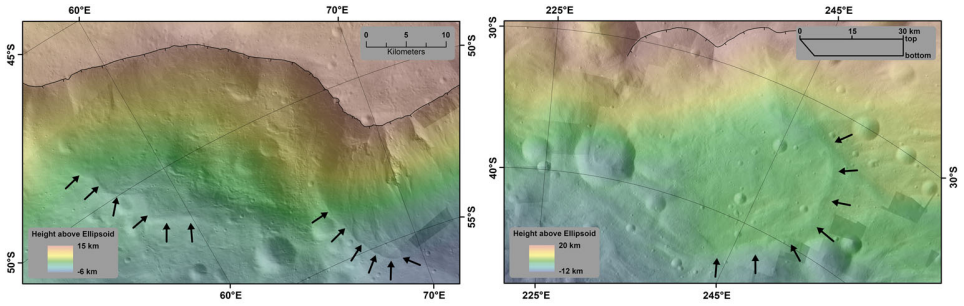

(a) (b)

Figure 11. (a) Recent landslides emanating from the Matronalia Rupes scarp within the region of 45°S to 55°S and 51°E to 75°E and (b) a rim slide within the area of 20°S to 49°S and 224°E to 266°E. The scarps from which the slides originate are outlined and arrows indicate their extent. In Figure 11a, note the spur formation on the right (∼40° slope) and the creep-like structures within the left landslide body (∼30° slope). In Figure 11b, the landslide forms a slope of ∼35° at the scarp (static angle of repose), decreasing to ∼5° at the toe of the slide (dynamic angle of repose). The images are in a stereographic projection with the scale bar applicable at the center of the images. They are overlaid by a DTM referenced to a 285 km by 229 km spheroid.

which might have been produced by the Coriolis Effect (section 5.2). The current topography may have been produced by structures generated during the Rheasilvia basin uplift and the subsequent movement of material along them.

[41] Figure 12 shows an example of a landslide being constrained by the surrounding topography. The landslide might have been triggered by the impact that formed nearby Canuleia (Figure 2b). Dark material emanates from the smooth rim of Canuleia in opposite directions: toward the crater center and outward from the crater rim. The crater rim is likely to have collapsed and the dark material moved toward topographic lows represented by both the cavity of Canuleia and the Rheasilvia floor. For comparison, examples of unconstrained landslides are shown in Figure 11.

[42] There are some slides not associated with an inward movement of material to the Rheasilvia floor. They show no evidence of curvature and can be found along the rim of Veneneia and close to the area of the flow-like feature shown in Figure 5 (within the area of 20°S to 45°S and 35°E to 95°E). In the case of Veneneia, the slides are compact and less elongated compared to those found along the Rheasilvia rim. Since the Veneneia basin has been extremely modified by the Rheasilvia impact and its ejecta, the identification of landslides associated with Veneneia is difficult.

[43] Along the Matronalia Rupes scarp, within the area of 50°S to 56°S and 66°E to 75°E (see Figure 11a), some smaller slides, with a gulley-like morphology [*Krohn et al.*, 2013], emanate downslope. The runout material cuts channels into the more solid slope material which sticks out as spurs. These slides are relatively young, with smooth surfaces and slopes of ∼40° or more. Larger slides usually self-flatten the slope to about 5° to 35° (Figure 11).

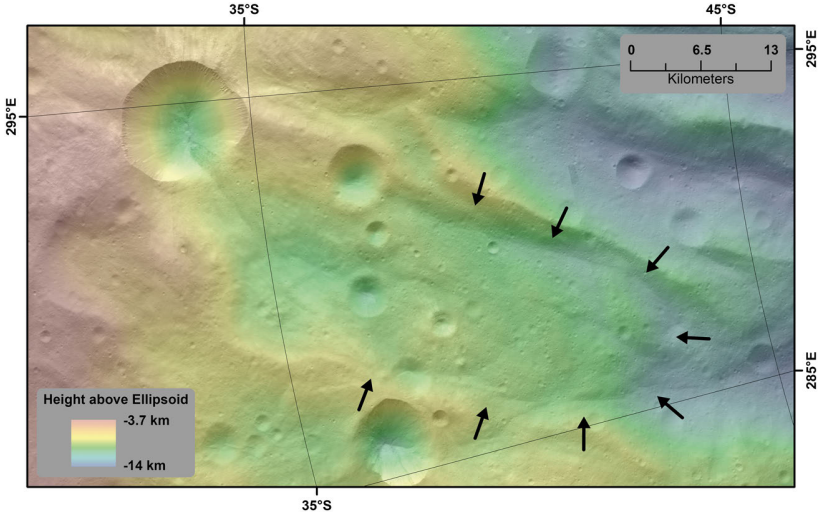

Figure 12. A landslide moving between two ridges of the underlying topography (arrows), located within the area of 30°S to 45°S and 285°E to 295°E. The landslide came to rest with a slope of ∼10° and was probably triggered by the impact crater in the top left of the image (Canuleia). The image is overlaid by a DTM referenced to a 285 km by 229 km spheroid. It is in a stereographic projection with the scale bar applicable at the center of the image.

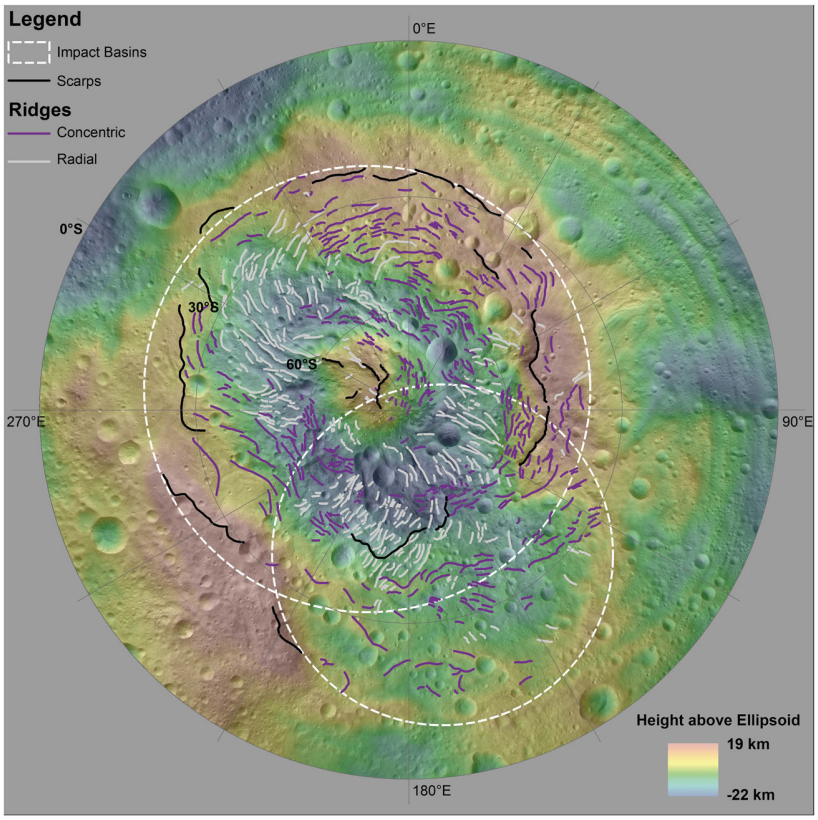

Figure 13. Curved ridges within the south polar basins. The outer scarps of the Rheasilvia basin and central uplift are outlined (black lines). The curved ridges are divided into radial ridges (grey lines) and concentric ridges (purple lines). A feature is labeled as a ridge when it is elongated and elevated from its surroundings in all directions. Scarps are a drop off from a plateau, resembling a step. The features were identified using the DTM. The map is a stereographic projection on a sphere of 255 km radius overlaid by a DTM referenced to a 285 km by 229 km spheroid.

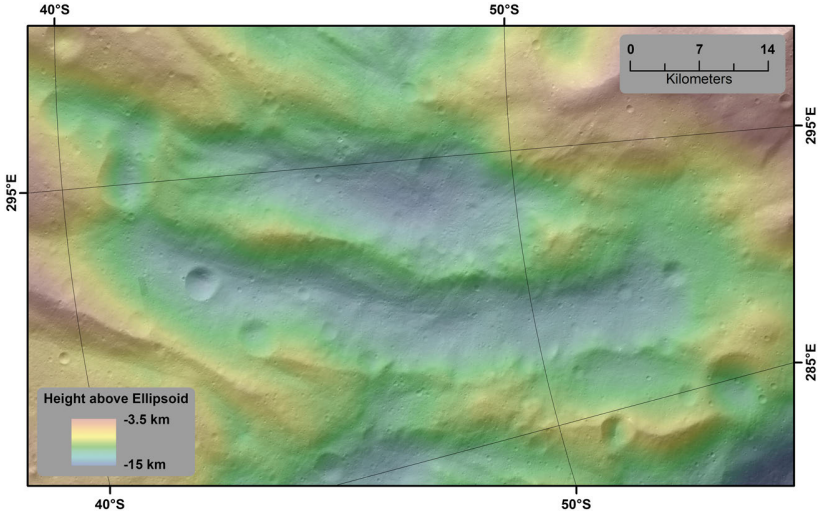

Figure 14. Curved radial ridges pointing toward the central peak within the area of 40°S to 55°S and 280°E to 300°E. The material in the valleys between the ridges shows flow-like structures, indicating movement of this material. The image is overlaid by a DTM referenced to a 285 km by 229 km spheroid. It is in a stereographic projection with the scale bar applicable at the center of the image.

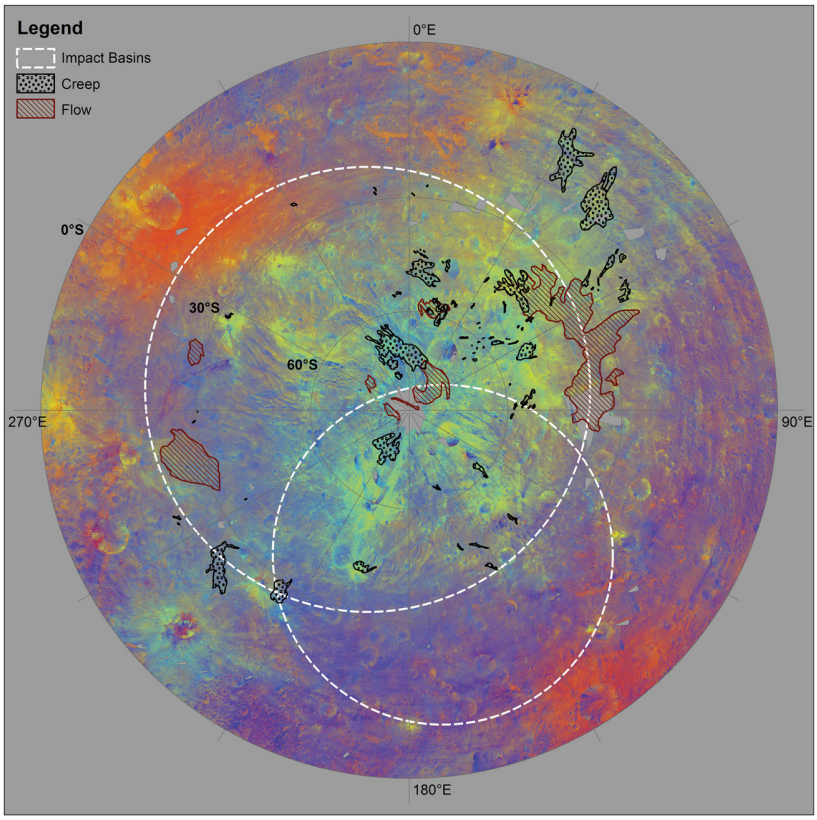

Figure 15. Distribution of flow-like and creep-like features on a color map of Vesta's southern hemisphere. The red, green, and blue colors represent the reflectance ratios of 749 nm/438 nm, 749 nm/917 nm, and 438 nm/749 nm, respectively (Clementine ratios equivalents). The clustering of the features agrees with the location of green-yellow material, which is a mixture of 749 nm/917 nm and 438 nm/749 nm ratios, indicating the depth of pyroxene absorption around 1000 nm and the change of absorption between visible infrared and ultraviolet wavelengths, respectively [*Tompkins and Pieters*, 1999]. The map is a stereographic projection on a sphere of 255 km radius.

[44] Slumping and sliding of material as part of gravitational collapse are ubiquitous within the Rheasilvia basin. Veneneia also shows some ancient slides. The relatively young slides and slumps at the Matronalia Rupes scarp demonstrate the ongoing collapse of the basin. Sliding and slumping have been the most effective degradation processes in the Rheasilvia basin because of their size and quantity.

4.6. Curved Ridges

[45] The Rheasilvia floor is characterized by numerous ridges and grooves that extend radially and concentrically over the impact basin (Figure 13) (see also *Mest et al.* [2013, in press]). They appear to be remnants of the early mass-wasting processes during the crater modification stage.

[46] The radial ridges are curved and up to 100 km long. The overall trend exhibits curvature against the rotational movement of Vesta close to the rim and toward the direction of rotation at the central peak (Figure 13, grey lines). They often run in parallel, with valleys separating them. In some cases, the valleys exhibit flow-like structures, indicating material migration. The radial ridges, which are ~2.5 km high with slopes varying from 10° to 20°, are present throughout the entire Rheasilvia basin but are most prominent between 270°E and 360°E (Figure 14). The base of the central peak also exhibits curved radial ridges between 330°E and 360°E and prominent curved scarps near the top.

[47] The curved radial ridges appear to be artifacts of the crater's early formation stage, shortly after the impact event. During the modification stage of a complex crater, material wastes toward the crater floor from the rim and rising central peak. The shocked material flowing downslope forms the substructure which may provide the general orientation of the ridges and grooves (Figure 13, grey lines) [*Melosh*, 1989]. Possible explanations for the curved nature of the ridges are given in section 5.2.

[48] The Rheasilvia basin also exhibits concentric ridges parallel to the crater rim (Figure 13, purple lines). They are generally smaller than the radial ridges with elevations of up to 1 km and lengths of up to 10 km. They often occur perpendicular to the slope which makes it likely they originated from the concentric crater collapse and relaxation after Rheasilvia had formed. The area between 0°E and 90°E is dominated by this type of ridge and also exhibits multiple larger craters likely to have trigged the concentric collapse by means of rotational slumping (see also section 4.4,

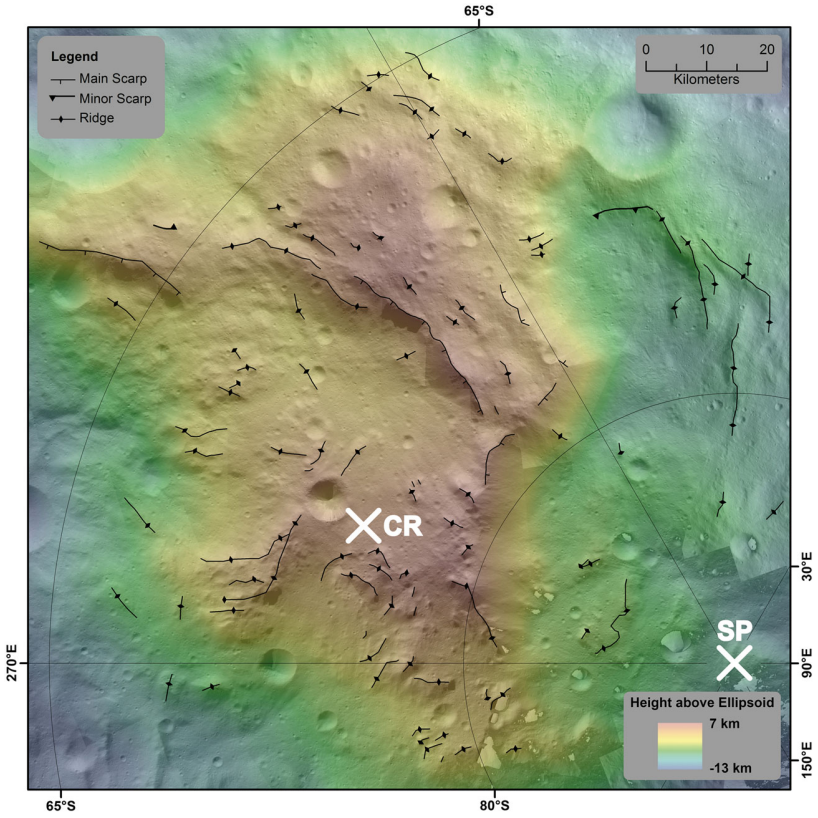

Figure 16. Scarps and ridges of Rheasilvia's central peak. The minor scarps indicate slumping from previously wasted material, and ridges represent degraded scarps and material accumulations. The main scarps are slightly curved in different directions suggesting a non-vertical stress component of the impact. The center of Rheasilvia (301°E and 75°S [*Jaumann et al.*, 2012]) and the south pole are labeled CR and SP, respectively. The image is in a stereographic projection with the scale bar applicable at the center of the image. It is overlaid by a DTM referenced to a 285 km by 229 km spheroid.

Figure 9). The Rheasilvia rim is interrupted at the intersection with Veneneia between 90°E and 220°E. Here the curved and concentric ridges cross with angles greater than 130°.

5. Discussion

[49] In the following passages, we discuss the correlation of mass-wasting features with spectral observations and the influence of the Coriolis Effect.

5.1. Flow-Like and Creep-Like Features

[50] *Reddy et al.* [2012] described Vesta's surface properties using color ratios determined with filters of the FC. They observed a swath of relatively higher 750 nm/920 nm and 980 nm/920 nm ratio material between 0°E and 90°E which they interpreted as Rheasilvia impact ejecta. In this area, the VIR spectrometer detects deeper absorption bands and shorter wavelengths that indicate a higher abundance of diogenites (lower crust material) [*De Sanctis et al.*, 2012]. The original upper crust material (eucritic material) was possibly covered by Rheasilvia impact ejecta.

[51] The diogenitic material (green-yellow in Figure 15) correlates with the flow-like and creep-like features. Diogenites originate from the lower crust of Vesta and thus must have been deposited as shocked and fragmented ejecta by Rheasilvia's impact event [*De Sanctis et al.*, 2012; *Reddy et al.*, 2012]. This material will therefore not only possess different spectral properties, aiding in its easy identification, but is also likely to have granular properties which differ from the other extant surface material and may encourage the formation of flow-like and creep-like features.

5.2. Spiral Pattern

[52] The ridge and groove patterns within the Rheasilvia basin show prominent spiral structures between 270°E and 360°E. Further, radial ridges are observed between 90°E and 220°E and on the central peak. These areas are dominated by curved radial ridges described in section 4.6 (Figure 13).

[53] A possible explanation for the curved pattern is the Coriolis Effect [*Schenk et al.*, 2012; *Jutzi et al.*, 2013]. The Coriolis force is a fictitious force that occurs in rotating inertial systems. A linear movement toward or away from the axis of rotation, seen from the outside, appears as a curved movement within the system. The curvature points against the direction of rotation for motion toward the rotation axis and in the direction of rotation for motion away from the axis. The structure on the crater wall of Rheasilvia

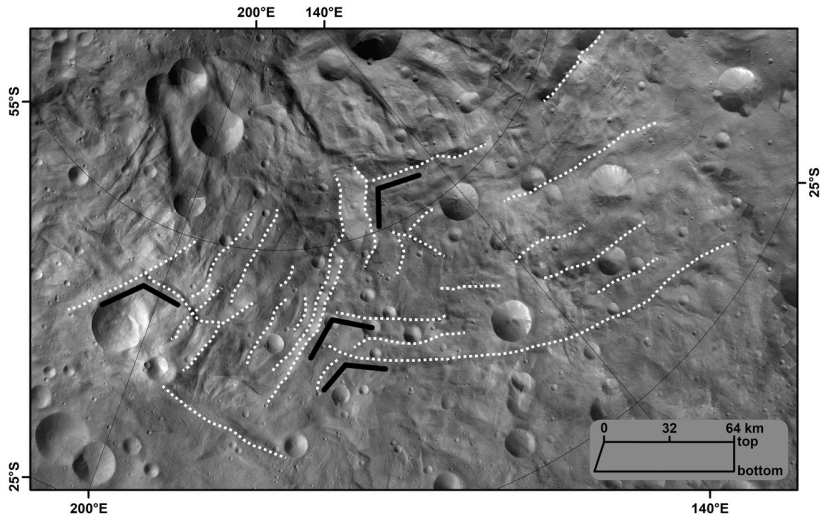

Figure 17. Curved ridges at the intersection of Rheasilvia and Veneneia in the area within 25°S to 65°S and 110°E to 210°E. The dashed lines mark the most prominent structures. Examples of the V-shaped crossings are indicated with black chevrons. They might be caused by the relaxation of a bi-layered target with ductile and brittle components. The image is in a stereographic projection with the scale bar applicable at the center of the image.

would therefore have been generated by a mass motion toward the rotation axis, which nearly agrees with the center of Rheasilvia. The patterns on the central peak suggest a motion away from the axis. This is consistent with the idea of masses moving downhill into the basin, off the crater rim and central peak, as the crater collapses.

[54] As described in section 4.6, the curved radial ridges appear to be remnants of the early gravitational crater collapse process. *Jutzi et al.* [2013] have simulated the Rheasilvia impact event on rotating Vesta using a 3-D smooth particle hydrodynamic impact code and found that gravitational crater collapse at velocities of ∼50 m/s is able to produce such a spiral pattern. The strength properties of material beneath the crater cavity during the early formation stage are plastic, with negligible internal friction [*Melosh*, 1989], which makes these relatively high wasting speeds likely. Thus, it is probable that the material wasting downslope during the early gravitational crater collapse was deflected by the Coriolis Effect.

[55] The ridge curvature can be used to infer the mass motion velocities. *Otto et al.* [2013] fitted a set of circular arcs to each curved ridge and using this method, the velocities could be estimated and are found to be in agreement with those predicted by *Jutzi et al.* [2013].

[56] The Coriolis Effect is capable of generating curved structures across the entire Rheasilvia crater. However, in some regions, for example, the central peak and the intersection of craters Rheasilvia and Veneneia, additional mechanisms may produce curved features.

[57] On Rheasilvia's central peak, an oblique impact might have been able to create curved scarps and ridges. A method for determining impact directions was devised by *Scherler et al.* [2006], who investigated the structure of ridges and faults of the central peak of Upheaval Dome (Utah, USA) to infer an impact direction. The Rheasilvia central peak exhibits bent fractures and faults visible as scarps from which material moved downhill (Figure 16). The analysis of the central imbrication structure of Rheasilvia after *Scherler et al.* [2006] is restricted by the small number of features and does not yield a definite impact direction. However, the curved main faults of the central peak, instead of straight radial expanded structures, indicate a non-vertical stress component, e.g., an oblique impact (Figure 13).

[58] At the intersection of Rheasilvia and Veneneia, the crater collapse of a two-layered target might have been able to produce the observed spiral pattern. The development of curved strike-slip faults has been demonstrated in experiments by *Allemand and Thomas* [1999]. They performed experiments in a two-layered target with the lower ductile layer and the upper brittle layer consisting of silicon and sand, respectively. A circular hole was cut through the layers, and the relaxation process with variable layer thicknesses was observed. The collapse process produced spiral strike-slip faults for low brittle-ductile thickness ratios. These faults crossed in a characteristic V-shaped pattern, meaning that the faults intersected at angles above 130° (Figure 17). The spirals developed on the crater wall but more prominently beyond the crater rim.

[59] The brittle-ductile thickness ratio of the intersection of Rheasilvia and Veneneia is reduced because the Veneneia impact removed parts of the brittle surface. The ratio might be sufficiently low to allow spirals, represented by curved ridges, to form during the relaxation process. Furthermore, the spiral pattern in this region expands beyond the Rheasilvia rim as expected by the *Allemand and Thomas* [1999] theory.

[60] The Coriolis Effect is the only process that can explain the curved pattern at all locations; however, the oblique impact and crater relaxation theory cannot be completely ruled out for the central peak and Rheasilvia-Veneneia intersection, respectively.

6. Summary

[61] The impact basins of Rheasilvia and Veneneia show various mass-wasting features that suggest different types of material properties and conditions. We identified six different mass-wasting types, including intra-crater mass wasting, flow-like movements, creep-like features, rotational slumping, landslides, and curved ridges.

[62] We classified five intra-crater mass-wasting features including lobate slides, rocky spurs along the rim, boulders inside the crater, dark albedo bands on the crater wall, and talus material in commonly fresh craters in the southern hemisphere. Not all craters exhibit every feature, but the occurrence is nearly homogeneously distributed.

[63] The flow-like and creep-like features are phenomena of shocked and fractured material. Their occurrence is increased in the region between 0°E and 90°E in the Rheasilvia basin. Outside the basin, they form on the slopes of the basin rim, again clustering between 0°E and 90°E. This correlates with the appearance of spectral variations observed with the color filters (green-yellow material applying Clementine ratios) and was suggested to be Rheasilvia impact ejecta [*Reddy et al.*, 2012].

[64] Slumping toward Rheasilvia's center occurs in a rotational form, meaning that larger cohesive slumping blocks slide on a spoon-like shaped surface of rupture. Some slumping regions indicate a concentric collapse of the basin, others are tilted relative to the crater rim of Rheasilvia. We identified three older slumping regions. The younger slumping area along the Matronalia Rupes scarp proves the ongoing erosional degradation of Rheasilvia.

[65] We observed features indicative of landslides in both the Rheasilvia and Veneneia basins. The landslides originate from the crater rims and also from Rheasilvia's central peak. Older landslides are generally widened features, whereas younger landslides, as those identified on the slope of Matronalia Rupes scarp, exhibit lobate structures. Slides and slumping areas are predominantly mutually exclusive because of the cohesive and granular material properties for slumping and sliding masses, respectively.

[66] The Rheasilvia basin exhibits curved ridges, both concentric to the crater rim and in a radial direction. The concentric ridges are likely to be remnants of the terraced crater rim collapse. The curved radial ridges are most prominent between 270°E and 360°E. As the center of Rheasilvia nearly coincides with the rotational axis, the Coriolis force is likely to have deflected radial mass motions of the early crater collapse process. This process is plausible for the entire Rheasilvia basin; however, at the intersection area of Rheasilvia and Veneneia and on Rheasilvia's central peak, additional processes may have played a role in the formation of the curved radial ridges. The curved features at the intersection of Rheasilvia and Veneneia cross in a characteristic V-shaped pattern and can be interpreted as strike-slip faults that are generated during the collapse process of Rheasilvia on a bi-layered target with brittle and ductile components. The bent pattern of scarps and ridges on Rheasilvia's central peak suggests a non-vertical stress component which might have been produced by an oblique impact.

[67] **Acknowledgments.** We thank D. P. O'Brien, the two anonymous reviewers and the associate editor for their helpful and constructive comments.

References

Allemand, P., and P. Thomas (1999), Small-scale models of multiring basins, *J. Geophys. Res.*, *104*(E7), 16,501–16,514, doi:10.1029/1999JE900008.

Archinal, B. A., et al. (2011), Report of the IAU working group on cartographic coordinates and rotational elements: 2009, *Celestial Mech. Dyn. Astron.*, *109*(2), 101–135, doi:10.1007/s10569-010-9320-4.

Binzel, R. P., and S. Xu (1993), Chips off of asteroid 4 Vesta: Evidence for the parent body of basaltic achondrite meteorites, *Science*, *260*(5105), 186–191, doi:10.1126/science.260.5105.186.

Collins, G. S., J. Morgan, P. Barton, G. L. Christeson, S. Gulick, J. Urrutia, M. Warner, and K. Wünnemann (2008), Dynamic modeling suggests terrace zone asymmetry in the Chicxulub crater is caused by target heterogeneity, *Earth Planet. Sci. Lett.*, *270*(3-4), 221–230, doi:10.1016/j.epsl.2008.03.032.

Consolmagno, G. J., and M. J. Drake (1977), Composition and evolution of the eucrite parent body: Evidence from rare earth elements, *Geochim. Cosmochim. Acta*, *41*(9), 1271–1282, doi:10.1016/0016-7037(77)90072-2.

De Blasio, F. V. (2011), *Introduction to the Physics of Landslides: Lecture Notes on the Dynamics of Mass Wasting*, Springer, Dordrecht, Heidelberg, London, New York.

De Sanctis, M. C., et al. (2010), The VIR Spectrometer, *Space Sci. Rev.*, *163*(1-4), 329–369, doi:10.1007/s11214-010-9668-5.

De Sanctis, M. C., et al. (2012), Spectroscopic characterization of mineralogy and its diversity across Vesta, *Science*, *336*(6082), 697–700, doi:10.1126/science.1219270.

Jaumann, R., et al. (2012), Vesta's shape and morphology, *Science*, *336*(6082), 687–690, doi:10.1126/science.1219122.

Jutzi, M., E. Asphaug, P. Gillet, J.-A. Barrat, and W. Benz (2013), The structure of the asteroid 4 Vesta as revealed by models of planet-scale collisions, *Nature*, *494*(7436), 207–210, doi:10.1038/nature11892.

Keil, K. (2002), Geological history of asteroid 4 Vesta: The "smallest terrestrial planet", in *Asteroids III*, edited by W. F. Bottke Jr. et al., pp. 573–584, Univ. of Ariz. Press, Tucson, Ariz.

Khosropour, R., J. Zirinsky, H. K. Pak, and R. P. Behringer (1997), Convection and size segregation in a Couette flow of granular material, *Phys. Rev. E*, *56*(4), 4467–4473, doi:10.1103/PhysRevE.56.4467.

Kleinhans, M. G., H. Markies, S. J. de Vet, A. C. in 't Veld, and F. N. Postema (2011), Static and dynamic angles of repose in loose granular materials under reduced gravity, *J. Geophys. Res.*, *116*, E11004, doi:10.1029/2011JE003865.

Krohn, K., et al. (2013), Mass movements at steep scarps and crater rims in the Sextilia Quadrangle on Vesta, paper presented at 15th EGU General Assembly 2013, EGU2013-3213, Vienna, Austria. 07-12 April 2013, Abstract available at http://meetingorganizer.copernicus.org/EGU2013/EGU2013-3213.pdf.

Li, J.-Y. (2012), Body-fixed coordinate systems for asteroid (4) Vesta, sbn.psi.edu/archive/dawn/fc/DWNVFC2_1A/DOCUMENT/VESTA_COORDINATES/VESTA_COORDINATES_120918.PDF.

Marchi, S., et al. (2012), The violent collisional history of asteroid 4 Vesta, *Science*, *336*(6082), 690–694, doi:10.1126/science.1218757.

McCord, T. B., J. B. Adams, and T. V. Johnson (1970), Asteroid Vesta: Spectral reflectivity and compositional implications, *Science*, *168*(3938), 1445–1447, doi:10.1126/science.168.3938.1445.

McCord, T. B., L. A. McFadden, C. T. Russell, C. Sotin, and P. C. Thomas (2006), Ceres, Vesta, and Pallas: Protoplanets, not asteroids, *Eos Trans. AGU*, *87*(10), 105–109, doi:10.1029/2006EO100002.

Melosh, H. J. (1986), The physics of very large landslides, *Acta Mech.*, *64*(1-2), 89–99, doi:10.1007/BF01180100.

Melosh, H. J. (1989), *Impact Cratering, Oxford Monographs on Geology and Geophysics No. 11*, Oxford Univ. Press, New York.

Miyamoto, H., et al. (2007), Regolith migration and sorting on asteroid Itokawa, *Science*, *316*(5827), 1011–1014, doi:10.1126/science.1134390.

Otto, K. A., et al. (2013), The Coriolis Effect on Vesta's southern basin Rheasilvia, paper presented at 8th European Planetary Science Congress 2013, EPSC2013-233, London, U. K., available at http://meetingorganizer.copernicus.org/EPSC2013/EPSC2013-233.pdf.

Pieters, C. M., L. A. McFadden, T. Prettyman, M. C. De Sanctis, T. B. McCord, T. Hiroi, R. Klima, J. Y. Li, and R. Jaumann (2011), Surface composition of Vesta: Issues and integrated approach, *Space Sci. Rev.*, *163*(1), 117–139, doi:10.1111/j.1945-5100.1999.tb01729.x.

Poelchau, M. H., and T. Kenkmann (2008), Asymmetric signatures in simple craters as an indicator for an oblique impact direction, *Meteorit. Planet. Sci.*, *43*(12), 2059–2072, doi:10.1111/j.1945-5100.2008.tb00661.x.

Prettyman, T. H., et al. (2011), Dawn's Gamma Ray and Neutron Detector, *Space Sci. Rev.*, *163*(1-4), 371–459, doi:10.1007/s11214-011-9862-0.

Preusker, F., F. Scholten, K.-D. Matz, T. Roatsch, R. Jaumann, C. A. Raymond, and C. T. Russell (2012), Topography of Vesta from Dawn FC stereo images, paper presented at 7th European Planetary Science Congress 2012, abstract EPSC2012-428-1, Madrid, Spain, available at http://meetingorganizer.copernicus.org/EPSC2012/EPSC2012-428-1.pdf.

Rayman, M. D., T. C. Fraschetti, C. A. Raymond, and C. T. Russell (2006), Dawn: A mission in development for exploration of main belt asteroids Vesta and Ceres, *Acta Astronaut.*, *58*(11), 605–616, doi:10.1016/j.actaastro.2006.01.014.

Raymond, C. A., et al. (2011), The Dawn topography investigation, *Space Sci. Rev.*, *163*(1-4), 487–510, doi:10.1007/s11214-011-9863-z.

Raymond, C. A., et al. (2012), Initial models of Vesta's crust and mantle, paper presented at 7th European Planetary Science Congress 2012, abstract EPSC2012-818-1, Madrid, Spain, available at http://meetingorganizer.copernicus.org/EPSC2012/EPSC2012-818.pdf.

Reddy, V., et al. (2012), Color and albedo heterogeneity of Vesta from Dawn, *Science*, *336*(6082), 700–704, doi:10.1126/science.1219088.

Richardson, J. E., H. J. Melosh, and R. J. Greenberg (2004), Impact-induced seismic activity on asteroid 433 Eros: A surface modification process, *Science*, *306*(5701), 1526–1529, doi:10.1126/science.1104731.

Richardson Jr., J. E., H. J. Melosh, R. J. Greenberg, and D. P. O'Brien (2005), The global effects of impact-induced seismic activity on fractured asteroid surface morphology, *Icarus*, *179*(2), 325–349, doi:10.1016/j.icarus.2005.07.005.

Roatsch, T., E. Kersten, K.-D. Matz, F. Preusker, F. Scholten, S. Elgner, R. Jaumann, C. A. Raymond, and C. T. Russell (2013), High-resolution Vesta Low Altitude Mapping Orbit Atlas derived from Dawn Framing Camera images, *Planet. Space Sci.*, *85*, 293–298, doi:10.1016/j.pss.2013.06.024.

Russell, C. T., and C. A. Raymond (2011), The Dawn mission to Vesta and Ceres, *Space Sci. Rev.*, *163*(1-4), 3–23, doi:10.1007/s11214-011-9836-2.

Russell, C. T., et al. (2004), Dawn: A journey in space and time, *Planet. Space Sci.*, *52*(5-6), 465–489, doi:10.1016/j.pss.2003.06.013.

Russell, C. T., et al. (2012), Dawn at Vesta: Testing the protoplanetary paradigm, *Science*, *336*(6082), 684–686, doi:10.1126/science.1219381.

Schenk, P., et al. (2012), The geologically recent giant impact basins at Vesta's south pole, *Science*, *336*(6082), 694–697, doi:10.1126/science.1223272.

Scherler, D., T. Kenkmann, and A. Jahn (2006), Structural record of an oblique impact, *Earth Planet. Sci. Lett.*, *248*(1-2), 43–53, doi:10.1016/j.epsl.2006.05.002.

Schultz, P. H., and D. E. Gault (1975), Seismically induced modification of lunar surface features, *Lunar Sci. Conf. Proc.*, *6*, 2845–2862.

Shingareva, T. V., and R. O. Kuzmin (2001), Mass-wasting processes on the surface of Phobos, *Sol. Syst. Res.*, *35*, 431–443.

Sierks, H., et al. (2011), The Dawn Framing Camera, *Space Sci. Rev.*, *163*(1-4), 263–327, doi:10.1007/s11214-011-9745-4.

Thomas, P. C., R. P. Binzel, M. J. Gaffey, A. D. Storrs, E. N. Wells, and B. H. Zellner (1997), Impact excavation on asteroid 4 Vesta: Hubble Space Telescope results, *Science*, *277*(5331), 1492–1495, doi:10.1126/science.277.5331.1492.

Thomas, P. C., et al. (2002), Eros: Shape, topography, and slope processes, *Icarus*, *155*(1), 18–37, doi:10.1006/icar.2001.6755.

Titley, S. R. (1966), Seismic energy as an agent of morphologic modification on the Moon, *Tech. Rep.*, U.S. Geol. Surv., Flagstaff, Ariz.

Tompkins, S., and C. M. Pieters (1999), Mineralogy of the lunar crust: Results from Clementine, *Meteorit. Planet. Sci.*, *34*(1), 25–41.

Williams, D. A., et al. (2013), Lobate and flow-like features on asteroid Vesta, *Planet. Space Sci.*, doi:10.1016/j.pss.2013.06.017, in press.

Zuber, M. T., H. Y. McSween, R. P. Binzel, L. T. Elkins-Tanton, A. S. Konopliv, C. M. Pieters, and D. E. Smith (2011), Origin, internal structure and evolution of 4 Vesta, *Space Sci. Rev.*, *163*(1-4), 77–93, doi:10.1007/s11214-011-9806-8.

D. Curriculum Vitae

Personal data are not part of the online publication.